

Energy Frontiers Focus Topic

Room: 15 - Session EN+NS-MoM

Nanostructured Solar Cells

Moderator: M.S. Arnold, University of Wisconsin Madison

8:20am EN+NS-MoM1 **Doping Control for the Development of Silicon Quantum Dot Solar Cell**, *K.J. Kim, J.H. Park*, Korea Research Institute of Standards and Science (KRISS), Republic of Korea, *H.-J. Baek, H.H. Hwang*, University of Science and Technology (UST), Republic of Korea, *J.S. Jang*, Chungbuk National University (CBNU), Republic of Korea

Si quantum dots (QDs) imbedded in a SiO₂ matrix is a promising material for the next generation optoelectronic devices, such as solar cells and light emission diodes (LEDs). However, low conductivity of the Si quantum dot layer is a great hindrance for the performance of the Si QD-based optoelectronic devices. The effective doping of the Si QDs by semiconducting elements is one of the most important factors for the improvement of conductivity. High dielectric constant of the matrix material SiO₂ is an additional source of the low conductivity.

Active doping of B in Si nano structures and the effect of internal polycrystalline bridge layer were investigated by secondary ion mass spectroscopy (SIMS) depth profiling analyses. Phosphorous and boron doped-Si / SiO₂ multilayers on Si wafers were fabricated by ion beam sputtering deposition as a model structure for the study of the diffusion behavior of the dopants. The distributions of the dopants after annealing at high temperatures were analyzed by SIMS depth profiling analyses.

In this study, the diffusion behaviors of various dopants in silicon nanostructures will be discussed and the effects of the various parameters for the improvement of conversion efficiency in Si quantum dot solar cell will be introduced.

8:40am EN+NS-MoM2 **Photocarrier Generation in Si Quantum-dot Sensitized Solar Cells**, *G. Uchida, H. Seo, Y. Wang, K. Kamataki, N. Itagaki, K. Koga, M. Shiratani*, Kyushu University, Japan

The pressing need for massively scalable carbon-free energy sources has focused attention on both increasing the efficiency and decreasing the cost of solar cells. Quantum-dot (QD) solar cells employing multiple exciton generation (MEG) have attracted much attention as a candidate for the third generation solar cells, because MEG represents a promising route to increased solar conversion efficiencies up to about 44 % in single junction. Our interest has been concerned with QD sensitized solar cells using Si nanoparticles [1]. The main purpose of this study is to discuss the characteristic of the quantum yield in view of the MEG effect.

QD thin films composed of size-controlled Si nanoparticles were deposited using double multi-hollow discharge plasma chemical vapour deposition (CVD) of a SiH₄/H₂ and CH₄ or N₂ gas mixture [2]. Short-circuit current density of Si QD sensitized solar cells increases by a factor of 2.5 by irradiation of CH₄ or N₂ plasma to Si nanoparticle surface. We also have measured incident photon-to-current conversion efficiency (IPCE) in the near-ultraviolet range using quartz-glass plates as front panels of QD sensitized solar cells. IPCE gradually increases by light irradiation in a wavelength range less than 600 nm around optical band-gap (E_g) of Si nanoparticle films, and then steeply increases below 280 nm around 2E_g. This rapid increase of IPCE under the ultraviolet light incidence may be explained by the theoretically predicted MEG, the creation of two electron-hole pairs from one high-energy photon incidence, in Si nanoparticle QDs.

[1] G. Uchida, et al., Phys. Status Solidi C 8 (2011) 3021.

[2] G. Uchida, et al., Jpn. J. Appl. Phys. 51 (2011) 01AD01-1.

9:00am EN+NS-MoM3 **Quantum Dot Solar Cells with External Quantum Efficiency Exceeding 100% by Multiple Exciton Generation**, *J.M. Luther, M.C. Beard, A.J. Nozik, O.E. Semonin*, National Renewable Energy Laboratory

INVITED

Traditional semiconductors used in photovoltaic devices produce one electron from each absorbed photon. On the other hand, new materials such as quantum dots, nanorods, carbon nanotubes and graphene can more efficiently convert high-energy photons into multiple electron-hole pairs through a process titled multiple exciton generation (MEG) provided that the energy of the photon is at least twice the bandgap of the absorber. This process has been shown to be more efficient in highly confined quantum dots than other forms of carrier multiplication (such as impact ionization) in bulk materials. Photovoltaic devices can benefit greatly from MEG by producing increased photocurrent from the multiple electrons and thus allowing a single junction solar cell to yield a theoretical maximum

efficiency as high as 44% compared to 33% for bulk semiconductors. In this talk, we will present recent findings from incorporating PbSe quantum dots (QDs) into semiconducting arrays that make up the absorber layer in prototype solar cells. In these devices, MEG is confirmed by demonstrating the first solar cell with external quantum efficiency (EQE) exceeding 100% for solar relevant photon energies. The EQE in our device reaches a maximum value of 114% at 380 nm and we have employed an optical model to determine that the PbSe QD layer produces as many as 1.3 electrons per photon (on average) for these photons. These findings are compared to ultrafast time resolved measurements of carrier quantum yields where we find reasonable agreement. We will also discuss future directions for materials designs that increase the quantum yield through more efficient MEG.

9:40am EN+NS-MoM5 **Quantum-Confined Nanocrystals as Building Blocks for Low-Cost Solution-Processed Multi-Junction Solar Cells**, *T. Hanrath, J.W. Choi, W.N. Wenger, R.S. Hoffman*, Cornell University

In light of recent advances in synthesis, characterization, and the emerging understanding of their size-dependent properties, there are many exciting opportunities for semiconductor nanomaterials to contribute to the development of next-generation energy conversion technologies. Semiconductor nanocrystal quantum dots are particularly attractive material candidates for the efficient capture of solar emission in inexpensive, thin film photovoltaic devices due to their large absorption cross sections, low-cost solution-phase processing and size-tunable energy gaps. The prospect of exploiting colloidal nanostructures for the creation of low-cost multi-junction solar cells has garnered immense scientific and technological interest. We recently demonstrated solution-processed tandem solar cells created from nanocrystal quantum dots with size-tuned energy levels. Bringing this prospect to fruition requires the connection of absorber layers with cascaded energy gaps subject to stringent electrical and optical constraints. We show that interlayers composed of ZnO/Au/PEDOT provide appropriate carrier density and energy-level alignment to resolve this challenge. With such interlayers we have been able to create nanocrystal quantum dot tandem cells that exhibit IR sensitivity and an open circuit voltage approaching 1V. These advances provide guidelines for the design of an effective interlayer in tandem cell devices and suggest a promising future for solution-processed nanocrystal quantum dot solar cells.

10:00am EN+NS-MoM6 **Improvement of Carrier Transport in PbSe Quantum Dot-Embedded Polymeric Solar Cells Fabricated by a Laser Assisted Spray Process**, *C. Hettiarachchi, D.M. Feliciano, D. Mukherjee, P. Mukherjee, S. Witanachchi*, University of South Florida

PbSe quantum dots (QD) in the size range of 4-8 nm are promising candidates for solar energy harvesting as they exhibit multi-exciton generation with ultraviolet (UV) photon absorption. While generation of multi-excitons has been demonstrated, dissociation of excitons to enhance current densities has not been realized. One of the main bottlenecks has been the difficulty in removing the surfactants on QDs to form a clear interface between the QD and the polymer matrix. We have developed a Laser Assisted Spray (LAS) deposition technique to deposit uniform coatings of surfactant-free QDs on substrates. This technique involves the transient heating of aerosols containing PbSe QDs by a CO₂ laser-gas interaction to burn the organic surfactants. Transmission electron micrographs and absorption spectroscopy show, under optimum conditions, the particles remain as single crystals and maintain quantum confinement. Growth parameters are optimized by monitoring the degree of surfactant removal by studying the Fourier Transform Infrared (FTIR) spectra of coatings grown by LAS technique. Two-layer solar cell structures of PbSe/polymer that is sandwiched between ITO and Al electrodes have been fabricated. Comparison of the IV characteristics of these cells and cells fabricated by PbSe QDs with ligand-exchange will be presented.

10:40am EN+NS-MoM8 **Single and Multiple Exciton Dissociation in Colloidal Nanoheterostructures**, *T. Lian*, Emory University

INVITED

The ability to control charge transfer dynamics to and from quantum dots (QDs) is essential to many QD-based devices, such as solar cells and light emitting diodes. Recent reports of multiple exciton generation (MEG) by one absorbed photon in some QDs offer an exciting new approach to improve the efficiency of QD-based solar cells and to design novel multi-electron/hole photocatalysts. Two major challenges remain. First, the efficiency of MEG process needs to be significantly improved for practical applications. Second, the utilization of multi-excitons requires ultrafast exciton dissociation to compete with the exciton-exciton annihilation process, which occurs on the 10s to 100s ps time scale. In this presentation we report a series of studies of exciton dissociation dynamics in QDs and nanorods by electron transfer to adsorbed electron acceptors. We show that

excitons in CdX (X=S, Se, Te) and PbS QDs can be dissociated on the picosecond and faster timescales and multiple excitons (generated by multiple photons) per QD can be dissociated by electron transfer to adsorbed acceptors. We discuss approaches for optimizing the single and multiple exciton dissociation efficiencies by controlling the spatial distributions of the electron and hole (i.e. wave-function engineering) in type II core/shell QDs and nanorods.

11:40am **EN+NS-MoM11 Intermediate Band Upconversion for Low-Cost, Solution Processed Photovoltaics**, *J. Lewis, E.J.D. Klem, C.W. Gregory, G.B. Cunningham, S. Hall, D.S. Temple*, RTI International

PV devices based on disordered semiconductors such as polymers, organic small molecules, and colloidal quantum dots have seen gradually improving performance in recent years, but are likely to be limited to efficiencies in the range of 10–15%. To increase efficiency further would require the use of tandem cells, which adds complexity and cost. Alternatively one can pursue devices such as intermediate band solar photovoltaics (IBPV) that can exceed the Shockley-Queisser efficiency limit. In an IBPV device mid-gap states are incorporated into a wider band-gap host, allowing infrared photons to contribute to the photocurrent of the device via sequential absorption of two photons. Ideally this occurs without compromising the open circuit voltage. We will present the first example of an IBPV solar cell using solution processed, low-cost disordered materials. We show that the nature of the defect states in Pb-salt quantum dots is uniquely suited to efficient upconversion at optical power densities that are relevant for unconcentrated solar illumination. This demonstration provides a path for a step-change in the efficiency of low-cost PV.

Graphene and Related Materials Focus Topic

Room: 13 - Session GR+EM+NS+PS+SS+TF-MoM

Graphene Growth

Moderator: M. Spencer, Cornell University, V.D. Wheeler, U.S. Naval Research Laboratory

8:20am **GR+EM+NS+PS+SS+TF-MoM1 Synthesis Ingredients Enabling Low Noise Epitaxial Graphene Applications**, *D.K. Gaskill, L.O. Nyakiti, V.D. Wheeler*, U.S. Naval Research Lab, *A. Nath*, George Mason Univ., *V.K. Nagareddy*, Newcastle University, UK, *R.L. Myers-Ward, N.Y. Garces, S.C. Hernández, S.G. Walton*, U.S. Naval Research Lab, *M.V. Rao*, George Mason Univ., *A.B. Horsfall*, Newcastle Univ., UK, *C.R. Eddy, Jr.*, U.S. Naval Research Lab, *J.S. Moon*, HRL Labs LLC

Sensors made from graphene flakes have demonstrated single molecule detection [Schedin *et al.*, Nat Mat 6, 652 (2007)]; this ultra-sensitivity is likely due to the high crystalline quality of the graphene and the associated relative lack of defects that give rise to noise. The low noise nature of high quality graphene should also facilitate other applications, e.g., low-noise amplifiers. Combined with the unique ambipolar property of graphene field effect transistors (FETs), the low noise character of graphene would significantly advance the performance of frequency multipliers, mixers and high-speed radiometers. To exploit these applications, high quality, reproducible wafer-scale epitaxial graphene (EG) with minimal thickness variations and defects are essential requirements. Here, crucial graphene synthesis elements required to achieve the wafer-scale quality goal are described. Understanding the effect of substrate misorientation as well as hydrogen etch and Si sublimation conditions for graphene synthesis on the (0001) SiC surface is essential to achieve improved and reproducible wafer-scale graphene quality. For example, the impact of processing factors such as temperature control, laminar gas flow and substrate rotation on large area EG uniformity are described using examples created in an Aixtron SiC epitaxy reactor. In addition, managing SiC step formation on the nominal (0001) orientation is significant for achieving uniform EG thickness on terraces and to minimize additional growth at the step edges; this is illustrated using data from atomic force microscopy and scanning electron microscopy images in combination with Raman spectroscopy maps and x-ray photoelectron spectroscopy analysis. Managing step formation combined with optimal growth leads to the suppression of the Raman defect “D” band confirming minimal grain boundaries and defects, which are additional sources of electronic noise. Lastly, contactless Leighton resistivity maps of 75 mm wafers are used to illustrate the overall uniformity of optimally synthesized graphene as well as to show the resistance state-of-the-art, with individual wafers exhibiting about a $\pm 3\%$ relative variation. Examples of the impact of this synthesis approach on chemical sensors devices and FETs will be shown, each exhibiting $1/f$ noise behavior down to 1 Hz and possessing noise spectral densities similar to reports from exfoliated graphene. Hence, careful control of EG formation across the wafer results in improved quality which subsequently leads to the

reduction or elimination of additional noise sources from graphene defects that would then adversely affect device performance.

8:40am **GR+EM+NS+PS+SS+TF-MoM2 Growth of Graphene by Catalytic Decomposition of Ethylene on Cu(100) and Cu(111) With and Without Oxygen Pre-dosing**, *Z.R. Robinson, P. Tyagi, T. Mowll, C.A. Ventrice, Jr.*, University at Albany- SUNY, *K. Clark, A.-P. Li*, Oak Ridge National Laboratory

Graphene growth on Cu substrates has become one of the most promising techniques for the mass production of graphene, and therefore significant effort has been put into developing growth conditions that lead to large area, defect and grain boundary free graphene films. One key consideration is the influence that the underlying copper substrate has on the growth of the graphene. In order to study this, graphene growth on Cu(100) and Cu(111) was carried out in a UHV system. The samples were heated using an oxygen series button heater. The hydrocarbon pressure was measured using a capacitive manometer instead of an ion gauge, which could cause dissociation of the hydrocarbon molecules. Initially, it was found that annealing the crystals to 900 °C resulted in impurity segregation at the surface. Several cycles of sputtering at 600 °C were required to remove all bulk impurities so that the surface remained clean even after annealing to 900 °C. Initial attempts to grow graphene by annealing each crystal to temperatures as high as 900 °C in UHV, followed by backfilling the chamber with up to 5×10^{-3} torr of C_2H_4 did not result in graphene formation. It was found that by first backfilling the chamber with C_2H_4 and then raising the temperature from 25 °C to 800 °C, graphene growth could be achieved. A four-domain epitaxial overlayer is observed for the Cu(100) surface. Pre-dosing the Cu(100) with oxygen at 300 °C, which forms a saturation coverage of chemisorbed oxygen, was found to result in a 2-domain graphene overlayer using similar growth conditions. A study of the effect of oxygen pre-dosing on the growth of graphene on Cu(111) has been initiated.

9:00am **GR+EM+NS+PS+SS+TF-MoM3 Impact of Growth Parameters on Uniformity of Epitaxial Graphene**, *L.O. Nyakiti, V.D. Wheeler, R.L. Myers-Ward, J.C. Culbertson*, U.S. Naval Research Laboratory, *A. Nath*, George Mason University, *N.Y. Garces*, U.S. Naval Research Laboratory, *J. Howe*, Oak Ridge National Laboratory, *C.R. Eddy, Jr.*, *D.K. Gaskill*, U.S. Naval Research Laboratory

Epitaxial graphene (EG) offers a facile method for attaining large area graphene for device applications. Since wafer uniformity and thickness control is vital, a systematic study of the parameters affecting the EG growth process was performed and the optimal conditions for obtaining uniform morphology and high electronic quality were determined. EG was synthesized in a low pressure Ar flowing ambient on $8 \times 8 \text{ mm}^2$ 6H-SiC(0001) substrates that were offset 0.8° from the basal plane, using an Aixtron VP508 reactor. The samples were placed on a rotating ~ 100 mm diameter susceptor and excellent EG layer uniformity and run-to-run reproducibility were obtained. The investigation focused upon the critical synthesis parameters of temperature (T) (1520-1660°C) and time (t) (15-60 min), an *in-situ* H_2 etch conditions (1520-1600°C for 10-30min). Morphology, layer thickness, chemical analysis, and strain variations across the samples were characterized using electron microscopy, AFM, XPS and μ -Raman spectroscopy. Large-area van der Pauw Hall effect was performed to quantify the graphene mobility (μ), and carrier density. Results show that growth T and t had the most significant impact on EG electronic and morphological properties. For example, synthesis at 1660°C for 30min resulted in 4-8 monolayers (ML) and a step-bunched morphology with high concentration of wrinkles originating from the step-edge and pinned at the nearest terrace edge. Other morphological features were pits primarily located at the step edges having a depth ~ 20 nm and density $6.4 \times 10^6 \text{ cm}^{-2}$. In contrast, EG synthesis at 1520°C for 30min results in uniform ML coverage along the terrace width that is devoid of pits and wrinkles. Mobility was found to have a drastic dependence on graphene thickness. Under optimal conditions, 1-2 ML were obtained and μ as high as $1240 \text{ cm}^2 \text{ V}^{-1} \text{ s}^{-1}$ was achieved; in contrast, for EG with >2 ML $\mu \sim 550 \text{ cm}^2 \text{ V}^{-1} \text{ s}^{-1}$, presumably due to interlayer interaction and electronic screening. XPS C1s and Raman 2D spectra of EG grown on substrates after undergoing *in-situ* H_2 etch at different times did not show shifts in peak position/intensity suggesting lack of etch time dependence on EG electronic or structural quality. Yet etch conditions affect the final morphology, as EG synthesis performed after an *in-situ* H_2 etch at 1600°C resulted in step-bunched morphology with step heights 5-10nm, whereas, substrates etched at 1520°C had EG with step-heights 10-15nm. In addition other growth parameters investigated were found to be of secondary importance, including: Ar pressure, flow rates, and sample cool down conditions.

9:20am **GR+EM+NS+PS+SS+TF-MoM4 Uniform Epitaxial Growth of Charge Neutral Quasi-Free-Standing Monolayer Graphene on a 6H-SiC(0001) Surface by Combination of Metal Silicidation and Intercalation**, *H. Shin, I. Song, C.-Y. Park, J.R. Ahn*, Sungkyunkwan University, Republic of Korea

Intrinsic high mobility of graphene are much reduced in graphene devices by various factors. Two critical factors degrading mobility are uniformity in an atomic structure such as number of a layer and an interaction with a substrate. Recently Shuai-Hua Ji *et al.* reported quantitatively that conductivity is much reduced by one sixth when electrons pass through a boundary between monolayer and bilayer graphene at a step edge in comparison to conductivity of monolayer graphene. This suggests that uniformity of number of graphene layer is a more crucial factor than expected. In particular, in epitaxial graphene on SiC, the uniformity of number of layer is an intrinsic and serious problem because Si is more rapidly sublimated near a step edge in the formation of epitaxial graphene by thermal evaporation of Si and, subsequently, epitaxial graphene with different layers coexists intrinsically on a terrace. Another factor degrading mobility is an interaction between graphene and a substrate. In epitaxial graphene, the interaction was reduced by intercalation of metal or molecule such as H, F, and Au between graphene and a substrate, which results in quasi freestanding graphene. Various charge neutral quasi freestanding graphene has been reported, but the charge neutrality was found at an optimal coverage of an intercalated element and annealing temperature. This makes it difficult to achieve spatially homogeneous charge neutrality of quasi freestanding graphene, and a method with a broad range of coverage and temperature is demanded. We demonstrate that charge neutral quasi freestanding monolayer graphene can be grown uniformly without coexistence of a buffer layer and a bilayer graphene which limit mobility of epitaxial monolayer graphene. Because coexistence of two different phases is inevitable on a SiC surface, uniform monolayer graphene was produced based on two different phases, a Si-rich phase and a C-rich phase called a buffer. Pd was deposited on both the Si-rich and C-rich phases and annealed up to 900°C. The Si-rich phase produced Pd silicide and charge neutral quasi freestanding monolayer graphene was produced on the Pd silicide while, on the C-rich phase, Pd was intercalated between the buffer layer and SiC resulting in charge neutral quasi freestanding monolayer graphene, where the quasi freestanding monolayer graphene on two difference regions was connected atomically. The combination of Si silicidation and intercalation result in uniform charge neutral quasi freestanding uniform monolayer on a SiC surface, where the electronic and atomic structures were observed using angle-resolved photoemission spectroscopy and scanning tunneling microscopy.

9:40am **GR+EM+NS+PS+SS+TF-MoM5 Epitaxial Graphene on Ir(111) - A Playground for the Fabrication of Graphene Hybrid Materials**, *T.W. Michely*, Universität zu Köln, Germany **INVITED**

Carefully optimizing the growth of graphene on Ir(111) yields a virtually defect free, weakly bound epitaxial monolayer ranging from quantum dot sizes to macroscopic extension. In the talk I will show how this system can be used to construct new types of graphene based materials. Specifically, patterned adsorption of transition metals results in dense cluster arrays with exciting magnetic and catalytic properties. Intercalation underneath the graphene allows one to manipulate the properties of graphene itself, e.g. its ability to adsorb atoms and molecules as well as its magnetism.

10:40am **GR+EM+NS+PS+SS+TF-MoM8 Graphene Growth Studied with LEEM, PEEM, EELS, ARPES, MEIS, and STM**, *R.M. Tromp, J.B. Hannon, M.W. Copel, S.-H. Ji, F.M. Ross*, IBM T.J. Watson Research Center **INVITED**

We have studied the growth of graphene on a variety of substrates, including SiC (both Si and C terminated), polycrystalline Cu and Ni foils, as well as single-crystal Ni foils. Low Energy Electron Microscopy (LEEM) and Photo Electron Emission Microscopy (PEEM) offer the unique opportunity to follow the growth in real time, as it proceeds at high temperature, and in the presence of processing gases such as disilane (for growth on SiC) or ethylene (for growth on the metal substrates). Low Energy Electron Diffraction (LEED) allows us to determine crystallographic orientations as well as atomic structure of areas well below a micrometer in extent. Information on electronic structure can be obtained from the plasmon loss features using Electron Energy Loss Spectroscopy (EELS), or from Angle Resolved Photo Electron Spectroscopy (ARPES). These spectroscopic experiments are carried out in the LEEM/PEEM microscope using an in-line energy filter with which energy and angle resolved analysis of the electrons can be performed on selected areas. Finally, to obtain information on the layer-by-layer evolution of the graphene films, particularly on SiC, we have used isotope sensitive Medium Energy Ion Scattering (MEIS), to follow the growth by thermal decomposition of ^{12}C vs ^{13}C graphene monolayers from a three-bilayer thick ^{13}C homoepitaxial film grown on a SiC substrate. Taken together, these

results provide a comprehensive view of the growth of graphene films. In this talk, we will review the most salient results of these studies, and their relevance to the use of graphene films for electronic applications. To address the latter, we will discuss the results of three-probe STM experiments in which we measured the excess resistivity of a graphene sheet as it crosses an atomic step of the underlying substrate.

11:20am **GR+EM+NS+PS+SS+TF-MoM10 Spatial Confinement of Epitaxy of Graphene on Microfabricated SiC to Suppress Thickness Variation**, *H. Fukidome, T. Ide, H. Handa*, RIEC, Tohoku Univ., Japan, *Y. Kawai*, Tohoku Univ., Japan, *F. Fromm*, Univ. Erlange-Nürnberg, Germany, *M. Kotsugi, T. Ohkouchi*, JASRI/SPring-8, Japan, *H. Miyashita*, Tohoku Univ., Japan, *Y. Enta*, Hirosaki Univ., Japan, *T. Kinoshita*, JASRI/SPring-8, Japan, *Th. Seyller*, Univ. Erlange-Nürnberg, Germany, *M. Suemitsu*, RIEC, Tohoku Univ., Japan

Epitaxial graphene on SiC (EG) is promising owing to a capability to produce high-quality film on a wafer scale [1]. One of the remaining issues is microscopic thickness variation of EG near surface steps, which induces variations in its electronic properties and device characteristics. To suppress the variation, spatial confinement of surface reactions is effective. The spatial confinement using substrate microfabrication, for instance homoepitaxy and sublimation on microfabricated Si substrates, can induce self-ordering of steps, and even produce step-free surfaces [2]. The spatial confinement is therefore anticipated effective to obtain EG without the thickness variation.

We have for this reason applied the spatial confinement to the epitaxy of graphene on 6H-SiC(0001). For the spatial confinement, 6H-SiC(0001) substrates were microfabricated by using electron beam lithography and fast atomic beam etching using sulfur hexafluoride [3, 4]. Epitaxial graphene on the microfabricated 6H-SiC(0001) substrates was obtained by annealing at 1923 K in Ar ambience [2]. It is verified by using low energy electron microscopy (LEEM) and photoemission electron microscopy (PEEM) that step-free SiC surface and EG without thickness variation can be formed on smaller patterns [4]. This result clearly demonstrate that the spatial confinement is effective for the epitaxy of graphene on SiC. Furthermore, Raman spectroscopy and LEEM reveals that the spatial confinement can suppress the fluctuations of the electronic properties, e.g. (unintentional) doping in EG [4].

In conclusion, we have demonstrated that the spatial confinement of EG is effective to control both structural and electronic properties. This novel technique can boost the development of electronic devices based on EG.

[References]

- [1] K. V. Emstev *et al.*, Nature Mater. 8 (2009) 203.
- [2] Y. Homma *et al.*, Jpn. J. Appl. Phys. 35 (1996) L241.
- [3] T. Ide *et al.*, accepted for the publication in Jpn. J. Appl. Phys.
- [4] H. Fukidome *et al.*, submitted.

11:40am **GR+EM+NS+PS+SS+TF-MoM11 Three-Dimensional Graphene Architecture Growth and Its Facile Transfer to Three-Dimensional Substrates**, *J.-H. Park*, Sungkyunkwan University, Republic of Korea, *H.-J. Shin, J.Y. Choi*, Samsung Advanced Institute of Technology, Republic of Korea, *J.R. Ahn*, Sungkyunkwan University, Republic of Korea

Recent development of large area graphene synthesis on metal layer by chemical vapor deposition (CVD) or epitaxial growth on silicon carbide (SiC) opened the possibility for applications such as transparent electrodes for ITO replacement. For instance, graphene has been demonstrated for use in a liquid crystal display (LCD) and/or organic light emitting diode (OLED) test cell as a bottom electrode. However, the actual device, e.g., an active-matrix (AM) LCD, operates by switching individual elements of a display, using a thin-film transistor (TFT) for each pixel. Here, the pixel electrode of a display should extend down to the transistor's source or drain, thereby making contact with a via hole, which demands that a three-dimensional (3D) architecture electrode be deposited on a flat surface as well as its side walls. Although large-area graphene growth can be applied for a wide range of applications, 3D graphene architecture growth has not been realized for actual devices due to the original limitation of planar graphene growth. Herein, we demonstrate for the first time 3D graphene architecture growth and its facile transfer to a planar and/or 3D substrate. To prevent agglomeration of nano-scale metal catalyst by the CVD process, we chose a SiC system. Graphene, a few layers thick, was epitaxially grown on a pre-patterned SiC substrate with nano-size thickness which was produced by photolithography and dry etching. Graphene on a vertical facet of the SiC pattern with a few-hundred nanometers in height was perfectly prepared using this approach, contrary to the CVD method. Furthermore, we suggest the use of a facile transfer method of graphene on SiC to a SiO₂ substrate using thermal release tape after hydrogen intercalation. In spite of the troublesome transfer issue of SiC, the geometry of the 3D graphene was

perfectly transferred onto the planar SiO₂ as well as the 3D SiO₂ structure. In other words, the 3D graphene architecture was maintained as a floating cap structure on planar SiO₂ and the vertical facet of the 3D SiO₂ structure was well covered. Moreover, the graphene bottom layer without a 3D cap and the inverted bowl structure in the 3D graphene architecture were selectively transferred by controlling intercalation and pressure. These approaches could provide a beneficial method for preparing a 3D graphene architecture as well as for modifying the ordered structure to be utilized in real devices.

Nanometer-scale Science and Technology

Room: 12 - Session NS-MoM

Nanoparticles and Quantum Structures

Moderator: G.S. Herman, Oregon State University

8:40am **NS-MoM2 Synthesis of Visible Light Emitting Self-assembled Ge Nanocrystals Embedded within a SiO₂ Matrix and Post-annealing Effects**, *A. Hernández-Hernández, F. De Moure-Flores, J.G. Quiñones-Galván*, CINVESTAV-IPN, Mexico, *L.A. Hernández-Hernández*, ESFM-IPN, Mexico, *J. Santoyo-Salazar, M. Meléndez-Lira*, CINVESTAV-IPN, Mexico

As-grown light emitting self-assembled Ge nanocrystals (Ge-NCs) embedded in a SiO₂ matrix were produced by a sequential deposition process of SiO₂/Ge/SiO₂ layers employing reactive radio frequency sputtering technique. Obtained Ge-NCs shown a crystallographic phase whose proportion, size, quality and specific orientation are determined by the oxygen partial pressure. Photoluminescence (PL) spectra indicate that the size distribution of Ge-NCs is reduced and centered at around 8 nm when higher oxygen partial pressure is employed; the formation of Ge-NCs is corroborated by transmission electron microscopy (TEM) measurements, their sizes are consistent with estimates from PL measurements. After vacuum annealing it is observed the elimination of an instable high pressure tetragonal phase of germanium present in as-grown samples. It is possible that this phase is related to the SiO₂ matrix stress on the Ge-NCs. In addition, the PL peaks shifted to higher energies indicating the formation of Ge-NCs probably from Ge dispersed within SiO₂ matrix. It was also found that the PL intensity increases drastically after annealing process. The strong size dependence of the PL spectra indicates that the observed PL originates from the recombination of electron-hole pairs confined in Ge-NCs.

† : partially funded by CONACyT-Mexico and ICYT-DF.

9:00am **NS-MoM3 A Single Atom Transistor**, *M.Y. Simmons*, University of New South Wales, Australia **INVITED**

Over the past decade we have developed a radical new strategy for the fabrication of atomic-scale devices in silicon [1]. Using this process we have demonstrated few electron, single crystal quantum dots [2], conducting nanoscale wires with widths down to ~1.5nm [3] and most recently a single atom transistor [4]. We will present atomic-scale images and electronic characteristics of these atomically precise devices and demonstrate the impact of strong vertical and lateral confinement on electron transport. We will also discuss the opportunities ahead for atomic-scale quantum computing architectures and some of the challenges to achieving truly atomically precise devices in all three spatial dimensions.

[1] F.J. Rueß et al., Nano Letters 4, 1969 (2004).

[2] M. Fuchsle et al., Nature Nanotechnology 5, 502 (2010).

[3] B. Weber et al., Science 335, 64 (2012).

[4] M. Fuchsle et al., accepted for Nature Nanotechnology (2012).

9:40am **NS-MoM5 Transforming Luminescent Silicon Nanocrystals Into a Direct-Bandgap Semiconductor via Surface-Capping-Induced Strain**, *P. Hapala, P. Jelinek, K. Kusova, I. Pelant*, Institute of Physics of ASCR, Czech Republic

We report combined experimental and theoretical work pointing out the possibility to convert Silicon Nanoparticles (SiNcs) to a luminescing direct-band gap material via the concerted action of the quantum confinement and tensile force induced by proper surface passivation.

The transformation of silicon, originally a very poor light emitter due to indirect band gap, into a light-emitting medium is key challenge from the application point of view. One promising way to achieve this ultimate goal is through dramatic shrinkage in the size of the crystal down to nanoscale. The observation of an efficient room-temperature luminescence [1] from SiNcs initiated the debate about the nature of their band structure. The most

common silicon-oxide-capped SiNcs maintain the indirect band gap showing long radiative lifetimes (>100 µs) [2].

Beside the size of the nanocrystal, a proper surface also plays an important role in the light emission process. Recently we have shown that SiNcs sized 2.5-3 nm with methyl-based surface passivating layer [3] exhibit luminescence properties (short radiative lifetime ~10 ns and enhanced quantum yield ~20%) analogical to direct-band gap semiconductor. This property is further supported by single-crystal luminescence experiment giving emission pattern very similar to that observed in direct-band gap CdSe nanoparticles [4].

To understand the impact of surface passivation on the electronic structure of SiNcs we performed large-scale total energy DFT calculations including up to 1500 atoms and different functional surface groups (-H,-CH₃,-OH). Our calculations show that the presence of methyl group leads to significant elongation of the Si-Si distance in core region. Further we restore band structure of SiNc mapping real space molecular orbitals into the momentum space [6].

The resorted band structure clearly shows, that combination of tensile stress and the quantum confinement strongly modifies dispersion of the conduction band along the Γ-X direction, with significant lowering of the Γ₁₅ even as lifting the conduction minimum band Δ₁.

References

[1] L. Canham, App. Phys. Lett. 57, 1046 (1990).

[2] D. Kovalev et al, Phys. Rev. Lett. 81, 2803 (1998).

[3] K. Kůsová et al ACS Nano, 4(8), 4495 (2010).

[4] X. Wang et al Nature 459, 686 (2009).

[5] K. K. Kůsová et al (submitted).

[6] P. Hapala and P. Jelinek (ArXiv:cond-mat/1204.0421).

10:00am **NS-MoM6 Plasma Synthesis and Hydrosilylation of Silicon Nanoparticles**, *S.L. Weeks, S. Agarwal*, Colorado School of Mines, B. Macco, Eindhoven University of Technology, the Netherlands

Silicon nanoparticles (NPs) are of interest in a variety of optoelectronic applications due to the observation of multiple exciton generation, room temperature photoluminescence, size tunable band gap, and optical gain. Design of any device employing Si NPs requires control over both the size and interfacial passivation as these parameters dictate the electronic properties of the NPs. Our synthesis process employs a capacitively-coupled tubular Ar/SiH₄ plasma to produce H-terminated Si NPs. The surface composition and functionalization of the Si NPs was characterized via *in situ* attenuated total reflection Fourier transform infrared (ATR-FTIR) spectroscopy. Organic passivation of the H-terminated Si NPs was achieved through a two-stage gas-phase hydrosilylation process using 1-alkynes with different numbers of C atoms that led to surface coverages comparable to the thermodynamic limit for alkenyl monolayers on bulk H:Si(111) surfaces. The hydrosilylation reaction requires abstraction of a surface hydride to stabilize an intermediate surface radical formed upon absorption of the 1-alkyne. Injection of H₂ into the afterglow region of the synthesis plasma was employed to manipulate the surface hydride composition, which led to an increase in the relative fraction of SiH_x(x = 2, 3) species on the surface compared to SiH. The impact of these higher hydrides on the hydrosilylation reaction of 1-alkynes was investigated through *in situ* ATR-FTIR spectroscopy. Finally, using *in situ* photoluminescence measurements, we also determined the effect of the various hydrosilylation processes on the relative quantum yield from these Si NPs.

10:40am **NS-MoM8 Exchange Bias in Pure and Core/Shell Structured γ-Fe₂O₃-based Nanoparticles**, *P. Lampen, H. Khurshid, M.H. Phan, H. Srikanth*, University of South Florida

Iron oxide nanoparticles, Fe₃O₄ and γ-Fe₂O₃, are of great interest for applications in high-density magnetic recording media, sensor technology, and biomedicine. These systems are also excellent candidates for probing fundamental properties due to well-established synthesis methods that yield uniform, high quality particles with good control over size and shape. It has recently been shown by polarized small angle neutron scattering that Fe₃O₄ nanoparticles possess a chemically uniform, but magnetically distinct, core and canted-spin shell structure [1]. While many similarities exist in the magnetic and microstructural properties of γ-Fe₂O₃ and Fe₃O₄, the exchange bias that can be observed in nanoparticles of γ-Fe₂O₃ [2] is not present in similarly sized Fe₃O₄ [3]. Therefore, an investigation of the evolution of spin canting angle and shell thickness with temperature in γ-Fe₂O₃ is expected to yield valuable information about subtly altered spin geometries that can be correlated with the presence of exchange bias in this nanoparticle system.

In order to compare results for both chemically distinct and chemically uniform exchange-biased systems, we report the synthesis and characterization of γ-Fe₂O₃ and core/shell Fe/γ-Fe₂O₃ nanoparticles. The p

articles used in the present study were synthesized by high temperature decomposition of iron organometallic compounds. X-ray diffraction and transmission electron microscopy techniques were used to study the structural and microstructural properties of the nanoparticles, which confirmed the presence of bcc iron and fcc γ -Fe₂O₃ in these particles. High-resolution TEM images evidenced monodisperse products with particle diameters of 9 ± 0.8 nm in the pure γ -Fe₂O₃, while the core/shell particles showed 9.8 ± 0.7 nm Fe cores surrounded by a shell of γ -Fe₂O₃ with 2 ± 0.4 thickness. The DC magnetic properties of the samples were characterized using a vibrating sample magnetometer over a temperature range of 5-300 K, revealing a superparamagnetic behavior. Pronounced exchange bias of up to ~ 4100 Oe was confirmed in these particles using cooling fields of up to 5T. While the spin-glass-like phase associated with disordered surface spins in γ -Fe₂O₃ plays an important role as a fixed phase in both systems, providing the pinning force to the reversible spins, the frozen spins at the interface between Fe and γ -Fe₂O₃ are also shown to contribute to EB in the core/shell Fe/ γ -Fe₂O₃ nanoparticles.

11:00am **NS-MoM9 Magnetic Polymer Nanocomposites with Tunable Microwave and RF Properties**, *K. Stojak, S. Chandra, H. Khurshid, S. Pal, C. Morales, J. Dewdney, J. Wang, T. Weller, M.H. Phan, H. Srikanth*, University of South Florida

There has been much interest in magnetic polymer nanocomposites (MPNCs) recently due to potential applications for EMI shielding, tunable electromagnetic devices and flexible electronics. We report synthesis, structural, magnetic and RF characterization on MPNCs ranging from 30-80wt-% loadings of uniformly dispersed CoFe₂O₄ nanoparticles (~ 10 nm) in a high-temperature, thermosetting resin from the Rogers Corporation (RP). Nanoparticles were synthesized by thermal decomposition and structurally characterized by XRD and TEM. Magnetic properties were studied using a Quantum Design PPMS. MPNCs displayed characteristic features of superparamagnetism at room temperature and blocking at low temperature. A blocking temperature (T_B) of ~ 298 K was observed for all weight percentages. The saturation magnetization (M_S) was found to increase with increasing weight percentages of CoFe₂O₄, from 9.7 emu/g for 30wt-% to 28.5 emu/g for 80wt-%. A large value of coercivity (H_C), ~ 18.5 kOe, is observed at 10K and is not affected by various loadings of CoFe₂O₄. Microwave transmission/reflection studies were done using a linear microstrip resonator. Strong tunability in the microwave absorption was observed, particularly in the 80wt-% sample and the quality factor shows a strong enhancement with applied magnetic field. We extend our study to include nanoparticle-filled multi-walled carbon nanotubes (CNTs) synthesized by CVD. These high-aspect ratio magnetic nanostructures, with tunable anisotropy, are of particular interest in enhancing magnetic and microwave responses in existing MPNCs. The CNTs have an average diameter and length of 300nm and 2 μ m, respectively and are partially filled with CoFe₂O₄ nanoparticles (~ 7 nm) [2]. When comparing the CoFe₂O₄ nanoparticles to the CoFe₂O₄-filled CNTs, T_B increases from 224K to 264K, and M_S increases from 36 emu/g to 37.1 emu/g. These results indicate that enclosing the nanoparticles within the CNTs enhances interparticle interactions, which is also independently confirmed with frequency-dependent AC susceptibility. This trend is also observed with NiFe₂O₄ and Fe₃O₄

nanoparticle fillers.

11:20am **NS-MoM10 Factors Controlling Thermodynamic Properties at the Nanoscale: Ab Initio Study of Pt Nanoparticles**, *G. Shafai, M. Alcántara Ortigoza, T.S. Rahman*, University of Central Florida

We analyze via density-functional-theory calculations how factors such as size, shape, and hydrogen passivation influence the bond lengths, vibrational density of states (VDOS), and thermodynamic quantities of 0.8-1.7 nm diameter Pt nanoparticles (NPs), whose shape was previously characterized via extended X-ray absorption fine structure spectroscopy (EXAFS) [1]. For a given shape, unsupported NPs display increasingly broader bond-length distributions with decreasing size. Since the VDOS is remarkably non-Debye-like (even for the largest NPs), the VDOS and the thermal properties are not correlated as they are in the bulk. Generally, the fundamental vibrational frequency of a NP is associated with the shape and decreases with increasing size, as in macroscopic systems. Not surprisingly, we find that the frequency of this fundamental mode largely characterizes the thermal properties. We demonstrate that the qualitative difference between the atomic mean-square-displacement and the corresponding mean bond-projected bond-length fluctuations should be taken into account when interpreting the Debye-Waller factor of NPs measured by X-ray (or neutron) scattering or EXAFS. We find that in H-passivated Pt NPs, H desorption with increasing temperature explains the appearance of negative thermal expansion.

This work was supported in part by DOE grant DE-FG02-07ER46354

[1] B. Roldán Cuenya, M. Alcántara Ortigoza, L. K. Ono, F. Behafarid, S. Mostafa, J. R. Croy, K. Paredis, G. Shafai, T. S. Rahman, L. Li, Z. Zhang, and J. C. Yang, PRB 84, 245438 (2011)

[2] G. S. Shafai, M. Alcántara Ortigoza, and T. S. Rahman; J. Phys.: Condens. Matter 24, 104026 (2012)

11:40am **NS-MoM11 Fabrication of Fe Doped Nano-engineered Matrix for Cholesterol Biosensor**, *R.R. Pandey, C. Kant*, CSIR-National Physical Laboratory, National Physical Laboratory, India, *M. Dhayal*, CSIR Centre for Cellular and Molecular Biology (CCMB), India, *K.K. Saini*, CSIR-National Physical Laboratory, National Physical Laboratory, India

In recent years, sol-gel chemistry has been a subject of intense investigations in the fields of chemical sensors and biosensors as it offers a cost effective route the fabrication of high surface area plate forms for sensitive biosensors. The inherent low temperature process of the technology, provide an attractive way for the immobilization of heat-sensitive biological entities (enzyme, protein, and antibody). This class of sol-gel silica (TiO₂) matrix possesses chemical inertness, non-toxic, physical rigidity, tunable porosity, high photochemical and thermal stability, and optical transparency.

Nanostructured nature of the metal-oxides films have been extensively reported, we have utilized this property of the material for effective enzyme adsorption per unit area to develop high sensitivity biosensors. We have further improved the matrix property to alter the surface properties (microstructure and charge transport) by Fe doping in the TiO₂ film. The modified matrix has been characterized by XRD, XPS, FTIR, SEM. The Fe³⁺ ion doped TiO₂ matrix successfully introduces redox property in the electrode and provides enhanced electron communication features. Sensing response obtained by the bioelectrocatalytic oxidation of cholesterol by cholesterol oxidase. Chox/ Fe³⁺ ion doped TiO₂/ITO electrode was studied using cyclic voltammetry (CV). These studies reveal that the Chox/ Fe³⁺ ion doped TiO₂/ITO bio-electrode exhibits improved biosensing response as compared to Chox/ Undoped TiO₂/ITO electrode. The results confirm promising application of the Fe³⁺ ion doped TiO₂ thin film matrix for the realization of efficient cholesterol biosensor.

Oxide Heterostructures-Interface Form & Function Focus Topic

Room: 7 - Session OX+EM+MI+NS+TF-MoM

Structure-Property Relationships in Epitaxial Oxide Interfaces

Moderator: E.I. Altman, Yale University

8:20am **OX+EM+MI+NS+TF-MoM1 Role of Dual-laser Ablation in Controlling Mn Oxide Precipitation during the Epitaxial Growth of Mn Doped ZnO Thin Films with Higher Doping Concentrations**, *D. Mukherjee, M. Hordagoda, R.H. Hyde, N. Bingham, H. Srikanth, P. Mukherjee, S. Witanachchi*, University of South Florida

The low solubility of Mn (equilibrium limit of 13 %) and precipitation of Mn oxides at slightly higher Mn doping (> 4 %) have remained major obstacles in the growth of Mn doped ZnO (ZnO:Mn) thin films for potential spintronic applications. In this work, epitaxial ZnO:Mn thin films were deposited on c-cut Al₂O₃ (0001) substrates, with increasing Mn concentrations from 2 to 12 %, using the dual-laser ablation process. In this process, an excimer (KrF) laser and a CO₂ laser pulses are spatially and temporally overlapped onto the target surface. Initially the target is heated by the CO₂ laser to produce a transient molten layer, from which the slightly time-delayed KrF laser initiates the ablation. Ablation for a momentary liquid target not only results in a drastic reduction of particulates in the deposited films but also overcomes the problem of non-congruent ablation of the ZnO:Mn target, leading to stoichiometric film deposition. Moreover, the optimum coupling of the laser energies produces an ablation plume that has a broader angular distribution, compared to the plume generated by KrF pulse alone, as observed from the intensified-charge-coupled-detector (ICCD) images of the ablated plumes. This allows the deposition of uniform films over larger area. Further, the higher ionization of the ablated species as seen in the optical emission spectra (OES) of the dual-laser ablated plumes leads to enhanced gas phase reaction and better film morphology and crystallinity. X-ray diffraction studies revealed that the dual-laser deposited ZnO:Mn films were single crystalline with no secondary phase formation even at 12 % doping while single-laser deposited ZnO:Mn films showed secondary Mn oxide phases. Room temperature magnetic measurements showed ferromagnetism (FM) with enhanced saturation magnetization (M_s) values from 1.3 emu/cm³ for 2 % ZnO:Mn films to 2.9 emu/cm³ for 12 % ZnO:Mn films. In- and out-of-plane magnetization

revealed absence of magnetic anisotropy. Further, temperature dependent Hall measurements showed a strong correlation between the effective carrier densities and the observed FM. All these measurements suggested a carrier mediated mechanism of FM in ZnO:Mn thin films. Using both the experimental data and theoretical analysis the FM in less conducting ZnO:Mn films was described by a bound magnetic polaron model whereas that in highly conducting films was consistent with a carrier mediated interaction via RKKY exchange mechanism.

8:40am **OX+EM+MI+NS+TF-MoM2 Structural Characterization of Heterojunction *n*-ZnO/*p*-NiO Thin Films Epitaxially Deposited on (0002)Al₂O₃ Substrates**, *Y.H. Kwon*, Sungkyunkwan University, Republic of Korea, *J.H. Lee*, KAIST, Republic of Korea, *S.H. Chun*, Sungkyunkwan University, Republic of Korea, *J.Y. Lee*, KAIST, Republic of Korea, *H.K. Cho*, Sungkyunkwan University, Republic of Korea

Recently, oxide semiconductors with superior electrical properties have been considered as candidates to replace Si based electronics. Furthermore, their thermally and chemically stable characteristic is preferable for devices. Especially, among a lot of oxides, ZnO based semiconductors have been extensively investigated to apply in wide application such as thin film transistor and light emitting diode. ZnO is an intrinsic *n*-type semiconductor which characteristic comes from Zn interstitials and O vacancies. And band-gap and exciton binding energy are 3.37 eV and 60 meV, respectively, which is suitable for optical application operating in ultra-violet region. Therefore, *p-n* homojunction diode structure combined with *n*-ZnO and *p*-ZnO having well matched interface had been studied by a lot of researchers.[1] However, it was not reliable since *p*-type ZnO synthesized by doping of group V elements is unstable and return to the *n*-type by self-compensation.[2]

Therefore, *p-n* heterojunction diode composed of *n*-ZnO and stable *p*-type oxide such as Cu₂O and NiO was alternatively studied.[3] Among the *p*-type oxides, NiO with wide direct band-gap (3.7 eV) have been expected to apply in optical applications. And conductivity of NiO could be significantly controlled by Li⁺ doping. Furthermore, according to T. Dutta et. al., (111) plane of NiO could well matched with (0002) of ZnO by domain match epitaxy.[4]

In this study, heterojunction diode structure was fabricated with *n*-type ZnO and *p*-type NiO on [0002] oriented Al₂O₃ substrates. RF magnetron sputtering method was used for deposition of NiO and ZnO films. After the deposition of NiO films at 400°C in O₂ atmosphere, ZnO films were grown at 600°C and in Ar and O₂ mixed gas atmosphere. XRD result showed the NiO films were fabricated with high crystallinity and preferred orientation of [111]_{NiO}. And sixfold symmetry of (100)_{NiO} plane obtained by phi-scan indicates that the NiO films were bi-epitaxially grown on Al₂O₃ substrates. In addition, electrical properties of NiO showed relatively low resistivity (1.648 Ωcm) and high mobility (14.52 cm²/Vs) due to Li⁺ doping. Sixfold symmetry of (1-102)_{ZnO} observed at phi-scan result indicates that ZnO films were also epitaxially grown on [111] oriented NiO films.

REFERENCES

- [1] F. Zhuge, L. Zhu, Z. Ye, D. Ma, J. Lu, J. Huang, F. Wang, Z. Ji, S. Zhang, Applied Physics Letters, 87 (2005) 092103.
- [2] C. Park, S. Zhang, S.H. Wei, Physical Review B, 66 (2002) 073202.
- [3] H. Kawazoe, H. Yanagi, K. Ueda, H. Hosono, MRS Bulletin, 25 (2000) 28.
- [4] T. Dutta, P. Gupta, A. Gupta, J. Narayan, Journal of Applied Physics, 108 (2010) 083715.

9:00am **OX+EM+MI+NS+TF-MoM3 Manipulating the Electrostatic Boundary Conditions of Polar Interfaces**, *Y. Hikita*, SLAC National Accelerator Laboratory **INVITED**

Transition metal oxides (TMO) offer various functionalities ranging from electronic devices to environmental catalysts [1, 2]. Often, the central part of such devices is the interface between different materials. In order to improve their device performance, control of charge transport across these interfaces is essential. Originally developed in semiconductor heterostructures, interface band alignment control is based on the interface electrostatic boundary conditions and is one of the most fundamental methods to tune the carrier transport across interfaces [3]. Given their strongly ionic nature and their accessibility to multiple valence states, the TMO interface should be more suitable than covalent semiconductors for manipulating interface band alignments. Here we focus on epitaxial metal-semiconductor Schottky interfaces between perovskite oxides to demonstrate the effectiveness of this technique. I will present two SrTiO₃ based perovskite Schottky junctions in which the interface energy barriers were modulated by interface dipoles controlled on the atomic scale [4]. Further, I will present the application of this technique in the form of an all-oxide hot electron transistor [5].

I. R. Ramesh and D. G. Schlom, MRS Bull. 33, 1006 (2008).

2. J. Suntivich *et al.*, Science **334**, 1383 (2011).
3. F. Capasso *et al.*, Appl. Phys. Lett. **46**, 664 (1985).
4. Y. Hikita *et al.*, Phys. Rev. B **79**, 073101 (2009).
5. T. Yajima *et al.*, Nature Mater. **10**, 198 (2011).

11:20am **OX+EM+MI+NS+TF-MoM10 Strain-induced Oxygen Vacancy Ordering at SrTiO₃/La_{0.5}Sr_{0.5}CoO₃ Interfaces, and its Impact on Magnetic “Dead” Layers**, *S. Bose*, *M. Sharma*, *M. Torija*, University of Minnesota, *J. Gazquez*, *M. Varela*, Oak Ridge National Laboratory, *J. Schmitt*, *C. He*, University of Minnesota, *S. El-Khatib*, American University of Sharjah, United Arab Emirates, *M. Laver*, *J. Borchers*, NIST Center for Neutron Research, *C. Leighton*, University of Minnesota

The remarkable functionality and epitaxial compatibility of complex oxides provides many opportunities for new physics and applications in oxide heterostructures. Perovskite cobaltites provide an excellent example, being of interest for solid oxide fuel cells, oxygen separation membranes, catalysis, ferroelectric RAM, resistive switching memory, and oxide spintronics. However, the same delicate balance between phases that provides this diverse functionality also leads to a serious problem - the difficulty of maintaining desired properties close to the interface with other oxides. Although this problem is widespread, manifests itself in several ways, and could present a significant roadblock to the development of heterostructured devices for oxide electronics, there is no consensus as to its origin. In our work, using SrTiO₃(001)/La_{1-x}Sr_xCoO₃ as a model system, we have combined epitaxial growth via high pressure oxygen sputtering [1] with high resolution x-ray diffraction, atomic resolution scanning transmission electron microscopy (STEM) and electron energy loss spectroscopy (EELS), and detailed magnetic, transport, and neutron scattering measurements to determine the fundamental origin of the deterioration in interfacial transport and magnetism [2,3]. The effect is found to be due to nanoscopic magnetic phase separation in the near-interface region driven by a significant depletion in interfacial hole doping due to accumulation of O vacancies. This occurs due to a novel mechanism for accommodation of lattice mismatch with the substrate based on formation and long-range ordering of O vacancies [4]. This fundamental link between strain state and O vacancy formation and ordering is explored in detail in this presentation. We demonstrate that the O vacancy density, depth profile, and ordering vector can all be controlled via strain, leading to a potential mechanism to substantially improve interfacial properties.

UMN support from NSF and DOE (neutron scattering). ORNL support from DoE; UCM support from the European Research Council.

- [1] Torija *et al.*, J. Appl. Phys. **104** 023901 (2008); Sharma *et al.*, J. Vac. Sci. Technol. **29** 051511 (2011).
- [2] Torija *et al.*, Adv. Mater. **23** 2711 (2011).
- [3] Sharma *et al.*, Phys. Rev. B., **84** 024417 (2011). [4] Gazquez *et al.*, Nano. Lett. **11** 973 (2011).

11:40am **OX+EM+MI+NS+TF-MoM11 Fabrication and Characterization of Titanium Oxide Films with Tunable Stiffness**, *K. Gotlib-Vainshtein*, *O. Girshevitz*, *C.N. Sukenik*, Bar Ilan University, Israel, *D. Barlam*, Ben Gurion University, Israel, *E. Kalfon-Cohen*, *S.R. Cohen*, Weizmann Institute of Science, Israel

The design of surfaces with controlled stiffness is attractive for a variety of applications ranging from controlling cell growth to mechanical and electrical engineering design. Here, the creation of layered composites with tunable surface stiffness has been achieved by coating a soft PDMS polymer with a stiff film of amorphous titanium oxide with thickness varying from 2 to 50 nm. The oxide layer is smooth (6 nm rms roughness at 2 μm² image size), and crack-free. Air plasma treatment was used to form a silica surface layer on the soft polymer base to promote of adhesion of the titania overlayer. To gain insight into the mechanics of the layered structure, nanomechanical quantification has been performed using different experimental approaches, as well as modeling studies. The surface mechanical properties of the samples have been probed using both instrumented nanoindentation and atomic force microscopy—based nanomechanical characterization. These results have been compared to finite element analysis (FEA) simulations.

By fitting the FEA simulations with experimental curves it is shown that the hard titania film and softer PDMS substrate individually maintain their characteristic elastic moduli, while the stiffness of the vertical nanocomposite can be controllably modified by changing the thickness of the stiff layer. Liquid phase deposition of the oxide allows control of its thickness at the nm level. During an indentation cycle, the stiff layer transmits the stress to the underlying PDMS base by deformation of its overall shape, but only negligible compression of the film thickness.

This synthetic approach can be quite versatile, and can, in principle, be extended to different oxides and a wide range of thicknesses. It allows

control of surface properties while maintaining bulk material properties. This exploratory work is a first step towards defining the range of surface stiffnesses that can be achieved in this way, as well as developing general methodologies for their characterization.

Advanced Surface Engineering Room: 22 - Session SE+NS-MoM

Nanostructured Thin Films and Coatings I: Interface Aspects

Moderator: J. Patscheider, EMPA, Switzerland

8:40am **SE+NS-MoM2 Ion-guided Phase Separation of Carbon-Nickel Composite Films during Ion Beam Assisted Deposition: 3D Sculpting at the Nanoscale**, *G. Abrasonis*, Helmholtz-Zentrum Dresden-Rossendorf, Germany, *M. Krause*, Helmholtz-Zentrum Dresden-Rossendorf and Technische Universität Dresden, Germany, *T.W.H. Oates*, Leibniz-Institut für Analytische Wissenschaft, Germany, *A. Mücklich*, *S. Facsko*, Helmholtz-Zentrum Dresden-Rossendorf, Germany, *C. Baehtz*, *A. Shalimov*, Helmholtz-Zentrum Dresden-Rossendorf, Germany and European Synchrotron Radiation Facility, France, *S. Gemming*, Helmholtz-Zentrum Dresden-Rossendorf, Germany

Ion assistance during film growth provides unique opportunities to influence the microstructure due to energy transfer and imposed directionality. During nanocomposite film growth at low temperatures, phase separation occurs at the growing film surface. Ion-assistance is a key parameter to control the surface processes during multiphase film growth, and hence the resulting nanocomposite morphology. A systematic study of ion irradiation as a pure energy and momentum transfer agent in the context of surface diffusion assisted phase separations is, however, lacking. Here the influence of low energy (50-130 eV) assisting Ar^+ ion irradiation on the morphology of C-Ni thin films will be reported. Ion-beam assisted deposition (IBAD) promotes the columnar growth of carbon encapsulated metallic nano-columns at low deposition temperatures for Ar^+ ion energy ranges of 50-100 eV. Moreover, the momentum transfer results in a tilting of the columns relative to the film surface. The potential to grow complex matrix encapsulated metallic structures such as chevrons is demonstrated. Furthermore, a window of deposition conditions will be reported where the ion assistance leads to the formation of regular 3D nanopatterns with well-defined periodicity. The influence of such anisotropic film morphology on the optical properties is highlighted.

Acknowledgements: Funding by the European Union, ECEMP-Project D1, "Nanoskalige Funktionsschichten auf Kohlenstoffbasis", Projektnummer 13857 / 2379, is gratefully acknowledged.

9:00am **SE+NS-MoM3 Interface Phenomena in Nanostructured Thin Films and Coatings**, *D. Rafaja*, Freiberg University of Technology, Germany **INVITED**

The properties of nanostructured thin films and coatings are strongly influenced by the structure of internal interfaces. Thus, the understanding of the formation of the interfaces and the knowledge of the relationship between the microstructure and the materials properties are the first steps in designing nanostructured materials with tailored properties. This talk will focus on partially coherent interfaces between adjacent crystalline phases in nanostructured thin films and coatings, discussing the mechanisms of their formation, showing the capabilities of experimental methods for microstructure analysis to detect these interfaces and to describe their structure on the atomic scale, and recognizing the influence of the interfaces on the materials properties.

The interface phenomena and their impact on hardness and thermal stability of nanostructured thin films and coatings will be illustrated on physical vapor deposited transition metal nitrides containing aluminum and/or silicon, where the internal interfaces form as a consequence of the decomposition of metastable supersaturated solid solutions. It will be shown how the local fluctuations of the chemical composition arising during the deposition process and the local strain fields resulting from differences in the interatomic distances at partially coherent interfaces influence the decomposition process and the stability of the metastable phases.

The description and quantification of the interface phenomena on atomic scale would be impossible without a detailed microstructure analysis that is required to reveal the constitution of the nanostructured materials, to reproduce the structure of the internal interfaces and to assess the coherence of the interfaces. Hence, this talk will also recapitulate the recent developments in the microstructure analytics on the nanostructured thin films and coatings.

9:40am **SE+NS-MoM5 Mechanical Properties, Fracture Toughness, and Thermal Stability of CrN/AlN Superlattice and Multilayer Thin Films**, *M. Schlögl*, *B. Mayer*, *J. Paulitsch*, *J. Keckes*, *C. Kirchlechner*, *P.H. Mayrhofer*, Montanuniversität Leoben, Austria

Transition metal nitrides, such as CrN are highly attractive materials for a wide range of applications due to their outstanding properties like high hardness, excellent corrosion and oxidation resistance. Consequently, many research activities deal with their synthesis-structure-properties-relations. However, it has been reported that CrN/AlN superlattice coatings improve the mechanical properties compared to single CrN especially when keeping the AlN in its metastable cubic phase. Hence, we investigated the influence of the layer thickness of CrN on the stabilization of c-AlN and the critical layer thickness for AlN before transforming into the stable wurtzite phase. Furthermore, stress measurements and thermal stability were accomplished by the in-situ wafer curvature method during vacuum annealing to 700°C, differential scanning calorimetry to 1500°C and hardness measurements after annealing up to 1100°C.

The fracture toughness of the coatings is studied by means of in-situ scanning electron microscopy and transmission electron microscopy microbending and microcompression tests. The small test-specimens are prepared by focused ion beam milling of individual free-standing thin films. As generally monolithic coatings with their columnar structure provide low resistance against crack formation and propagation we perform our studies for CrN films, CrN/AlN multilayers and the CrN/AlN superlattice as mentioned above. Especially the multilayers and superlattices provide additional interfaces perpendicular to the major crack-propagation-direction. Adjusting the AlN layer-thicknesses to allow for cubic or wurtzite structure enables to study the influence of the extremely stress sensitive cubic-to-wurtzite AlN phase transformation on the crack propagation.

The microtests clearly demonstrate that the monolithic CrN as well as the CrN/AlN multilayer coating with the wurtzite AlN layers crack with the behavior and features for brittle fracture. Contrary, the CrN/AlN multilayer coatings composed of cubic stabilized AlN layers are able to provide resistance against fatal crack propagation. Hence, they allow for significantly higher loads during the microbending and microcompression tests. Detailed structural investigations, in-situ and after the tests, suggest that the cubic AlN layers, which are stabilized by coherency strains in the CrN/AlN multilayer coatings, phase transform with the connected nature expansion when experiencing additional strain fields and thereby hinder crack propagation.

10:00am **SE+NS-MoM6 High-temperature Nanoindentation of Hard Coatings**, *M. Rebelo de Figueiredo*, University of California Berkeley, *M. Tkadletz*, Materials Center Leoben, Austria, *M. Schlögl*, *R. Hollerweger*, *P.H. Mayrhofer*, *C. Mitterer*, Montanuniversität Leoben, Austria, *P. Hosemann*, University of California Berkeley

In the past decades, measurement techniques to probe the mechanical properties of hard coatings have been evolved dramatically and nowadays a wide variety of methods and devices are available. Within the field of evaluating the hardness of coating materials, nanoindentation has been established as a standard method utilizing the Oliver and Pharr approach. The measurements are commonly performed at room temperature. Industrial applications like metal cutting, however, demand resistance to wear also at temperature levels of up to 1000°C, which can easily be reached in the contact zone between a coated tool and the machined part. Therefore, knowledge about the mechanical properties of hard coatings at elevated temperatures is of vital importance. Nanoindentation devices allowing to go to temperatures as high as 750°C became available in recent years. While it appears simple to install heating devices in a nanoindenter, the minimization of the thermal drift, tip durability, and environmental control are a particular challenge to perform measurements at these temperatures. Therefore, significant efforts in monitoring all effects of a measurement performed at these conditions need to be spent in order to gain valid indentation data.

Within the present work, a series of different hard coatings were analyzed, utilizing nanoindentation experiments up to 750°C. The coatings evaluated cover selected samples representing the state-of-the-art employed in cutting operations like Al_2O_3 and TiAlN as well as newly developed coating materials like TiAlTaN. Possibilities and experimental limitations of high-temperature nanoindentation are critically discussed. A sound knowledge of the dependence of hardness on microstructural changes occurring at elevated temperatures provides the basis for the further development of coating materials and design.

10:40am **SE+NS-MoM8 Improving the Phase Stability of Metastable Aluminum Oxide Thin Films**, *F. Nahif*, *H. Bolvardi*, *D. Music*, *S. Mráz*, *J.M. Schneider*, RWTH Aachen University, Germany

Charge state resolved ion energy distribution functions (IEDFs) of Al^+ , Al^{2+} and Al^{3+} were measured as a function of Ar

pressure in the range from 5.7×10^{-5} to 2.13 Pa (0.01 to 256 Pa cm). A close to monoenergetic beam of Al^+ ions was obtained in an Ar/O₂ mixture at 128 Pa cm. Al₂O₃ films are deposited employing this monoenergetic Al⁺ beam using a substrate bias potential to increase the ion energy. A critical Al⁺ ion energy of 40 eV for the formation of the α -Al₂O₃ phase at a substrate temperature of 720 °C is determined. This energy is used as input for classical molecular dynamics and Monte-Carlo based simulations of the growth process, as well as *ab initio* calculations. The combination of theory and experiment indicates that in addition to the well known surface diffusion the previously non considered diffusion in sub-surface regions is an important atomistic mechanism in the phase formation of Al₂O₃. Using density functional theory and cathodic arc deposition experiments the effect of Si and Y addition on the stability of γ - and α -Al₂O₃ has been investigated. Si additives clearly shift the relative stability towards the γ -phase which can be understood based on the electronic structure. As the additive concentration increases, strong silicon-oxygen bonds are formed giving rise to the observed stabilization of the γ -phase.

11:00am **SE+NS-MoM9 Thermal Stability of (Al_xCr_{1-x})₂O₃ Solid Solution Coatings Grown by Cathodic Arc Evaporation.** *V. Edlmayr, M. Pohler*, University of Leoben, Austria, *I. Letofsky-Papst*, Graz University of Technology, Austria, *C. Mitterer*, University of Leoben, Austria

Corundum-type (Al_xCr_{1-x})₂O₃ coatings were grown by reactive cathodic arc evaporation in an oxygen atmosphere using AlCr targets with an Al/Cr atomic ratio of 1. Since the (Al_xCr_{1-x})₂O₃ solid solution shows a miscibility gap below 1300°C, where spinodal decomposition is predicted, the microstructural changes upon annealing were investigated by a combination of transmission electron microscopy, X-ray diffraction, Raman spectroscopy and differential scanning calorimetry. The as-deposited coating consists primarily of the corundum-type (Al_xCr_{1-x})₂O₃ solid solution, with smaller fractions of cubic (Al_xCr_{1-x})₂O₃. An additional Al-rich amorphous phase and a Cr-rich crystalline phase stem from the droplets incorporated. The corundum-type (Al_xCr_{1-x})₂O₃ was still present after vacuum annealing at 1050°C for 2 hours, whereas additional α -Al₂O₃ and Cr₂O₃ phases were formed due to decomposition of the cubic (Al_xCr_{1-x})₂O₃ phase. Likewise, Cr and Cr₂O₃ have been detected in the annealed coating, most probably originating from the partial oxidation of Cr-rich droplets. Upon crystallization of the amorphous phase fractions present, γ -Al₂O₃ is formed, which partially transforms in α -Al₂O₃. No evidence for decomposition of the corundum-type (Al_xCr_{1-x})₂O₃ solid solution could be found within the temperature range up to 1400°C.

11:20am **SE+NS-MoM10 Protective Coatings Against Corrosion and Wear for 3D Components with Combined ALD and PVD Techniques.** *S. Ek*, Picosun, Finland

Corrosion-related problems have always been a major challenge in various industries because of the components' shortened lifetime. Huge efforts are being made to improve the current corrosion protection procedures and to develop new corrosion preventing techniques. The objective is to find more efficient, environmentally sustainable, and cost-effective solutions for advanced corrosion protection of materials. However, in some applications it is not only corrosion protection that is needed but also wear resistance is required.

Relatively thick PVD coatings are generally used in applications where wear resistance is required. However, achieving simultaneous corrosion protection with that kind of coatings is challenging because the coating doesn't grow conformally and uniformly enough on the nano/microscale details of the surface of the protected material. This is where ALD coatings are needed: they enable reliable, long-term corrosion resistance through dense, uniform and conformal layers and they block the possible cracks, pinholes and nano/microscale voids and irregularities of the PVD layer, thus improving and securing the performance of the PVD coatings. At the same time, ALD contributes to structural strengthening and better chemical stability.

The choice and composition of the ALD coatings for corrosion protection depend on the substrate material and the kind of environmental conditions to which the protected components are exposed. Especially, certain metal oxides or their laminates or mixtures deposited by ALD form efficient and functional corrosion protection layers. Optimization of the protective thin film thickness and composition has been performed during the last three years in the European Union 7th Framework Program collaborative project CORRAL ("Corrosion protection with perfect atomic layers" [CPFP213996-1]).

In the present work, high-quality coatings with less than 0.001 % porosity were achieved. The coatings were able to seal 100Cr6 steel substrates for over 800 h in neutral salt spray tests (NSS). The lifetime of 3D test components was increased by a factor of 3-10 depending on the substrate material.

Monday Afternoon, October 29, 2012

Graphene and Related Materials Focus Topic
Room: 13 - Session GR+EM+ET+NS+TF-MoA

Electronic Properties and Charge Transport
Moderator: T.W. Michely, Universität zu Köln, Germany

2:00pm **GR+EM+ET+NS+TF-MoA1 Influence of Substrate Offcut on Electrical and Morphological Properties of Epitaxial Graphene, R.L. Myers-Ward, V.D. Wheeler, L.O. Nyakiti, T.J. Anderson, F.J. Bezares, J.D. Caldwell, A. Nath, N. Nepal, C.R. Eddy, Jr., D.K. Gaskill, U.S. Naval Research Laboratory**

The promise of graphene-based device technologies is critically dependent on uniform wafer-scale graphene films and is most directly met through epitaxial graphene (EG) growth on silicon carbide (SiC) substrates. An essential parameter which influences this uniformity is the substrate offcut, as any deviation will result in a local change in the terrace width, impacting the growth rate and step-bunched heights observed after EG formation. For nominally on-axis SiC substrates, typical offcuts can range from $\sim 0^\circ$ to $\sim 1^\circ$ off-axis toward the [11-20] direction. Offcuts approaching 0° produce wide terraces with short step-bunched heights which offers the possibility of reduced anisotropy of transport properties [M. Yakes, et al., Nano Lett. **10**(5), 1559 (2010)] and improved EG layer uniformity. Thus, it is of interest to understand the influence of substrate offcut on carrier mobility, surface morphology, step heights, and graphene growth rate. This study investigates EG grown on a unique single 3-inch substrate possessing a large variation in offcut, from $+0.1$ to -1° toward the [11-20] direction, enhancing the information obtained on offcut influence while eliminating other substrate influences. X-ray diffraction rocking curve and peak position maps of the (0012) reflection were performed prior to growth to evaluate the crystalline quality and local offcut, respectively. Electron mobilities of EG films were determined by van der Pauw Hall measurements. Surface morphology of the EG was investigated with scanning electron microscopy, while the step heights and terrace widths were measured using atomic force microscopy.

For a given set of conditions (1620°C for 30 min in 10 slm Ar), the EG morphology is dominated by straight steps that become wavy in character as the offcut decreases to zero degrees. Close to zero degrees, the step direction rotates from [11-20] to the [1-100] direction and the steps become further distorted. The step bunch heights generally decreased (from 8 to 3 nm) as the offcut decreased and the terrace widths increased (from 0.3 to ~ 3 μm); however, for the latter, the trend is interrupted near zero degrees offcut. In addition to such morphological assessments, the impact of growth parameters, where the growth temperatures investigated were 1540, 1580 and 1620 °C and growth times were 15, 30 and 45 min, on the electrical and structural properties of EG grown on this unique substrate will be reported. For example, samples grown at 1540 °C for 30 min on witness substrates with offcuts ranging from ~ 0.4 to 0.9° had large area mobilities ranging from 780 to 1100 cm^2/Vs , where larger offcuts led to lower mobilities.

2:20pm **GR+EM+ET+NS+TF-MoA2 Direct Determination of Dominant Scatterer in Graphene on SiO₂, J. Katoch, D. Le, T.S. Rahman, M. Ishigami, University of Central Florida**

Freely suspended graphene sheets display high-field effect mobility, reaching 2×10^5 cm^2/V s. Yet, suspended graphene sheets are fragile and impractical for most experiments and applications. Graphene sheets on SiO₂ are easier to handle but possess low-carrier mobilities, which can vary by an order of magnitude from sample to sample. Poor and unpredictable transport properties reduce the utility of SiO₂-bound graphene sheets for both fundamental and applied sciences. Therefore, understanding the impact of substrates is crucial for graphene science and technology.

We have measured the impact of atomic hydrogen with kinetic energy less than 250 meV on the transport property of graphene sheets as a function of hydrogen coverage and initial, pre-hydrogenation field-effect mobility. The saturation coverages for different devices are found to be proportional to their initial mobility, indicating that the number of native scatterers is proportional to the saturation coverage of hydrogen. In order to understand this correlation between the field effect mobility and the apparent affinity of atomic hydrogen to graphene, we have performed a detailed temperature programmed desorption study on hydrogen-dosed graphene sheets. Atomic hydrogen is found to physisorb on graphene with activation energy for desorption of 60 ± 10 meV, consistent with our theoretical calculations. The associated charge transfer expected for such small desorption energy indicates that atomic-scale defects and ripples are not responsible for

determining the mobility of graphene on SiO₂ and that charged impurities in substrates define the transport property of graphene on SiO₂.

1. J. Katoch, J.H. Chen, R. Tsuchikawa, C. W. Smith, E. R. Mucciolo, and M. Ishigami, Physical Review B Rapid Communications, **82**, 081417 (2010).

2:40pm **GR+EM+ET+NS+TF-MoA3 Tuning Electronic Properties of Graphene by Controlling its Environment, K.I. Bolotin, Vanderbilt University**
INVITED

Every atom of graphene, a monolayer of graphite, belongs to the surface. Therefore, the environment of graphene -- the substrate onto which graphene is deposited and any coating on top of graphene -- intimately affects the properties of graphene. In this talk, we demonstrate that both the mechanical and electrical properties of graphene can be tuned by varying its environment.

First, we discuss the dependence of electrical transport in graphene on the dielectric constant (k) of graphene's environment. For graphene in vacuum ($k=1$) we observe very strong electron-electron interactions leading to robust fractional quantum Hall effect at temperatures up to 15K. By suspending graphene in liquids, we explore the regime of dielectric constants between ~ 1.5 and ~ 30 . We observe the dependence of carrier scattering in graphene on k and demonstrate large values for room temperature mobility ($>60,000$ cm^2/Vs) in ion-free liquids with high k . We also explore the rich interplay between the motion of ions inside liquids and transport of electrons in graphene. We observe signatures due to streaming potentials and Coulomb drag between ions in the liquid and electrons in graphene.

We also briefly address the mechanical properties of graphene and their dependence on graphene's environment. We demonstrate that the built-in strain, the substrate adhesion force and even the thermal expansion coefficient of graphene depend on the substrate supporting graphene.

3:40pm **GR+EM+ET+NS+TF-MoA6 Study of Impurity-Induced Inelastic Scattering on Suspended Graphene by Scanning Confocal Micro-Raman Spectroscopy, L.W. Huang, C.S. Chang, Academia Sinica, Taiwan, Republic of China**

We utilized a polymer-based procedure to transfer the CVD-grown graphene onto a TEM copper grid. The heat treatment was performed on the graphene membrane in an argon/hydrogen (Ar/H₂) atmosphere at 400 °C. After the transfer and heat treatment, TEM images, acquired by an ultra-high-vacuum transmission electron microscopy (UHV-TEM), demonstrated areas with distinguishable impurity distribution on the suspended graphene membrane. These areal impurity distributions can also be mapped by the scanning Raman spectroscopy correspondingly, indicating the influence of impurity-induced inelastic scattering. The results of this experiment show that the intensity ratio of Raman spectra 2D band over G band (I_{2D}/I_G) is proportional to minus fourth power of the inelastic scattering rate.

4:00pm **GR+EM+ET+NS+TF-MoA7 The Adsorption of Molecules with Large Intrinsic Electrostatic Dipoles on Graphene, L. Kong, Univ. of Nebraska-Lincoln, G.J. Perez Medina, Univ. of Nebraska-Lincoln, Univ. of Puerto Rico, J. Colón Santana, Univ. of Nebraska-Lincoln, L. Rosa, Univ. of Nebraska-Lincoln, Univ. of Puerto Rico, L. Routaboul, P. Braunstein, Maître de conférences de l'Université de Strasbourg, France, B. Doudin, Institut de Physique et Chimie des Matériaux de Strasbourg, France, C.-M. Lee, J. Choi, Kyung Hee Univ., Korea, P.A. Dowben, Univ. of Nebraska-Lincoln**

Both gold and graphene are excellent conductors, and one might expect that both conductors would fully screen the photoemission and inverse photoemission final states of a molecular adsorbate, but in fact this is not the case. The comparison of the electronic structure of p-quinonoid zwitterionic type molecules with a large intrinsic dipole of 10 Debyes adsorbed on both gold and graphene on copper substrates, shows that the interaction between the adsorbate molecules and graphene is very weak, confirming that graphene is chemically inert. We find that the photoemission and inverse photoemission final states are well screened for p-quinonoid zwitterionic dipolar molecules on gold. This is not observed in the case of this quinonoid zwitterion adsorbed on graphene on copper. This weaker screening is evident in a larger highest occupied molecular orbital to lowest unoccupied molecular orbital gap for the molecules on graphene. The larger highest occupied molecular orbital to lowest unoccupied

molecular orbital gap for the molecules on graphene indicates that a much weaker screening on the photoemission and inverse photoemission final states for these dipolar molecules on graphene than that on gold. This work is reviewed in the context of other studies of molecular adsorption on graphene.

4:20pm **GR+EM+ET+NS+TF-MoA8 Growth of and Interactions in Epitaxial Graphene Layers.** *A. Bostwick*, Lawrence Berkeley National Laboratory, *A. Walter, Th. Seyller*, Lawrence Livermore National Laboratory, *K. Horn, E. Rotenberg*, Lawrence Berkeley National Laboratory **INVITED**

The electronic properties of graphene has been investigated using angle-resolved photoemission spectroscopy at the MAESTRO* facility of the ALS** synchrotron in Berkeley, California. This laboratory is unique in its ability to grow sophisticated samples for *in situ* study using angle-resolved photoemission spectroscopy, and to subtly alter their properties by engineering their surfaces by chemical doping or thickness control. In this talk I will discuss the electronic properties of graphene, focusing on the role of dopants to control the charge density and as defects to disrupt the metallic conduction. By measuring the spectrum of "plasmonic" quasiparticle excitations, we can demonstrate the scale-free nature of the Coulomb interaction in Dirac systems. Such effects are readily observed on quasi-free standing graphene samples doped with long-range scatterers. Doping with short-range scatterers, on the other hand, results in a loss of conduction which we interpret as a manifestation of strong (Anderson) localization.

*Microscopic and Electronic Structure Observatory

**Advanced Light Source

5:00pm **GR+EM+ET+NS+TF-MoA10 Squeezing of the Graphene Dirac Cone Observed by Scanning Tunneling Spectroscopy.** *J. Chae, S. Jung, Y. Zhao, N.B. Zhitenev, J.A. Stroscio*, Center for Nanoscale Science and Technology / NIST, *A. Young, C. Dean, L. Wang, Y. Gao, J.C. Hone, K.L. Shepard, P. Kim*, Columbia University

The single-particle spectrum of graphene is described by massless Dirac quasiparticles with a linear energy-momentum dispersion relation. In this talk I examine the effect of electron interactions on the graphene energy dispersion as a function of both excitation energy E away from the Fermi energy and density n . To analyze the dispersion, we measure the Landau levels (LLs) in graphene on a hexagonal boron nitride (hBN) insulator in low magnetic fields by scanning tunneling spectroscopy. The experiments were performed in a custom designed cryogenic scanning tunneling microscope system operating at 4 K with applied magnetic fields from 0 T to 8 T. The graphene devices were fabricated by the method detailed in Dean *et al.* [1]. The disorder in graphene on hBN is reduced in comparison with the previous measurements in graphene on SiO₂ [2] allowing us to observe the LLs in fields as low as 0.5 T. By fitting the LL energies obtained at constant density, we find that the energy dispersion remains linear, characterized by a momentum-independent renormalized velocity. However, the renormalized velocity is density dependent, showing a strong increase as the charge neutrality point is approached. The overall spectrum renormalization can be described as a *squeezing* of the Dirac cone angle due to electron-electron interactions at low densities. Interestingly, we also find that the renormalization of the dispersion velocity is affected by the local disorder potential and magnetic field, which is not described by current theory.

[1]. C. Dean, A. Young, I. Meric, C. Lee, L. Wang, S. Sorgenfrei, K. Watanabe, T. Taniguchi, P. Kim, K. L. Shepard, and J. Hone, *Nature Nanotech.* 5, 722–726 (2010).

[2]. S. Jung, G. M. Rutter, N. N. Klimov, D. B. Newell, I. Calizo, A. R. Hight-Walker, N. B. Zhitenev, and J. A. Stroscio, *Nature Phys.* 7, 245–251 (2011).

5:20pm **GR+EM+ET+NS+TF-MoA11 Interfacial Interaction of Graphene and Metal Surfaces Investigated by Resonant Inelastic X-ray Scattering.** *L. Zhang*, University of Science and Technology of China, Advanced Light Source, *J.H. Guo*, Advance Light Source, *J.F. Zhu*, University of Science and Technology of China

The synthesis of graphene on metal surfaces by chemical vapor deposition (CVD) is the most promising method to prepare single-layer and large-area graphene, which is a prerequisite for the fabrication of graphene-based electronic devices. Therefore, the graphene/metal interfaces have attracted much attention due to their importance in graphene synthesis by CVD processes. In this presentation, we report our recent studies on the electronic structure and band dispersion of graphene on different metal surfaces (Cu, Ir and Ni) by the means of X-ray absorption spectroscopy (XAS), X-ray emission spectroscopy (XES) and resonant inelastic X-ray scattering (RIXS). The XAS spectra for graphene on metal surfaces show strong π^*

and σ^* resonant features, indicating that the single-layer graphene films preserve the intrinsic symmetry of graphite. The resonant XES spectra of graphene on different metal surfaces change dramatically, especially for the features of π^* resonances, which can be directly related to the different strength of hybridization between graphene and metal substrates. These significant spectra changes have been proved to be an effective measure for the bonding strength of graphene on different substrates: strong band dispersion can be observed when the interaction between graphene and metal substrate is weak (such as Cu), while the band dispersion is seriously disturbed when a strong hybridization between graphene and metal substrate (such as Ni) exists. These results provide basic understanding of graphene/metal interfacial interaction, which helps to develop graphene-based electronic devices with high performances.

Nanomanufacturing Science and Technology Focus Topic

Room: 16 - Session NM+NS+MS+EM-MoA

ALD and Scalable Processes for Nanomanufacturing

Moderator: T.S. Mayer, Penn State University

2:00pm **NM+NS+MS+EM-MoA1 From R&D Towards Industrial Atomic Layer Deposition: Challenges in Scaling up.** *M. Putkonen*, Beneq Oy, Finland

More and more ALD-enabled applications are emerging. Most of the ALD processes and applications are first demonstrated by small scale experiments. In optimal cases, the innovations lead to material-application combinations which have solid commercial interest. In the subsequent verification and pilot production phase, there is need for increased throughput and reduced costs also for the ALD processed materials.

There are two main features of ALD, that should be optimized when industrial scale production is being considered. Firstly, in large-area coating processes, more attention should be paid to the properties of the precursors. For large-area coatings, large doses of precursors are delivered to the substrates, preferably in very short pulses in order to keep the total cycle time as short as possible. This often requires either DLI-type sources or increased vapor pressure (i.e. increased thermal stability of metal precursors). In addition, although the ALD chemistry should be surface controlled and not dependent on the substrate surface area, deposition rates and film uniformities are habitually dependent on the tool configuration.

Secondly, ALD has so far been largely confined to laboratories due to non-availability of efficient, larger scale, high-throughput ALD systems. Whereas sputtering and CVD have been mainstream coating tools for decades, ALD has only recently started to gain acceptance as a mainstream industrial coating method. For example, ALD is widely seen as the desired manufacturing technology for producing high-quality functional layers for solar cells and packaging materials, but ALD is commonly considered too slow for high throughput manufacturing. However, large-area batch ALD tools, such as the Beneq P800, can operate up to 10 m² batch sizes and still maintain ALD cycle times in the range of 3-5 s. Currently, industrial ALD is diffusing into various industrial thin film areas where single wafer, batch or roll-to-roll ALD is the preferred coating method.

In this presentation, we discuss the different requirements for single wafer, conventional batch, cross-flow batch as well as spatial ALD deposition processes and tools for large throughput applications. In addition to conventional Al₂O₃ and TiO₂ processes, SiO₂ processes are used as examples when scaling up chemistry from single wafer to batch ALD. In addition, process transfer from an R&D scale Beneq TFS 200R rotating drum reactor to the true roll-to-roll Beneq WCS 500, developed for OLED encapsulation applications, is discussed in detail. Results of the studies using this system are presented including temperature dependence of growth rate, RI and WVTR measurements.

2:20pm **NM+NS+MS+EM-MoA2 Enabling ALD for Semiconductor Manufacturing.** *D. Chu*, Applied Materials Inc. **INVITED**

Atomic layer deposition (ALD) is being extensively studied for semiconductor applications because of its precise, atomic level thickness control for very thin films; ALD is extremely conformal and the overall thermal budget is lower than its CVD alternatives. However, ALD is inherently slow which makes it cost prohibitive.

Adoption of ALD processes into manufacturing requires consideration of multiple factors. At Applied Materials, we focus on three main areas to enable ALD for volume manufacturing.

1. Atomic level engineering to create differentiated solutions that boost device performance.

2. Tool architecture and methods to allow integration of multiple films without vacuum break. This is particularly of importance when films scale to Angstrom level, stability of the film becomes an issue. Extendable tool architectures allow integration of other films such as capping layers and pre-post treatments to address this issue

3. Accelerate adoption of standalone ALD films by improving manufacturability and productivity while maintaining single wafer performance

Example applications and challenges for each area will be discussed in this paper.

3:00pm NM+NS+MS+EM-MoA4 Migration to ALD Techniques in the Semiconductor Industry: Pattern Effects, Microloading and Film Thickness Variability in Dielectric Thin Films Deposition, M.P. Belyansky, IBM Semiconductor R&D Center

The continuation of scaling in the microelectronics industry is having a profound effect on thin film deposition techniques and processes. One of the consequences of the scaling is a decrease in average film thickness to accommodate the shrinking device dimensions which amplifies the problem of film thickness variability. Most of the CVD deposition techniques and tooling are reaching the limit of reliable thickness control of very thin films. At the same time, circuit designs are becoming more complex, which leads to significant pattern density variation on macro scale. Therefore CVD technology is facing a tremendous challenge in controlling film thickness and properties across variable pattern density which has been one of the major reasons that facilitated the transition to ALD-like deposition techniques and processes in the industry.

The paper discusses the microloading effect (dependence of thin film deposition rate on pattern density) as well as other manifestations of pattern effects in the semiconductor manufacturing. The data shows the effect of microloading on the variation of as deposited film thickness across features of different size as well as for identical features with different pattern density in the surrounding areas. The microloading performance of CVD and ALD silicon oxide and silicon nitride dielectric thin films is covered as well as methods aimed at quantifying and improving thin film variability. The effects of major process parameters, precursor chemistry and tool design on the thin films microloading performance are delineated. Thin films step coverage over a nano scale feature and pitch to pitch film thickness dependence for CVD and ALD dielectric processes are also discussed.

3:40pm NM+NS+MS+EM-MoA6 Interface Analysis of PEALD TaCN Deposited on HfO₂ using Parallel Angle Resolved X-ray Photoelectron Spectroscopy for sub-20nm Gate Last CMOS Transistors, F. Pierrat, ST Microelectronics, France, V. Beugin, R. Gassilloud, P. Michallon, CEA Grenoble, France, L. Dussault, B. Pelissier, LTM - MINATEC - CEA/LETI, France, C. Leroux, CEA Grenoble, France, P. Caubet, ST Microelectronics, France, C. Vallée, LTM - MINATEC - CEA/LETI, France

Sub-20 nm high-k/metal CMOS devices require about 2 nm thin metal gate electrode with adapted work function (WF) and chemical inertness regarding the high-k dielectric sub-layer. TaCN material deposited by Plasma Enhanced Atomic Layer Deposition (PE-ALD) has been investigated as a possible gate electrode candidate [1-2]. Depending on the carbon content TaCN can presents a *p-type* behavior with a WF from 4.5 to 4.7eV [3]. Besides plasma used for deposition may have an impact on the under-layer dielectric such as an increase of the EOT [4]. A deviation from bulk material characteristics of the metal gate WF is induced by the intimate bond linking environment at high-k/TaCN interface, but these chemical mechanisms are still unclear. Thus, in this work, interface of TaCN and HfO₂ dielectric is carefully analyzed by X-Ray Photoelectron Spectrometry (XPS), using Ta4f, Hf4f, O1s, C1s, N1s and Si2p core levels, and obtained bonding environments are correlated to work function extracted from MOS capacitors.

Thanks to chemical stability of SiO₂ [5], bonding environments of TaCN/SiO₂ and HfO₂/SiO₂ stacks were chosen as reference for XPS analysis. Then, by comparing TaCN deposited on HfO₂ spectra with these references, the evolution of the chemical environments can be determined, thus a mechanism of interaction between the two materials is proposed. Furthermore, it appeared that, when deposited on HfO₂, TaCN oxidation is higher than on SiO₂, which is attributed to the higher capacity of HfO₂ to have O deficiency [6].

In addition, TaCN/HfO₂/SiO₂ stack was measured using Parallel Angle Resolved XPS (PARXPS) in order to build a depth composition profile. This profile confirms the modifications of chemical environment such as oxidation of the electrode close to high-k/metal interface, it also shows N penetration in HfO₂, which could be induced by plasma densification.

Finally, electrical results from MOS capacitors with TaCN/HfO₂/SiO₂ stacks and TiN/W plug have shown an evolution of the *p-like* metal flat band voltage (Vfb) with plasma conditions. The modifications of chemical bonding environment observed at the high-k/metal interface can give insight on this deviation of Vfb with plasma.

[1] W. S. Hwang, D. Chan, B. Jin Cho, IEEE Transactions on Electron Devices, 55, (2008)

[2] H. Zhu and R. Ramprasad, Journal of Applied Physics 109, 083719 (2011)

[3] H. N. Alshareef, et al., Electrochemical and Solid-State Letters, 11, H182 (2008)

[4] H. C. Shin and C. Hu, Semiconductor Science Technologie, 11, 463, (1996)

[5] M. Zier, et al., Applied Surface Science 252, 234 (2005)

[6] G. D. Wilk, R. M. Wallace and J. M. Anthony, Journal of Applied Physics 89, 5243 (2001)

4:20pm NM+NS+MS+EM-MoA8 Atmospheric Pressure Atomic Layer Deposition of Al₂O₃ using Trimethylaluminum and Ozone, M.B. Mousa, D.H. Kim, C.J. Oldham, G.N. Parsons, North Carolina State University

Atomic layer deposition (ALD) is used for nanoscale coatings with high uniformity and precise thickness control. Currently, most commercial ALD processes operate in batch mode. Expanding to ambient pressure can increase throughput and facilitate its integration for applications such as smart textiles, flexible electronics and synthetic polymer coatings. We find that under certain flow conditions in the trimethylaluminum (TMA)/water ALD process for Al₂O₃, increasing the reactor pressure from ~2 Torr to 760 Torr can produce excess film growth per cycle.

For this work, we studied ALD of Al₂O₃ using TMA/O₃ and compared growth at ~2 Torr to that at 760 Torr in a flow tube reactor. We measured film thickness by ellipsometry and surface morphology by AFM. Also, we plan to monitor in-situ growth using a quartz crystal microbalance (QCM). At 2 Torr, by changing the ozone and TMA exposure times, we saw clear ALD saturation at ~0.45 Å/cycle at 170°C. A shorter purging time after the ozone exposure tends to increase the growth per cycle. Deposition at higher pressure results in growth rates between ~0.3 and 0.6 Å/cycle at 205°C, with lower growth rates obtained under higher gas flow rate conditions. For both the water and O₃ processes at 760 Torr, a low gas flow rate of 0.5 standard liters per minute (slm) in our flow-tube reactor leads to a high growth rates of ~3 Å/cycle (for water) and 0.6 Å/cycle (for O₃). For the water process at 760 Torr, increasing the flow rate to 10 slm somewhat decreases the growth per cycle to ~1.35 Å /cycle. However, for the O₃ processes at 760 Torr, we need only a relatively small increase to 1.5 slm to achieve growth of 0.3 Å/cycle. This could be due to enhanced ozone desorption kinetics compared to the rate of water desorption under the conditions used. Also interestingly, we find for the water process that films deposited at high pressure have higher surface roughness than films deposited at low pressure. These results will help to identify the key parameters for new continuous atmospheric pressure ALD reactors designs.

4:40pm NM+NS+MS+EM-MoA9 An Industrial Solution for Surface Passivation of c-Si using AlO_x Film Deposited by In-line Atmosphere Chemical Vapor Deposition, K. Jiang, Gebr. Schmid GmbH + Co, Germany, K.O. Davis, University of Central Florida, C. Demberger, H. Zunft, H. Haverkamp, Gebr. Schmid GmbH + Co, Germany, W.V. Schoenfeld, University of Central Florida, D. Habermann, Gebr. Schmid GmbH + Co, Germany

Among the different dielectric passivation layers for crystalline silicon (c-Si) solar cells, AlO_x has recently received a great attention due to its excellent chemical and field effect passivation performance for p-type c-Si surface. It offers great promise as a rearside passivation material for passivated emitter and rear cell (PERC) designs. However, up to this point in time, most of the development has been based on laboratory scale deposition systems and methods. Common approaches for synthesizing these passivation layers are thermal or plasma-assisted atomic layer deposition (ALD), whose deposition rates are typically too low (< 10 nm/min) to be compatible with high-volume manufacturing. Other deposition methods like PECVD or spatial separated ALD enable an increase in deposition rate by one order of magnitude (i.e. 100 nm/min). An industrially-compatible deposition technique with low processing cost, easy-handling, compact size, and high throughput that still retains comparable passivation performance to ALD films remains a challenging task.

Using an in-line atmosphere chemical vapor deposition (APCVD) tool, we have synthesized amorphous AlO_x films from precursors of trimethylaluminum and O₂, yielding a maximal deposition rate of up to 150 nm/min per wafer. Deposition rate is determined by the film thickness divided by wafer transportation time through the CVD injector. Both top

view and the cross-sectional SEM images present an intact AlO_x/Si interface. A smooth surface is shown without any outgassing (blistering) after deposition and a subsequent firing step. The as-deposited layers exhibit an over stoichiometric O/Al ratio of 1.65–1.75 due to the incorporation of an OH group inside the layer. For both high and low doped p-type c-Si wafers deposited with APCVD AlO_x , excellent surface passivation is achieved with a maximum effective surface recombination velocities ($S_{\text{eff,max}}$) of 8 cm/s following by a firing step. These findings are attributed to the buildup of a large negative charge ($Q_f \approx -3 \times 10^{12} \text{ cm}^{-2}$) and low interface defect density ($D_{\text{it}} \approx 4 \times 10^{11} \text{ eV}^{-1} \text{ cm}^{-2}$) following the firing process. It is believed that the incorporated OH group plays an essential role during the firing step. During the annealing/firing step, a certain degree of dehydration takes place (i.e. Al sites bonded OH termination start to bond via an O bridge), which may involve an octahedral to tetrahedral coordination change. This could facilitate the negative charge formation and release of atomic H for passivating the Si dangling bonds at the AlO_x/Si interface.

This data implies a high application potential of APCVD AlO_x for low cost industrial solar cell applications.

5:00pm **NM+NS+MS+EM-MoA10 Solution Based Processing of Floating Gate Memory using Additive-Driven Self-Assembly and Nanoimprint Lithography, J. Watkins**, University of Massachusetts **INVITED**

Polymer and polymer-inorganic hybrid materials organized at the nanoscale are at the heart of many devices that can be created on flexible substrates for applications in energy generation and storage, microelectronics, optoelectronics, communications and sensors. The challenge is to produce these materials using process platforms and materials sets that are environmentally and economically sustainable and can be scaled for cost-effective, high value-added manufacturing. Here we describe a resource efficient, additive approach based on roll-to-roll coating of self-assembled hybrid materials. Specifically we report that nanostructured templates with periodic spherical, cylindrical, and lamellar morphologies exhibiting sub-10 nm domains can be easily obtained through the blending of commercially available disordered polymer surfactants with commodity homopolymers that selectively associate with one segment of the surfactant. We further demonstrate that order in the surfactant systems and in block copolymer templates can be induced by nanoparticle additives that undergo multi-point hydrogen bonding with one of the segments of the polymer template. These additives, which include metal and semiconducting nanoparticles, fullerenes, and other active components, impart functionality to the device. The strong interactions further enable particle loadings of more than 40% in the target phase, resolving a crucial constraint for many applications. These systems can be scaled in our newly constructed R2R processing facility, which includes a custom microgravure coater for hybrid materials that is equipped for in-line substrate planarization and a precision R2R UV-assisted nanoimprint lithography (NIL) tool.

We illustrate the capabilities of these approaches by the fabrication of floating gate field effect transistor memory devices. For this application, the charge trapping layer is comprised of well-ordered polymer/gold NP composites prepared via additive-driven self-assembly; the addition of gold nanoparticles that selectively hydrogen bond with pyridine in poly(styrene-*b*-2-vinyl pyridine) copolymers yields well-ordered hybrid materials at gold nanoparticle loadings of more than 40 wt.%. The charge trapping layer is sandwiched between a dielectric layer and a poly(3-hexylthiophene) semiconductor layer. We can achieve facile control of the memory windows by changing the density of gold nanoparticles. The devices show high carrier mobility ($> 0.1 \text{ cm}^2/\text{Vs}$), controllable memory windows (0–50V), high on/off ratio ($> 10^5$) between memory states and long retention times. Strategies for patterning of the device using NIL will be discussed.

Nanometer-scale Science and Technology

Room: 12 - Session NS+SP-MoA

Nanopatterning and Nanolithography

Moderator: P.E. Sheehan, U.S. Naval Research Laboratory

2:00pm **NS+SP-MoA1 Optical Properties of As-Prepared and Annealed Gold Nanostructures Fabricated by Interference Lithography, A.B. Tsargorodska**, University of Sheffield, UK, *A.V. Nabok*, Sheffield Hallam University, UK, *A.J. Lee*, University of Leeds, UK, *G.J. Legget*, University of Sheffield, UK

Gold nanostructures were fabricated by interferometric lithography (IL) with a view to their application for optical bio-sensing based on localized surface plasmon resonance. This approach relies upon very modest instrumentation, high processing speed and capacity for fabrication of dense

arrays of nanostructures over macroscopic areas. The dimensions and morphology of nanostructures obtained were characterized by AFM/SEM. The arrays of 65-200nm wide and 125-400nm long gold nano-dots and nano-rods with spacing of 120-220nm were fabricated by IL.

UV-vis absorption spectra of gold nanostructures showed a characteristic peak at ca. 520nm associated with localized surface plasmons. A spectroscopic ellipsometry study of the gold nanostructures was carried out. Raman spectra of a thin film of phthalocyanine adsorbed on gold nanostructures showed an enhancement of Raman scattering of up to 200 times compared with the same film deposited on continuous gold layer.

Post-lithographic processing by annealing was found to improve the optical properties of the nanostructure arrays still further. Annealed samples appear higher and smaller compared to as-prepared samples. AFM images show that all the samples annealed at between 450–470°C for 50–120min retain a regular pattern. XRD analysis of annealed gold nanostructures evinces formation of crystal clusters on the surface.

In order to demonstrate the biosensing capabilities of annealed and as-prepared nanostructures, the LSPR response of nanostructures to changes in the bulk refractive index (RI) was investigated. The RI sensitivity of the annealed samples is found to be 145nm/RIU. Compared to the RI sensitivity value of the as-prepared sample (52.5nm/RIU) this value is ~ 2.7 times higher due to smaller size of nanostructures and larger spacing between them.

A model biosensing of streptavidin-biotin binding and BSA were successfully performed on as-prepared and annealed gold nanostructures. Measurements were based on the LSPR shift induced by local RI change when proteins are immobilized on the nanostructures. Streptavidin concentrations were washed over the nanostructured surface in cumulative succession ranging from 0.1 $\mu\text{g/ml}$ to 0.1mg/ml, followed by an identical protocol with biotin. Characteristic increases and saturation are noted through shifts in the absorption of the LSPR peak at ca. 635nm. Annealed nanostructures demonstrated a higher detection limit (DL) compare to as-prepared one: the DL for BSA is 1.5fM and 50pM for annealed and as-prepared nanostructures, respectively. Our results demonstrate the potential of interference lithography for the application of plasmon-based biosensing devices.

2:20pm **NS+SP-MoA2 Fast Turnaround 3D Nanolithography using Heated Probes – from Nanofabrication to Directed Assembly, A.W. Knoll**, P. Paul, IBM Research - Zurich, Switzerland, *F. Holzner*, IBM Research - Zurich, ETH Zurich, Switzerland, *J.L. Hedrick*, IBM Research - Almaden, *M. Despont*, IBM Research - Zurich, Switzerland, *C. Kuemin*, IBM Research - Zurich, ETH Zurich, Switzerland, *H. Wolf*, IBM Research - Zurich, Switzerland, *N.D. Spencer*, ETH Zurich, Switzerland, *U. Duerig*, IBM Research - Zurich, Switzerland **INVITED**

A novel thermal scanning probe lithography (tSPL) method based on the local removal of organic resist materials has been developed at the IBM Research Laboratory in Zurich [1-3]. A polymeric polyphthalaldehyde resist [2-4] responds to the presence of a hot tip by local material decomposition and desorption. Thereby arbitrarily shaped patterns can be written in the organic films in the form of a topographic relief, constrained only by the shape of the tip. The combination of the fast 'direct development' patterning of a polymer resist and the in-situ metrology capability of the AFM setup allows to reduce the typical turnaround time for nanolithography to minutes.

Patterning rates of 500 kHz have been achieved. For this, the mechanics and drive waveform of the scan stage were optimized, achieving high speed linear scanning with an overall position accuracy of $\pm 10 \text{ nm}$ over scan-ranges and scan-speeds of up to 50 μm and 20 mm/s, respectively. A pre-tension-and-release strategy was used to actuate the cantilever above its resonance frequency of 150 kHz.

Fabrication of three dimensional patterns is done in a single patterning step by controlling the amount of material removal at each pixel position. The individual depths of the pixels are controlled by the force acting on the cantilever.

The structuring capability in the third dimension adds an entirely new feature to the lithography landscape and finds applications e. g. in multi-level data storage, nano/micro-optic components and directed positioning of nanoparticles. For the latter, shape-matching guiding structures for the assembly of nanorods of size 80nm \times 25nm have been written by thermal scanning probe lithography [4]. The nanorods were assembled into the guiding structures by means of capillary interactions. Following particle assembly, the polymer was removed cleanly by thermal decomposition and the nanorods are transferred to the underlying substrate without change of lateral position. As a result we demonstrate both the placement and orientation of nanorods with an overall positioning accuracy of $\approx 10 \text{ nm}$ onto an unstructured target substrate.

- [1] D. Pires, J. L. Hedrick, A. De Silva, J. Frommer, B. Gotsmann, H. Wolf, M. Despont, U. Duerig, and A. W. Knoll, *Science* **328**, 732 (2010).
- [2] A. W. Knoll, D. Pires, O. Coulembier, P. Dubois, J. L. Hedrick, J. Frommer, U. Duerig, *Adv. Mat.* **22**, 3361 (2010).
- [3] P. C. Paul, A.W. Knoll, F. Holzner, M. Despont and U. Duerig, *Nanotechnology* **22**, 275306 (2011).
- [4] F. Holzner, C. Kuemin, P. Paul, J. L. Hedrick, H. Wolf, N. D. Spencer, U. Duerig, and A. W. Knoll, *NanoLetters*, **11**, 3957 (2011).

3:00pm NS+SP-MoA4 Laser Assisted Electron Beam Induced Deposition of Platinum, *N.A. Roberts*, University of Tennessee Knoxville, *J.D. Fowlkes*, Oak Ridge National Laboratory, *G.A. Magel, T.M. Moore*, Omniprobe, Inc. an Oxford Instruments Company, *P.D. Rack*, University of Tennessee Knoxville

We introduce a laser assisted electron beam induced deposition (LAEBID) process which is a nanoscale direct write method that implements a synchronized electron beam induced deposition (EBID) process with a pulsed laser step for thermal desorption of the reaction by-product. The pseudo-localized (~ 100 nm spot), pulsed laser enables thermal desorption of the reaction by-product without the issues associated with bulk substrate heating, which shortens the precursor residence time and distort pattern fidelity due to thermal drift. Current results show a significant purification of platinum deposits (~35% Pt) with the addition of synchronized laser pulses as well as a significant reduction in deposit resistivity. Measured resistivity from platinum LAEBID structures (1.2×10^4 mW-cm) are more than 3 orders of magnitude lower than standard EBID platinum structures (2.2×10^7 mW-cm) from the same precursor and are lower than the lowest reported EBID platinum resistivity with post-deposition annealing (1.4×10^4 mW-cm).

3:40pm NS+SP-MoA6 Parallel Stacking of Extended π -conjugated Molecules on Si(100)-H Surface, *M.Z. Hossain*, Gunma University, Japan, *H. Kato*, Osaka University, Japan, *M. Kawai*, The University of Tokyo and RIKEN, Japan

Understanding and controlling of intermolecular interaction in highly organized π -conjugated molecules is crucial for the development of the high performance organic devices. Molecule-molecule interaction through frontier orbital states is assumed to be substantially varies with the packing pattern and intermolecular distance. H-terminated Si(100) surface has appeared as an ideal template for controlled stacking of π -conjugated molecules, where the intermolecular distance is defined by the dimer-dimer distance on the surface. To date, a number of studies have been reported on the controlled growth of different types of molecular assemblies and their junctions on the surface. It is expected that intermolecular interaction between such assemblies should strongly varies with substituent and extent of π -conjugation of the molecules. Here we report various nanopattern formation with some simple acene molecules such as 9-vinyl anthracene, 2-vinyl naphthalene and styrene on H-terminated Si(100) using scanning tunneling microscope (STM) and ultraviolet photoelectron spectroscopy (UPS).

Controlled stacking of styrene molecules on H-terminated Si(100) surface through chain reaction mechanism is well known. Self-directed growth of molecular stacking is exclusively directed along the dimer row on the surface, where the phenyl rings are stacked in parallel along the dimer row. Unlike styrene molecule, 9-vinyl anthracene forms both orderly stacking pattern along the dimer row and disorderly nanopattern on the surface. The relative appearances of these orderly and disorderly nanopatterns in STM images depend on the applied sample bias while scanning. At lower bias, the orderly pattern appears much brighter than that of the disorderly pattern. This contrast difference between two structures relates to the enhanced π - π interaction in the case of orderly stacked nanopattern. We also observe that the orderly nanopattern of anthracene molecules undergoes reversed chain reaction very frequently compared to that of styrene molecule.

The 2-vinyl naphthalene molecules form relatively shorter assemblies along the dimer row. Some short disorderly structures are also seen in STM images. UPS measurements of different surfaces containing high-density nanopatterns of these acene molecules have been performed. The observed peaks in UPS spectra are reasonably in agreement with the theoretical calculations reported earlier. The details of the UPS spectra and the reaction mechanism of each molecule forming different nanopatterns will be discussed.

4:00pm NS+SP-MoA7 Kinetics of disilane reaction on Si(100)-(2x1): Flux, Temperature, and H-coverage Dependence, *D. Dick, J.-F. Veyan*, University of Texas at Dallas, *P. Mathieu*, Mc Gill University, Canada, *J.N. Randall*, Zyvex Laboratories, *Y.J. Chabal*, University of Texas at Dallas
Atomic Layer Epitaxy (ALE) is a fundamental process in the Atomically Precise Manufacturing (APM) of nanoscale devices. Si₂H₆ has been shown

to be a good precursor molecule for patterned growth on Si(100) using Chemical Vapor Deposition (CVD). For ALE of silicon, three parameters have to be considered: the incident Si₂H₆ flux, the temperature, and partial H coverage of the surface. These parameters have been investigated experimentally using in-situ infrared absorption spectroscopy to characterize the nature and coverage of species on a Si(100)-(2x1) surface in a well-controlled environment (2×10^{-10} Torr base pressure).

The flux dependence was studied over two orders of magnitude and temperature dependence from 173 K to 473 K for varying fluxes. It was found that the nature of SiH_x species formed at the surface was strongly dependent on the flux, with higher silanes (e.g. $x > 1$) for higher fluxes. Furthermore, the time required for saturation also decreased with increasing flux and temperature.

The impact of partial H coverage was also investigated with H coverage from 0.01 to 1 ML Monolayer, achieved by partial desorption of a H saturated surface. On the substrate's surface has been also investigated with FT-IR under UHV conditions. It has been found that even a very small amount of Hydrogen (~1% ML) substantially reduces the chemisorption of disilane on the clean parts of Si(100)-(2x1).

This complex dependence on flux and temperature arises from the complex and highly temperature dependent adsorption/dissociation behavior of disilane on Si(100). The dependence on partial H coverage highlights the spatial requirements of the dissociation products, as uncovered in our earlier work.¹

1 J.-F. Veyan, et al., *Journal of Physical Chemistry C* **115**, 24534.

4:20pm NS+SP-MoA8 SPM Lithography on Silicon Reconstructed and Hydrogen-Passivated Surface, *J. Fu, K. Li, N. Pradeep, L. Chen, R. Silver*, National Institute of Standards and Technology

We are using Scanning Probe Microscope (SPM) to write patterns directly on a single crystal silicon surface that was reconstructed and hydrogen-passivated in the ultra high vacuum (UHV) chambers, and are followed by the process of reactive ion etching to transfer the patterns into the silicon bulk. The patterns were written either by an atomic force microscope (AFM) in the ambience or by a scanning tunneling microscope (STM) in UHV chambers and was immediately proceeded by an oxidation process in a separate vacuum chamber. AFM or STM patterned samples were immediately transferred to a RIE chamber via an argon back-filled inflatable glove box.

In terms of patterning, the AFM in the ambient environment and the STM in the UHV both can perform lithograph; however, the mechanism are quite different: the AFM is adding species, OH⁻, to the surface, and the STM is removing species, H, from the silicon surface.

The features patterning by the AFM prior to RIE process were 1~2nm in height, and were 15~20nm height after RIE and 6nm wide (FWHM) that were measured and confirmed by a critical dimension AFM (CD-AFM). For the features patterning by STM, it was conjectured the height were 0.2~0.3nm prior to RIE. After the RIE process, the height was measured to be 0.7nm.

4:40pm NS+SP-MoA9 Ultra-High Frequency Surface Acoustic Wave Generation in Silicon Using Inverted Nanoimprint Lithography, *S. Büyükköse*, University of Twente, Netherlands, *B. Vratzov*, NT&D – Nanotechnology and Devices, Germany, *D. Ataç*, *J. van der Veen*, University of Twente, Netherlands, *P.V. Santos*, Paul-Drude-Institut für Festkörperelektronik, Germany, *W.G. van der Wiel*, University of Twente, Netherlands

Surface acoustic waves (SAWs) are widely used and very important phenomena in both research and industry. SAWs are mechanical vibrations propagating along the surface by confining the acoustic energy over a depth of typically one wavelength. In piezoelectric materials, they can be excited through the inverse piezoelectric effect by using interdigital transducers (IDTs): two interlocking comb-shaped metallic electrode pairs. A piezoelectric potential wave accompanies the mechanical wave. The unique SAW properties make them suitable for wide range of applications. Among the most exciting applications of SAWs are acousto-optical modulators as well as the control of excitons, electrons, and spins in semiconductors. For almost all SAW applications, there is a strong demand for higher frequencies, for example to enhance processing speed or to reach the quantum regime. There are two main factors determining the IDT resonant frequencies: the acoustic properties of the substrate, and the IDT period constrained by lithography resolution. In latter case, the resolution of standard photolithography (minimum finger width of approx. 0.5 μ m) limits the operation frequency to around a few GHz, even for high acoustic-velocity substrates.

In this study, an alternative lithography technique, "step-and-flash nanoimprint lithography" (SFIL), with a novel material system for lift-off was used to reach very high resolution and higher reproducibility. Hydrogen

silsequoxane (HSQ) was used as a planarization layer and an excellent etching mask to get inverted replication of the IDT features on the SFIL template. A sufficient undercut profile of the electrode features, which is essential for metal lift-off at nanoscale, was successfully achieved. Very high critical dimension (CD) control has been obtained for the electrode dimensions from 125nm down to 65 nm. While this method has the advantage of EBL resolution, it is nearly substrate independent with higher throughput compared to EBL. For the IDT fabrication, we have deliberately chosen a rather standard Si substrate to demonstrate that our method can result in extremely high-frequency SAW devices, which can be monolithically integrated with common electronic circuitry. Integration of high-frequency SAW devices is normally restricted by the incompatibility of piezoelectric films with CMOS processing. We showed that SAW delay line devices with 125nm down to 65 nm metal lines can reach resonance frequencies up to 16 GHz in ZnO/SiO₂/Si multilayer system, which is the highest frequency for ZnO based transducers on Si reported so far. The finite element analysis confirmed the results and showed good agreement with the experiment.

5:00pm **NS+SP-MoA10 Variance of Proximity Effect Correction Parameter Measured on Silicon**, *D.A. Czaplewski, L.E. Ocola*, Argonne National Laboratory

We present data showing that the relative intensity of the backscattered electrons, h , to primary write electrons varies depending on the experimental setup. Our data is consistent with the wide range in values reported in the literature for h . The value of h was determined using a doughnut and cross method [1] where the range of the backscattered electrons was measured to an uncertainty of less than 1%. We find that using this method to determine h provides values that are dependent on the dose of the doughnut. Such a result raises questions on the effectiveness of standard proximity effect correction models (PEC) if they rely on a single h value. Standard PEC models attempt to load level the dose received by the desired pattern in the e-beam resist from all sources of electrons, including the forward and backward scattered electrons during an electron beam exposure.

The relative dose of the backscattered electrons was measured using a set of intersecting lines at the center of tori patterns in a doughnut and cross method [1], (Fig. 1). The backscattered electron dose contribution was varied by changing the dose of the tori with respect to the dose of the intersecting lines as can be seen in Fig. 2. The expected behavior would be a consistent ratio of the backscattered contribution and the line dose; however, as the backscattered electron dose is decreased, the relative contribution to the pattern increases faster than the line dose contribution (Fig. 3). The causes of this phenomenon are not certain yet, but the implications could change existing PEC models. Through further study of this phenomenon, it is possible that the models used in PEC could be updated to accommodate this data and therefore give more accurate dose assignments.

[1] D. A. Czaplewski, L. E. Ocola, *Appl. Phys. Lett.* **99** 192105 (2011).

5:20pm **NS+SP-MoA11 Nanopatterning of Poly(N-isopropylacrylamide) based Hydrogel – Gold Nanoparticle Composite**, *K.J. Suthar, D.C. Mancini, R.S. Divan*, Argonne National Laboratory, *O.N. Ahanotu*, University of Michigan

This paper presents the nanopatterning of the hydrogel-gold nanocomposite. We synthesized water based colloidal suspension of covalently bound gold nanoparticles (5-10nm) on the backbone of Poly(Allyl amine) by reduction of gold salt on the amine groups of polymeric chain. Poly(N-isopropylacrylamide) was dissolved in Poly(Allyl amine) based gold colloidal solution. This solution then spun-coated on Hexamethyldisilazane primed Si wafer for nanolithography. The hydrogel precursor was dried in air. Resulting thickness of the hydrogel precursor was approximately 1 mm. The samples were then exposed to 110-180 $\mu\text{C}/\text{cm}^2$ e-beam. The exposure does was optimized for different thickness of precursor. Different characterization techniques such as UV-vis spectroscopy, differential scanning calorimetry, FTIR, scanning electron microscopy, and atomic force microscopy were employed for characterization. Thus, gold nanoparticles were incorporated into a three dimensional, cross-linked, polymeric hydrogel network by nanopatterning technique. With the ability of hydrogels to expand or contract with changes in pH and temperature, the spacing between nanoparticles can be controlled, allowing a single material being able to resonate at different frequencies. The ability to perform lithography to form a patterned hydrogel with homogeneous nanoparticles opens the door to development of nanoswitches, sensors, MEMS as well as drug delivery devices.

Advanced Surface Engineering
Room: 22 - Session SE+NS-MoA

Nanostructured Thin Films and Coatings II:
Multifunctional Properties

Moderator: E. Broitman, Linköping University, Sweden

2:00pm **SE+NS-MoA1 Layered Binary Metal Oxide Solid Lubricants for High Temperature Moving Assemblies**, *S. Aouadi, D. Stone*, Southern Illinois University Carbondale, *A. Martini*, University of California Merced, *C. Muratore, A.A. Voevodin*, Air Force Research Laboratory **INVITED**

Oxides exhibit an unparalleled variety of physical properties that give them great promise for many applications in optics, magnetism, and electronics. Oxides that possess layered crystal structure inherently display anisotropic properties as a result of their non-symmetrical crystal structure. This flexibility in their structural skeleton offers a great opportunity to create new materials with designed functionality. This paper provides an overview of the current research developments in understanding how a class of layered binary metal oxides is effective at reducing friction at moderate and high temperatures. Oxides, known to be abrasive at low temperatures, are particularly desirable lubricious materials at high temperatures considering that most materials will oxidize in air under these conditions. Four different, non-exclusive, mechanisms are reported to cause their enhanced lubricity: (1) oxide softening due to the working temperatures between 0.4-0.7 of the absolute melting temperature (T_m), (2) melting of the oxide by exceeding T_m , (3) the creation of a material with a lamellar crystal structure with weak interplanar bonds, and, (4) shearing due to dislocations or grain boundary sliding. We will focus on understanding the fundamental mechanisms that impart their advantageous material properties at high temperatures using computational (density functional theory and molecular dynamics simulations) and experimental tools (in situ Raman spectroscopy, X-Ray diffraction, scanning electron microscopy, and transmission electron microscopy). The frictional and wear properties of these materials, tested in various controlled environmental conditions, will be discussed in detail.

2:40pm **SE+NS-MoA3 Free-standing Nanoscale Gold Pyramidal Films with Milled Nanopores**, *J.A. Grant-Jacob, W.S. Brocklesby, T. Melvin*, Optoelectronics Research Centre

Thin films of micro and nanostructured metals are important for the construction of plasmonic devices and microelectromechanical systems (MEMS). The fabrication of individual metallic, pyramidal shells as well as ultra-smooth metal films with grooves, bumps, pyramids and holes has previously been demonstrated^{1,2}, as has direct raster milling with 5 nm machining precision in 100 nm thick gold films³. Routine fabrication of micro and nanostructured thin films is desirable. In this work, the fabrication of arrays of nanoscale pyramidal structures in free-standing gold films is demonstrated, and single nanopores are milled into the nanostructures for DNA translocation.

Silicon Klarite® pyramidal micro-structured substrates are an effective tool for surface enhanced Raman scattering (SERS) experiments, owing to the strong field enhancement within the pyramids. Here, the substrates are used as moulds for creating pyramidal structured gold as free-standing thin films. The silicon substrates contain an array of pyramids etched into a 4 mm x 4 mm square region on the substrate's surface. These pyramids are 1.5 μm x 1.5 μm square and 1 μm deep on a pitch of 2 μm . An Edwards E306A Thermal Evaporator is used to coat silicon samples in a 50 nm layer of Teflon® and then a 100 nm layer of gold. Epoxy is then deposited on top of the gold layer using a pipette. Once the epoxy has cured, the epoxy together with the gold is mechanically lifted from the Teflon® coated substrate. The gold-coated epoxy is then placed over a micron-sized aperture and the epoxy dissolved away using acetone. Initial imaging is performed using a Carl Zeiss SMT, Inc., Evo® scanning electron microscope (SEM), while the subsequent imaging and milling of 50 nm holes through the free-standing gold is carried out using an Carl Zeiss SMT, Inc., Orion® Plus helium ion microscope (HIM). These films are suspended over micron-sized apertures for integration into platforms already proven for DNA translocation, and to optically interrogate the structures using Raman based techniques.

¹ Q. Xu, I. Tonks, M.J. Fuerstman, J.C. Love, and G.M. Whitesides, *Nano Letters* **4**, 2509-2511 (2004).

² P. Nagpal, N.C. Lindquist, S.-H. Oh, and D.J. Norris, *Science* (New York, N.Y.) **325**, 594-7 (2009).

³ L. Scipioni, D.C. Ferranti, V.S. Smentkowski, and R. a. Potyrailo, *Journal of Vacuum Science & Technology B: Microelectronics and Nanometer Structures* **28**, C6P18 (2010).

3:00pm **SE+NS-MoA4 Synthesis of Superhydrophobic PTFE-like Thin Films by Self-Nanostructuring in a Hybrid Plasma Process**, *F. Henry*, University of Mons, Belgium, *F. Renaux*, *S. Coppée*, Materia Nova Research Center, Belgium, *R. Lazzaroni*, University of Mons, Belgium, *N. Vandencastele*, *F. Reniers*, ULB, Belgium, *R. Snyders*, University of Mons, Belgium

Superhydrophobic Poly(tetrafluoro-ethylene) (PTFE) like thin films were grown using a plasma-based hybrid process consisting on sputtering a carbon target in a Ar/CF₄ atmosphere. The influence of the bias voltage applied to the substrate (VBias) as well as of the gas mixture composition (%CF₄) on the chemical composition, the wettability and the morphology of the deposited thin films were evaluated.

The chemical composition measured by X-Ray photoelectron spectroscopy (XPS) reveals that the fluorine content is lower than in conventional PTFE (50 at.% maximum >< 66%) and that it decreases when VBias increases (from 50 at.% for VBias = -100 V to 30 at.% for VBias = -200 V). This behaviour is associated with the preferential etching of the fluorine atoms during the plasma-assisted growth of the films. Consecutively to this etching, a self-nanostructuring enhanced by increasing VBias, is observed. As a consequence, the water contact angle (WCA) measurements range from 70° up to 150° depending on (i) the fluorine content and (ii) on the magnitude of the nanostructuring. In addition, for the films presenting the highest WCA angles, a small hysteresis between the advancing and receding WCA is observed (< 10°) allowing these films to fulfil completely the requirements of superhydrophobicity.

In order to get more understanding on the wettability mechanisms of these surfaces, the topology of the films has been evaluated by atomic force microscopy (AFM). The data reveal, for all films, a dense and regular structure composed by conic objects for which the dimensions increase with Vbias. We were able to correlate the ratio of the average height (AvH) of the objects and the average distance (AvD) between them with the WCA. Theoretical evaluations of the WCA using the Wenzel and Cassie equations with, as inputs, the features of the deposited thin films surfaces measured by AFM suggest that the wetting regime is intermediate between these two ideal situations.

3:40pm **SE+NS-MoA6 Creation of Highly Functionalized Polymer-Metal Oxide Nanomaterials Using A Novel Rotating Drum Plasma Reactor**, *J.C. Shearer*, *E.R. Fisher*, Colorado State University

The use of nanoparticles in biological applications has grown rapidly in recent years. Understanding the surface chemistry and protein-nanoparticle interactions is critical in the fabrication of biomedical devices. Some nanoparticle surfaces are not compatible with specific applications, and thus must be modified to make them viable. Plasma processing of nanomaterials is an effective method for functionalization and encapsulation of nanoparticles. Our lab has designed a rotating drum inductively coupled plasma reactor that has afforded the ability to create specifically tailored nanoparticle surfaces. The rotating drum apparatus was utilized to encapsulate Fe₂O₃ and Au nanoparticles with various polymer films. Allyl alcohol, allylamine, and acrylic acid plasmas were used to incorporate alcohol, amine, and carboxylic acid functionality to nanoparticle surfaces, respectively. Tailoring of film composition was achieved by lowering the duty cycle (d.c.) of the plasma to facilitate less fragmentation of the monomer. This resulted in the deposited films being more stoichiometrically similar to the parent monomer gas and thus having a high concentration of functional groups present within the film. For example, the alcohol functionality of plasma polymerized allyl alcohol films on Fe₂O₃ nanoparticles can be substantially increased by lowering the d.c. of the plasma from 100 % to 10 %. Specifically, x-ray photoelectron spectroscopy elemental analysis shows that films deposited under low d.c. conditions increase O/C ratios from 0.17 to 0.35, which is comparable to that of the parent monomer (0.33). FTIR data reveal complementary results, where increases in OH functionalities are observed for low d.c. plasmas. Electron microscopy confirms there is no appreciable change in size and shape of the nanoparticles upon plasma treatment. The solubility and stability of the encapsulating films were analyzed to measure the longevity of the particles in biological systems. Highly functionalized films were also deposited onto supported nanoparticle substrates to investigate how plasma processing affects surface roughness, as this can affect cell adhesion. We have demonstrated that plasma processing can change the RMS roughness of supported nanoparticles by 0.2 μm, thereby affording the ability to tailor the roughness of a surface for specific cell interactions. A variety of gas-phase and surface analysis data will be presented to show how plasma processing can tailor the composition of deposited films of as a function of plasma parameters and gas-phase species. Understanding how these films are produced will undoubtedly advance the fabrication of novel biomedical devices.

4:00pm **SE+NS-MoA7 Field Emission Dynamic Investigation of the Polymer-MWCNT Composite Films Depending from Vacuum Conditions**, *E.O. Popov*, *A.G. Kolosko*, *M.V. Ershov*, *S.V. Filippov*, A.F. Ioffe Physico-Technical Institute, Russian Federation

It is obvious that research I-V characteristics remains the basic criterion of an estimation of field emission process. However the techniques, allowing to do exhaustive conclusions about the physical processes occurring on nano dimensional emission sites by macroscopical values of a current and voltage does not exist yet. Especially it is expressed at research of dynamics of field emission, the phenomena accompanying functioning flat multityps cold cathodes (emitters).

Attempts to observe other phenomena that can accompany emission processes, except for observation of I-V characteristics, are being made. There are the registration of radiation of the emitter and the anode, heating of electrodes, change of vacuum conditions, mass spectrometer researches. Application of computer processing during record I-V characteristics opens additional possibilities of knowledge of evolution and emitter work, allows to approve models of physical processes is directly during emission experiment.

In our work was developed the technique of multichannel record and *in situ* data processing about evolution of field emitters. On-line processing of signals is performed on the basis of own program written on Labview 10. The technique includes multichannel system of gathering of signals of a current and voltage, record of vacuum values and temperature. As a part of mass spectrometer installation the given system collects the data about kinetics allocation of the volatile products accompanying emission process. Data for representation in a kind convenient for the analysis is in addition processed: beta values of field increasing, active resistance of inter-electrode gap, visualization of height of emitters and the estimation of a total emitting surface and number of the emission centers is made.

Some characteristic areas in dependence SK [1,2] which are treated as desorption gases from surface MWNT, area of growth of number of sites without change of the geometrical sizes (almost vertical growth SK), area of smooth change of geometry of the emitter (increase in intensity of a field and increase in the area of the emitter - intercept increasing) have been found out.

[1] M. Kawasaki, Z. He, Y. Gotoh, H. Tsuji, J. Ishikawa, *J. Vac. Sci. Technol. B* 28, (2010) C2A77.[2] E.O.Popov, M.V. Ershov, *IEEE*, 24th INVC, Wuppertal, (2011) 158.

4:20pm **SE+NS-MoA8 Cost Efficiency Trade Off in Nanostructured Thermoelectric Energy Conversion Systems**, *A. Shakouri*, *K. Yazawa*, Birck Nanotechnology Center, Purdue University **INVITED**

Energy consumption in our society is increasing rapidly. A significant fraction of the energy is lost in the form of heat. In this talk we introduce thermoelectric devices that allow direct conversion of heat into electricity. Some new physical concepts and nanostructures make it possible to modify the trade-offs between the bulk electrothermal material properties through the changes in the density of states, scattering rates and interface effects on the electron and phonon transport. We will review recent experimental and theoretical results on nanostructured materials as well as solid-state thermionic power generation devices. Theory and experiment are compared for several III-V and nitride nanocomposites and multilayers. Potential to increase the energy conversion efficiency and bring the cost down to \$0.1-0.2/W will be discussed.

5:00pm **SE+NS-MoA10 The Effects of Interfacial Bond Stiffness on Heat Transport: An Experimental Study Using Self-Assembled Monolayers**, *M.D. Losego*, *M. Grady*, *N.R. Sottos*, *D.G. Cahill*, *P.V. Braun*, University of Illinois at Urbana Champaign

Compared with our ability to precisely control the flow of electrons or light within a material, our capacity to design the flow of heat, particularly at the nano-scale, is rather rudimentary. For example, billions of microscopic transistors with coordinated electronic transport are routinely fabricated for computers, cell phones, and iPods. In contrast, thermal management is largely limited to macroscopic solutions (e.g. fans, insulation). Examples of confining and controlling heat with precision at micro- or nanometer length scales are relatively rare

Crucial to nanoscale thermal management is an understanding of interfacial heat transport. Interfaces between two materials act as a barrier to heat flow. For nano-scale systems, interfacial heat conduction and not just bulk thermal conductivity is important and possibly dominant in controlling heat transfer. However, thermal transport across interfaces is still not well understood. Historically, differences in bulk acoustic properties and/or phonon densities of states have been used to explain the interfacial thermal boundary resistance. However, more recently, atomic level structural features, such as interfacial roughness and interfacial bonding, have been proposed as contributors to the thermal boundary resistance.

This talk will describe experimental work that attempts to validate recent molecular dynamics (MD) simulations suggesting that interfacial thermal conductance can be strongly modulated by adjusting the strength of interfacial bonds. Our experimental system consists of self-assembled monolayers (SAMs) on SiO₂ substrates having either methyl or mercapto terminations. Gold films are transfer printed onto these surfaces forming either a van der Waals or covalent bond respectively. The interfacial thermal conductance across the Au/SAM interface is measured via time-domain thermoreflectance (TDTR) and found to increase by nearly 2x when the interface is switched between a van der Waals interaction and a covalent bond. The interfacial bond stiffness is independently measured using picosecond acoustics. Together these experiments represent the first clear demonstration of how changing the stiffness of a single atomic-scale interfacial bonding layer affects thermal conductance.

To further elucidate the mechanism for this change in interfacial thermal conductance, we will present temperature dependent thermal conductance measurements. This data reveals that high frequency phonon modes cannot traverse interfaces with lower stiffness. Finally, we will show proof-of-concept experimental results that outline a scheme for designing materials with specified values of interfacial thermal conductance.

5:20pm **SE+NS-MoA11 Growth, Nanostructure Formation, and Physical Properties of Single-Phase, Epitaxial, SrTiO₃-TiO₂ Nanocomposites: A Topological Insulator Approach to High-T Thermoelectrics**, *B.M. Howe*, Air Force Research Laboratory, *E. Thomas*, University of Dayton Research Institute, *D. Dudis*, Air Force Research Laboratory

Here, we present a novel approach towards creating efficient thermoelectric materials for energy conversion and thermal management under high-temperature and oxidizing environments. Several transition-metal oxide systems have recently been investigated, however most studies involve the doping of single-phase compounds to enhance electrical conductivity; while very few address decreasing thermal conductivity (in the same direction as electron transport). Thus, we present an investigation into the growth, nanostructure formation, and physical properties of epitaxial, immiscible SrTiO₃-TiO₂ nanocomposites. Sr_(1-x)Ti_(1+x)O_(3+2x) layers with 0 ≤ x ≤ 0.67 were grown on SrTiO₃ (001) substrates at 700°C in 1 × 10⁻⁶ Torr O₂ by high-vacuum pulsed laser deposition using a KrF excimer laser (λ = 248nm) operating at 10 Hz pulse rate and 1.7 J/cm² fluence. HRXRD and XTEM results show that perovskite-structure layers grow epitaxially with a cube-on-cube orientational relationship to the substrate. The lattice parameter increases linearly while crystalline quality decreases from x=0 to x=0.67. We find a remarkably broad metastable single-phase field given the immiscible nature and crystal structure mismatch of the two alloy components. Alloying SrTiO₃ with TiO₂ leads to the formation of nanostructured compositional modulations due to the onset of spinodal decomposition, resulting in increased in electrical conductivities (due to the formation of 2D electron gas layers at the SrTiO₃-TiO₂ interfaces), decreased thermal conductivities, and enhanced thermoelectric figure of merit, large enough to compete with current state-of-the-art high-temperature thermoelectric materials.

Nanometer-scale Science and Technology

Room: 12 - Session NS+EN-TuM

One-Dimensional Nanowires and Nanotubes

Moderator: M.C. Hersam, Northwestern University

8:00am NS+EN-TuM1 **Direct Observation of Selective Band Engineering of an Isolated Subnanometer Wire.** *I. Song, D.-H. Oh, C.-Y. Park, J.R. Ahn*, Sungkyunkwan University, Republic of Korea

Band engineering has been achieved mainly by substituting an atom of a pristine nanomaterial with an extra atom. At the ultimate nanometer scale, subnanometer scale, a nanowire becomes closer to an ideal 1D system and the band engineering by the atomic substitution enters a different regime. The strong disorder by the atomic substitution tends to break a pristine 1D system. In the band engineering of the subnanometer wire (hereafter subnanowire), we need to find a way of circumventing the dilemma of doping and disorder. There is another challenging problem to find out a conclusive experimental proof that its electronic band structure is changed within a single isolated subnanowire. A unique experimental way is to measure its electronic band structure by angle-resolved photoemission spectroscopy (ARPES). Because a photon beam in ARPES measurement cannot be focused down to subnanometer scale, a single subnanowire cannot be used and rather subnanowires have to be aligned along a specific direction on a surface. A fundamental requirement to resolve the puzzling problem is that subnanowires have to be aligned by a self assembly method. In comparison to the atomic structure, its electronic structure is required to be decoupled to observe a 1D electronic structure change of a single isolated subnanowire by a dopant. In this study, self-assembled subnanowires on a stepped surface, Au-induced subnanowires on a Si(553) surface, were chosen. A Si(553) surface, which is one of stepped Si(111) surfaces, has an appropriate terrace width to assemble subnanowires along its step edge direction and its step edge structure can decouple subnanowires electronically. Three different metallic subnanowires exist on its single terrace and each metallic wire has only a single metallic band. After extra Au atoms were adsorbed on the self-assembled subnanowires at room temperature, only one of metallic bands moved rigidly to a higher binding energy without a change in other metallic bands, which was directly observed by ARPES measurement. Here we note that if the three metallic subnanowires are coupled electronically to each other, all of the three metallic bands have to shift rigidly. This experimentally proves that only one of self-assembled multiple metallic wires can be controlled electronically by a dopant and the electronic structure of an isolated wire can be controlled down to a subnanometer scale.

8:20am NS+EN-TuM2 **Growth of ZnO Nanowires on Retroreflector Microspheres and the Resulting Plasmonic Light Channeling Properties.** *S.M. Prokes, O.J. Gembocki, E. Cleveland*, Naval Research Laboratory

We investigated the growth of ZnO nanowires on retroreflectors in order to potentially enhance the optical response of these composite structures. Results show that the growth of ZnO aligned NW arrays can be achieved on the retroreflectors, but it occurs far away from the Zn vapor source compared to the standard ZnO nanowire growth on a flat Si substrate. In the case of the ZnO nanowires on flat Si, the nanowires that formed in nearly aligned arrays were short and significantly thicker, suggesting that the growth occurred both longitudinally and laterally in this process. For the NW growth on the curved retroreflectors, as the distance from the vapor source increased, the NW density increased and for the substrates farthest from the source, growth of nearly aligned NW arrays was noted. Initially, the ZnO growth on the retroreflectors resulted in a high rate of deposition of a polycrystalline ZnO film and as the amount of Zn vapor decreased, the vapor-solid (VS) nucleation of random NWs began, and aligned nanowire arrays only formed where the vapor supply was the lowest. The fact that it is more difficult to nucleate and grow ZnO NW arrays on the retroreflectors is likely due to the surface roughness, as well as the crystal structure of the retroreflector bead.

Once nearly aligned arrays of ZnO nanowires on the retroreflectors were formed, we investigated their optical properties by forming ZnO/Ag composite NW structures and using a self assembled monolayer of benzenethiol to measure a surface enhanced Raman (SERS) response. The ZnO/Ag NW composites were formed by atomic layer deposition (ALD) of Ag, and the surface enhanced Raman (SERS) response was measured and compared to nanowire composites deposited on a flat Si substrate. Results indicated that the SERS response was 29 times greater in the case of the ZnO/Ag NW aligned arrays grown on the retroreflectors. Since one would

only expect a factor of 4 enhancement due to the light reflecting properties of the retroreflector, it is suggested that the enhancement in the SERS signal is due to light channeling by the nearly aligned nanowire arrays as a result of plasmonic effects. These results have been modeled using COMSOL electric field simulations, which support the light channeling concept.

8:40am NS+EN-TuM3 **Optical and Electrical Characteristics of Al-doped ZnO Nanowires Grown by Chemical Vapor Deposition.** *G. Shen, N. Dawahre, J. Waters, J. Krafcik, S.M. Kim, P. Kung*, University of Alabama, Tuscaloosa

Zinc oxide (ZnO) is a well-known major semiconductor material for optoelectronic devices due to its wide bandgap (~3.3 eV) and large exciton binding energy (~60 meV). One dimensional ZnO nanowires have been successfully synthesized by various techniques ranging from as simple as thermal chemical vapor deposition and solution growth, to more complex such as metal organic chemical vapor deposition, with good structural, optical and electrical properties. These are promising as an alternative to indium tin oxide as a more abundant, lower cost transparent window for a number of optoelectronic devices, including photovoltaics, while at the same time offering potentially more efficient electron charge transport. ZnO is also capable of harvesting the short wavelength spectral bands more efficiently.

In this work, we present the growth, doping and characterization of vertical well-aligned ZnO nanowire arrays. The wires are synthesized without metal catalyst by thermal chemical vapor deposition on basal plane sapphire substrates following the carbo-thermal reduction of zinc oxide powder. Control of the aluminum doping is accomplished by adjusting the ratio of Al and ZnO in the source material. The effects of doping and synthesis conditions on the nanowire optical and electrical properties are investigated through a number of techniques. The concentration of Al in the crystal is determined by energy dispersive spectroscopy, while atom probe tomography enables us to investigate the distribution of aluminum within the ZnO matrix. Micro-Raman spectroscopy and micro-photoluminescence, including their temperature dependence, are used to probe the vibrational and optical properties of the nanowires as a function of doping. It is observed that a defect related radiative green emission in ZnO is significantly reduced after Al doping. The electrical characteristics of undoped and doped nanowires are compared by leading electrical nano-connections to individual nanowires, which show a more than 1 order of magnitude decrease in the resistivity after doping down to 1 ohm.cm.

9:00am NS+EN-TuM4 **Rational Defect Engineering in Silicon Nanowires.** *N. Shin, M. Filler*, Georgia Institute of Technology

Group IV nanowires synthesized via the vapor-liquid-solid (VLS) technique do not frequently exhibit planar defects and/or polytypic domains. Even in group III-V nanowires, where these structural motifs are common, rational control of their position remains challenging. Since defect energetics are similar in both systems, the observed structural differences are especially striking and indicate that the underlying physical phenomena are not sufficiently well understood. Here, we demonstrate how user-defined changes in surface chemistry near the triple-phase line can introduce twin planes and stacking faults during the growth of <111> oriented Si nanowires. More specifically, the addition of atomic hydrogen during Si nanowire growth enables {111} defects that begin at the <112> sidewall and continue to propagate across the nanowire even after the flux of atomic hydrogen ceases. Real-time *in-situ* infrared spectroscopy measurements reveal that covalent Si-H bonds are responsible for the defect initiation process and a simple mechanistic model will be presented to explain these results. Our findings are an important step toward a fundamental understanding of the chemistry that governs semiconductor nanowire synthesis and suggest a new route to engineer the properties of Si.

9:20am NS+EN-TuM5 **Ultrafast Carrier Dynamics of Si Nanowires Grown by LPCVD.** *A. Seyhan*, Tokyo Institute of Technology and Nigde University, Turkey Japan, *T. Ishikawa, S. Koshihara, M. Simanullang, K. Usami, S. Oda*, Tokyo Institute of Technology, Japan

This paper reports the ultrafast carrier dynamics in silicon nanowires (NWs) grown by vapour-liquid-solid (VLS) mechanism in the low pressure chemical vapour deposition (CVD) reactor at 425°C. The femtosecond transient absorption measurements were studied by tuning probe wavelength in visible range to investigate the effect of pump and probe beam polarization, NW diameter, and pump fluence on the carrier dynamics. The fast carrier relaxation with lifetime of several picosecond in Si NWs can be attributed to surface trap states. This study has important implications in the understanding of ultrafast carrier dynamics of Si NWs.

9:40am **NS+EN-TuM6 Selective Deposition of Germanium Nanowire Segments via a Hybrid Oxide-Stabilized/Vapor-Liquid-Solid Growth Method**, *C.J. Hawley, T. McGuckin, J.E. Spanier*, Drexel University

The introduction low levels of oxygen during the vapor-liquid-solid growth (VLS) of germanium nanowires causes an oxide sheath to form at the catalyst/nanowire/vapor interface for the extent that the growth persists. This results in extremely high aspect ratio nanowires due to the removal of homoepitaxial deposition and the finite energy required for heterogeneous nucleation of germanium on its oxide. Furthermore, with the removal of oxygen, the catalyzed oxide sheath terminates and conventional growth with finite sidewall deposition dominates subsequent growth. The successful transition between the aforementioned oxide-stabilized and conventional VLS regimes can be deliberately manipulated to grow finite conical nanowires segments with discontinuous changes in diameter.

Work was supported by the U.S. Army Research Office (W911NF-08-1-0067).

10:40am **NS+EN-TuM9 Electronics and Opto-Electronics with Semiconducting Carbon Nanotube Arrays**, *M.B. Steiner*, IBM TJ Watson Research Center **INVITED**

While field-effect transistors made of single semiconducting carbon nanotubes have excellent electrical DC characteristics, the measurement of their AC characteristics is complicated and their output current is not sufficient for technological applications. Utilizing an array of semiconducting carbon nanotubes could resolve these problems. However, there are issues associated with the separation of carbon nanotubes with respect to the electronic type, their aligned assembly in high densities, as well as the scaling of device dimensions.

In this talk, I will present recent advancements with respect to the solution-assisted, electric-field driven assembly of highly separated (>99%) semiconducting carbon nanotubes into regular arrays on a device platform with embedded electrodes. The planar device platform is based on manufacturing processes known to the semiconductor industry and provides a basis for future enhancements of the carbon nanotube assembly and the scaling of critical device dimensions. Electrical transport measurements (AC and DC) of assembled carbon nanotube array transistors reveal intrinsic current gain cut-off frequencies of 150GHz and electrical current saturation behavior at a gate length of 100nm. The requirements for future applications of carbon nanotube array transistors in high-frequency electronics will be discussed.

In the second part of my talk, I will discuss high-resolution optical mapping of the internal electrostatic potential landscape of carbon nanotube array devices. Laser-excited photocurrent measurements provide insights into the physical principles of device operation and reveal performance-limiting local heterogeneities that cannot be detected with the electron microscope. The experiments deliver photocurrent images from the underside of nanotube-metal contacts and enable the direct measurement of the charge carrier transfer length at a nanotube-metal interface. Moreover, the external control of the electrostatic potential profile in carbon nanotube array devices by means of local metal electrodes is demonstrated. The results are important for the design and optimization of optoelectronic devices based on carbon nanotube arrays, such as polarized light detectors and emitters.

11:20am **NS+EN-TuM11 Observation of the Impact of Pseudospin Conservation in Carbon Nanotubes**, *R. Tsuchikawa*, University of Central Florida, *Z. Zhang, X. Guo, J.C. Hone*, Columbia University, *M. Ishigami*, University of Central Florida

It has long been accepted that pseudospin conservation in metallic carbon nanotubes prevents backscattering by long-range potentials such as Coulomb potential. This unique property is expected to be valid only for metallic nanotubes [1]. Here, we have directly tested this yet untested theoretical result by measuring the impact of charged impurities on transport property of chiral-angle known carbon nanotubes. Single-walled carbon nanotubes (SWNTs) were grown to as long as a few hundred microns with minimal number of defects, followed by Rayleigh scattering spectroscopy to identify the chirality. In order to minimize the extrinsic impurities, electron transport measurements were performed in an ultra high vacuum environment after cleaning nanotubes down to atomic scale. Furthermore, we employed length-dependent resistance measurements to eliminate the impact of the metal-nanotube contact. Finally, transport property was measured at increasing coverage of cesium to determine the impact of charged impurities. Our results show chiral angle dependence of the impact of cesium and enable us to directly test the properties of pseudospin in carbon nanotubes.

1. P.L. McEuen, M. Bockrath, D.H. Cobden, Y.-G. Yoon, and S.G. Louie, Disorder, Pseudospin, and Backscattering in Carbon Nanotubes, *Physical Review Letters*, 83, 5098 (1999)

11:40am **NS+EN-TuM12 Properties and Application of Electronically Monodisperse Carbon Nanomaterials Functionalized with Nonionic Block Copolymers**, *J.-W.T. Seo*, Northwestern University

Carbon nanomaterials, including carbon nanotubes and graphene, have garnered significant attention from the research community in recent years. In an effort to refine their properties and better integrate them into device structures, chemical functionalization methods have been employed including aqueous dispersion with ionic surfactants, proteins, and DNA. While these strategies have proven effective for tuning the optical properties of carbon nanomaterials, the residual charge from the ionic dispersants complicate efforts to utilize them in electronic and/or electrochemical technologies. In contrast, we demonstrate here that nonionic, amphiphilic block copolymers (e.g., Pluronics and Tetronics) are effective surfactants for grapheneⁱ and carbon nanotubes,ⁱⁱ thus yielding chemically and electronically monodisperse samples without spurious charged impurities.

Pluronics and Tetronics are biocompatible block copolymers that are composed of hydrophilic polyethylene and hydrophobic polypropylene oxide domains. By tuning the relative length of these domains, their dispersion efficiency for carbon nanomaterials can be tailored. For example, Pluronics possess the ability to sort semiconducting single-walled carbon nanotubes (SWCNTs) via density gradient ultracentrifugation with shorter hydrophobic domains resulting in higher purity levels. Furthermore, Pluronic F68 has shown pH-sensitive, switchable sorting affinity towards both metallic and semiconducting SWCNTs, thus providing a novel route for the production of electronically monodisperse SWCNTs that are encapsulated with biocompatible, nonionic speciesⁱⁱⁱ. In addition to biomedical applications, the nonionic character of these block copolymers yields more reliable and enhanced performance of SWCNT-based electronic and electrochemical devices such as thin film transistors and lithium ion batteries.

Tuesday Afternoon, October 30, 2012

Graphene and Related Materials Focus Topic
Room: 13 - Session GR+AS+NS+SP+SS-TuA

Graphene Characterization Including Microscopy and Spectroscopy

Moderator: J.C. Hone, Columbia University

2:00pm **GR+AS+NS+SP+SS-TuA1 High Resolution Real and Reciprocal Space Photoelectron Emission Microscopy on Heterogeneous Graphene/SiC(000-1)**, *K. Winkler, B. Kroemker, 10micron NanoTechnology, Germany, N. Barrett, IRAMIS, Saclay, France, E. Conrad, GeorgiaTech*

We present energy filtered electron emission spectromicroscopy with high spatial and wave-vector resolution on few-layer epitaxial graphene on SiC(000-1) grown by furnace annealing.

Conventional electron spectroscopy methods are limited in providing simultaneous real and reciprocal or k-space information from small areas under laboratory conditions. Therefore, the characterization of materials with only micron scale sample homogeneity such as epitaxially grown graphene requires new instrumentation. Recent improvements in aberration compensated energy-filtered photoelectron microscopy (PEEM) can overcome the known limitations in both synchrotron and laboratory environments. Here we report 2D maps of the k-parallel π - π band dispersion in micron-scale regions and correlate them with spatially resolved chemical information on the same regions. Only the combination of high lateral, high energy, high k-resolution and controlled switching between real space and k-space allows detailed understanding of micron size sample sites with 1-3 layers graphene. The experiments underline the importance of simultaneous lateral, wave vector and spectroscopic resolution on the scale of future electronic devices in order to precisely characterize the transport properties and band alignments.

2:20pm **GR+AS+NS+SP+SS-TuA2 Evidence of Nanocrystalline Semiconducting Graphene Monoxide during Thermal Reduction of Graphene Oxide in Vacuum**, *C. Hirschmugl, E. Mattson, H. Pu, S. Cui, M. Schofield, S. Rhim, G. Lu, M. Nasse, University of Wisconsin Milwaukee, R.S. Ruoff, University of Texas at Austin, M. Weinert, M. Gajdardziska-Josifovska, J. Chen, University of Wisconsin Milwaukee*

As silicon-based electronics are reaching the nanosize limits of the semiconductor roadmap, carbon-based nanoelectronics has become a rapidly growing field, with great interest in tuning the properties of carbon-based materials. Chemical functionalization is a proposed route, but syntheses of graphene oxide (G-O) produce disordered, nonstoichiometric materials with poor electronic properties. We report synthesis of an ordered, stoichiometric, solid-state carbon oxide that has never been observed in nature and coexists with graphene. Formation of this material, graphene monoxide (GMO)[1], is achieved by annealing multilayered G-O. A combination of transmission electron microscopy and infrared microspectroscopy have provided critical experimental evidence to identify the novel structure. These results indicate that the resulting thermally reduced G-O (TRG-O) consists of a two-dimensional nanocrystalline phase segregation: unoxidized graphitic regions are separated from highly oxidized regions of GMO. GMO has a quasi-hexagonal unit cell, an unusually high 1:1 O:C ratio, and a calculated direct band gap of approximately 0.9 eV.

This work was supported by the NSF (CMMI-0856753 and CMMI-0900509). This work is based upon experiments performed at the Synchrotron Radiation Center. The SRC is funded by the University of Wisconsin-Madison and the University of Wisconsin-Milwaukee. Work performed at the SRC IRENI beamline been done with support from an NSF Major Research Instrumentation grant (DMR-0619759). The authors thank Bruker Technologies for the Grazing Angle Objective used for this work.

[1] Mattson, E.C. et al., ACSNano (2011) 5 (2011) 9710-9717.

2:40pm **GR+AS+NS+SP+SS-TuA3 Scanning Tunneling Spectroscopy of Epitaxial Graphene: Local Band Mapping and Wavefunction Engineering**, *P.N. First, Georgia Tech* **INVITED**

Because the crystalline orientation is determined prior to growth, epitaxial graphene (EG) on silicon carbide is an excellent material to consider for 2D wavefunction engineering, where device properties are designed through wavefunction confinement and material strain. In pursuit of this goal, we use scanning tunneling microscopy (STM) and spectroscopy (STS) to characterize the local structural and electronic properties of EG and a

simple EG nanostructure. With some care, STS can be used to measure the full energy-momentum dispersion of both filled and empty states, on length scales determined by the coherence of the graphene wavefunctions. Applying a magnetic field introduces a field-tunable comb of discrete Landau level energies that we use to obtain high momentum resolution, to characterize the tip-induced surface potential, and to detect subtle interlayer interactions in a multilayer graphene stack. * Work performed in collaboration with NIST Center for Nanoscale Science and Technology ** Funded in part by NSF and by NRI-INDEX.

4:00pm **GR+AS+NS+SP+SS-TuA7 Intercalation of O₂ an CO Controlled by the Mesoscopic Structure of Graphene**, *E. Grånäs, J. Knudsen, Lund University, Sweden, U. Schröder, T. Gerber, C. Busse, Universität zu Köln, Germany, M.A. Arman, K. Schulte, J.N. Andersen, Lund University, Sweden, T.W. Michely, Universität zu Köln, Germany*

Intercalation of gases between epitaxial graphene and its substrate has become a topic of interest for studies due to, for example, the unique opportunities to modify the graphene-substrate interaction and the possibilities to perform chemistry under the graphene layer. Further, a profound knowledge about graphenes stability in gases at elevated temperatures and pressures is essential for, among other things, the correct interpretation of gas adsorption studies on graphene supported metal cluster arrays.

We have studied intercalation and etching of Ir(111) supported graphene upon gas exposure to common gasses such as O₂ and CO in the entire pressure interval from 10⁻⁸ to 0.1 mbar. Comparing perfect graphene layers without holes with graphene films, that only covers a fraction of the Ir(111) surface, we reveal that the holes - or more specific the graphene edges - are essential for intercalation.

For oxygen exposed graphene we develop a coherent picture of temperature dependent oxygen etching and intercalation. Using X-ray photoemission spectroscopy (XPS) and scanning tunnelling microscopy (STM) we show that a perfect graphene layer is stable against etching and intercalation up to 700 K, whereas at higher temperatures etching, but no intercalation, takes place. In contrast, a partial graphene coverage on Ir(111) enables dissociative oxygen adsorption on the bare Ir and subsequent intercalation underneath graphene flakes at 355 K and above. Intercalated oxygen remains stable up to a temperature of 600 K, above this temperature it desorbs in the form of CO or CO₂. We have determined XPS and STM fingerprints for the intercalated oxygen structure and we unambiguously assign it to a p(2x1)-O structure similar to the one observed on clean Ir(111). The decoupling of the intercalated graphene film from the metal substrate is directly visualized through the inability to form well-ordered Pt cluster arrays on the O-intercalated areas of graphene on Ir(111). Further, we have identified the rate limiting step for oxygen intercalation to be unlocking of the graphene edge and propose that this takes place through bond breaking between graphene edge bonds and the Ir substrate.

Using a combination of high pressure X-ray photoemission spectroscopy (HP-XPS) and STM we also show that CO intercalation takes place at room temperature and pressures in the 1 mbar range. The adsorption structure of intercalated CO is determined to be (3√3 × 3√3)R30°, identical to the structure observed on clean Ir(111) upon high pressure CO exposure.

4:20pm **GR+AS+NS+SP+SS-TuA8 Long-range Atomic Ordering and Variable Interlayer Interactions in Two Overlapping Graphene Lattices with Stacking Misorientations**, *T. Ohta, T.E. Beechem, Sandia National Laboratories, J.T. Robinson, Naval Research Laboratory, G.L. Kellogg, Sandia National Laboratories*

We report a method to examine the effect of stacking misorientation in bilayer graphene by transferring chemical vapor deposited (CVD) graphene onto monolithic graphene epitaxially grown on silicon carbide (SiC) (0001). The resulting hybrid bilayer graphene displays long-range Moiré diffraction patterns having various misorientations even as it exhibits electron reflectivity spectra nearly identical to epitaxial bilayer graphene grown directly on SiC. These varying twist angles affect the 2D (G')-band shape of the Raman spectrum indicating regions of both a monolayer-like single π state and Bernal-like split π states brought about by the differing interlayer interactions. This hybrid bilayer graphene fabricated via a transfer process therefore offers a means to systematically study the electronic properties of bilayer graphene films as a function of stacking misorientation angle.

The work at Sandia National Laboratories was supported by LDRD and by the US DOE Office of Basic Energy Sciences, Division of Materials Science and Engineering. Sandia National Laboratories is a multi-program laboratory managed and operated by Sandia Corporation, a wholly owned subsidiary of Lockheed Martin Corporation, for the U.S. Department of Energy's National Nuclear Security Administration under contract DE-

AC04-94AL85000. The work at NRL was funded by the Office of Naval Research.

4:40pm **GR+AS+NS+SP+SS-TuA9 Chemically-resolved Interface Structure of Epitaxial Graphene on SiC(0001)**, *J.D. Emery*, Northwestern Univ., *B. Detslefs*, European Synchrotron Radiation Fac., France, *H.J. Karmel*, Northwestern Univ., *V.D. Wheeler*, U.S. Naval Research Lab, *J.M.P. Alaboson*, Northwestern Univ., *L.O. Nyakiti*, *R.L. Myers-Ward*, *C.R. Eddy, Jr.*, *D.K. Gaskill*, U.S. Naval Research Lab, *M.C. Hersam*, Northwestern Univ., *J. Zegenhagen*, European Synchrotron Radiation Fac., France, *M.J. Bedzyk*, Northwestern Univ.

The implementation of graphene into next-generation electronics will require production high-quality graphene at the wafer scale. One promising route for the production of wafer-scale graphene is to grow epitaxial graphene (EG) via thermal decomposition of Si-terminated SiC (SiC(0001)). This method produces high-quality EG, but is accompanied by the formation of the so-called "buffer layer" at the interface, which is known to affect the electronic properties of the graphene. Despite numerous efforts to determine the nature of the buffer layer, debate persists concerning its atomic and chemical structure. Here, we use the X-ray Standing Wave (XSW) technique to create a precise chemically-sensitive description of the distributions of Si and C at the interface. This technique, which combines X-ray scattering and X-ray Photoelectron Spectroscopy (XPS), is capable of locating coherent distributions of chemically distinct species above a single crystal surface. This allows for a more detailed description of the interface than those afforded by scattering or XPS alone. Our analysis shows that the buffer layer, which is present in both UHV and furnace-grown EG/SiC(0001), contains no substantial non-bulk or oxide silicon component, and is thus purely carbon. We identify two chemically distinct carbon species within the interface layer, each with a distinct location above the Si-terminated surface, and report their positions and distributions with sub-angstrom precision. These results help to clarify long-standing uncertainties about the interfacial structure of graphene/SiC(0001). Further, we also highlight the potential for XSW with XPS as a valuable tool in the structural determination of complex interfaces, such as functionalized, doped, or intercalated epitaxial graphene.

5:00pm **GR+AS+NS+SP+SS-TuA10 Formation of Graphene on SiC(000-1) in Disilane and Neon Environments**, *G. He*, *N. Srivastava*, *R. Feenstra*, Carnegie Mellon University

We have prepared graphene on the SiC(000-1) surface (the so-called *C-face* of the {0001} surfaces), by heating the SiC in a Si-rich environment produced either by using disilane ($\approx 10^{-4}$ Torr) or cryogenically-purified neon (1 atm). With the Si-rich environments, we obtain considerably better uniformity in the thickness for thin, \approx ML-thick graphene on the C-face compared to that observed in samples prepared in vacuum or in an argon environment. We also find that different interface structures occur in these environments. In particular, we find a graphene-like buffer layer forming at the interface, analogous to the well known behavior of the SiC(0001) surface (the Si-face).

Studies are performed using atomic force microscopy (AFM), low-energy electron diffraction (LEED), and low-energy electron microscopy (LEEM). For graphene prepared in vacuum, LEED patterns show a characteristic 3×3 pattern together with graphene streaks. In contrast, for the graphene produced in either the disilane environment ($\approx 10^{-4}$ Torr) or 1 atm of neon, LEED patterns reveals a complex $\sqrt{43} \times \sqrt{43} - R \pm 7.6^\circ$ arrangement along with graphene spots. This structure is somewhat similar to the well known $6\sqrt{3} \times 6\sqrt{3} - R30^\circ$ "buffer layer" of the Si-face, with satellite spots surrounding the primary Si spots, and is interpreted as arising from a C-rich buffer layer on the SiC. Selected area diffraction on those surface areas reveals a wavevector magnitude precisely equal to that of graphene, thus proving that the buffer layer does indeed have structure very close to that of graphene (the pattern is interpreted as a distortion of the buffer-layer graphene due to bonding to the underlying SiC). Using LEEM, measurements from the buffer layer of the reflected intensity of the electrons as a function of their energy reveal a new characteristic reflectivity curve, not seen for vacuum-prepared graphene.

After oxidation of the samples, the $\sqrt{43} \times \sqrt{43} - R \pm 7.6^\circ$ spots disappear and $\sqrt{3} \times \sqrt{3} - R30^\circ$ spots appear on the surface. This latter behavior is interpreted as oxidation of the SiC surface beneath the buffer layer. Selected area diffraction on portions of the surface that were previously identified as buffer layer still reveal a wavevector magnitude precisely equal to that of graphene. However, LEEM reflectivity curves on those areas reveal a completely new spectrum, indicative of a "decoupling" of the buffer from the SiC. This decoupling is consistent with our interpretation of this new interface structure as being a graphene buffer layer on C-face SiC.

This work is supported by NSF.

5:20pm **GR+AS+NS+SP+SS-TuA11 Characterization of Few Layer Graphene Films Grown on Cu-Ni and SiC Substrates**, *P. Tyagi*, *J.D. McNeilan*, *J. Abel*, *F.J. Nelson*, *Z.R. Robinson*, *R. Moore*, *A.C. Diebold*, *V.P. LaBella*, *C.A. Ventrice, Jr.*, University at Albany - SUNY, *A.A. Sandin*, *D.B. Dougherty*, *J.E. Rowe*, North Carolina State Univ., *C. Dimitrakopoulos*, *A. Grill*, *C.Y. Sung*, IBM T.J. Watson Res. Center, *S. Chen*, *A. Munson*, *Y. Hao*, *C.W. Magnuson*, *R.S. Ruoff*, Univ. of Texas at Austin

The electronic structure of graphene depends on the number of graphene layers and the stacking sequence between the layers. Therefore, it is important to have a non-destructive technique for analyzing the overlayer coverage of graphene directly on the growth substrate. We have developed a technique using angle-resolved XPS to determine the average graphene thickness directly on metal foil substrates and SiC substrates. Since monolayer graphene films can be grown on Cu substrates, these samples are used as a standard reference for a monolayer of graphene. HOPG is used as a standard reference for bulk graphite. The electron mean free path of the C-1s photoelectron is determined by analyzing the areas under the C-1s peaks of monolayer graphene/Cu and bulk graphite and results in a value of 12.3 ± 0.8 Å. With this electron mean free path, the graphene coverage of a film of arbitrary thickness can be determined from the areas under the C-1s peaks of the sample of interest, the monolayer graphene/Cu, and HOPG samples. Analysis of graphene coverages for graphene films grown on Cu-Ni substrates shows that a uniform monolayer is first formed before the growth of a second layer. The thickness of both the graphene overlayer and intermediate buffer layer has been determined on 6H-SiC substrates. Raman spectroscopy data have also been taken on these samples and compared to the overlayer coverages determined with XPS. This research was supported in part by the National Science Foundation (grant no. 1006350/1006411).

5:40pm **GR+AS+NS+SP+SS-TuA12 Thickness-related Electronic Properties of Single-layer and Few-layer Graphene Revealed by Single-pass Kelvin Force Microscopy and dC/dZ Measurements**, *J. Yu*, *S. Wu*, Agilent Technologies, Inc.

Graphene has attracted much attention recently due to their exotic electronic properties. Potential applications of graphene sheets as ultrathin transistors, sensors and other nanoelectronic devices require them supported on an insulating substrate. Therefore, a quantitative understanding of charge exchange at the interface and spatial distribution of the charge carriers is critical for the device design. Here, we demonstrate that atomic force microscopy (AFM)-based technique Kelvin force microscopy (KFM) can be applied as an experimental means to quantitatively investigate the local electrical properties of both single-layer and few-layer graphene films on silicon dioxide. Our measurements indicate that the surface potential of single-layer graphene is 60 mV higher than that of the silica interfacial layer. The effect of film thickness on the surface potential of few-layer graphene is observed. For example, a 66 mV increase in the surface potential is detected for an eleven-layered film with respect to a nine-layer film. Furthermore, with the introduction of multiple lock-in amplifiers (LIAs) in the electronics for scanning probe microscopes, single-pass kelvin force microscopy and probing of the other electric property such as local dielectric permittivity via the capacitance gradient dC/dZ measurements are allowed by the simultaneous use of the probe flexural resonance frequency ω_{mech} in the first LIA targeting the mechanical tip-sample interactions for surface profiling, and a much lower frequency ω_{elec} (both in the second LIA and its second harmonic in the third LIA) for sample surface potential and dC/dZ measurements, respectively. In contrast to surface potentials, the dC/dZ measurements show that local dielectric permittivity of few-layer graphene films maintain at the same level regardless of the film thickness. Such simultaneous monitoring of multiple electronic properties that exhibit different behaviors in response to the graphene layers provides us a way to achieve both a comprehensive characterization and a better understanding of graphene materials.

In Situ Microscopy and Spectroscopy Focus Topic Room: 7 - Session IS+AS+BI+ET+GR+NS-TuA

In Situ Studies of Organic and Soft Materials and In Situ Microscopy

Moderator: K. Artyushkova, The University of New Mexico, J.A. Eastman, Argonne National Laboratory

2:00pm **IS+AS+BI+ET+GR+NS-TuA1 Micronutrient Detection and Quantification from Data Obtained from Plasma Pencil Atmospheric Mass Spectrometry**, *M.J. Stein, E. Lo, C. Waterton, D.G. Castner, B.D. Ratner*, University of Washington

The analysis of micronutrient quantities is one component in the strategy to reduce the global burden of malnutrition-related disease. Accessibility of the proper equipment and equipment complexity impede nutrient testing in the areas that might benefit most from these studies. In this work, we present an analysis of micronutrients in a physiological range from blood plasma using plasma pencil atmospheric mass spectrometry (PPAMS), a method for sampling a sample's surface at ambient temperature and pressure conditions. The effectiveness of our PPAMS system is demonstrated using characteristic and tandem mass spectra on raw nutrient controls. Key micronutrient peaks and fragmentation patterns are observed. Next, we analyze a sample matrix of micronutrients in porcine plasma in which the nutrient concentrations are varied. Principal component analysis (PCA) is then employed on the spectra. The resulting PCA scores showed that these nutrients are separable at different nutrient concentrations to 95% confidence. The loadings peaks are shown to contain several of the key peaks observed in the raw nutrient powders as principal separators. The PPAMS technique is compared to several traditional techniques such as time-of-flight secondary ion mass spectrometry (ToF-SIMS) and electrospray ionization mass spectrometry (ESI-MS). Separation of the nutrients at concentrations relevant for human blood-based nutrient detection is possible in both ESI-MS and PPAMS. However, ToF-SIMS is found to require 5x to 1000x higher concentrations than PPAMS for folate, vitamin A, and iodine in order to achieve similar separation of the micronutrients. In addition to the qualitative information obtained from the PCA results, quantitative predictive values are obtained by the application of a Bayesian wavelet-based functional mixed model. Since the mass spectra are modeled as functions in this model, peak detection methods are not required and the final results utilized the full spectral response. The final predicted values are compared to the known concentration values and the mean standard error of prediction (MSEP) is calculated. The accuracy of the predictive model was found to be dependent on the ionization potential of the individual nutrients. Metallic-nutrients were hypothesized to be more sensitive to outside cationization effects than their larger organic counterparts. In addition to quantitation, the physical properties of the ionization process were explored. Using XPS and ellipsometry in conjunction with carefully timed exposures and concurrent fragment PCA, it is determined that the PPAMS ionization is a softer form of ionization than most vacuum-based techniques.

2:20pm **IS+AS+BI+ET+GR+NS-TuA2 In Situ Real Time Examination of the Thin Film Growth of Pentacene on Polymeric Dielectrics Using X-Ray Synchrotron Radiation: Unexpected Changes in the Evolution of Surface Morphology with Substrate**, *T.V. Desai, A.R. Woll, J.R. Engstrom*, Cornell University

We have examined the thin film growth of pentacene on SiO₂ and on three different polymeric dielectrics using *in situ* synchrotron x-ray scattering and *ex situ* atomic force microscopy (AFM). The polymeric dielectrics investigated spanned the range from a low surface energy hydrophobic surface (polystyrene, PS), to a medium surface energy hydrophobic surface (polymethylmethacrylate, PMMA), to a high surface energy hydrophilic surface [poly(ethylene imine), PEI]. We have also compared these results to pentacene growth on clean SiO₂. On all surfaces, pentacene forms a polycrystalline thin film, whose structure is that of the previously identified "thin film" phase. From *in situ* real-time x-ray scattering, we find that pentacene exhibits layer-by-layer (LbL) growth on all surfaces investigated, but the extent of LbL growth is a strong function of the underlying substrate. This result is unexpected as the transition to more 3D-like growth occurs for thicknesses where the underlying substrate is effectively almost entirely covered by the growing pentacene thin film. Layer-by-layer growth is significantly more prolonged on PEI (up to ~6 MLs), followed by SiO₂ and PMMA (up to ~4 MLs) and finally PS (up to ~3 MLs). This trend is also seen in the variation of both the roughness and the in-plane feature sizes of ~10 ML thick films, where the films are the smoothest, and the feature sizes are the largest for growth on PEI, whereas on PS, the films are roughest, and the feature sizes are the smallest. Concerning possible reasons for this behavior, we can exclude the effects of the structure of the

crystalline thin film (they were the same in all cases), and the roughness of the polymeric dielectric (rms roughness differed by < 0.1 nm) as major contributing factors. Surface energy of the polymeric thin films, however, provided the best explanation for the observed behavior, suggesting that thermodynamic driving forces play an important role in the evolution of thin film structure. In terms of molecular scale phenomena, interlayer transport and step-edge crossing events may be influenced by the mobility of the near-surface polymeric layers in the underlying substrate, which can be quite different for the ultrathin PEI layers vs. the much thicker PMMA and PS thin films.

2:40pm **IS+AS+BI+ET+GR+NS-TuA3 In Situ, Real-Time Diagnostics of Colon Cancer and Inflammatory Bowel Diseases by Direct Combination of Endoscopy and Rapid Evaporative Ionization Mass Spectrometry**, *Z. Takats*, Imperial College, UK, *L.A. Sasi-Szabo*, University of Debrecen, Hungary, *J. Kinross*, Imperial College, UK, *J. Balog*, Medimass Ltd., *L. Muirhead, K.C. Schafer, C. Guallar-Hoyas*, Imperial College, UK

INVITED

Rapid identification of biological tissues is a long-standing problem on various fields of interventional medicine, with special regard to cancer diagnostics and cancer surgery. While histological techniques provide the ultimate solution for the cellular-level identification of cancer cells, the approach is extremely complex and time consuming. Nevertheless, accelerated version of histopathology (so-called 'frozen section' method) is widely used for the intraoperative characterization of tissue samples removed from the surgical area. Since frozen section histology is less reliable than the traditional approaches, and the accelerated procedure still takes approx. 30 minutes for a single sample, there has been ongoing research for the development of more accurate and faster methods.

Molecular spectroscopy techniques including IR, Raman, solid state NMR and mass spectrometry have been used for the characterization of intact biological tissues and showed enormous potential for the differentiation of tissues with various histologies, including multiple different types of cancer.

Rapid Evaporative Ionization Mass Spectrometry is based on the observation that electrosurgical dissection of vital tissues involves the ionization of various tissue constituents, with special emphasis on membrane lipids. Electrosurgical methods employ electric current for the rapid heating and evaporation of tissue material and they are widely used both for dissection and coagulation on practically all fields of surgery. Hence, the direct combination of electrosurgery with mass spectrometry provides a tissue identification methodology, where the tissue manipulation part is already widely used by surgeons and fully approved from regulatory point of view. Electrosurgical methods are also employed on the field of endoscopy, both for coagulation and dissection. Combination of endoscopy with *in-situ* mass spectrometric tissue identification resulted in a diagnostic device which can potentially identify lesions in body cavities *in-situ*, in real-time.

Electrosurgical electrode assembly and ion transfer device were embedded into working channel of commercially available colonoscope. The device was coupled with a linear ion trap mass spectrometer, and the system was utilized during diagnostic colonoscopic interventions. Adenomae, adenocarcinomae and mucosal areas affected by inflammatory bowel diseases were successfully identified, in complete agreement with histopathological examination.

4:00pm **IS+AS+BI+ET+GR+NS-TuA7 Nanocrystal Phase Transformations in ZBLAN Glass Ceramics**, *J.A. Johnson*, University of Tennessee Space Institute, *C. Alvarez*, Northwestern University, *Y. Lui*, Argonne National Laboratory, *C.E. Johnson*, University of Tennessee Space Institute, *A. Petford-Long*, Argonne National Laboratory

In-situ and *ex-situ* TEM investigations of fluorochlorozirconate (FCZ) glass have led to the discovery of previously unreported BaF₂ in the face-centered-cubic (FCC) and orthorhombic phases. These FCZ glasses are a class of material based on ZBLAN glasses, which are being developed for uses in advance mammography systems. The FCZs of interest have been doped with Eu (II) for use as either a scintillator or a storage phosphor material but need to be partially crystalline to show good optical properties. The photo-stimulated luminescence of this material, for use as storage phosphor, is attributed to the characteristic 5d-4f emission of Eu²⁺ present in the BaCl₂ nanocrystals. The crystals formed are known from XRD experiments to be hexagonal and orthorhombic BaCl₂ depending on the annealing temperature, 265 and 295°C respectively. *In-situ* and *ex-situ* TEM heating experiments were used to study the nucleation and growth process of the nanocrystals at the EMC. The nanocrystals nucleate and grow through-out the glass matrix when annealing FCZ glasses, therein producing a nanocomposite glass-ceramic system. The traditional BaCl₂ orthogonal phase in addition to the unreported FCC and orthogonal BaF₂ phase have been found in multiple ZBLAN compositions in which the content of Cl and F has been varied. This indicates that annealing FCZ

glasses produces polymorphic crystals of both BaCl₂ and BaF₂, which vary in size from 10 nm to 100 nm.

Mössbauer Spectroscopy has also given indisputable evidence that the divalent Europium enters the nanocrystals.

4:20pm IS+AS+BI+ET+GR+NS-TuA8 *In Situ* Microscopy of Organic Film Growth: Zn-Phthalocyanine on Ag(100). A. Al-Mahboob, J.T. Sadowski, Brookhaven National Laboratory

Metal phthalocyanines are attracting significant attention, owing to their potential for applications in chemical sensors, solar cells and organic magnets. As the electronic properties of molecular films are related to their crystallinity and molecular packing, the optimization of film quality is important for improving the performance of organic devices.

In this work, we studied the dynamics of nucleation and structural evolution of zinc-phthalocyanine (ZnPc) films on Ag(100) surface, employing real-time low-energy electron microscope (LEEM) complemented by DFT calculations. We have observed two different modes of ZnPc nucleation, depending on the growth temperature. At lower temperatures ZnPc nucleates in a double domain structure, with bulk-like square lattice similar to one reported by Dou et al. [2]. LEED patterns recorded in LEEM experiment show that ZnPc monolayer (ML) grows epitaxially, having a square lattice with $(4/3)\sqrt{13} \times (4/3)\sqrt{13} R33.69^\circ$ unit cell (denoted R33.69) with respect to the substrate lattice. At temperatures of 170°C or above, nucleation of less dense epitaxial ZnPc, having single domain orientation, was observed, with square lattice parameters exactly 5 times larger (5x5) than the Ag(100) substrate.

Utilizing LEEM to observe the ZnPc nucleation at varying substrate temperatures – from room temperature (RT) to 225°C – we have observed that the nominal ZnPc coverage required for the onset of nucleation has strong temperature dependence. The nucleation commences at about 0.2 ML at RT, while 0.7 ML is required at 190°C. At the same time the completion of 1st layer occurs at constant nominal coverage of ZnPc, independent of substrate temperature. Based on that observation, the delay in onset of nucleation could be understood as a result of increased equilibrium concentration of diffusing ZnPc molecules at higher temperatures. This is in contrast to a delay in nucleation and giant island growth observed during vacuum deposition of anisotropic molecules like pentacene (Pn), in which case the energy barrier for the reorientation of the molecule from diffusing state into its crystalline orientation plays a critical role [3]. Real-time tracking of the evolution of ZnPc island area at varying deposition conditions combined with DFT analysis revealed that the 5x5 structure has both, a detachment barrier with respect to attachment, and a pre-factor (or attempt frequency), lower than those for bulk-like structures, allowing for controlling of the resulting ZnPc structure.

[1] E. Bauer, Rep. Prog. Phys. **57**, 895 (1994).

[2] W. Dou et. al, J. Chem. Phys. **133**, 144704 (2010).

[3] Al-Mahboob et al, Phys. Rev. **B 82**, 235421 (2010).

4:40pm IS+AS+BI+ET+GR+NS-TuA9 *In Situ* Sub-Micrometer Scale Chemical Imaging with Scanning Transmission X-ray Microscopy. S.T. Kelly, P. Nigge, Lawrence Berkeley National Laboratory, A. Laskin, B. Wang, Pacific Northwest National Laboratory, A. Tivanski, S. Ghorai, University of Iowa, T. Tyliczszak, M.K. Gilles, Lawrence Berkeley National Laboratory

Spatially resolved chemical information on length scales shorter than 50 nm has become crucial in many areas of science and engineering -- from analyzing the chemistry of geological and environmental samples to quantifying the detailed chemical structure of novel materials engineered on the nanoscale. Scanning transmission x-ray microscopy (STXM) allows collection of specific chemical speciation data on these length scales through the acquisition and analysis of near-edge x-ray absorption fine structure (NEXAFS) spectra at each image pixel. However, the full usefulness of the STXM instrument may ultimately be realized in the *in situ* analysis of chemical transformations by controlling the local sample environment.

In situ STXM/NEXAFS measurements have been made in several ways thus far, ranging from simple to very complex. Introducing gases directly into the microscope chamber is effective, yet the presence of the gas along the entire optical path of the x-rays reduces signal at the detector. Furthermore, gas choice with this configuration is limited to those compatible with the microscope components. Separate *in situ* reactor cells circumvent these limitations by confining the gaseous environment to a small region immediately around the sample. Several groups have used reactor cells to this end, with reactors ranging widely in complexity -- from simple cells with limited capability to complex systems which require substantial instrument reconfiguration.

Ideally, an *in situ* reactor for STXM should be capable, flexible, easy to install and configure, and easily fabricated. We have developed a gas phase

STXM reactor cell to meet many of these requirements. The reactor mounts directly to the standard STXM sample mount (making installation relatively simple) and contains an integrated sensor to actively measure relative humidity inside the cell for experiments using water vapor. We present here recent results using the reactor cell to examine two different systems. In the first system, we observed the hygroscopic properties of mixed organic/inorganic aerosol particles at increasing levels of relative humidity. In the second system, we monitored carbon dioxide sorption in metal organic framework materials. The advantages afforded by this reactor (and future improvements to it) will enable new scientific discoveries across a wide range of fields.

5:40pm IS+AS+BI+ET+GR+NS-TuA12 *In Situ* SEM and ToF-SIMS Imaging of Liquids for Biological Applications. L. Yang, X.-Y. Yu, Z. Zhu, S. Thevuthasan, Pacific Northwest National Laboratory, J. Cowin, Cowin In-Situ Science, L. L. C.

A vacuum compatible microfluidic interface was developed to enable surface analysis of liquids. The unique feature of the liquid flow cell is that the detection window is open to the vacuum allowing direct probing of the liquid surface. The flow cell is composed of a silicon nitride membrane and polydimethylsiloxane; and it is fully compatible with vacuum operations for surface analysis. The aperture can be drilled through the 100 nm silicon nitride membrane by using the focused ion beam/scanning electron microscope (FIB/SEM). Alternatively the primary Bi⁺ ions in ToF-SIMS can be used to fabricate the aperture window in real-time. New results using this vacuum interface and recent development will be presented in this paper. Several aqueous solutions containing conjugated IgG gold nanoparticles and representative biological solutions were studied *in situ* using scanning electron microscope (SEM) and time-of-flight secondary ion mass spectrometry (ToF-SIMS). Characteristic signals of the conjugated gold nanoparticles were successfully observed through the aperture by both energy-dispersive X-ray spectroscopy (EDX) in SEM and ToF-SIMS. Comparisons were also made among wet and dry samples and liquid sample in the flow cell using SEM/EDX. Stronger gold signal can be observed in our novel portable device by SEM/EDX compared with the wet or dry samples, respectively. Our results indicate that analyses of the nanoparticle conjugated antibodies are better made in their native liquid environment. Our unique microfluidic flow cell permits *in situ* liquid observations. In addition, a variety of aqueous solutions relevant to biological systems were analyzed. Our results indicate that chemical imaging by SEM and ToF-SIMS is applicable in analyzing more complicated aqueous solutions when coupled with our novel portable microfluidic platform.

Nanometer-scale Science and Technology

Room: 12 - Session NS+EN+GR-TuA

Nanomaterials in Two and Three Dimensions

Moderator: V.P. LaBella, University at Albany-SUNY

2:20pm NS+EN+GR-TuA2 Nanopatterning of SPRi Sensor Surfaces for Sub-Nanomolar Biomarker Detection. M.A. Parracino, M.J. Perez Roldan, J. Hanus, V. Spampinato, G. Ceccone, P. Colpo, F. Rossi, Nanobiosciences Unit, JRC, Italy

In this work we report the detection of low-molecular weight biomarkers on two kinds of nanostructured surfaces by using a SPRi sensor. Nanopatterned surfaces are fabricated by combining functionalization and patterning techniques. Two different methods were used for the surface nanopatterning: electro-beam lithography (EBL) and colloidal lithography (CL). Maltose binding protein (MBP) and transthyretin (TTR) are respectively immobilized on the two types of nanopatterns and used as biological recognition elements. Chemical contrast adhesive/non adhesive at nanoscale has been created in order to control protein binding at nanoscale. Plasma deposited (PEO)-like film was used as passivation layer to prevent non-specific binding of protein in between the protein adhesives nano-areas. All the fabrication steps of both surfaces have been carefully controlled and analyzed using several techniques such as AFM, XPS, and SEM. The gold nanostructures were 185 nm width lines, for the patterned created with EBL, and holes of 250 nm in diameters for the pattern fabricated using CL. The gold grating surface made using EBL was functionalized with sugar via a thiol-linker. Maltose Binding Protein (MBP) was bound on sugar modified surface in order to develop a competitive assay for maltose detection. In this competitive assay, the protein binding on the sugar functionalized surface depends on the concentration of his free competitor in solution: by measuring the protein binding, it is possible to evaluate the concentration of the small molecule in solution. In the second methods, NTA functionalized nanoholes in PEO like background were fabricated and subsequently activated with nickel (Ni II) for a selective immobilization of

histidines tagged TTR, which underlies to a direct detection of Thyroxine 4 (T4). In both case, the biological intermediates, MBP and TTR, are selectively immobilized onto nanopatterned surfaces. The ligand protein binding on the nanostructure is higher than on the flat surface. The better ligand orientation and immobilization on the nanostructures results in analyte detection at sub-nanomolar concentration. The combination of nanopatterning features with the two different methods of detection presented in this work provides a description for a more generalized approach for the development of stable and reliable biosensor platforms for the detection of different small molecules having an high impact in environmental, and biomedical field.

4:00pm NS+EN+GR-TuA7 Single Layer of MoS₂ on Close-Packed Metal Surfaces, D. Le, T.S. Rahman, University of Central Florida

We present results of first principles electronic structure calculations, using van der Waals density functional theory, of the adsorption of a single layer of Molybdenum disulfide (MoS₂) on several close-packed metal surfaces. On Cu(111) we find three energetically equivalent stacking types and a Moiré pattern whose periodicity is in agreement with experimental findings [1]. The layer is found not to be purely physisorbed on the surface, rather there exists a chemical interaction between it and the Cu surface atoms. We also find that the MoS₂ film is not appreciably buckled, while the top Cu layer gets reorganized and vertically disordered. The sizes of Moiré patterns for a single layer of MoS₂ adsorbed on other close-packed metal surfaces are also estimated by minimizing the lattice mismatch between the film and the substrate. The Moiré patterns on Ir(111), Pt(111), and Ru(0001) are particularly interesting as the MoS₂ layer is found to bind more strongly on them than on Cu(111). We compare the nature of the bond in these three substrates with that on Cu(111).

[1] D. Kim, D. Sun, W. Lu, Z. Cheng, Y. Zhu, D. Le, T. S. Rahman, and L. Bartels, *Langmuir* **27**, 11650 (2011).

* This work was supported in part by the U.S. Department of Energy under Grant No. DE-FG02-07ER15842.

4:20pm NS+EN+GR-TuA8 Chemically Exfoliated Two Dimensional Materials for Energy Applications, M. Chowalla, Rutgers University INVITED

Chemical exfoliation of layered two-dimensional materials such as graphite and transition metal chalcogenides allow access to large quantities of atomically thin nanosheets that have properties that are distinctly different from their bulk counterparts. Although 2D materials have recently become popular, their fabrication via exfoliation of bulk crystals has been known for decades. For example, Brodie first exfoliated graphite into atomically thin oxidized form of graphene in 1859. In the case of layered transition metal dichalcogenides (LTMDs) such as MoS₂, WS₂, MoSe₂, WSe₂, etc., Frindt et al. performed seminal work in the '70s and '80s. We have revived these techniques to obtain a wide variety of chemically exfoliated two-dimensional nanosheets and utilized these materials in wide variety of electronic and energy applications. In this presentation, I will highlight some of our key contributions with graphene oxide (GO) and LTMD nanosheets. Specifically, I will present their implementation into large area electronics, strategic implementation into solar cells, and as catalyst for hydrogen evolution.

5:00pm NS+EN+GR-TuA10 Isolation and Surface Structure of Ultrathin Nanosheets formed by Atomic Layer Deposition, K.M. Lee, D.H. Kim, G.N. Parsons, North Carolina State University

Ultrathin nanosheets are two-dimensional structures that are often exfoliated from layered compounds. The nanosheets are flat with large surface area (100's of nm²) but with very small thickness in several nm scale. A common example of a nanosheet is graphene which is exfoliated from graphite. Other nanosheet materials that are chemically exfoliated from layered crystals include MoS₂, VS₂, and many oxide materials such as MnO₂, TiNbO₅, or LaNb₂O₇. These materials show unique capabilities for nanoelectronic devices, photocatalysts, and electrochemical sensor applications. For our work, we explore atomic layer deposition (ALD) as an effective technique to fabricate metal oxide nanosheets with precisely controlling thickness and chemical composition. To form nanosheets, we spin-coated a substrate with polymer such as polymethylmethacrylate (PMMA), polyvinyl alcohol (PVA), or polyacrylic acid (PAA) as a sacrificial layer, then deposited TiO₂, Al₂O₃ or ZnO on polymer layer by ALD. Dissolving the polymer in solvent releases nanosheets from the substrate. We successfully attained two dimensional TiO₂ nanosheets with several hundred μm in lateral size and less than 10 nm in thickness. Attaining nanosheets with thickness near 1nm proved to be rather challenging. For Al₂O₃ and TiO₂, nanosheets with thickness of ~ 1 nm can be isolated by two-immiscible liquid separation process. For ZnO, the thinnest nanosheet obtained to date is closer to 15 nm. We characterized nanosheets using AFM to confirm their thickness and found that the surface

structure and roughness depends on the materials and thickness. We also examined the functionality of TiO₂ nanosheets as an agent for photocatalytic degradation of organic dyes. This work demonstrates and defines the capabilities and limits for functional nanosheets fabrication by atomic layer deposition.

5:20pm NS+EN+GR-TuA11 All Solution Processed InGaO₃(ZnO)_m Thin Films with Layered Structure and their Thermoelectric Properties, J.H. Kim, H.K. Cho, Sungkyunkwan University, Republic of Korea

As the materials currently in use have been reached terminal and showed low productivity in a few field, the development of advanced materials are demanded. In the middle of atmosphere, low-dimensional nanostructures have been introduced in recent studies such as 1-D nanowire and 2-D superlattice. Among them, a multi-layered structure shows unique properties originating from the confinement of carriers in the two-dimensional layer. For example, LaFeO₃-LaCrO₃ superlattice structures fabricated by pulsed layer deposition (PLD) have shown enhanced ferromagnetism [1] and InGaO₃(ZnO)_m superlattice structure grown by sputtering method has improved thermoelectric properties [2].

These homologous series of RAO₃(MO)_m (R=In or rare earth elements; A=Ga, In, Al, or Fe ; M=Mg, Co, Cu, or Zn ; m=integer) comprise alternating stacks of RO₂⁻ and AO⁺(MO)_m layers and are candidate to exhibit the quantum effect due to its natural superlattice [3]. Despite these materials being widely investigated, the fabrication of RAO₃(MO)_m thin film with layered structure is limit due to their fabrication which requires expensive high-vacuum equipment and shows low productivity.

In this study, all solution process (an epitaxial ZnO buffer layer growth on sapphire substrate, amorphous IGZO layer on ZnO buffer layer by composition controlled solution process, and post-annealing at 900°C for 9hours) enables us to fabricate InGaO₃(ZnO)_m thin film with periodic superlattice structure. Crystallinity of thin film was analyzed by X-ray diffraction and TEM results. And also, TE properties such as Seebeck coefficient, electrical conductivity, thermal conductivity were evaluated to identify the degree of crystallization of superlattice with layered structure.

Reference

- [1] K. Ueda, H. Tabata and T. Kawai, *Science*, 1998, **280**, 1064
- [2] D. K. Seo, B. H. Kong and H. K. Cho, *Cryst. Growth Des.*, 2010, **10**, 4638
- [3] J. L. F. Da Silva, Y. F. Yan and S. H. Wei, *Physical Review Letters*, 2008, **100**, 255501.

Scanning Probe Microscopy Focus Topic

Room: 16 - Session SP+AS+BI+ET+MI+NS-TuA

Advances in Scanning Probe Imaging

Moderator: S. Allen, The University of Nottingham, UK, Z. Gai, Oak Ridge National Laboratory

2:00pm SP+AS+BI+ET+MI+NS-TuA1 Molecules Investigated with Atomic Resolution using Scanning Probe Microscopy with Functionalized Tips, L. Gross, F. Mohn, N. Moll, G. Meyer, IBM Research - Zurich, Switzerland INVITED

Single organic molecules were investigated using scanning tunnelling microscopy (STM), noncontact atomic force microscopy (NC-AFM), and Kelvin probe force microscopy (KPFM). With all of these techniques submolecular resolution was obtained due to tip functionalization by atomic manipulation. The techniques yield complementary information regarding the molecular structural and electronic properties.

Using NC-AFM with CO terminated tips, atomic resolution on molecules has been demonstrated and the contrast mechanism was assigned to the Pauli repulsion [1]. On the other hand, by using STM the molecular frontier orbitals, i.e., the highest occupied and the lowest unoccupied molecular orbitals (HOMO and LUMO), were mapped [2]. Using a CO terminated tip for orbital imaging with the STM, the resolution can be increased and the images correspond to the gradient of the molecular orbitals due to the *p*-wave character of the tip states [3]. Finally, KPFM reveals information about the distribution of charges within molecules by measuring the *z*-component of the electrostatic field above the molecule, as demonstrated on the hydrogen tautomerization switch naphthalocyanine [4].

References :

- [1] L. Gross et al. *Science* **325**, 1110 (2009).
- [2] J. Repp et al. *Phys. Rev. Lett.* **94**, 026803 (2005).

[3] L. Gross *et al.* *Phys. Rev. Lett.* **107**, 086101 (2011).

[4] F. Mohn *et al.* *Nature Nanotechnol.* **7**, 227 (2012).

2:40pm SP+AS+BI+ET+MI+NS-TuA3 Functional Imaging of Jahn-Teller Dynamics at the Single-molecule Scale. *J. Lee, S.M. Perdue, A. Rodriguez Perez, P.Z. El-Khoury, V.A. Apkarian*, University of California, Irvine

Taking advantage of both elastic and inelastic tunneling processes of a molecule isolated at the double-barrier tunneling junction of a scanning tunneling microscope, both static and dynamic parts of the Hamiltonian can be visualized with submolecular resolution. This is illustrated by imaging Jahn-Teller (JT) driven vibronic dynamics within Zn-etiochlorophyllin (ZnEtio), in its various reduced forms, in what may be regarded as nature's choice of a molecule as a controllable current switch. Unique interpretations are afforded through simultaneously recorded functional images, such as maps of: a) energy resolved differential current, b) spectrally resolved electroluminescence, c) conduction bistability, d) reduction/oxidation potentials (maps of charging and discharging). We focus on the radical anion, ZnEtio⁻, which is reduced by injecting an electron to a single ZnEtio molecule adsorbed on a thin aluminum oxide film grown on NiAl(110). In contrast with the neutral, the saddle-shaped radical anion lies flat on the surface of the oxide. The discharge map directly shows that the excess electron is localized in the ²p_x orbital of the entire porphyrin macrocycle, as a result of the JT active rectangular (B_{1g}) distortion of the molecule. The static JT potential leads to conduction bistability, with reversed switching polarity depending on whether tunneling electrons are injected into the occupied ²p_x orbital or the diamond (B_{2g}) coordinate which serves as a transition state that connects the p_x and p_y orbitals at the two B_{1g} minima. In addition to the JT switching, the dynamic JT states are directly imaged through electroluminescence spectra, induced by injection of a second electron in the anion. The spectra consist of a continuum due to radiative ionization of the dianion, and sharp Fano resonances of the vibronic progression of the JT active modes. A detailed analysis of the spectra yields the vibronic couplings and the wavefunctions. Vibronic structure is inherent in STM topographic images, and has hitherto not been fully recognized.

3:00pm SP+AS+BI+ET+MI+NS-TuA4 Atomic and Chemical Resolution of Heterogeneous 1-D Metallic Chains on Si(100) by Means of nc-AFM and DFT. *M. Setvin, M. Ondracek, P. Mutombo, Z. Majzik, P. Jelinek*, Institute of Physics of ASCR, Czech Republic

Scanning Probe techniques are widely used to image atomic and electronic structure of surfaces and nanostructures. However atomic and chemical resolution of complex nanostructures (e.g. molecules, nanoparticles or nanowires) is still the large challenge. Several methods (see e.g. [1-3]) have been already proposed to achieve the single-atom chemical resolution. In the work [3] it was showed that the single-atom chemical identification can be achieved via force-site spectroscopy measurements using Frequency Modulation Atomic Force Microscopy (FM-AFM). The validity of the method was demonstrated on semiconductor surface alloy composed of isovalent species (Si, Sn and Pb). In this particular case, the valence electrons of surface atoms possess very similar electronic structure close to sp³ hybridization with characteristic dangling bond state. Hence the maximum short-range force is mainly driven by the position of the dangling bond state with respect to the Fermi level.

In this work, we investigated atomic and chemical structure of heterogeneous 1-D chains made of III and IV group metals grown on Si(100) surface [4] by means of room-temperature (RT) FM-AFM measurements combined with DFT simulations. Here 1D chains consist of heterogeneous buckled-dimer structures with unknown chemical ordering. What more, the presence of buckled dimers composed by chemical species of different valence makes this system very challenging for true atomic and chemical resolution by means of SPM.

In this contribution, we will show first that FM-AFM technique even at RT is able to achieve atomic resolution of individual atoms forming dimers, much superior to the contrast obtained by the traditional STM technique. Secondly, we will demonstrate that the single-atom chemical identification is still possible combining the force-site spectroscopy at RT with DFT simulations even in such complex systems as the heterogeneous 1D metallic chains.

[1] M. Schmid, H. Stadler, P. Varga *Phys. Rev. Lett.*, **70**, p. 1441 (1993)

[2] L. Gross *et al.*, *Science* **325**, 5944 (2009).

[3] A. Foster *et al.* *Phys. Rev. Lett.* **102**, 256103 (2009).

[4] Y. Sugimoto, P. Pou, M. Abe, P. Jelinek, R. Perez, S. Morita, O. Custance, *Nature* **446**, 64 (2007)

[5] L. Magaud, A. Pasturel, and J.-Y. Veuillen, *Phys. Rev. B* **65**, 245306 (2002).

4:00pm SP+AS+BI+ET+MI+NS-TuA7 Simple Routes to High Speed and Super Resolution AFM. *J.K. Hobbs*, University of Sheffield, UK
INVITED

Over the past two decades atomic force microscopy has developed to become the workhorse of molecular nanotechnology. However, despite this success, it has failed to deliver consistently in two areas where it arguably has most potential, namely sub-molecular resolution imaging and the following of processes in real time. Here our work to tackle these challenges will be discussed.

We have developed a new approach to reaching high resolution within a conventional AFM, based on torsionally driven T-shaped cantilevers, dubbed "torsional tapping AFM". The use of torsional oscillations gives improved dynamics (high Q-factor, high frequency), without excessively increasing the spring constant. The small offset of the tip from the axis of rotation gives improved lever sensitivity. Combined, these result in an approximately 12 fold improvement in sensitivity when compared to the same AFM with a conventional tapping cantilever. This improved sensitivity allows ultra-sharp whisker tips to be used in a routine manner, giving true molecular resolution even on soft materials presenting surfaces with tens of nanometres of topography. For example, individual polyethylene chains both in the crystalline phase, and at the interface with the amorphous phase, can be clearly imaged in a conventionally processed sample of plastic, with polymer chain-to-chain resolution down to 0.37 nm [1]. Data from semi-crystalline polymers to naturally occurring protein crystals will be presented.

High speed AFM requires methods for scanning rapidly, for maintaining tip-sample contact ("feedback"), and for constructing the topography image. We have shown that resonant scanners [2] give a robust method for rapid scanning. In a conventional AFM the feedback and the topographic image are inextricably linked. However, this places a limit on scan speed as it demands that the tip has reached equilibrium at each point on the image if the height is going to be accurately obtained. We have adopted a different approach, in which the height of the tip is directly measured using an interferometric approach, freeing the feedback loop to minimising tip-sample forces. This allows topographic images with height traceable to the wavelength of the interferometric laser to be obtained at imaging rates greater than one frame a second. Coupled with resonant scanners, giving scan areas up to 40×40 μm² an AFM platform capable of in-line industrial applications is obtained.

1. Mullin, N.; Hobbs, J. K., *Phys Rev Lett* **2011**,107

2. Humphris, A. D. L.; Miles, M. J.; Hobbs, J. K. *Appl Phys Lett* **2005**,86 (3)

4:40pm SP+AS+BI+ET+MI+NS-TuA9 A Scanning Probe Microscopy Study of Trimesic Acid Self-Assembly on Highly Oriented Pyrolytic Graphite. *V. Korolkov, S. Allen, C.J. Roberts, S.J.B. Tendler*, The University of Nottingham, UK

We have investigated trimesic acid (1,3,5-benzenetricarboxylic acid, TMA) adsorption on highly oriented pyrolytic graphite (HOPG) surfaces from aqueous medium at room temperature. Both atomic force (Peak Force Tapping mode) and scanning tunnelling microscopy were utilized to follow the adsorption dynamics and molecular arrangements. A chicken-wire arrangement for adsorbed molecules with an average pore size of 11 ± 1 Å was established and observed using both scanning techniques. We found that this structure forms a monolayer within ~ 100 seconds of exposure of the HOPG surface to 50 μM TMA solution in H₂O. The monolayer structure was found to be stable for at least 48h under ambient conditions. STM was observed to lead to some desorption of TMA from a dynamically formed TMA film, and was only able to image the monolayer of TMA molecules in intimate contact with the HOPG. AFM revealed that TMA films formed using higher concentrations or longer adsorption times formed multilayers with similar molecular spacings and displayed an island growth morphology.

We have achieved an excellent resolution on an ambient running AFM. We have demonstrated that the combination of STM and AFM is essential, if not a must, to look at ultimate monolayers in the ambient conditions. Overall a facile green chemistry method for TMA monolayer fabrication from aqueous media on a HOPG surface has been established.

5:00pm SP+AS+BI+ET+MI+NS-TuA10 Understanding the Role of the Probe in SPM Imaging of Metal Oxides: New Opportunities for In-Depth Surface Analysis. *H. Mönig*, Univ. of Münster, Germany, *M. Todorovic*, Univ. Autónoma de Madrid, Spain, *M.Z. Baykara*, Yale Univ., *T.C. Schwendemann*, Southern Connecticut State Univ., *J. Götzten*, Ö. Ünverdi, *E.I. Altman*, Yale Univ., *R. Perez*, Univ. Autónoma de Madrid, Spain, *U.D. Schwarz*, Yale Univ.

Metal oxide surfaces play an indispensable role in a number of catalytic processes of technological and scientific importance. A fundamental understanding of the role that metal oxide surfaces play in such applications

requires an experimental technique that allows analyzing chemical and electronic surface properties down to the atomic scale. The powerful method of three-dimensional atomic force microscopy (3D-AFM) in combination with scanning tunneling microscopy (STM) can be used towards this goal with great success. However the interpretation of results is not straightforward, particularly because the structure and chemistry of the probe tip employed in the experiments influences the measured data.

In this talk, using a combination of experimental STM data and density functional theory (DFT) calculations, we will study the effect of changing the tip structure and chemistry, as well as imaging parameters such as tip-sample distance and bias voltage on STM images obtained on the model surface of Cu(100)-O, a surface oxide layer consisting of nearly co-planar copper (Cu) and oxygen (O) atoms. We observe that STM image contrasts and atomic species with highest tunneling probability vary greatly with changing tip properties and imaging parameters. Reasonable matches between calculated and experimentally recorded STM images are observed, allowing the determination of particular tip models used in the experiments. Additionally, the effect of rotating the model tip structures with respect to the sample surface results in asymmetric features in simulated STM images, reproducing certain peculiar patterns observed experimentally. To sum up, the results presented here underline the significant role that the tip plays in SPM measurements and describe potential routes to optimize the gathered information through deliberate manipulation of tip properties as well as imaging parameters.

5:20pm SP+AS+BI+ET+MI+NS-TuA11 Characterizing the Best Tips for NC-AFM Imaging on Metal Oxides with Force Spectroscopy and Theoretical Simulations, D. Fernandez-Torre, Universidad Autónoma de Madrid, Spain, A. Yurtsever, Osaka University, Japan, P. Pou, Universidad Autónoma de Madrid, Spain, Y. Sugimoto, M. Abe, S. Morita, Osaka University, Japan, R. Perez, Universidad Autónoma de Madrid, Spain

Metal oxides play a key role in a wide range of technological applications. To optimize their performance, it is essential to understand their surface properties and chemistry in detail. Noncontact atomic force microscopy (nc-AFM) provides a natural tool for atomic-scale imaging of these insulating materials. Some of these materials, including ceria (CeO₂), and particularly titania (TiO₂), have been extensively studied with nc-AFM in the last few years. Experiments on the rutile TiO₂(110) surface show, at variance with STM, that a variety of different contrasts can be obtained, and frequent changes among different imaging modes are observed during scanning. The two most common contrasts are the “protrusion” and the “hole” mode imaging modes, that correspond, to imaging bright the positive or the negative surface ions respectively, but other contrasts like the “neutral” mode and the “all-inclusive” mode—where all the different chemical species and defects are imaged simultaneously—have been also identified.

Understanding the image contrast mechanisms and characterizing the associated tip structures is crucial to extract quantitative information from nc-AFM measurements and to identify the nature of the observed defects. While in many cases the same nc-AFM image can be explained by different models, and even different underlying tip-sample interactions, we show here that the combination of force spectroscopy (FS) measurements and first-principles simulations can provide an unambiguous identification of the tip structure and the image contrast mechanism. In particular, we show that the best tips to explain the protrusion and hole mode forces are TiO_x-based clusters differing in just one H atom at the tip apex, discarding previously proposed Ti-terminated tips that would lead to forces much larger than the ones observed in the experiments. The less frequent neutral and all-inclusive images are associated to Si tips where contamination is limited to just an O atom or OH group at the apex. These models provide a natural explanation for the observed contrast reversals by means of H transfer to/from the tip, an event that we indeed observe in our simulations. As tip contamination by surface material is common while imaging oxides, we expect these tips and imaging mechanisms to be valid for other oxides. Our results for the imaging of CeO₂ surfaces and of metal atoms (K, Pt) adsorbed on TiO₂ support this conclusion.

5:40pm SP+AS+BI+ET+MI+NS-TuA12 Direct Probe of Interplay between Local Structure and Superconductivity in FeTe_{0.55}Se_{0.45}, M.H. Pan, W.Z. Lin, Q. Li, B.C. Sales, S. Jesse, A.S. Sefat, S.V. Kalinin, Oak Ridge National Laboratory

A key challenge in high-temperature superconductivity is to determine the role of local crystallographic structure and chemical effects on the superconducting critical temperature, T_c . Iron chalcogenide superconductors (‘11’) are ideal model systems for deciphering the role of local effects on the superconductivity, primarily because they cleave leaving non-polar surfaces unlike other families of iron arsenide superconductors (‘1111’ or ‘122’) and cuprates. Here, we explore the interplay between local crystallographic structure, composition and local electronic and superconductive properties. Direct structural analysis of scanning tunneling microscopy (STM) data allows local lattice distortions and

structural defects across a FeTe_{0.55}Se_{0.45} surface to be explored on a single unit-cell level. Concurrent superconducting gap (SG) mapping reveals suppression of the SG at well-defined structural defects, identified as a local structural distortion (Guinier-Preston zone). The strong structural distortion is related to the vanishing of the superconducting state. This study provides insight into the origins of superconductivity in iron chalcogenides by providing an example of atomic-level studies of the structure-property relationship.

Surface Science

Room: 21 - Session SS+NS-TuA

Reactivity of Size and Shape Selected Nanoparticles

Moderator: C.T. Campbell, University of Washington

2:00pm SS+NS-TuA1 2012 AVS Gaede-Langmuir Award Lecture: Surface Photochemistry on Compact Crystals and on Metal Nanoparticles, D. Menzel*, Fritz-Haber Institut, and Techn. Univ. Muenchen, Germany **INVITED**

Adsorbing a molecule on a substrate changes its photochemistry. I shall briefly review characteristics of surface photochemistry, established mechanisms, and effects such as whether the substrate acts mainly as source or sink of electronic excitations of adsorbates, how long the latter survive, and how effects which influence their localization and delocalization influence the success rate of excitations. For laser excitation, linear and nonlinear response to excitations can occur.

Use of nanoparticles (MNPs) instead of bulk metals further changes surface photochemistry, mainly by changing the substrate optical excitations (e.g. the Mie plasmon of MNPs), and excitation lifetimes and efficiency (by confinement). This will be illustrated by data obtained in the past years in Berlin on NO dimers adsorbed on Ag NPs with varied size (2 to 10 nm) supported on thin alumina films on NiAl single crystals, laser-excited with 2 to 5 eV, with in situ comparison with Ag(111). The main channel is photodesorption of NO; conversion to N₂O + O, and to NO(ad) stabilized by O also occur. Adsorption energies were characterized by TPD, cross sections (PCS) by photo-depletion, and desorbate energy distributions (translation, rotation, vibration) by TOF and REMPI analysis. Linear and nonlinear fluence dependencies of desorption signals have been found with n_s and f_s laser pulses, respectively. The main changes in NO photodesorption are found in the PCS which are strongly enhanced by plasmon excitation and more weakly by excitation confinement, and show clear size dependences interpreted by counteracting influences. The branching into the minor photoreaction channels is also changed at Ag NPs compared to Ag(111) which is due to varying PCS enhancement factors. The photochemical mechanism, however, as evidenced by state-resolved analysis of the desorbing NO molecules, remains the same – formation of transient negative ions by hot electrons in the substrate - for most of the investigated range (with an exception for high energy and small particles). With f_s laser pulses further drastic PCS increases are found even at low fluences at the NPs but not at Ag(111). This nonlinear effect is explained by re-excitation of hot electrons confined in the NPs within a single laser pulse. But even here the individual dynamics stay the same. This action of NPs on the success probability of excitations with essentially unchanged dynamics appears to be the typical behavior for photochemistry on MNPs. Only in an unusual case (Xe/Ag NPs) we have seen a direct influence of plasmon excitation on desorption.

These findings may help in the understanding of photocatalysis on MNPs.

2:40pm SS+NS-TuA3 Photocatalytic Deposition of Au onto Ordered Linear Arrays of TiO₂ Nanoparticles, J. Taing, A. Margarella, Y. Liu, J.C. Hemminger, University of California Irvine

TiO₂ nanoparticles were decorated onto the step edges of highly oriented pyrolytic graphite (HOPG) via physical vapor deposition. Gold shells and nanoparticles were then grown on the TiO₂ nanoparticles using a photoelectrochemical cell whereupon a photocatalytic reduction mechanism is verified by photocurrent measurements. Samples of TiO₂ nanoparticles on HOPG, acting as a photoelectrode, were placed in a half-cell and immersed in either an electrolyte solution of 1.0 M NaCl or 1.0 M NaNO₃. Bare HOPG, acting as a counter electrode, was placed in a second half-cell and immersed in the same electrolyte solution. The two half-cells were connected by a salt bridge and the electrodes by a picoammeter. Upon irradiation of the TiO₂ nanoparticles by 365 nm UV light from a 200 W Hg lamp, photogenerated electrons produced a photocurrent. Subsequent to introducing 1 mL of 15 μM HAuCl₄ into the cell containing the TiO₂

* Gaede Langmuir Award Winner

nanoparticles, the photocurrent decreased as a result of the reduction of Au³⁺ to Au on TiO₂. Scanning electron microscopy (SEM), transmission electron microscopy (TEM), x-ray dispersive spectroscopy (EDS), and x-ray photoelectron spectroscopy (XPS) were used to characterize the morphology, crystal structure, and chemical identity of the nanoparticles. Images of TiO₂ nanoparticles encapsulated in Au are included in the supplement.

3:00pm SS+NS-TuA4 Catalytic Activity of Gold-supported TiO₂ Nanocrystals Towards Simple Alcohols, D.V. Potapenko, Z. Li, Y. Lou, R.M. Osgood, Columbia University

Titanium oxide is a versatile photocatalytic material and it has been the subject of much research throughout the last two decades. Nanostructuring is one approach for tailoring the properties of a catalyst. Previously we have developed a method of preparation of structurally homogenous TiO₂ nanocrystals on Au(111) substrate through oxidation of Ti-Au surface alloy. In this work we explore catalytic properties of the nanocrystals through a series of temperature programmed desorption (TPD) studies with simple alcohols: ethanol and 2-propanol. Similarly to the single crystal TiO₂ rutile(110) surface, TiO₂ nanocrystals on Au(111) catalyze dehydrogenation of ethanol and 2-propanol into ethylene and propene. Dehydrogenation was observed in a wide range of temperatures from 400 to 550 K, which is lower than the temperature of the corresponding reaction on rutile(110). More interestingly, we have observed formation of acetone from 2-propanol on our TiO₂/Au(111) surface at around 450 K; this reaction was not observed on rutile(110). The reactivity patterns of TiO₂/Au(111) show strong dependence on geometry and structure of the nanocrystals.

4:00pm SS+NS-TuA7 Structure, Chemical State, and Reactivity Investigations of Size- and Shape-Selected Nanocatalysts under Operando Conditions, B. Roldan Cuenya, University of Central Florida
INVITED

The rational design of the next-generation of catalysts requires detailed knowledge of the correlation between structure, chemical composition, and reactivity. Even though Pt and Pd are among the most industrially relevant and widely investigated nanocatalysts, their complex interaction with common reactants such as oxygen still provides many challenges to the scientific community. In this work, the relation between the structure and reactivity of nanocatalysts "at work" was obtained via X-ray absorption fine-structure spectroscopy, X-ray photoelectron spectroscopy, and mass spectrometry. Homogeneous size- and shape-selected metal nanoparticles (NPs) have been synthesized by means of diblock copolymer encapsulation.

The influence of the nanoparticle *shape* on the reactivity of Pt nanocatalysts on γ -Al₂O₃ will be described. Nanoparticles with similar size distributions (~0.8-1 nm) but with different shapes were found to display distinct reactivities for the oxidation of 2-propanol. A correlation between the number of undercoordinated atoms at the NP surface and the onset reaction temperature was observed. Furthermore, platinum oxides were found to be the active species for the partial oxidation of 2-propanol, while the complete oxidation was catalyzed by oxygen-covered metallic Pt NPs.

The evolution of the structure and oxidation state of ZrO₂-supported Pd nanocatalysts during the *in situ* reduction of NO with H₂ will also be discussed. Prior to the onset of the reaction, NO-induced redispersion of the Pd NPs over the ZrO₂ support was observed, and Pd^{δ+} species detected. This process parallels the high production of N₂O observed at the onset of the reaction (>120°C), while at higher temperatures (≥ 150°C) the selectivity shifts toward N₂. Interestingly, concomitant with the onset of N₂ production, the Pd atoms re-aggregate into large metallic Pd NPs, which were found to constitute the active phase for the H₂-reduction of NO. The evolution of the oxidation state of Pd and Pt NPs during the oxidation of NO and the role of the NP size will also be presented.

Our findings highlight the decisive role of the nanoparticle structure and chemical state in catalytic reactions and the importance of *in situ* reactivity studies to unravel the microscopic processes governing catalytic reactivity.

4:40pm SS+NS-TuA9 Particle Size, Support and Alloying Effects in Electro-catalysis: Relationships with Heterogeneous Catalysis, B.E. Hayden, University of Southampton, UK
INVITED

High-Throughput Physical Vapour Deposition (HT-PVD) based on Molecular Beam Epitaxy methods¹ has been used to synthesize libraries of catalysts which have subsequently been screened for their electrochemical activity and stability. A screening method is briefly described² which has been applied to measurements on model supported metal nano-particle HT-PVD catalyst libraries.

Considerable effort has been made to find alternative supports for platinum based catalysts in order to improve the particle stability and improve the three-phase boundary in fuel cell applications. HT-PVD model catalyst

methodology has been applied to the study of support and particle size effects in electrocatalysis.³ Experiments have demonstrated the potential for using a support such as titania to induce CO oxidation electro-catalytic activity in gold particles,⁴ with an optimum particle size observed at ca. 3nm (Figure). No induced activity is observed for carbon supports. The similarities with the low temperature oxidations exhibited by supported Au in heterogeneous catalytic are highlighted. Extending this methodology to supported platinum based catalysts, the effect of particle size is demonstrated in the reduction of oxygen for the model carbon supported platinum catalysts, highlighting the limitations of catalyst dispersion. Supporting platinum on titania can result in a strong poisoning of the oxygen reduction catalysis.⁵

The combination of ab-initio theory and electrocatalyst screening also provides a powerful combination in the search for precious metal alloy and non noble metal alloy catalysts. Examples are given for anode hydrogen oxidation (HOR) catalysts such as Pd based,⁶ and tungsten copper⁷ alloys.

References

1. S. Guerin and B. E. Hayden; J. Comb. Chem. 8 (2006) 66-73.
2. S. Guerin, B.E. Hayden, et.al.; J. Comb. Chem. 6 (2004) 149 - 158.
3. S. Guerin, B.E. Hayden, D. Pletcher, et.al.; J. Comb. Chem. 8 (2006) 791-798.
4. B.E. Hayden, D. Pletcher and J.-P. Suchsland; Angewandte Chemie Int. Ed. 46 (2007) 3530-3532.
5. B.E. Hayden, D. Pletcher, J.-P. Suchsland et.al.; Phys. Chem. Chem. Phys. 11 (2009) 1564-1570. *ibid*: Phys. Chem. Chem. Phys., 2009, 11, 9141-9148.
6. F. A. Al-Odail, A. Anastasopoulos, and B. E. Hayden; Phys. Chem. Chem. Phys. 12 (2010) 11398-11406. *Ibid*; Topics in Catalysis 54 (2011) 77-82.
7. A. Anastasopoulos, J. Blake, John and B.E. Hayden; J. Phys. Chem. C, 115 (2011) 19226-19230.

5:20pm SS+NS-TuA11 The Growth and Structures of Metal Nanoparticles on Ordered ZrO₂(111) Surfaces, Y. Han, S.W. Hu, Y.H. Pan, J.B. Hou, H.B. Pan, J.F. Zhu, University of Science and Technology of China

Metal nanoparticles supported on zirconia have attracted much attention in recent years owing to their variety of technological applications such as heterogeneous catalysis and gas sensor operation. In particular, as catalysts, the interface properties of metal/ZrO₂ referring to the morphology, charge transfer, thermal stability and reactivity play crucial roles in determining their real applications. In this presentation, we report our recent studies on the growth, electronic structures and thermal stabilities of metal nanoparticles (Cu, Ag and Au) on well-defined ZrO₂ thin films by synchrotron radiation photoemission spectroscopy (SRPES) together with scanning tunneling microscopy (STM) and low electron energy diffraction (LEED). The well-defined ZrO₂(111) oxide thin films were epitaxially grown on Pt(111). It was found that the growth behavior of metals on ZrO₂(111) strongly depends on the morphologies of oxide surfaces and the interfacial interactions between the metal deposits and the ZrO₂(111) films. The binding energies of all three metal core-level peaks shift monotonically toward higher binding energy with decreasing the metal particle sizes. The contributions of initial and final state effects to the core level binding energy shifts are differentiated using the Auger parameters. At very low coverages, most likely Au forms Au^{δ+}, while Ag remains the metallic state and Cu forms Cu⁺ on ZrO₂(111).

5:40pm SS+NS-TuA12 Structure and Electronic Properties of Ni Nanoparticles Supported on Reducible CeO₂(111) Thin Films, Y.H. Zhou, Xiamen University, Republic of China, J. Zhou, University of Wyoming

Ceria-supported Ni nanoparticles have been of great interest as ethanol and methane reforming catalysts for hydrogen production in fuel cell applications. Recent studies have indicated that the catalytic reactivity of these ceria-supported Ni nanoparticles can be influenced by the redox properties of ceria as well as the synergistic effect between the two. To elucidate the nature of their activity, we studied Ni particles deposited on fully oxidized CeO₂(111) and reduced CeO_{1.88}(111) thin films using scanning tunneling microscopy and x-ray photoelectron spectroscopy at the fundamental level. Ceria thin films were grown *in situ* on Ru(0001) under ultrahigh vacuum conditions. Ni was vapor-deposited onto ceria thin films. At 300 K, metallic Ni is the only species present on the reduced ceria. However, a small amount of Ni is oxidized to Ni²⁺ on CeO₂. Oxidation of

Ni on CeO₂ can be facilitated by annealing as well as by depositing Ni at 500 K. Scanning tunneling microscopy studies show that Ni forms two-dimensional particles on ceria at room temperature, which suggests a strong Ni-ceria interaction. The particles can agglomerate into large three-dimensional structures with further heating. The structure and electronic properties of Ni metal particles on ceria were further compared to those of bimetallic Ni-Au and Ni-Rh particles.

Wednesday Morning, October 31, 2012

Biomaterial Interfaces

Room: 23 - Session BI+SS+NS-WeM

Bio/Nano Interfaces with Applications in Biomedicine and Energy

Moderator: G.J. Leggett, University of Sheffield, UK

8:00am **BI+SS+NS-WeM1 Combining Colloidal Lithography and Photolithography to Create Dual Length-Scale Topographical Features to Study Stem Cell Behavior**, *D.T. Bennetsen, D.C.E. Kraft, R. Ogaki, M. Foss*, Aarhus University, Denmark

It is well known that topographical features influence cellular response. A novel combination of colloidal- and photolithography has been developed to create a dual length scale topographical platform. The presented approach permits rapid parallel fabrication of micro/nanoscale patterns. The aim is to study the response of primary human dental pulp stem cells (hDPSC) to such topographies in a systematic way.

Colloidal lithography is performed using the "lift-off" method, which is applicable to surfaces with a non-flat surface. This enables the combination of using photolithography pre-made wafers as substrates, resulting in a complex topographical structure, spanning two length scales (Figure 1). Topographical patterns are created using the colloidal mask with either evaporation or sputtering via physical vapor deposition (PVD). The principle combination of materials investigated is tantalum covered with tantalum features. These dual scale substrates are exposed to hDPSC and proliferation, attachment and differentiation are examined. Differentiation is examined using osteogenic markers and MyoD1 expression.

Initial cell proliferation data indicates that variations in the colloidal pattern heights do not seem to elicit a statistical significant response (Figure 2). A set of experiments to clarify the effect of the colloidal pattern on the proliferation and cell cycle of the hDPSC is thus currently being performed. Furthermore, the effect of the dual scale topographical substrates on proliferation, differentiation and cell cycle is also being explored.

Concurrently we are investigating the combined effects of topographical/chemical patterns on cellular response. This can be achieved by depositing different materials site-specifically, followed by a material-specific self-assembly route. E.g. silanes and thiols with specific chemical moieties on oxides and gold, respectively. Characterization is performed using atomic force microscopy (AFM), scanning electron microscopy (SEM), X-ray photoelectron spectroscopy (XPS) and time-of-flight secondary ion mass spectrometry (ToF-SIMS).

Our fabrication approach enables the opportunity to increase the complexity of artificial 2D platforms thus by gaining a better understanding of cellular behavior for a range of biomedical and biotechnological applications.

8:20am **BI+SS+NS-WeM2 Genetically Modified Tobacco Mosaic Virus (TMV)-based Electrochemical Detection of 2, 4, 6-trinitrotoluene (TNT)**, *F. Zang, H. Ben-Yoav, X. Fan, A. Brown, J. Culver, R. Ghodssi*, University of Maryland

Detection of chemical hazards and explosive compounds has received growing attention for applications in environmental monitoring, food science, and national security. Explosives, such as TNT, show low vapor pressure, molecular mass, and volume, which makes the detection of these molecules challenging for most mass and refractive index based sensors. Thanks to the redox reaction of nitro groups in TNT molecules, electrochemical methods may be used for detection of low concentrations of TNT in aqueous environments. Electrochemical sensors are suited for on-site explosive detection due to high sensitivity, low volume and convenient integration with miniaturized devices. However, to distinguish TNT from other electrochemically active compounds in complex environments, high selectivity is a more critical factor for development of TNT sensors.

The TMV has a high aspect ratio, rod-like nanostructure that can be genetically modified to express tailored chemical receptors. In this work, a 12-amino acid (WHWQRPLMPVSI) sequence peptide with multivalent recognition properties of TNT was expressed on the coat protein of TMV (TMV-p) which was utilized to develop a sensitive and selective electrochemical sensing mechanism for TNT detection. Selective binding of TMV-p with TNT molecules will decrease the free TNT concentration in solution, reducing the number of nitro groups available for redox reactions.

In preliminary studies, background signals generated from electrolytes were characterized and the signal-to-noise ratio was optimized by long term scans of square wave voltammetry. Three concentration dependent current peaks from the reduction of nitro groups in TNT were observed at the

potentials of -0.53V, -0.72V and -0.86V vs. Ag/AgCl reference electrode, respectively, which agreed with the results in literatures. The initial results showed a stable and reliable electrochemical response by the TMV-p sensing system. By comparing the reduction currents in the mixtures of TMV-p and unmodified TMV with TNT solutions, we will demonstrate that TMV-p preserves the peptide binding affinity to TNT molecules while increasing the binding site density.

The approach described in this study is a sensitive and selective label-free method to detect TNT based on the binding of target molecules with peptide modified TMV. In addition to the highly selective peptide binding with analytes and a high binding site density, the genetically modified TMV is also capable of self-assembly, coating the active surfaces of a wide range of transducers. This work can potentially be implemented in the development of miniature sensors for selective TNT detection in complex environments.

8:40am **BI+SS+NS-WeM3 Nanoparticles in Biology: Engineering the Interface for Sensing and Delivery**, *V. Rotello*, University of Massachusetts **INVITED**

A key issue in the use of nanomaterials is controlling how they interact with themselves and with the outer world. Our research program focuses on the tailoring of nanoparticles of surfaces for a variety of applications, coupling the atomic-level control provided by organic synthesis with the fundamental principles of supramolecular chemistry. Using these engineered nanoparticles, we are developing particles for biological applications, in particular delivery and sensing. This talk will focus on the interfacing of nanoparticles with biosystems, and will discuss our use of nanoparticles for delivery applications including our *in vitro* studies of small molecule, nucleic acid, and protein delivery. This presentation will also feature the use of nanoparticles for diagnostic applications, including the use of array-based sensing paradigms for the sensing and identification of proteins, bacteria and cell type and state.

9:20am **BI+SS+NS-WeM5 Hydrophobic Forces, Electrostatic Steering, and Acid-Base Bridging between Atomically Smooth Self-Assembled Monolayers and End-Functionalized PEGolated Lipid Bilayers**, *M. Valtiner*, Max-Planck-Institut fur Eisenforschung, Germany, *S.H. Donaldson, M.A. Gebbie, J.N. Israelachvili*, University of California, Santa Barbara

A molecular-level understanding of interaction forces and dynamics between *asymmetric* apposing surfaces plays a key-role in utilizing molecular structures for functional surfaces in biological and materials applications. To quantify interaction forces and binding dynamics between apposing surfaces in terms of their molecular architecture we developed a novel surface-forces-apparatus experiment, using self-assembled monolayers (SAMs) on *atomically-smooth* gold. Varying the SAM head-group allowed to quantitatively identify and control which interaction forces dominated between the SAM surfaces and surfaces coated with short-chain, end-functionalized polyethylene-glycol (PEG) polymers extending from lipid-bilayers [1].

Three different SAM-terminations were studied: (a) carboxylic-acid, (b) alcohol, and (c) methyl head-group terminations. These functionalities allowed for the quantification of (a) specific acid-base bindings, (b) steric effects of PEG chains, and (c) adhesion of hydrophobic segments of the polymer-backbone, all as function of the solution pH. The pH-dependent acid-base binding appears to be a *specific, charge-mediated hydrogen bond* between oppositely-charged carboxylic-acid and amine functionalities, above the acid- pK_A and below the amine- pK_A . The long-range electrostatic "steering" of acid-base pairs leads to high binding probability even at distances close-to-full-extension of the PEG tethers, a result which has potentially important implications for protein-folding, enzymatic catalysis and biomaterial development.

[1] M. Valtiner et al., *JACS*, **2012**, 1746

9:40am **BI+SS+NS-WeM6 Viral Encapsulation in Lecithin Liposomes to Enhance the Therapeutic Effect of Oncolytic Viral Therapy**, *N. Mendez, V. Herrera, A.C. Kummel*, University of California San Diego

Oncolytic viruses have emerged as a novel platform for cancer therapeutics due to their tumor-selective replication in cancer cells. In particular, the oncolytic virus TAV-255 has shown viral replication attenuation in normal cells while retaining cytolytic activity in tumor cells by taking advantage of defects in the p53-tumor suppressor pathway. Extensive testing of oncolytic viruses has shown a limited therapeutic effect due to rapid clearance by the reticuloendothelial (RE) system and antibody neutralization. With the aim to overcome an immune response and to enhance localized delivery, an oncolytic virus-liposomal encapsulation method has been designed to increase tumor uptake and the therapeutic efficacy of oncolytic viruses in

cancer cells. An inexpensive, non-toxic liposome has been prepared by self-assembly of Lecithin phospholipid bilayers around the Adenovirus capsid. Cholesterol and DSPE-PEG were incorporated into the lipid formulation to improve retention and stability. The developed method has shown that non-targeted encapsulated viral particles retain their ability to transfect cancer cells. In addition, surface functionalization of the liposomes may be applied to specifically target cancer cells and to compensate for decreased infectivity due to viral encapsulation.

10:40am **BI+SS+NS-WeM9 Engineering Bio-Interfaces using Electric Field-Induced Nanolithography**, S. Zauscher, R.J. Ferris, B. Yellen, Duke University

Field-Induced Nanolithography (FINL) offers a convenient tool to create physically or chemically distinct patterns for bio-interfacial sensing applications. For pattern transfer, FINL merely requires a conductively coated SPM tip or stamp, connected to a conductive substrate via a voltage source. The patterning electrode is placed in contact with the target surface and a bias voltage is applied. Few sub-diffraction limit surface patterning techniques offer FINL's versatility to function in both a serial and parallel fashion. Recently we demonstrated the use of FINL to pattern a range of polymer brushes: poly(acrylic acid) (PAA), poly(N-isopropylacrylamide) (PNIPAAm), poly(sulfobetaine methacrylate) (PSBMA), and poly(oligo(ethylene glycol) methyl methacrylate) (POEGMA). Our results show that FINL of non-fouling polymer brushes provides a novel patterning technique that results in the localized topographical and chemical modification of the polymer brush surface only. The resulting chemical modification allowed selective addressing of the brush surface with aldehyde reactive coupling chemistries. Our approach thus shows significant promise for fabricating large-scale sensing devices, as patterning can be accomplished in a step-and-repeat fashion. Using FINL, we also demonstrated patterning of surface charges onto ferroelectric thin films (FETFs). FETFs are materials that are able to maintain a bi-stable polarization state, and that once polarized, maintain a high surface charge density. Using FINL, it is possible to locally align unit-cell dipole moments within the film to produce nano-scale polarization patterns. Although to date the use of FETFs is isolated to semiconductor and memory applications, we demonstrate that FETFs have great potential for biological and interfacial sensing applications. We show that FETF surface charge patterns can be used to control the lateral extent of electric double layer formation in dilute electrolyte solutions, with clear implications for field assisted particle deposition and programmed self assembly.

11:00am **BI+SS+NS-WeM10 Supramolecular Bioassemblies at Solid-Liquid Interfaces: Binding Control through Redox-Driven Multivalent Host-Guest Interactions**, G.V. Dubacheva, CIC biomaGUNE, Spain, L. Guerente, D. Boturny, Joseph Fourier University, France, R. Auzély, CERMAV, France, R.P. Richter, CIC biomaGUNE, Spain; Joseph Fourier University, France; Max Planck Institute for Intelligent Systems, Germany, P. Labbé, Joseph Fourier University, France

The design of kinetically stable bioassemblies while keeping binding control is of high current interest for bioanalytical and biomedical sciences. The development of tunable biointerfaces is also a key issue in nanobiotechnology as they can be used for modeling cell surface-associated biological processes. In this context, supramolecular host-guest chemistry is particularly attractive as it allows controllable molecular recognition and structural modification at specific areas of a nanoassembly, i.e. purpose-designed molecules can be confined in time and space in a highly controlled manner.

Cyclodextrin (CD) is well-known to form host-guest complexes with hydrophobic molecules while being soluble at physiological conditions. Taking advantage of redox-driven β -CD-ferrocene (Fc) multivalent interactions, we designed stimuli-responsive biomaterials composed of linear polymers, their multilayer assemblies and biomolecules. For this aim, we developed a new method to create β -CD self-assembled monolayers (SAMs) allowing precise varying β -CD surface density.1 We showed that Fc-functionalized polymers can be reversibly attached to such β -CD SAMs.1 We also showed a possibility to build up multilayer host-guest polymer assemblies on β -CD surfaces.2 In addition, we applied these β -CD SAMs for the reversible attachment of biomolecules using orthogonal Fc/ β -CD- and specific bio-interactions under biological conditions.3 Finally, combined with guest-modified polysaccharide hyaluronan, the β -CD surfaces were explored as a model system to understand multivalent interactions at the cell-hyaluronan matrix interface associated to a variety of cellular functions and biological processes.

Physico-chemical properties of supramolecular assemblies were characterized by QCM-D, ellipsometry, cyclic voltammetry and contact angle goniometry. The redox-driven binding of polymers and biomolecules to β -CD surfaces was assessed by *in situ* combining electrochemistry/QCM-D and SPR ellipsometry/microfluidic systems. The developed tunable

biointerfaces can be applied to investigate other topics in soft condensed matter physics, molecular physics and biophysics.

1Dubacheva et al., *Langmuir*, **2010**, 26:13976

2Dubacheva et al., *Soft Matter*, **2010**, 6:3747

3Dubacheva et al., *Chem Commun*, **2011**, 47:3565

11:20am **BI+SS+NS-WeM11 High-resolution *In Situ* Electrochemical STM Imaging of Phospholipid Model Cell Membrane**, H. Shimizu, S. Matsunaga, University of Tokyo, Japan, T. Yamada, T. Kobayashi, RIKEN, Japan, M. Kawai, University of Tokyo, Japan

We obtained molecular-scale images of phospholipid layers spread on a modified Au(111) immersed in a buffer solution, by means of *in situ* electrochemical scanning tunneling microscopy (EC-STM). Real cell membranes consist of a bilayer of phospholipids which continually gather and interact. There are various kinds of phospholipids in the real cell membranes. To understand the action of these molecules, a dynamic molecular-scale method of observation is necessary. Lipkowski [1] first visualized static monolayers of phospholipid on Au(111) by *in situ* EC-STM. Matsunaga *et al.* [2] revealed dynamic, microscopic motion of phospholipid monolayer on alkanethiol-modified Au(111) immersed in a buffer solution. We intended to compose a bilayer of phospholipid on a hydrophilic substrate in order to mimic the real cell membrane more truly. We used a hydrophilically modified Au(111), anticipating that the first lipid monolayer with the hydrophilic head group down to the surface, and the second lipid monolayer with the hydrophobic alkyl chains down, all spontaneously in aqueous buffer solution.

For this purpose, we used 3-mercaptopropionic acid (MPA) self-assembled monolayer (SAM) on Au(111), in which the COOH groups are expected to be exposed out of the surface. We first observed a ($\sqrt{3} \times \sqrt{3}$) type adlattice of MPA SAM by STM. Then the sample was immersed in 50 mM phosphate buffer containing minimal lipid particles of 200 μ M 1-palmitoyl-2-oleoyl-*sn*-glycero-3-phosphocholine (POPC) with or without 50 μ M cholesterol.

We uniquely observed a 2-dimensional adlattice with a parallelogram unit cell of 1.0 nm x 1.9 nm. Along the short segment, bright spots are aligned. The adlattice did not change with or without cholesterol, indicating that it was composed exclusively of pure POPC. The interval of 1.9 nm is apparently shorter than the full length of POPC molecule (≈ 2.5 nm). To interpret the adlattice structure, we considered a model structure composed of tilted POPC, with the head group attached to the MPA SAM. This model involves a strong affinity between the hydrophilic groups.

Although this frozen adlattice does not completely match our target structure of mobile lipid bilayer, we consider we could partly utilize the hydrophobicity/hydrophilicity of the phospholipid molecules to compose a uni-directional membrane. We will further develop this kind of methods by choosing the proper modifier on Au(111), aiming the bilayer structure. By this we expect to go closer to the nanometer-scale reality of cell membranes containing functional proteins.

[1] J. Lipkowski, *Phys. Chem. Chem. Phys.* **12**, 13874 (2010).

[2] S. Matsunaga *et al.*, *Electrochem. Commun.* **9**, 645 (2007).

11:40am **BI+SS+NS-WeM12 Characterization of Polymer/Drug Films as Model for Drug Eluting Coronary Stent Coating Layers**, V. Ciarnelli, M.R. Alexander, M.C. Davies, C.J. Roberts, University of Nottingham, UK

This work describes the characterization of a polymeric based drug eluting stent coating, used in coronary stenting to prevent restenosis [1]. The work examines thin films as models for drug eluting stent coatings. Complementary surface analysis techniques are used to investigate the drug polymer distribution on the surface and throughout the depth of the model films.

The first goal of this project is to establish the feasibility of certain surface analysis techniques in the characterisation of a drug eluting stent coating layer. Secondly, this study will act as a standard reference to determine the ideal operating conditions for characterizing the more complex stent device.

Thin film models were produced varying the substrate materials (silicon or glass), preparation procedures (spin casting or spray coating) and drying methods (oven or warm air). The different drug to polymer ratios used were: 1:3, 1:1 and 3:1 (w:w).

Complementary surface analysis techniques such as atomic force microscopy (AFM), time of flight secondary ion mass spectrometry (ToF-SIMS) and x-ray photoelectron spectroscopy (XPS) were employed for the characterization of the films. Depth profiling has also been performed using XPS and ToF-SIMS.

AFM imaging of the oven dried spun cast films shows domains of drug, characterized by a circular organization with features of 100 - 250 nm in

diameter. These domains are not observed in other samples and appear to be related to phase separation during the drying step.

Surface characterization using XPS shows enrichment of the drug at the surface for all the model films with the exception of the spray coated films at the 1:3 drug-to-polymer weight ratio.

Depth profiling using both ToF-SIMS and XPS confirms that the drug is enriched at the surface, posing significant implications for drug loaded polymer delivery systems.

Complementary surface analysis techniques have proven extremely successful in characterizing the model films. Suitable techniques and their operative conditions have now been established for the characterization of a stent device.

[1] I. Iakovou et al., Incidence, predictors, and outcome of thrombosis after successful implantation of drug-eluting stents. *JAMA*, **293** (2005): p. 2126-2130.

Nanometer-scale Science and Technology

Room: 12 - Session NS+AS+SS+SP-WeM

Nanoscale Catalysis and Surface Chemistry

Moderator: U.D. Schwarz, Yale University

8:20am **NS+AS+SS+SP-WeM2 Preparation and Performance of Solid Rocket Propellant Containing *In Situ*-Synthesized Nanoparticle Catalysts and Fuels**, *D. Reid, R. Draper*, University of Central Florida, *M. Johnson, T. Allen, A. Demko, E. Petersen*, Texas A&M University, *S.S. Seal*, University of Central Florida

Energetic nanocomposites have the potential to substantially increase the performance of rocket propulsion systems, but adoption outside the laboratory has been slow, largely due to manufacturing difficulties, safety challenges, and performance that falls short of theoretical potentials. In this study, we explore some novel synthesis methods to significantly improve performance and alleviate the difficulties of incorporating nanoparticles into energetic materials. Solid rocket propellants containing in-situ synthesized catalytic TiO₂ and energetic aluminum nanoparticles were prepared. These propellants exhibited significant performance improvements over those containing conventionally prepared nanoparticles. The performance gains are attributed to the small particle sizes, high degree of dispersion, and surface property control afforded by the in-situ synthesis methods.

9:00am **NS+AS+SS+SP-WeM4 Synthesis and Catalytic Activity of WS₂ Nanotube Supported Cobalt and Nickel Catalysts Towards Thiophene Hydrodesulfurization**, *M. Komarneni, Z. Yu, A. Chakradhar, U. Burghaus*, North Dakota State University, *Y. Tsvetin, R. Popovitz-Biro, Y. Feldman, R. Tenne*, Weizmann Institute of Science, Israel

Inorganic nanotubes (INT) including WS₂ INT are promising materials for heterogeneous catalysis due to their intriguing properties like enhanced surface area, defects, and confinement effects. The promotion effects of Co and Ni combined with novel nanomaterials such as INT-WS₂ may create the next generation hydrodesulfurization (HDS) catalysts. To verify this, M/INT-WS₂ (M = Co or Ni) catalysts were synthesized and their catalytic activity towards HDS of thiophene was characterized by gas chromatography/ambient pressure catalytic tests and ultra-high vacuum (UHV) thermal desorption spectroscopy (TDS) experiments. Synthesis of M/INT-WS₂ involved two steps: Surface activation of INT-WS₂ by palladium seeding process and electroless plating method to coat nanoparticles of M. The deposited nanoparticles of M formed non-uniform layer on the INT surface. Nanoparticles of size 10-20 nm for Co (*hcp* structure) and 10-20 nm for Ni (*fcc* structure) were coated on INT-WS₂. Next, the catalytic activity of M/INT-WS₂ towards thiophene HDS was characterized using an atmospheric flow reactor. M/INT-WS₂ catalysts exhibited enhanced HDS activity when compared to pristine INT-WS₂ mainly due to the promotion effects of Co and Ni. Hydrogen sulfide and hydrocarbons such as 1,3-butadiene, butane, cis-2-butene, and trans-2-butene were formed as HDS products by both pristine and M/INT-WS₂. Commercial HDS catalysts, CoMo and NiMo from Haldor Topsoe were found to show ~ 4 times higher activity than M/INT-WS₂ synthesized in this study. These results are promising and show that further optimization of the nanofabrication process yields better HDS nanocatalysts. Furthermore, the adsorption kinetics of thiophene on M/INT-WS₂ was studied by TDS at UHV conditions. Thiophene adsorbed on internal, external, and groove sites of the M/INT-WS₂ bundles. Binding energies of thiophene on Ni/INT-WS₂ are ~ 10 kJ/mol smaller than that of pristine INT-WS₂. Thiophene also decomposed on M/WS₂ NT at UHV conditions. In addition, catalytic screening of nanocatalysts such as Au and Co-Ni coated INT-WS₂, pristine MoS₂ nanoparticles with fullerene-like structure (IF), and Re-doped IF-

MoS₂ for HDS was also performed. Overall, M/INT-WS₂ catalysts were the best HDS catalysts among the new nanocatalysts studied. The results also reflected the promotion effects of Co and Ni on the M/INT-WS₂ catalysts for higher thiophene conversion rates.

11:20am **NS+AS+SS+SP-WeM11 Charge Exchange and Molecule/Metal Coupling in Fulvalene Surface Chemistry**, *G. Rojas, B.G. Sumpster*, Oak Ridge National Laboratory, *J.A. Schlueter*, Argonne National Laboratory, *P. Maksymovych*, Oak Ridge National Laboratory

Understanding the epitaxy of organic semiconductors on the surface, and the ensuing processes of charge transfer and band-alignment is vitally important for the deterministic design of energy harvesting and light-emitting devices based on molecular heterojunctions. While most of the attention so far has been directed to pi-conjugated aromatic compounds, little is known about the properties of the fulvalene family in contact with metal surface. Here we will present a spectroscopic study of bis(ethylenedithio)tetrathiafulvalene (ET) on Ag(111) in the sub-monolayer to monolayer coverage. Varying coverages of ET adsorption show the molecules dimerize in parallel, bonding to the Ag surface along the long-axis of the molecule. The dimers remain mobile after adsorption, resulting in the formation of a two-phase surface material: unidimensional loosely stacked nanoclusters and finely packed, two-dimensional domains of interlocked molecules. These structures are an intermediate kinetic state, as the molecules further chemically react with the underlying Ag surface following annealing to temperatures as low as 40 C. It is thought based on these data that the dimers form chemical bonds with a single, shared Ag adatom upon adsorption, as observed for other pi orbital dominated aromatic molecules such as PTEDA. Formation of a reactive layer has significant implications for the orbital alignment at the interface. We have therefore probed the properties of the 2D ordered layer and the reacted layers using a combination of current-distance and image-potential state spectroscopy. The interpretation of these results will be presented in conjunction with the first-principles calculations of the respective structures, and correlated with the induced density of interface states (IDIS) model for orbital alignment at metal-molecule interface.

This research was conducted at the Center for Nanophase Materials Sciences, sponsored at the Oak Ridge National Laboratory by the Division of User Facilities, U.S. Department of Energy.

11:40am **NS+AS+SS+SP-WeM12 Subpicosecond-pulse Photoinduced Chemistry on Nanoscale Palladium Model Catalyst Surfaces**, *A. Bhattacharya*, Brookhaven National Laboratory, *R. Palomino, J.C. Lofaro*, Stony Brook University, *H. Park, M.G. White, N. Camillone*, Brookhaven National Laboratory

To date, time-resolved investigations of surface chemical reaction dynamics have almost exclusively been conducted on metal single crystals. However, current and proposed catalysts and photocatalysts generally consist of nanometer-scale metal particles supported on metal oxides. To conduct time-resolved investigations of the surface chemical dynamics of such systems we have synthesized and characterized arrays of palladium nanoparticles (approximately 4 to 10 nm in diameter) supported on clean rutile TiO₂(110). We will present our synthetic approach and the results of chemical and morphological characterization and thermal chemistry experiments on these arrays. We will also discuss the results of subpicosecond-pulse photoinduced desorption of molecular oxygen and carbon monoxide, as well as the photoinduced bimolecular reaction between adsorbed atomic oxygen and carbon monoxide. Comparisons to the same reactions on single crystal Pd(111) surfaces will be made, and the unique features of the chemistry and dynamics at the nanoscale highlighted.

Scanning Probe Microscopy Focus Topic

Room: 16 - Session

SP+AS+BI+ET+MI+NM+NS+SS+TF-WeM

Probe-Sample Interactions, Nano-Manipulation and Fabrication

Moderator: S. Allen, The University of Nottingham, UK,
A.-P. Li, Oak Ridge National Laboratory

8:20am **SP+AS+BI+ET+MI+NM+NS+SS+TF-WeM2 Controlled Coupling of Silicon Atomic Quantum Dots at Room Temperature: A Basis for Atomic Electronics?**, R.A. Wolkow, University of Alberta and The National Institute for Nanotechnology, Canada, J. Pitters, The National Institute for Nanotechnology, Canada, G. DiLabio, M. Taucer, P. Piva, L. Livadaru, University of Alberta and The National Institute for Nanotechnology, Canada **INVITED**

Quantum dots are small entities, typically consisting of just a few thousands atoms, that in some ways act like a single atom. The constituent atoms in a dot coalesce their electronic properties to exhibit fairly simple and potentially very useful properties. It turns out that collectives of dots exhibit joint electronic properties of yet more interest. Unfortunately, though extremely small, the finite size of typical quantum dots puts a limit on how close multiple dots can be placed, and that in turn limits how strong the coupling between dots can be. Because inter-dot coupling is weak, properties of interest are only manifest at very low temperatures (milliKelvin). In this work the ultimate small quantum dot is described – we replace an “artificial atom” with a true atom - with great benefit.

It is demonstrated that the zero-dimensional character of the silicon atom dangling bond (DB) state allows controlled formation and occupation of a new form of quantum dot assemblies - at room temperature. Coulomb repulsion causes DBs separated by less than ~2 nm to experience reduced localized charge. The unoccupied states so created allow a previously unobserved electron tunnel-coupling of DBs, evidenced by a pronounced change in the time-averaged view recorded by scanning tunneling microscopy. It is shown that fabrication geometry determines net electron occupation and tunnel-coupling strength within multi-DB ensembles and moreover that electrostatic separation of degenerate states allows controlled electron occupation within an ensemble.

Some speculation on the viability of a new “atomic electronics” based upon these results will be offered.

9:00am **SP+AS+BI+ET+MI+NM+NS+SS+TF-WeM4 Atomic Forces and Energy Dissipation of a Bi-Stable Molecular Junction**, C. Lotze, Freie Universität Berlin, Germany, M. Corso, K.J. Franke, F.V. Oppen, J.I. Pascual, Freie Universität Berlin, Germany

Tuning Fork based dynamic STM/AFM is a well established method combining the advantages of scanning tunneling and dynamic force microscopy. Using tuning forks with high stiffness, stable measurements with small amplitudes, below 1 Å can be performed. In this way, conductance and frequency shift measurements of molecular junction can be obtained simultaneously [1] with intramolecular resolution [2].

One of the most intriguing aspects of molecular junctions relates to the effect of structural bi-stabilities to the properties of the junction. These lead, for example, to conductance fluctuations, telegraph noise and the possibility to switch the electrical transport through the junction.

In this presentation, we characterize a model bi-stable molecular system using dynamic force spectroscopy. The effect of current-induced stochastic fluctuations of conductance are correlated with fluctuations in force. In our experiment we identified the last from both, frequency shifts and energy dissipation measurements, picturing a regime in which electrical transport and mechanical motion are coupled.

[1] N. Fournier *et. al*, PhysRevB 84, 035435 (2011),

[2] L. Gross *et. al*, Science 324, 1428 (2009)

9:20am **SP+AS+BI+ET+MI+NM+NS+SS+TF-WeM5 Acetylene on Cu(111): Imaging a Molecular Pattern with a Constantly Rearranging Tip**, Y. Zhu, J. Wyrick, K.D. Cohen, K. Magnone, C. Holzke, D. Salib, Q. Ma, D.Z. Sun, L. Bartels, University of California Riverside

Abstract: Using variable temperature STM and DFT simulation, we identify the phases of acetylene adsorbed on the Cu(111) surface. Depending on the coverage, a diffraction-derived surface pattern of acetylene on Cu(111) is validated by STM. The modification of the STM image transfer function

through the adsorption of an acetylene molecule onto the tip apex is taken into account. In this case, the images of acetylene patterns on Cu(111) also include direct evidence of **the rotational orientation and dynamics of the acetylene species attached to the tip apex**. DFT modeling of acetylene/Cu(111) reveals that the molecular orientation and separation is governed by a balance of repulsive interactions associated with stress induced in the top surface layer and attractive interactions mediated by the electronic structure of the substrate. Computationally modeling of the substrate with 3 layers obtains the periodicity of the intermolecular interaction that provides a theoretical underpinning for the experimentally observed molecular arrangement.

9:40am **SP+AS+BI+ET+MI+NM+NS+SS+TF-WeM6 Atomic Scale Imaging and Electronic Structure of Trimethylaluminum Deposition on III-V Semiconductor (110) Surfaces**, T.J. Kent*, M. Edmonds, E. Chagarov, A.C. Kummel, University of California San Diego

Silicon based metal oxide semiconductor field effect transistors (Si-MOSFETs) are quickly approaching their theoretical performance limits, as a result many semiconductors are being explored as an alternative channel material for use in MOSFETs. III-V semiconductors are an appealing alternative to Si because of their higher electron mobilities. The limiting factor in III-V based MOSFET performance is defect states which prevent effective modulation of the Fermi level. The InGaAs (001) As-rich (2x4) surface contains two types of unit cells: ideal unit cells with double As-dimers and defect unit cells with single As-Dimers. The missing As-dimer unit cells, which comprise ~50% of the surface, are believed to cause electronic defect states at the semiconductor-oxide interface, specifically at the conduction band edge of the semiconductor. *In-situ* scanning tunneling microscopy and spectroscopy (STM/STS) and density function theory (DFT) modeling show that TMA readily passivates the As-As dimers in the ideal unit cell but the missing InGaAs(001)-2x4 may not be fully passivated by TMA. To improve the electronic structure of the interface, the sidewalls of the finFETs on InGaAs(001) can be fabricated along the (110) direction. The (110) surface contains only buckled III-V heterodimers in which the lower group III atom is sp² hybridized with an empty dangling bond and the upper group V atom is sp³ hybridized with a full dangling bond. This results in an electrically unpinned surface.

To investigate the benefits of using a (110) surface as a channel material, the atomic and electronic structure of the ALD precursor trimethylaluminum (TMA) monolayer deposited on III-V (110) surfaces has been studied using *in-situ* STM and STS. Both GaAs and InGaAs samples were studied. GaAs wafers were obtained from Wafertech with a Si doping concentration of 4x10¹⁸/cm³. The (001) samples were cleaved *in-situ* to expose the (110) surface. Samples were transferred to the STM chamber (base pressure 1x10⁻¹¹ torr) where the atomic bonding structure of the precursor monolayer unit cell was determined. STS, which probes the local density of states (LDOS), was used to determine Fermi level pinning. A model of TMA chemisorption was developed in which TMA chemisorbs between adjacent As atoms on the surface, giving a highly ordered monolayer with a high nucleation density which could allow for aggressive effective oxide thickness (EOT) scaling.

10:40am **SP+AS+BI+ET+MI+NM+NS+SS+TF-WeM9 A New Experimental Method to Determine the Torsional Spring Constants of Microcantilevers**, G. Haehner, J.D. Parkin, University of St Andrews, UK
Cantilever based technologies have seen an ever increasing level of interest since the atomic force microscope (AFM) was introduced more than two decades ago. Recent developments employ microcantilevers as stand-alone sensors by exploiting the dependence of their oscillating properties on external parameters such as adsorbed mass [1], or the density and the viscosity of a liquid environment [2,3]. They are also a key part in many microelectromechanical systems (MEMS) [4]. In order to quantify measurements performed with microcantilevers their stiffness or spring constants have to be known. Following calibration of the spring constants a change in oscillation behavior can be quantitatively related to physical parameters that are probed. The torsional modes of oscillation have attracted significant attention due to their high sensitivity towards lateral and friction forces, and recent developments in torsional-tapping AFM technology [5]. However, the methods available to determine the torsional spring constants experimentally are in general not simple, not very reliable, or risk damage to the cantilever [6].

We demonstrate a new method to determine the spring constants of the torsional modes of microcantilevers experimentally with high accuracy and precision. The method is fast, non-destructive and non-invasive. It is based on measuring the change in the resonance frequencies of the torsional

* ASSD Student Award Finalist

modes as a function of the fluid flow escaping from a microchannel. Results for rectangular cantilevers will be presented and compared to results obtained with other methods [7].

- [1] J. D. Parkin and G. Hähner, Rev. Sci. Instrum. **82** (3), 035108 (2011).
- [2] N. McLoughlin, S. L. Lee, and G. Hähner, Appl. Phys. Lett. **89** (18), 184106 (2006).
- [3] N. McLoughlin, S. L. Lee, and G. Hähner, Lab Chip, 1057 (2007).
- [4] S. Beeby, G. Ensell, N. Kraft, and N. White, *MEMS Mechanical Sensors*. (Artech House London, 2004).
- [5] O. Sahin and N. Erina, Nanotechnology **19** (44), 445717 (2008).
- [6] M. Munz, Journal of Physics D-Applied Physics **43** (6), 063001 (2010).
- [7] C. P. Green, H. Lioe, J. P. Cleveland, R. Proksch, P. Mulvaney, and J. E. Sader, Rev. Sci. Instrum. **75** (6), 1988 (2004).

11:00am **SP+AS+BI+ET+MI+NM+NS+SS+TF-WeM10 A Torsional Device for Easy, Accurate and Traceable Force Calibration of AFM Cantilevers, J.F. Portoles, P.J. Cumpson, Newcastle University, UK**

Accurate measurement of biologically-relevant forces in the range of pN to μ N is an important problem in nanoscience.

A number of force probe techniques have been applied in recent years. The most popular is the Atomic Force Microscope (AFM). Accuracy of force measurement relies on calibration of the probe stiffness which has led to the development of many calibration methods[1], particularly for AFM microcantilevers. However these methods typically exhibit uncertainties of at best 15% to 20% and are often very time consuming. Dependency on material properties and cantilever geometry further complicate their application and take extra operator time. In contrast, one rapid and straightforward method involves the use of reference cantilevers (the "cantilever-on-cantilever" method) or MEMS reference devices. This approach requires that a calibrated reference device is available, but it has been shown to be effective in providing measurement traceability[2].

The main remaining difficulty of this approach for typical users is the positional uncertainty of the tip on the reference device, which can introduce calibration uncertainties of up to around 6%. Here we present a new reference device based on a torsional spring of relatively large dimensions compared to the typical AFM cantilever and demonstrate how it is calibrated. This method has the potential to calibrate the reference device traceably[3] to the SI with a 1% accuracy by applying techniques typically used for the characterisation of micromechanical devices. The large dimensions of the device reduce the positional uncertainty below 1% and simultaneously allow the use of the device as an effective reference array with different reference stiffnesses at different positions ranging from 0.090 N/m to 4.5 N/m

- [1] P J Cumpson, C A Clifford, J F Portolés, J E Johnstone, M Munz Cantilever Spring-Constant Calibration in Atomic Force Microscopy, pp289-314 in Volume VIII of Applied Scanning Probe Methods, Ed. B Bhushan and H Fuchs (Springer, New York, 2009)
- [2] P J Cumpson PJ, J Hedley, Nanotechnology 14 (2003) pp. 1279-1288
- [3] J F Portolés, P J Cumpson, J Hedley, S Allen, P M Williams & S J B Tendler, Journal of Experimental Nanoscience 1 (2006) pp51-62.

11:20am **SP+AS+BI+ET+MI+NM+NS+SS+TF-WeM11 Nanoscale Surface Assembly by Single-Molecule Cut-and-Paste, H.E. Gaub, Ludwig-Maximilians Universität, Germany** **INVITED**

Bottom up assembly of functional molecular ensembles with novel properties emerging from composition and arrangement of its constituents is a prime goal of nanotechnology. With the development of Single-Molecule Cut-and-Paste (SMC&P) we provided a platform technology for the assembly of biomolecules at surfaces. It combines the Å-positioning precision of the AFM with the selectivity of DNA hybridization to pick individual molecules from a depot chip and allows to arrange them on a construction site one by one. An overview on different applications of this technology will be given in this talk. One recent example demonstrates the functional of receptors for small molecules. By SMC&P we assembled binding sites for malachite green in a molecule-by-molecule assembly process from the two halves of a split aptamer. We show that only a perfectly joined binding site immobilizes the fluorophore and enhances the fluorescence quantum yield by several orders of magnitude. To corroborate the robustness of this approach we produced a micron-sized structure consisting of more than 500 reconstituted binding sites. To the best of our knowledge this is the first demonstration of a one by one bottom up functional bio-molecular assembly. Figure included in supplemental document. S. Kufer, Puchner E. M., Gump H., Liedel T. & H. E. Gaub *Science* (2008), Vol 319, p 594-S. Kufer, Strackharn, M., Stahl S.W., Gump H., Puchner E. M. & H. E. Gaub *Nature Nanotechnology* (2009), Vol 4, p 45-M. Erdmann, R. David. A.N. Fornof, and H. E. Gaub, *Nature*

Chemistry (2010), Vol 2, p 755-M. Strackharn, S. Stahl, E. Puchner & H.E. Gaub, *Nanoletters* (2012) in press

Thin Film

Room: 11 - Session TF+SE+NS-WeM

Glancing Angle Deposition (GLAD)

Moderator: T. Karabacak, University of Arkansas at Little Rock

8:00am **TF+SE+NS-WeM1 Tunable-Refractive-Index Materials – A New Class of Optical Thin-Film Materials with Applications in Solid-State Lighting and Solar Photovoltaics, E.F. Schubert, Rensselaer Polytechnic Institute** **INVITED**

Among the properties of optical materials, the refractive index is a most fundamental one. It determines many optical characteristics such as Fresnel reflection, Bragg reflection, Snell refraction, diffraction, and the phase and group velocity of light. The refractive index was introduced centuries ago by Isaac Newton who correlated the refractive index with the relative strength of refraction at the liquid-to-air interface. He realized that the degree of refraction is proportional to the mass density of the liquid, and therefore called the new optical quantity the "optical density." Nowadays, this key quantity is known as the "refractive index."

Among transparent dense materials, MgF₂ has the lowest refractive index: $n = 1.39$. Air and other gases have a refractive index very close to 1.0 but these materials are not viable for thin-film optoelectronic applications. Therefore, there are no dense materials with a refractive index in the range $1.0 < n < 1.39$. That is, this range has remained unavailable and unexplored.

Over the last few years, a new class of materials, tunable-refractive-index materials, has been developed. Optical thin-film materials, with a refractive index as low as 1.05, have been demonstrated. The tunable-index materials are based on nano-porous materials, such as, for example, nano-porous SiO₂, nano-porous indium-tin oxide (ITO), and nano-porous TiO₂. The porosity can be precisely controlled by using oblique-angle deposition, a technique in which the substrate is at non-normal angle with respect to the deposition source. Whereas dense films form for normal-incidence deposition, porous films with a self-organizing nano-structure form for oblique-angle deposition.

In this presentation, we will present examples of novel structures and devices that exploit the newly gained controllability of the refractive index. Devices to be discussed include distributed Bragg reflectors, light-emitting diodes, and solar cells, along with the performance enhancements enabled by the control of the refractive-index.

8:40am **TF+SE+NS-WeM3 Nanostructured Homogenous CdSe/TiO₂ Composite Visible Light Photoanodes Fabricated by Oblique Angle Codeposition, G.K. Larsen, University of Georgia, B.C. Fitzmorris, University of California Santa Cruz, C. Longo, University of Campinas, Brazil, J.Z. Zhang, University of California Santa Cruz, Y.-P. Zhao, University of Georgia**

A unique fabrication method, oblique angle codeposition, is used to deposit well-aligned nanorod arrays and thick films of homogeneously mixed CdSe/TiO₂ composites. The structural, optical, and photoelectrochemical properties of the films are investigated using a variety of experimental techniques. Ultrafast exciton dynamics are studied using femtosecond transient absorption (TA) spectroscopy. The CdSe/TiO₂ composites are compared with pure CdSe and TiO₂ films in order to determine their utility for photoelectrochemical (PEC) applications and to understand the mechanisms underlying the observed behaviors. The morphology of the deposited nanorods changes with film composition due to atomic collisions occurring in the vapor column, which can be modeled using a simplified Keller-Simmons expression. Furthermore, the two phase evaporation process of CdSe creates three different cluster types within the TiO₂ film structures: isolated Se, Se-deficient CdSe, and Se-rich CdSe. The prevalence of each cluster type is dependent on predicted film composition, and each is affected differently by open-air annealing. Isolated Se can be incorporated into the TiO₂ lattice, resulting in low energy rutile phase. Se-deficient CdSe clusters crystallize preferentially into cubic CdSe and are easily oxidized into CdO, while Se-rich CdSe clusters crystallize into hexagonal CdSe and are more stable. Furthermore, each of these cluster types interacts differently with the surrounding TiO₂ matrix, resulting in diverse optical and PEC behaviors. Interestingly, the stoichiometry of the CdSe domains is more important than overall CdSe content within the film in determining the structural, optical, and PEC properties of the films. The composite nanorod structure is a more efficient photoanode under visible light illumination than both the pure CdSe and TiO₂ nanorod array films.

The higher efficiency of the composite films is attributed to efficient charge transfer and separation in the homogeneously mixed composite. This is confirmed by the extremely high electron injection rate from CdSe into TiO₂ observed in the ultrafast TA studies.

9:00am TF+SE+NS-WeM4 Control the Biaxial Texture of Vertically Aligned Nanostructures using Oblique Angle Sputtering Deposition with Substrate Flipping Rotation, G.-C. Wang, L. Chen, T.-M. Lu, Rensselaer Polytechnic Institute

It is known that oblique angle deposition can be used to grow 3D nanostructures with a variety of morphology such as nanorods and nanospirals. For a selective set of materials, the technique can also produce a preferred crystal orientation, particularly a biaxial texture where the texture selection occurs in both the out-of-plane and in-plane directions. Most frequently biaxial texture created using the oblique angle deposition is in the form of slanted nanorods. It is desirable to produce a biaxial structure in the form of vertically aligned nanostructures which may be useful as a buffer layer to grow functional films on top of it. In this talk we will discuss several strategies to grow vertically aligned nanostructures including nanorods with a biaxial texture by dynamically varying the incident flux angle with respect to the surface normal during deposition. A particularly robust technique to achieve this goal is a flipping rotation scheme where the substrate is rotated continuously at a fixed speed around an axis lying within and parallel to the substrate [1]. This is very different from the conventional substrate rotation mode where the rotational axis is perpendicular to the substrate surface. In the flipping rotational mode the incident flux is perpendicular to the rotational axis, and the incident flux angle changes continuously. Mo vertical nanorod films, grown on amorphous substrates under three orders of magnitude different rotation speeds, different flipping directions, and different ending deposition angles, were characterized using scanning electron microscopy. For texture characterization of these Mo nanostructures we used our newly developed reflection high energy electron diffraction surface pole figure technique [2]. Despite very different morphologies, such as 'C'-shaped, 'S'-shaped, and vertically aligned nanorods grown by the flipping rotation, the same (110)[1-10] biaxial texture with an average out-of-plane dispersion of ~15° was observed. In contrast, we showed that only a fiber-textured Mo film was obtained by using the conventional rotation mode with a fixed incident flux angle. These biaxial Mo vertical nanorod films have potential applications as buffer layers to grow near-single crystal semiconductor films through nanoheteroepitaxy. These films may find important applications in energy conversion and light emitting devices.

Work was supported by the NSF DMR-1104786.

[1] L. Chen, T.-M. Lu, and G.-C. Wang, *Nanotechnology* **22**, 505701 (2011).

[2] F. Tang, T. Parker, G.-C. Wang, and T.-M. Lu, *J. of Physics D: Applied Physics* **40**, R427 (2007).

9:20am TF+SE+NS-WeM5 Flux Engineering to Control In-Plane Crystal and Morphological Orientation, J.M. LaForge, G. Ingram, M.T. Taschuk, M.J. Brett, University of Alberta, Canada

Texture evolution during oblique angle deposition (OAD) and glancing angle deposition (GLAD) is of fundamental interest and important applications. As the distribution of size, shape and orientation of crystal grains impacts film electrical, optical, magnetic and mechanical properties control over texture evolution is important to optimizing performance. Morphology and crystal texture of OAD or GLAD nanostructured films is influenced by the orientation of the substrate relative to the collimated vapor flux, namely angle of incidence and the azimuthal angle, during deposition. Previous work has demonstrated control over the out-of-plane orientation through changes in the angle of incidence or azimuthal motion of substrate (e.g. stationary or continuous rotation).^{[1][2]} However, work on the development of in-plane orientation has focused on material kinetic effects, such as deposition temperature, residual gas concentration, and deposition rate rather than substrate motion.^{[3][4]}

We have deposited iron nanocolumns that have a tetrahedral apex and an out-of-plane texture (fiber texture) at a deposition angle of 88° under continuous substrate rotation. It is possible to induce in-plane crystal texture and morphological orientation by engineering the azimuthal distribution of the flux to match the symmetry of the nanocolumns (i.e. 3-fold rotational symmetry). Thus, biaxially textured nanocolumns with an in-plane alignment that is predominantly controlled by substrate motions (or flux configuration) can be created using this technique. In principle, this method could be generalized to nanocolumns with 4-fold and 6-fold azimuthal symmetry and therefore provides a mechanism to form biaxially textured, nanostructured films from a variety of materials deposited on amorphous or crystalline substrates.

[1] P. Morrow, F. Tang, T. Karabacak, P.-I. Wang, D.-X. Ye, G.-C. Wang, T.-M.T.-M. Lu, *Journal of Vacuum Science & Technology A: Vacuum, Surfaces, and Films* **2006**, *24*, 235.

[2] R. Krishnan, T. Parker, S. Lee, T.-M. Lu, *Nanotechnology* **2009**, *20*, 465609.

[3] K. Okamoto, T. Hashimoto, K. Hara, M. Kamiya, H. Fujiwara, *Thin Solid Films* **1985**, *129*, 299-307.

[4] K. Okamoto, T. Hashimoto, K. Hara, M. Kamiya, H. Fujiwara, *Thin Solid Films* **1987**, *147*, 299-311.

9:40am TF+SE+NS-WeM6 Bi-axial Texture Development in AlN Layers during Off-axis Sputter Deposition, R. Deng, D. Gall, Rensselaer Polytechnic Institute

Polycrystalline AlN layers were deposited by pulsed-DC reactive magnetron sputtering from a variable deposition angle $\alpha = 0-84^\circ$ in 5 mTorr pure N₂ at room temperature. X-ray diffraction pole figure analyses show that layers deposited from a normal angle ($\alpha = 0^\circ$) exhibit fiber texture, with a random in-plane grain orientation and the c-axis tilted by $42 \pm 2^\circ$ off the substrate normal, yielding wurtzite AlN grains with the {10-12} plane approximately parallel ($\pm 2^\circ$) to the substrate surface. However, as α is increased to 45° , two preferred in-plane grain orientations emerge, with populations I and II having the c-axis tilted towards and away from the deposition flux, by $53 \pm 2^\circ$ and $47 \pm 1^\circ$ off the substrate normal, respectively. Increasing α further to 65 and 84° , results in the development of a single population II with a $43 \pm 1^\circ$ tilt. This developing bi-axial texture is attributed to a competitive growth mode under conditions where the adatom mobility is sufficient to cause inter-grain mass transport but insufficient for the thermodynamically favored low energy {0001} planes to align parallel to the layer surface. Consequently, AlN nuclei are initially randomly oriented and form a kinetically determined crystal habit exposing {0001} and {11-20} facets. The expected direction of its highest growth rate is $49 \pm 5^\circ$ tilted relative to the c-axis, in good agreement with the $42-53^\circ$ measured tilt. The in-plane preferred orientation for $\alpha > 0^\circ$ is well explained by the orientation dependence in the cross-section of the asymmetric pyramidal nuclei to capture off-normal directional diffusion flux. The observed tilt is ideal for shear mode electromechanical coupling, which is maximized at 48° .

10:40am TF+SE+NS-WeM9 Engineered Indium Tin Oxide Nanowhiskers via Vapour Liquid Solid Glancing Angle Deposition, A.L. Beaudry, R.T. Tucker, J.M. LaForge, M.T. Taschuk, University of Alberta, Canada, M.J. Brett, University of Alberta, Canada and The National Institute for Nanotechnology

The vapour liquid solid (VLS) nanowire growth technique has been recently modified with spatially modulated vapour flux through glancing angle deposition (GLAD).^{1,2} Using this new technique, named VLS-GLAD, our group has demonstrated improved morphological control over indium tin oxide (ITO) nanowhiskers.¹ Single crystal ITO nanowhiskers are grown via a self-catalyzed VLS growth mechanism, resulting in branched structures.³ VLS-GLAD exhibits improved control over the diameter, spacing, branching density and branching orientation of ITO nanowhiskers. As the angle of deposition is increased to glancing angles, there is a transition from a dense interconnected network to a porous film of individual ITO nanowhisker structures. In addition, branching was found to increase significantly with increasing deposition angle. This result is attributed to an increase in the proportion of vapour flux incident on the sides of the structures, resulting in an increase in self-catalytic VLS growth of branches. This effect has been used to engineer branch morphology and orientation. Vapour flux rate modulation at glancing angles results in further in-situ control over ITO nanowhisker features. HRTEM imaging revealed a continuation of crystal planes from the trunk into the branch. XRD results indicated single crystal cubic bixbyite structures with a <400> growth direction. Haacke's figure of merit was used to assess the suitability of ITO nanowhisker films as transparent electrodes.⁴

¹ Beaudry, A.L. et al. *Nanotechnology* **23**, 105608 (2012).

² Alagoz, A.S. and Karabacak, T. *MRS Proceedings* **1350**, (2011).

³ Castañeda, S.I. et al. *Journal of Applied Physics* **83**, 1995 (1998).

⁴ Haacke, G. *Journal of Applied Physics* **47**, 4086 (1976).

11:00am TF+SE+NS-WeM10 CoPt Nanopillars for Advanced Media by Glancing Angle Deposition, H. Su, A. Natarajarathinam, S. Gupta, The University of Alabama

We report for the first time the fabrication of CoPt+AlN "granular nanorods" utilizing glancing angle deposition (GLAD) on a multi-gun, planetary sputtering system. Initially, AlN was deposited by reactive sputtering from an Al target while CoPt multilayers were simultaneously sputtered using cobalt and platinum targets. Various ratios of Co and Pt, ranging from Co80Pt20 to Co50Pt50, were used to deposit CoPt-AlN

nanorods with different AlN volume percentages. X-ray diffraction (XRD), electron dispersive X-rays (EDX), scanning electron microscopy (SEM), and alternating gradient magnetometry (AGM) were employed to characterize the structural and magnetic properties, respectively. SEM micrographs indicated that the nanorods were approximately 16 nm in diameter, the angle between the substrate plane and the growth direction was about 78 degrees, while the lengths of the nanorods ranged from 30 to 50 nm, depending on deposition time. The angles between the substrate plane and incident flux ranged from 47 degrees to 82 degrees as the substrate presented itself at different angles to the target during the planetary deposition. The composition of CoPt-AlN has been studied by EDX for different ratios of AlN. M-H loops showed that the planetary GLAD sample had twice the coercivity of the flat sample.

We have also compared stationary vs. planetary GLAD, and sequential deposition of AlN/CoPt multilayers with true co-deposition, using an annular CoPt target with an Al insert. Simulations of the deposition have been carried out to gain a better understanding of where the AlN segregates with respect to the CoPt grains. These preliminary results indicate a novel and promising approach to nanopatterned graded media that is the subject of intense research in the data storage industry.

11:20am **TF+SE+NS-WeM11 Through-post Electrical Characterization of GLAD Thin Films**, *A. Lalany, R.T. Tucker, M.T. Taschuk*, University of Alberta, Canada, *M.D. Fleischauer*, University of Alberta and The National Institute for Nanotechnology, Canada, *M.J. Brett*, University of Alberta, Canada

Glancing Angle Deposition (GLAD) [1] thin films are increasingly used in optoelectronic applications that benefit from their unique optical properties or ultra-high surface area. GLAD produces porous nanostructured thin films which have found applications as high surface area electrodes. Potential performance benefits of these nanostructured thin-films for optoelectronic devices include, but are not limited to, increased charge extraction [2]. Suitable electrical conductivity along the length of GLAD structures (normal to substrate plane) is necessary to exploit a GLAD film's high surface area for electronic devices. However, optimization of GLAD films for these devices has proven difficult without direct measurements of post resistivity.

In-plane resistivity measurements of metals and conductive oxide GLAD films have been performed [3-5], showing increasing in-plane resistivity with increasing oblique deposition angle (due to decreased film density resulting in fewer conductive pathways). Electrical anisotropy has also been observed, with differing in-plane resistivity for different nanocolumn orientations [3-5]. Through post conductivity measurements present additional challenges - it has been shown that as crystallite grain size approaches the range of bulk electron mean free path, column-boundary scattering effects begin to dominate standard bulk-scattering mechanisms [6]. As such, the extensive boundaries present in GLAD structures can result in complex electrical behavior. While several attempts have been made to access through-post electrical properties, results have been limited to relative measures or are extremely low yield processes [7, 8].

We require a measurement technique that is both time and cost effective, statistically robust, and has high yield. This has been achieved with a Kelvin Cross-Bridge Resistor architecture specifically designed to measure through-post resistivity. Our devices can measure resistivities between $100 \mu\Omega \text{ cm} < \rho < 11 \text{ G}\Omega \text{ cm}$, and we have successfully measured through-post conductivities for Indium-tin-oxide (ITO) and Cr GLAD films. Here, we will present device fabrication, validation and current experimental results.

- [1] M.M. Hawkeye et al., *J. Vac. Sci. Technol. A* 25 (2007) 1317.
- [2] D.A. Rider et al., *Nanotech.* 22 (2007) 0857060.
- [3] J. Lintymer et al., *Surf. & Coat. Tech.* 174-175 (2003) 316.
- [4] K.D. Harris et al., *Adv. Funct. Mater.* 18 (2008) 2147.
- [5] D. Vick et al., *J. Vac. Sci. Technol. A* 24 (2006) 156.
- [6] A. Besnard et al., *J. Phys. D: Appl. Phys.* 44 (2001) 215301.
- [7] M.F. Cansizoglu et al., *ACS Nano.* 4 (2010) 733.
- [8] S.P. Chiu et al., *Nanotech.* 20 (2009) 105203.

11:40am **TF+SE+NS-WeM12 Direct Label-Free Detection of microRNA Using a Multi-well SERS Chip Fabricated By Oblique Angle Deposition**, *J.L. Abell*, University of Georgia, *J.M. Garren*, Georgia Health Science University, *J.D. Driskell*, Illinois State University, *R.A. Tripp*, *Y.-P. Zhao*, University of Georgia

Direct label-free nucleic acid detection is a desirable yet challenging task. The current mainstay detection and screening technologies, namely polymerase chain reaction (PCR) and DNA microarrays (i.e. DNA chips), rely heavily upon the use of extrinsic reporter molecules to detect the

hybridization of a probe sequence to a target sequence. Removing the need for external labels reduces the cost and complexity of DNA detection assays. This, however, requires a sensing platform capable of highly sensitive, specific, direct chemical analysis. Surface-enhanced Raman spectroscopy (SERS) is an analytical technique capable of detecting highly resolved chemical signatures with superior sensitivity, and can be used to determine the relative quantities of a compound adsorbed on a nanostructured metal surface. The challenge for SERS detection is to produce a large area, uniform and highly sensitive substrate. Here, we report the use of Ag nanorod (AgNR) SERS substrates fabricated by oblique angle deposition (OAD) for microRNA (miRNA) detection. With such a large area (wafer size) and uniform response (signal intensity variation $\leq 10\%$) of the AgNR substrates, we have developed a simple molding technique to pattern the substrates into multi-well arrays. We demonstrate a 40-well 1" x 3" glass slide allowing for parallel screening of multiple specimens with uniform response. This multiwell substrate has been used in conjunction with a linear least squares (LS) analysis method by assuming that the SERS spectrum of miRNA is a convolution of the individual signals of each of the four A, C, G, and T components, where the contribution of each source signal to the total DNA signal is weighted by the relative quantities of A, C, G, and T present within the sequence. Experimentally we have demonstrated this method for detection and differentiation of four different DNA sequences. In addition, we show for the first time the subtle spectral changes observed after label-free hybridization can be quantified with LS to confirm the capture of the target sequence. This study reveals that the use of OAD SERS substrate could be a potential technique to replace to current microarray technique for DNA/RNA detection.

Wednesday Afternoon, October 31, 2012

Applied Surface Science

Room: 20 - Session AS+NS+SS+TF-WeA

3D Imaging & Nanochemical Analysis - Part 2 (2:00-3:20 pm)/ Advanced Data

Analysis and Instrument Control (4:00-6:00 pm)

Moderator: V.S. Smentkowski, General Electric Global Research Center, M.R. Linford, Brigham Young University, S.J. Pachuta, 3M Company

2:00pm AS+NS+SS+TF-WeA1 From Atomic Scale to Materials Behavior: Using Atom-Probe Tomography to Understand the Behavior of Alloys and Ceramics, E.A. Marquis, University of Michigan INVITED

The ability to improve the performance of functional materials is driven by how well microstructure can be understood and controlled. The three-dimensional distribution of solutes, dopants or impurities in particular, in relation to structural features determines such properties as fracture toughness, strength, ductility, as well as electrical and magnetic response. After a brief introduction to atom-probe tomography, I will illustrate how high resolution characterization approaches can be used systematically to understand the atomic scale processes controlling materials microstructures and their evolution, focusing on alloys and ceramic systems. Several topics will be presented: precipitation and coarsening behavior of Al-based alloys, grain boundary chemistry and role of impurities during irradiation in ferritic steels which may play an important role in fracture and corrosion resistance, the development of oxide-dispersion strengthened steels for structural applications in future nuclear reactors and the role of minor elements in controlling the oxidation behavior of Ni-base alloys for high temperature power generation applications.

2:40pm AS+NS+SS+TF-WeA3 Three Dimensional Atomic Scale Characterization of Binary and Complex Oxides using Atom Probe Tomography, A. Devaraj, R. Colby, D.E. Perea, S. Thevuthasan, EMSL, Pacific Northwest National Laboratory

The development of three dimensional, high spatial and mass resolution characterization techniques is important for several materials used in applications ranging from catalysis, sensors to optoelectronics. Laser assisted atom probe tomography (APT) technique offers such an opportunity to perform atomic scale three dimensional analysis of materials including metals, semiconductors and dielectrics, with subnanometer spatial resolution and sub-ppm level mass resolution. The Cameca LEAP 4000XHR Atom Probe equipped with 355nm UV pulsed laser is used to analyze technologically important binary bulk oxides like MgO, Al₂O₃, TiO₂ and CeO₂. A strong correlation between applied UV laser energy and measured stoichiometry was observed for all these binary oxides. Using those results the importance of laser energy optimization on obtaining accurate stoichiometric composition analysis for oxides will be highlighted. Extension of such laser parametric investigation to complex oxides including SrTiO₃, LaCrO₃ and LaSrMnO₃ will also be presented. In addition the impact of laser pulsing on atomic scale structure of the oxide APT sample surface was studied by a direct cross correlation with aberration corrected TEM. The information on the atomic scale structure of the field evaporated oxide APT samples will be utilized to postulate the laser-oxide material interaction occurring during APT analysis of such oxides leading to the dependency of applied laser energy on measured stoichiometry.

3:00pm AS+NS+SS+TF-WeA4 Atom Probe Tomography of Complex Heterogeneous Low Dimensional Materials, S. Thevuthasan, A. Devaraj, R. Colby, D.E. Perea, V. Subramanian, V. Shutthanandan, Pacific Northwest National Laboratory

EMSL, a national scientific user facility of the DOE, is developing a comprehensive chemical imaging capability combining atom probe tomography with high resolution (scanning) transmission electron microscopy(HR(S)TEM) and high resolution Rutherford back scattering spectrometry (HRRBS) to provide solutions to problems pertaining to energy and environmental applications. We will emphasize on a chemical imaging effort aimed at atomically-resolved composition and structural analysis of low dimensional materials such as nanowires and embedded metal nanoparticles highlighting the benefits and challenges for APT. A unique benefit of APT is the ability to characterize the ppm level concentration and distribution of dopants across semiconducting nanowire heterojunctions. The preferential incorporation of dopants at specific atomic facets at the heterojunction interface in Si-Ge nanowires can only be characterized by using APT. Another important class of low dimensional

materials includes embedded metal nanoparticles in oxides with applications in catalysis, sensors and optoelectronic applications. In order to extent APT analysis capability to such materials a cross correlative approach of combining APT with aberration corrected HRSTEM is employed. The results from the model system of ion beam synthesized Au and Ag nanoparticles embedded in MgO will be presented.

4:00pm AS+NS+SS+TF-WeA7 Upgrading a 25 Year Old ims-4f Magnetic Sector SIMS Instrument: Teaching an Old Dog New Tricks and Keeping Research in its Future, A.J. Fahey, B.E. Naes, G. Hager, Pacific Northwest National Laboratory

The CAMECA ims-4f at PNNL is nearly 25 years old. Although much of the vacuum system, electrostatic optics and associated apertures and slits have been maintained and remain operational the electronics that control the critical components of this machine has gone beyond the typical "mean-time-between failure" of nearly all components, which is typically 10 years.

The original electronics designs, many of which are no longer employed on the newer CAMECA models, incorporated multiple series of relays to control lens voltages that allowed isolation of low control and high voltage output. These relays, among other components, are failing.

Some components of the electrostatic optics and vacuum system are targeted to be replaced to upgrade the capabilities of the instrument and to use physical components from our "surplus" ims-4f system than would enhance the operation of the PNNL ims-4f giving in near-equivalence to the operation of an ims-7f.

The upgraded electronics and control systems are being designed in a modular way using as many commercial components as possible, such as modular high voltage power supplies and commercially available high-voltage operational amplifiers. The new system will allow for complete control of all subsystems on the instrument and will improve repeatability of settings and measurements. We will be able to perform measurements sets and sequences that are currently not possible on any existing SIMS instrument. In addition, the new computer controlled system should make operation of the SIMS instrument more accessible to other investigators as it should reduce the level of training needed to operate the instrument. Currently, the operator must adjust "knobs" to tune the instrument and reproduce prior operating conditions. With the upgraded system conditions will be recalled from saved files.

All modular components are being housed in ANSI-standard DIN modules and sub-racks. Control, monitoring and data acquisition will largely be performed via PXI subsystems. The Vacuum will be controlled and monitored via a commercial process control system. Also, several other individual instruments will be used in critical positions around the instrument.

Details of the upgrade will be discussed as well as improvements to the flexibility of measurements and the performance of the system. An outline of the types of measurements that should be available with all modern systems will be presented and discussed as well as the results of improvements implemented to the PNNL ims-4f SIMS instrument.

4:20pm AS+NS+SS+TF-WeA8 Automated Processing of X-ray Photo-Electron Spectra, K. Macak, E. Macak, S.J. Coultas, S.J. Hutton, A.J. Roberts, R. Raso, S.J. Page, C.J. Blomfield, Kratos Analytical Ltd, UK

Modern XPS instruments are capable of generating a large amount of data in a hands-off automated fashion. Many new material challenges are increasingly reliant upon XPS for sample screening and other high throughput, low operator intervention applications.

The interpretation of XPS data and reliable quantification from the acquired results presents an opportunity to improve the whole experimental automation still further. We present an algorithm for fully automated processing of X-ray photo-electron spectra. The analysis is split into three stages: background subtraction, peak identification and quantification of element composition.

Each step can be carried out separately and the user can provide prior knowledge of the sample by manually selecting regions, assigning their labels and/or explicitly include/exclude specific elements. This additional information then helps to improve the accuracy of the results.

The algorithm was tested on more than 1000 spectra, selected from a wide range of different materials; including steels, polymers, semiconductors and ceramics. These spectra were processed using the automated procedure and the outcomes were compared to those determined by expert users. The average element detection success rate was 87 %.

The influence of various experimental conditions (such as signal-to-noise ratio and operating conditions) on the identification procedure is also discussed.

4:40pm AS+NS+SS+TF-WeA9 Correlating Structure and Chemistry – A Multitechnique Study using Light Microscopy (LM), SEM and XPS, M.L. Pacholski, P.Y. Eastman, The Dow Chemical Company

Understanding the distribution of carbon-rich chemistries on organic substrates can be very difficult, particularly when the substrates are not uniform, such as cellulose fibers. Recently we have been challenged to measure the distribution of an olefin polymer on a fibrous cellulose sheet. In order to verify that measured chemical distributions were definitively from polymer, as well as to understand the morphology of the deposited polymer, it was highly desired to study identical areas using SEM and other imaging techniques. Although several chemical imaging methods were investigated, it became apparent that XPS imaging was the only chemical technique capable of obtaining distributions over the desired fields of view (1 mm-3 mm). Registry of the SEM images with XPS images proved to be difficult since many of the traditional registry methods, such as marking with ink or gluing markers to the surface are ill-suited to absorbent cellulose. The first step was to align relatively low magnification light microscope images from a stereoscope with optical images captured directly in the XPS instrument. These images were then used as a “bridge” to align the higher magnification SEM and XPS images. With this method, deposited polymer and chemical information were correlated with high spatial accuracy. Composite images showing the chemical information as colored overlays on the SEM images were generated to clearly display the correlation.

**Graphene and Related Materials Focus Topic
Room: 13 - Session GR+AS+EM+NS+SS-WeA**

Dopants and Defects in Graphene; Graphene Interfaces with Other Materials

Moderator: D. Gunlycke, Naval Research Laboratory

2:00pm GR+AS+EM+NS+SS-WeA1 Increasing Interface Bonding and Tuning Doping Behavior at Metal-Graphene-Metal Sandwich Contact, C. Gong, R.M. Wallace, K.J. Cho, Y.J. Chabal, The University of Texas at Dallas

Two types of interfaces can be formed between metals and graphene depending on the strength of the metal-graphene interaction: weak (metal physisorption) and strong (metal chemisorption) interfaces. “Physisorption” interfaces (e.g., with Al, Ag, Cu, Ir, Pt and Au) are characterized by a larger metal-carbon distance ($>3 \text{ \AA}$) with some charge transfer between metal and graphene (i.e. doping of graphene) that maintains its overall π -band dispersion. “Chemisorption” interfaces (e.g. with Ni, Co, Pd, and Ti) are characterized by a smaller metal-carbon distance ($<2.5 \text{ \AA}$) and strong orbital hybridization between metal- d and carbon- p_z orbitals, resulting in the destruction of the graphene’s π -band dispersion around the Dirac point. Till now, only a small fraction of all available metals has been used as electrode materials for carbon-based devices due to metal-graphene interface debonding problems. The issue therefore is to keep graphene’s intrinsic π bandstructure by using weakly interacting metals while enhancing the interface stability.

We report an enhancement of the bonding energy of weakly interacting metals by using a metal-graphene-metal sandwich geometry, without sacrificing the intrinsic π -electron dispersions of graphene that is usually undetermined by strong metal-graphene interface hybridization. This sandwich structure further makes it possible to effectively tune the doping of graphene with an appropriate selection of metals. Density functional theory calculations reveal that the strengthening of the interface interaction is ascribed to an enhancement of interface dipole-dipole interactions. Raman scattering studies of metal-graphene-copper sandwiches are used to validate the theoretically predicted tuning of graphene doping through sandwich structures.

2:20pm GR+AS+EM+NS+SS-WeA2 Defects in Two-Dimensional Materials and their Heterostructures, L. Adamska, I.I. Oleynik, University of South Florida

Recent developments in graphene electronics have stimulated an interest in other two dimensional materials such as hexagonal boron nitride (BN) and molybdenum disulfide (MoS_2). In contrast to graphene, BN and MoS_2 possess appreciable band gap and may form good interfaces with graphene, which opens up exciting opportunities for development of novel nanoelectronic devices. For practical applications, it is important to

understand the effect of defects, which appear during growth and processing, on resulting electronic properties. The defects in graphene, BN, MoS_2 and their heterostructures have been investigated by first-principles density functional theory. Their effect on electronic properties including density of states and simulated STM images will be discussed.

4:00pm GR+AS+EM+NS+SS-WeA7 Metal Oxide Growth and Characterization on CVD Graphene, A. Matsubayashi, College of Nanoscale Science and Engineering, University at Albany

Thin metal oxide layers deposited on graphene can be utilized as dielectric barriers between metals and graphene to help isolate a metal contact from the graphene channel. This is important for graphene based spintronic devices as dielectric layers between the ferromagnetic electrode and graphene have been shown to increase the spin relaxation time measured utilizing non-local detection and spin precession measurements^[1]. However, simply depositing metal oxide layers such as aluminum oxide on graphene results in non-uniform film lowering the quality of the interface barrier^[2]. In addition it is important to understand the stoichiometry of the resulting film. We will present a systematic study of aluminum oxide layers grown on CVD (chemical vapor deposition) graphene under ultra-high vacuum conditions with and without titanium seed layers. The aluminum oxide layers with the titanium seed layers showed reduced surface roughness. The chemical and structural composition determined by XPS (X-ray photoelectron spectroscopy) will be also presented that shows full oxidation of the aluminum and partial oxidation of the titanium.

References:

- (1) E. I. Rashba, Phys. Rev. B, **62**, 16267 (2000)
- (2) W. Han *et al*, Phys. Rev. Lett., **105**, 167202 (2010)

4:20pm GR+AS+EM+NS+SS-WeA8 Bi-layer Graphene Growth on Ni(111): The Role of Monolayer Graphene Rotation, A. Dahal, A. Rafik, University of South Florida, P.W. Sutter, Brookhaven National Laboratory, M. Batzill, University of South Florida

Bi-layer graphene synthesis by chemical vapor deposition is of importance for field effect devices because the band gap can be tuned in bi-layer graphene by an applied electric field. Here, we demonstrate that bi-layer graphene can be synthesized above 650°C by chemical vapor deposition on thin Ni(111) films grown on YSZ(111) substrates in ultra high vacuum (UHV). We characterize the bi-layer graphene growth by low energy electron microscopy (LEEM), Auger electron spectroscopy (AES) and low energy electron diffraction (LEED). Below 600°C graphene grows in registry with the Ni(111) lattice and no second layer graphene is formed upon cooling. At 650°C rotationally misaligned graphene domains are formed on Ni(111) and we observe second layer graphene to grow by carbon-segregation under those rotated monolayer graphene domains. The difference in second layer graphene nucleation and growth is explained by the graphene-Ni interaction, which is much stronger for graphene in registry with the substrate than for rotated graphene. The segregated second layer graphene sheet is in registry with the Ni(111) substrate and this suppresses further carbon-segregation, effectively self limiting graphene formation to two layers.

4:40pm GR+AS+EM+NS+SS-WeA9 Energetic and Kinetic Factors of Graphene Nucleation on Cu, N. Safran, M.S. Arnold, University of Wisconsin-Madison

Chemical Vapor Deposition (CVD) of graphene on Cu substrates uniquely allows for growth of uniform monolayer graphene and is a promising route for its scalable production for many industrial applications due to low cost. The growth is a purely surface driven process, due to carbon’s low solubility in the Cu substrate, and relies on the Cu surface catalytically decomposing a carbon precursor (methane). As the growth of graphene proceeds across the surface, the reactivity of the Cu is passivated by the graphene, making the growth self-limiting to monolayer coverage. Research interest on the control of nucleation is intensifying, as the polycrystalline character of the graphene films can limit mobility, thermal conduction, and mechanical strength via grain boundaries.

In this paper, we study the nucleation dependencies of graphene at ambient pressure CVD in the context of surface nucleation theory. At low methane partial pressures, the concentration of carbon on the surface on the copper is low and carbon clusters cannot grow to a critical size for nucleation. As the partial pressure is increased, the methane partial pressure reaches a critical value and nucleation occurs. Tracking the critical pressure as a function of temperature from 880 to 1075°C , we have determined the formation energy of the critical graphene nucleus to be $\sim 1.5 \text{ eV/carbon atom}$, via the relation $c_{\text{nuc}} \sim \exp(-E_{\text{form}}/k_B T)$. Additionally, we have found that the nucleation density of the graphene varies by 5 orders of magnitude over this temperature range at the critical methane concentration. The results are

described under the desorption controlled regime of surface cluster nucleation.

Growths near the critical methane concentration yield hexagonal growing graphene domains characteristic of attachment limited kinetics, while at higher rates yield other growth shapes. Characterization by Raman Spectroscopy has been used to identify defects in the graphene layers. We find that the Raman defect band (D-Band) scales with the root of the nucleation density, indicating the majority of defects are located at the domain boundaries and the D-band intensity scales with the distance between them. Electrical mobility measurements show nearly constant values in samples across the range of temperatures indicating other limiting factors besides internal defects. Growths at 900⁰ C yield $\mu > 1000 \text{ cm}^2/\text{Vs}$, ON/OFF ratio ~ 10 , and Raman D/G ratio < 1 , demonstrating high quality of growth even at relatively low temperatures.

5:00pm GR+AS+EM+NS+SS-WeA10 Magnetic Spin Reorientation Transition in Graphene Covered Cobalt on Iridium(111). *A.T. N'Diaye*, Lawrence Berkeley National Laboratory, *J. Coraux, N. Rougemaille, C. Vo-Van, O. Fruchart*, Institut NÉEL, CNRS & Université Joseph Fourier, France, *A.K. Schmid*, Lawrence Berkeley National Laboratory

One of graphene's promises is to be material for spintronic applications. While the influence of a magnet on graphene is under intense investigation by many groups little attention is given to the influence of graphene on a magnet.

With spin polarized low energy electron microscopy (SPLEEM) we studied thickness dependent spin reorientation transition on this system and compare with Co/Ir(111) without graphene. Monitoring the spin orientation in three dimensions while increasing the film thickness by one ML at a time, we find that the presence of graphene on the film at least doubles the thickness at which the spin reorientation from out-of-plane to in-plane occurs from 6ML Co to transition to 12ML-13ML at 300°C and to between 14ML and 20ML at room temperature.

We attribute the significant contribution of the graphene/Cobalt interface to the magnetic anisotropy energy to a strong hybridization of graphene with Cobalt in directional bonds.

This work was supported by the U.S. Department of Energy under Contract No. DE-AC02-05CH11231, by the French ANR contract ANR-2010-BLAN-1019-NMGEM and by the Alexander von Humboldt Foundation.

5:20pm GR+AS+EM+NS+SS-WeA11 Nucleation and Growth of Rh and Au Clusters on Graphene Moiré/Ru(0001). *B. Habenschicht*, Oak Ridge National Laboratory, *D. Teng*, Georgia Institute of Technology, *L. Semidey-Flecha*, Oak Ridge National Laboratory, *D. Sholl*, Georgia Institute of Technology, *Y. Xu*, Oak Ridge National Laboratory

Nanometer and sub-nanometer sized metal clusters may possess electronic and catalytic properties that differ greatly from those of the corresponding bulk metals. For potential applications, dense arrays of uniform metal clusters are desirable. However, the synthesis of such cluster materials remains a formidable challenge. Moiré superstructures that develop in graphene supported on certain metals have been shown to be viable templates for driving the formation of uniform metal clusters.[1] On graphene moiré (GM) on Ru(0001), dispersed clusters are obtained for Rh whereas Au coalesces into very large 2D islands.[2,3] We carry out a computational study to understand the disparate morphologies of Rh and Au clusters on GM/Ru(0001) via a multi-scale approach. DFT calculations are performed to study the adsorption and diffusion of the adatom and ad-clusters of Rh and Au on GM/Ru(0001) and the bonding mechanism between the metals, graphene, and Ru substrate. The potential energy landscape is then used to perform kinetic Monte Carlo simulations for the diffusion, nucleation, and growth of Rh and Au clusters. This approach allows us to predict the spatial and size distribution of the metal clusters and may be generally applicable to identifying the conditions necessary for obtaining desired cluster morphologies on GM.

(1) N'Diaye, A. T.; Bleikamp, S.; Feibelman, P. J.; Michely, T. *Phys. Rev. Lett.* **2006**, *97*, 215501.

(2) Zhou, Z.; Gao, F.; Goodman, D. W. *Surf. Sci.* **2010**, *604*, L31.

(3) Xu, Y.; Semidey-Flecha, L.; Liu, L.; Zhou, Z.; Goodman, D.W. *Faraday Discuss.*, **2011**, *152*, 267.

5:40pm GR+AS+EM+NS+SS-WeA12 Graphitic and Pyridinic N Species on N-doped HOPG Studied by STM, STS, PES and DFT. *M. Sakurai, T. Shikano, D. Ushigome, T. Suzuki*, University of Tsukuba, Japan, *Y. Harada, M. Oshima*, University of Tokyo, Japan, *S. Casolo*, University of Milan, Italy, *M.I. Trioni*, ISTM, Italy, *G.F. Tantardini*, University of Milan, Italy, *T. Kondo, J. Nakamura*, University of Tsukuba, Japan

Nitrogen doped graphene and carbon nanotube have been reported to show superior catalytic activity or superior support effect in the fuel cell. However, effects of the dopant nitrogen on the modification of the electronic structure of such graphite-related materials have not been clarified because a wide variety of defects with different types of C-N bonding configurations can coexist in nitrogen doped graphite.

Here, we report comprehensive atomic-resolution characterization of the defects in a nitrogen-doped graphite surface by scanning tunneling microscopy (STM), scanning tunneling spectroscopy (STS), Photoemission spectroscopy (PES) and first-principles calculations based on the density functional theory (DFT). Nitrogen-doped graphite was produced by nitrogen ion bombardment of the HOPG (highly oriented pyrolytic graphite) followed by thermal annealing at about 900 K.

Two types of nitrogen species were identified at the atomic resolution. One is pyridinic N (N having two C nearest neighbors) with single-atom vacancy. The other is graphitic N (N having three C nearest neighbors). In the case of pyridinic N with single vacancy, the local electronic states of the non-bonding pz orbital of carbon are found to appear at occupied region near the Fermi level at the carbon atoms around pyridinic N. On the other hand, the local electronic states of the non-bonding pz orbital of carbon are found to appear at unoccupied region near the Fermi level at the carbon atoms around graphitic N.

These results indicate that in both cases more than 300 carbon atoms are found to be modified by the dopant N to show the non-bonding pz orbitals. Moreover, these results suggest that the graphitic-N and pyridinic-N as well as their surrounding carbon atoms may act as "acid" and "base", because their non-bonding pz orbitals appear at empty and occupied region, respectively.

Helium Ion Microscopy Focus Topic Room: 19 - Session HI+AS+NS-WeA

Basics of Helium Ion Microscopy

Moderator: A. Götzhäuser, University of Bielefeld, Germany

2:00pm HI+AS+NS-WeA1 Basics of Imaging with Ions. *D. Joy*, University of Tennessee **INVITED**

Imaging with a helium ion microscope (HIM) offers numerous advantages, both fundamental and practical, as compared to a conventional scanning electron microscope (SEM). At the same time, however, many aspects of ion microscopy seem very different to those found in the SEM. In this presentation therefore we will examine ;

Why ions are a better choice for imaging than electrons and which ion (or ions) might be the best

In which areas of performance and operation the ion beam image is 'better'

The optimum beam energy for ion imaging for different materials; how typical imaging conditions compare to those for the SEM; and why they are different

The types of signals that are available for imaging in the ion microscope and how they compare with their electron beam counterparts

The problems of specimen charging and beam damage with the ion beams

The options available for microanalysis with the HIM

2:40pm HI+AS+NS-WeA3 Surface Analysis using Channeling Contrast in NUHV Helium Ion Microscopy. *B. Poelsema*, University of Twente, Netherlands **INVITED**

Helium Ion Microscopy, HIM, is a novel high-performance technique to image surfaces and with its high resolution, great surface sensitivity, enhanced material contrast, ability to investigate insulating material and large depth of field, it provides a viable alternative to classical scanning electron microscopy. A number of applications require improved vacuum conditions to achieve ultimate performance. The sharply focused He ion beam is, compared to an electron beam in SEM set-ups, very efficient in

decomposing, e.g., hydrocarbons present in the chamber and thus on the sample surface, which may obscure a clear view of the sample. Where this phenomenon is beneficial for high resolution structuring, it may well negate the benefits of small spot size and reduce the acquisition time available for spectroscopy in material analysis. To substantially reduce this problem a Near UHV version of the HIM has been developed in close collaboration between the manufacturer, Carl Zeiss NTS, LLC and our group at the University of Twente [1].

We will report on a number of recent observations with special attention for a new contrast mechanism, i.e. dechanneling of ions that extends the high surface sensitivity – usually achieved in secondary electron images – to backscattered ions. We demonstrate [2-4] how monolayer “thick” organic and inorganic films, as well as self assembled monolayers can be visualized, even when adsorbed on heavier substrates, by changes in the backscatter yield. Normally thin layers of a light element on a heavy substrate are “invisible” in backscattered ion yields. The results can be explained semi-quantitatively in terms of changes of the channelling probability. These results highlight the relevance of proper vacuum conditions for achieving monolayer sensitivity.

[1] R. van Gastel, L. Barriss, C. Sanford, G. Hlawacek, L. Scipioni, A.P. Merkle, D. Voci, C. Fenner, H.J.W. Zandvliet and B. Poelsema: *Microscopy and Microanalysis* **17(S2)**, 928-929 (2011)

[2] A. George, M. Knez, G. Hlawacek, D. Hagedoorn, H.H.J. Verputten, R. van Gastel and J.E. ten Elshof: *Langmuir* **28(5)**, 3045-3052 (2012)

[3] G. Hlawacek, V. Veligura, S. Lorbek, T.F. Mocking, A. George, R. van Gastel, H.J.W. Zandvliet, B. Poelsema: submitted

[4] V. Veligura, G. Hlawacek, R. van Gastel, H.J.W. Zandvliet, B. Poelsema: submitted

Acknowledgments: Gregor Hlawacek, Vasilisa Veligura, Raoul van Gastel, Harold J.W. Zandvliet.

4:00pm **HI+AS+NS-WeA7 Evaluation of W(111) Gas Field Ion Sources Based on Single Atom Tips**, R. Urban, University of Alberta and The National Institute for Nanotechnology, Canada, J.L. Pitters, National Institute for Nanotechnology, NRC Canada, R.A. Wolkow, University of Alberta and The National Institute for Nanotechnology, Canada

Atomically defined tips gained significant attention over the past decade because they serve as high brightness electron and ion sources. The success of the Scanning Helium Ion Microscope is dependent on the development of an appropriate Gas Field Ion Source (GFIS) to generate the helium ion beam. Single atom tips (SATs) represent a unique subgroup of atomically defined tips where emission only occurs from a single atom at the tip apex. Small virtual source size makes these tips attractive candidates for advanced scanning imaging applications such as SEM, TEM, and scanning ion microscopy (SIM) as well as for non-staining ion beam writing applications.

In this study SATs were fabricated from single crystal W(111) wire using a gas and field assisted etching process. By carefully controlling etching parameters SATs with extraction voltages between 5 and 17 kV were formed for various tips. During tip formation, we also used neon as an imaging gas to evaluate a W(111) tip shape during nitrogen-assisted etching. The neon image allows for the observation of atomic structure not available while imaging with helium and helps to elucidate the atomic structure of the tip during and after the etching to a single atom. The field ion microscopy (FIM) patterns (intensity maps) from SAT were fitted with 2D Gaussian curve to evaluate ion beam divergence and amplitude. The divergence of helium beam with respect to helium pressure and applied voltage will be discussed for various SATs.

Angular current density of various SATs was evaluated from their FIM patterns recorded by a microchannel plate and ion current measurements using a Faraday cup. The volume under the 2D Gaussian surface was found to be directly proportional to total ion current carried by an ion beam. The ion current was found to be linearly proportional to He pressure. However, comparing various tips it was found that the ion current increased faster than the extraction voltage. This suggests improved He capture by a broader tip base. The effect of the shape of the base of the tip was also evaluated and it was found that the beam opening angle varied with the size of the tip base leading to a forward focussing effect. The relative angular current densities from SATs supported on different tip curvatures were also evaluated and found to increase at a faster rate than current, also indicating that a forward focusing effect was in effect. This indicates that SATs on large bases would prove optimal for ion current generation in a scanning ion microscope.

4:20pm **HI+AS+NS-WeA8 Single-atom Tip as an Emitter of Gas Field Ion Sources**, I.-S. Hwang, H.-S. Kuo, Academia Sinica, Taiwan, Republic of China, T.-Y. Fu, National Taiwan Normal University, Taiwan, Republic of China, J.-L. Hou, C.-Y. Lin, Y.-H. Lu, W.-T. Chang, T.T. Tsong, Academia Sinica, Taiwan, Republic of China

Thermally and chemically stable single-atom tips (SAT) or nanotips are highly desirable for emission of high-brightness gas field ion beams. In 2001, Fu et al. demonstrated a Pd-covered W(111) SAT through vacuum deposition of an ultra-thin Pd film on a clean W tip surface followed by thermal annealing [1]. Later, Kuo et al. further simplified the preparation process by replacing the tip cleaning and the vacuum deposition with electrochemical processes and successfully prepared several different types of noble metal-covered W(111) SATs [2]. This type of SATs is thermally stable and chemically inert, and thus can be regenerated through a gentle annealing if the apex is contaminated.

We have successfully generated hydrogen, helium, argon, and oxygen ion beams using a Ir/W SAT and characterized these ion sources [3]. The first two lightest ions provide the lowest sputtering rates, which is beneficial for scanning ion microscopy. The argon ion has a large mass and can provide a high sputtering rate, suitable for ion milling. Due to the high secondary ion yields, an oxygen ion beam may be applied to secondary ion mass spectrometry. The ion beam profiles indicate that the half opening angle is $\sim 0.5^\circ$. This single spot indicates that emission occurs only from the topmost atom. This small source size and the small opening angle are particularly favorable for achieving high angular intensity, high brightness, and low spherical aberration, which are important characteristics for a focused ion beam system. The ion current of these gas ion beams are very stable and the tip does not show any degradation under fields above 5 V/Å after a total operation time of 80 hours. Since the SAT can be regenerated for more than 50 times, therefore its lifetime is long enough for most practical applications.

In addition, we have also prepared a pure iridium SAT based on oxygen-induced crystal faceting of the Ir(210) [4]. We have shown that the Ir-SAT can be a good field ion emitter, capable of emitting a variety of gas ion beams, including He⁺, H₂⁺, N₂⁺, and O₂⁺, with high brightness and stability. In particular, nitrogen is a very corrosive gas for metal tips under strong positive electric fields. If we can achieve a stable emission of nitrogen ion, it also means many other gas field ion beams may also be emitted from this Ir-SAT. This may greatly broaden the application of focused ion beam technology.

[1] T.-Y. Fu et al., *Phys. Rev. B* **64** (2001), 113401.

[2] H.-S. Kuo et al., *Nano Lett.* **4** (2004), 2379.

[3] H.-S. Kuo et al., *Appl. Phys. Lett.* **92** (2008), 063106.

[4] H.-S. Kuo et al., *Nanotechnology* **20** (2009), 335701.

4:40pm **HI+AS+NS-WeA9 Helium Ions for Imaging and Nanofabrication on the nm Scale**, E. Van Veldhoven, H.H.P.Th. Bekman, F.T. Molkenboer, N.B. Koster, D.J. Maas, TNO Technical Sciences, The Netherlands

The Helium ion microscope (HIM, Zeiss Orion Plus™) has unique features. This microscope unravels a new application area for imaging sensitive and charging surfaces with (sub) nm resolution [1]. The beam-sample interaction generates secondary electrons with low energy and a low quantity of backscattering ions. These properties are very interesting for using the microscope not just for imaging only, but for nanofabrication too [2]. To explore all the capabilities for nanofabrication, the HIM is equipped with a pattern generator (Raith Elphy Multibeam™) and a gas injection system (Omniprobe Omnigis™) to explore direct write, lithography and gas induced applications.

In this contribution we would like to focus on imaging charging materials and our latest results for using the HIM for developing new applications for mainly the Semiconductor Industry. We consider a few HIM-based methods for TEM sample preparation. It is possible to use the HIM for making a thin wedge without significant artifacts like bubble formation and amorphization. With the gas injection system we develop new recipes for very local deposition and etching. These recipes are used for feasibility studies for mask repair and circuit editing. The helium ion microscope offers a novel way for nanofabrication and imaging on the nm scale.

5:00pm **HI+AS+NS-WeA10 Towards Secondary Ion Mass Spectrometry on the Helium Ion Microscope**, T. Wirtz, N. Vanhove, L. Pillatsch, D. Dowsett, Centre de Recherche Public – Gabriel Lippmann, Luxembourg, S. Sijbrandij, J. Notte, Carl Zeiss

The ORION Helium Ion Microscope (HIM) has become a well-established tool for high-resolution microscopy [1]. The high brightness ALIS gas field ion source can operate with helium and, after special prototype modifications, with neon [2]. However, the detection of backscattered atoms can provide only limited specimen composition information. By

contrast, Secondary Ion Mass Spectrometry (SIMS) is an extremely powerful technique for analyzing surfaces due to its excellent sensitivity, high dynamic range, very high mass resolution and ability to differentiate between isotopes. In order to get chemical information with a higher sensitivity and a high lateral resolution, we have investigated the feasibility of performing SIMS on the HIM.

Therefore, the secondary ion formation process under He⁺ and Ne⁺ bombardment has to be investigated and optimized. To investigate secondary ion formation an experimental study was performed; to investigate sputtering effects on resolution and practical implementation aspects a simulation approach was taken.

First, secondary ion yields for different elements sputtered from different materials exposed to helium and neon ion beams were experimentally determined on a test set-up. The basic yields could be increased by several orders of magnitude by using reactive gas flooding (i.e. O₂ and Cs⁰ [3,4]). Afterwards, detection limits have been calculated taking into account the experimentally obtained useful yields. Depending on the dwell time, ppm sensitivity can be obtained for Ne⁺ bombardment on silicon with oxygen flooding. Second, a detailed study of the sputtering phenomena using TRIM simulations was carried out in order to determine the effect of the collision cascade on the lateral resolution. The diameter (FW₅₀) of the area from which sputtered atoms originate has been determined for 10 keV He⁺ and Ne⁺ bombardment on different materials. While the obtained results are very encouraging, the practical instrumentation aspects have to be investigated as well in order to obtain a high secondary ion transmission and maintain the excellent primary beam characteristics. Therefore, the practical limitations imposed by adding an extraction system to the HIM have been studied in detail with respect to the extraction geometry.

In general, the combination of high-resolution microscopy and high-sensitivity chemical mapping on a single instrument will lead to a new level of correlative microscopy.

[1] L. Scipioni *et al.*, *J. Vac. Sci. Technol. B* **27**, 3250 (2009)

[2] F. Rahman *et al.*, *Scanning* **33**, 1 (2011)

[3] K. Franzreb *et al.*, *Surf. Sci.* **573**, 291 (2004)

[4] P. Philipp *et al.*, *Int. J. Mass Spectrom.* **253**, 71 (2006)

Nanometer-scale Science and Technology

Room: 12 - Session NS-WeA

Nanophotonics and Plasmonics

Moderator: D. Wei, University of Florida

2:00pm NS-WeA1 **Plasmon Induced Current In Hybrid Nanostructures**, *D.A. Bonnell, D. Conklin, S. Nanayakkara, X. Chen*, The University of Pennsylvania, *T.H. Park*, University of Michigan, *M. Therien*, Duke University

Interest in plasmon-exciton interactions is increasing owing to potential impact in light harvesting and optical signal manipulation. Recently a new mechanism of plasmon induced current generation was observed in porphyrin-Au nanoparticle hybrid nanostructures.[1] The plasmons associated with the gold nanoparticles enhanced photo conduction by many factors... even an order of magnitude. To understand this phenomena we have first developed an approach to the analysis of temperature dependent transport measurements that can lead to an unambiguous determination of mechanism in complex systems. [2] Then the temperature and wavelength dependent transport is examined as a function of nanoparticle size and distribution and molecule optical properties. [3] A Au-porphyrin combination is designed to distinguish the various potential mechanisms for plasmon induced current. We will show new evidence for a mechanism involving 'hot electron' generation. This has the potential to vastly increase efficiency of energy harvesting devices.

[1] Banerjee *et al* *ACS Nano* **4** (2010) 1019-1025

[2] Conklin *et al* *NanoLetters* **12** (2012) doi 10.1021/nl300400a

[3] Conklin *et al* *Advanced Materials* **21** (2011) 4712-4718.

2:20pm NS-WeA2 **Absorption from Plasmonic Antenna Arrays**, *K.E. O'Brien, P. Wang, P.H. Holloway, M.R. Davidson*, University of Florida

Photomixing over nano/micro scale plasmonic structures is a novel concept for generating narrow band radiation, specifically in the terahertz (THz) range. The plasmonic structures can serve as antennas for absorbing incoming photons and conversely emit radiation of a lower frequency if it is generated from mixing. In this experiment, antenna structures are excited by two tuned laser diodes to output THz radiation. Various designs for these antennas are have been considered, with presented results focusing on 2

dimensional arrays of elliptical antennas fabricated from Ag using electron-beam lithography and lift-off. The plasmonic antenna arrays exhibit polarization-dependent absorption when excited by visible light in agreement with results from simulations. The effect of varying antenna size on absorption will be discussed, as well as results from photomixing experiments.

2:40pm NS-WeA3 **New Directions in Plasmonics: Pushing the Sensitivity, Space, and Time Limits**, *R.P. Van Duyne*, Northwestern University **INVITED**

During the last few years, there has been an explosion of interest and activity in the field of plasmonics. The goal of plasmonics is to control and manipulate light on the nanometer length scale using the properties of the collective electronic excitations in noble metal films or nanoparticles, known as surface plasmons. An improved understanding of the interactions between adsorbed molecules and plasmonic nanostructures (i.e., molecular plasmonics) is having a significant impact in a number of research areas. These include surface-enhanced Raman spectroscopy (SERS), localized surface plasmon resonance (LSPR) spectroscopy, sub-wavelength optical microscopy, and nanolithography.

This talk will begin with some background material on the basic physical concepts underlying plasmonics with an emphasis on SERS and LSPR spectroscopy. Next, I will turn to two very recent developments. For the first time, the revolutionary techniques of surface enhanced Raman spectroscopy and femtosecond stimulated Raman spectroscopy (FSRS) have been combined. Thus, plasmonically enhanced broadband Raman spectra using an ultrafast four wave mixing process, which can simultaneously achieve spectral and temporal resolution below the time-energy uncertainty limit, has been achieved! Further we report substantial progress in tip-enhanced Raman spectroscopy (TERS). The isotopologue proof of single molecule specificity in ambient TERS has been demonstrated. We calculated the total TERS enhancement factor to be 10¹³, which includes a molecular resonance Raman contribution of 10⁷. Further, an ultrahigh vacuum (UHV) TERS instrument has been constructed with atomic resolution of the surface and sub-molecular resolution of the adsorbate. For the first time, multiple vibrational modes for copper phthalocyanine (CuPc) adlayers on Ag (111) have been resolved in TERS spectra obtained concurrently with molecular resolution UHV Scanning Tunneling Microscopy (STM). All sample preparation and tip degassing are performed in-situ, maintaining atomically clean surfaces, greatly enhancing the stability of the tip-sample junction, and ensuring minimal contamination in the field enhancement region beneath the STM tip. We can now foresee the day when it will be possible to combine UHV-TERS and surface enhanced FSRS to enable single-molecule spectroscopy with simultaneous nanometer spatial resolution and femtosecond time resolution.

4:00pm NS-WeA7 **Near-Field Spatio-Temporal Control of Optical Fields for Spectroscopic Nano-imaging: Ultrafast Spectroscopy Reaching the Single Molecule Limit**, *M.B. Raschke*, University of Colorado **INVITED**

Combining plasmonic and optical antenna concepts with ultrafast and shaped laser pulses allows for the precise control of an optical excitation on femtosecond time and nanometer length scales. I will present several new concepts extending tip-enhanced spectroscopy into the nonlinear and ultrafast regime for nano-scale imaging and spectroscopy of surface molecules and nano-solids. Examples include the adiabatic nano-focusing on a tip for background free tip-enhanced Raman nano-spectroscopy, and spatio-temporal superfocusing with optical control at the 10 nm-10 fs level. Furthermore, the combination of ultrafast mid-IR femtosecond pulses with scattering-scanning near-field optical microscopy (s-SNOM) allows for the control of the ultrafast free-induction decay of infrared molecular vibrations with an increase in sensitivity of IR surface spectroscopy by 10⁹ compared to conventional IR micro-spectroscopy, reaching the single molecule limit.

4:40pm NS-WeA9 **Tuning the Optical Properties of Arrays of Pure and Doped Au Nano Chains**, *N. Nayyar, V. Turkowski, T.S. Rahman*, University of Central Florida

We apply time dependent density functional theory to study the absorption spectrum of arrays of nano-scale pure Au chains and those doped with transition metal (TM) atoms. We find that as the number of chains in the array increases the plasmon peak shifts to higher energies and appears in the visible range for an array of three gold chains, each consisting of 10 atoms. Doping with TM atoms also leads to the formation of additional plasmon peaks close in energy to the main one for the undoped case and is especially pronounced for Ni-doped chains. However, the response is very different when we have two chains in the array each doped with one TM atom in the middle. We trace the origin of the additional modes to the interplay between the collective and local plasmon oscillations of the chains. We compare the calculated optical absorption spectrum of the doped chains for several

different types of TM atoms at different positions in the chains, and provide rationale for the trends. We also analyze the case of arrays consisting of chains of two different noble metal atoms (Au-Ag) and of arrays in which one chain is of noble metal atoms and the other of TM atoms. We find that the plasmon mode is suppressed when the second chain is composed of TM atoms. In addition we study the effect of plasmon –exciton interaction in arrays of infinite Au chains.

Work supported in part by DOE Grant DE-FG02-07ER46354

5:00pm **NS-WeA10 Synthesis, Characterization and Plasmonic Properties of Horizontally and Vertically Aligned Ag Nanorods and Nanowires**, *S. Vilayrganapathy, A. Pandey, A. Devaraj, D.E. Perea, S. Thevuthasan*, EMSL, Pacific Northwest National Laboratory, *A. Kayani*, Western Michigan University

One dimensional metal nanostructures such as nanorods and nanowires exhibit interesting linear and non-linear optical properties and find various applications as electronic, photonic and sensing devices. The optical properties of these composites are dominated by localized surface Plasmon resonance (LSPR) which results from the oscillations of conduction electrons in response to an external field. The resonant frequency of the electrons depends strongly on size, shape, distribution and the surrounding dielectric medium. By controlling the physical and chemical properties of the nanorods and nanowires the electronic and optical properties of the material can be tuned for appropriate applications. Nanorods and wires with well controlled aspect ratios can be grown by Electrodeposition and Polyol synthesis methods.

We have successfully employed the above two methods to grow both vertically and horizontally aligned Ag nanorods and wires. Vertically aligned and free standing Ag nanorods were grown by electrodepositing Ag onto an Anodized Aluminum oxide (AAO) template containing a sputtered layer of Ag on one side. The length of the nanorods varies linearly as a function of deposition time allowing us to obtain excellent control over the aspect ratio. The template was subsequently etched away using 6 wt. % Phosphoric acid/1.8 wt. % chromic acid solution leaving behind free standing vertically aligned nanorods. A Polyol process in which we reduce silver nitrate with ethylene glycol in the presence of a capping agent (PVP) was employed to grow nanorods in solution. A high yield of nanorods was obtained after centrifuging. The above grown nanorods were horizontally aligned onto a substrate by the Langmuir-Blodgett method. Scanning electron Microscope (SEM) was used to image the nanorods. The change in plasmonic response of both vertically and horizontally aligned nanorods as a function of aspect ratio as well as the influence of the surrounding dielectric medium on the plasmonic resonance of the nanorods embedded in a dielectric matrix will be discussed.

5:20pm **NS-WeA11 Localized Surface Plasmon Resonances in Silicon**, *L.-W. Chou, N. Shin, S. Sivaram, M. Filler*, Georgia Institute of Technology

Localized surface plasmon resonances (LSPRs) in semiconductors offer new opportunities to engineer the interaction of electromagnetic radiation with solid-state materials. Importantly, the carrier density of semiconductors, and thus LSPR frequency, can be modulated via doping and/or electric field. In addition to realizing novel plasmonic devices, the direct integration of plasmonic and excitonic behavior also promises fundamentally distinct functionality. Here, we demonstrate and systematically control LSPRs in nanoscale Si for the first time. More specifically, Si nanowires are synthesized via the vapor-liquid-solid (VLS) technique with a combination of Si_2H_6 and PCl_3 precursors. PCl_3 simultaneously introduces P atoms to the nanowire core and delivers Cl atoms to the sidewall so as to minimize radial dopant incorporation. This chemistry enables growth sufficiently far from equilibrium such that dopant concentrations can exceed thermodynamic limits. Electron microscopy reveals that these nanowires are single crystalline and $\langle 111 \rangle$ oriented with very few lattice defects. Polarization dependent *in-situ* infrared spectroscopy measurements show intense mid-IR absorption bands only for the P-doped nanowires, which we assign to longitudinal LSPRs. A significantly weaker transverse mode is occasionally observed as well. The LSPR frequency can be readily adjusted by varying nanowire length. Mie-Gans theory supports our experimental results and indicates that electrically active dopant concentrations exceed 10^{20} cm^{-3} .

Thursday Morning, November 1, 2012

Electronic Materials and Processing

Room: 14 - Session EM+SS+AS+NS-ThM

Nanoelectronic Interfaces, Materials, and Devices

Moderator: M. Filler, Georgia Institute of Technology

8:00am EM+SS+AS+NS-ThM1 **Tensilely Strained Ge Nanomembranes for Applications in Group-IV Infrared Photonics**, *R. Paiella*, Boston University **INVITED**

Single-crystal semiconductor nanomembranes have emerged as a new materials platform offering unique opportunities for strain engineering, by virtue of their ultrasmall thicknesses that result in extremely high thresholds for plastic deformation under stress. This talk will review our recent work aimed at exploiting this property for the development of CMOS-compatible group-IV semiconductor light sources for the technologically important near-infrared spectral region. It is well known that Si, Ge, and related alloys are very inefficient light emitters and generally unsuitable for laser action, due to the indirect nature of their fundamental energy bandgap. A possible solution to this important drawback is provided by the ability of biaxial tensile strain in Ge to lower the conduction-band edge at the direct (Γ) point relative to the L-valley minima, until at a strain of about 1.9% the fundamental bandgap becomes direct. In our work, mechanically stressed Ge nanomembranes capable of accommodating the required strain levels have been developed, and used to demonstrate strong strain-enhanced photoluminescence. A maximum biaxial tensile strain of over 2% in a 24-nm-thick nanomembrane has been measured, above the accepted threshold for the formation of direct-bandgap Ge. A detailed theoretical model of the light-emission and optical gain properties of tensilely strained Ge has also been developed and applied to the measured luminescence spectra, providing evidence of population inversion at strain levels as low as about 1.4%. More recent work is focused on integrating optical cavities on these strained nanomembranes for the development of infrared photonic active devices.

8:40am EM+SS+AS+NS-ThM3 **Self-activating and Self-limiting Features of the Thermally Assisted Growth Mechanisms of Thin Oxide-, Nitride- and Carbide Films on Si Surfaces at Low Gas or Plasma Pressures**, *P. Morgen, J. Drews, R. Dhiman*, University of Southern Denmark, *Z.S. Li*, Aarhus University, Denmark

The thermally assisted growth of oxide-, nitride-, and carbide films on Si surfaces, in direct reactions, carried out with neutral gases or remote plasmas under ultrahigh vacuum background conditions, are self-limiting processes, reaching different thicknesses. The mechanisms have been studied using photoelectron spectroscopies with synchrotron radiation or conventional x-ray induced photoelectron spectroscopy (XPS). For the oxidation with neutral oxygen molecules, or microwave-excited remote oxygen plasmas, and for the nitride formation reaction with microwave-excited remote nitrogen plasmas, the "kinetics" (uptake versus exposure plots) is well described with a Hill-function. For the nitrogen reaction, the variation of the temperature causes the Hill parameters to vary because this reaction has more latitude than the oxidation, in temperature range and final thickness, as well as in the resulting structure of the nitride, going from amorphous to crystalline at higher temperatures. One known instance of the "Hill reaction" is a self-activating enzymatic-like reaction, and such a mechanism is believed to be relevant also in our systems. The carbide reaction is different, due to defects in the growing film, which allow a relatively unhindered transport of Si to the surface, where it reacts with carbon species arriving at the surface, from remote microwave-excited plasmas of methane. Thus the limiting thickness of SiC/Si (111) is around 100 nm, while the thickness of oxide is 0.8 nm, and the nitrides between 1 and 3 nm.

9:00am EM+SS+AS+NS-ThM4 **Functional Conductive Polymer to Inexpensive and Portable Chemiresistive Biosensor**, *D. Bhattacharyya, K.K. Gleason*, Massachusetts Institute of Technology

Extensive research has focused on developing different types of biosensors for detecting bio-threat risks and the occurrence of toxins in the food supplies. However, these food screening processes involve many steps, have high labor costs, reagent costs and time delays of at least 2-3 days to obtain reliable data. Despite the current availability of various types of sensors, limitations of the current state-of-the-art biosensors for molecular recognition of biomolecules are well known. Among these limitations are the unacceptably long process times required for detection and user non-compliance as a result of the excessive weight of the sensor modules coupled with the inflexibility of the sensor platforms for routine uses.

Chemiresistive biosensors detect changes in resistance when analyte molecules specifically bind to the sensor surface. Chemiresistive biosensing technique is attractive because it is label-free and can be developed for faster detection of analytes. In this work, oxidative chemical vapor deposition (oCVD) technique is employed for deposition of functional conductive copolymer thin films on the electro-spun fiber mats. The dry oCVD process allowed us to deposit uniform and conformal conducting -OH functional copolymeric film on the electro-spun fiber mat in a single step. For the proof-of-concept of the biosensor application, avidin molecules were covalently immobilized to the -OH functional groups. Various concentrations of biotin solutions were employed as the analytes. The responses and the response times of the devices were significantly improved when the high surface area electro-spun mat were used as a substrate in contrast to a flat substrate.

9:20am EM+SS+AS+NS-ThM5 **Semiconductor Nanomembranes for Biomedical Applications**, *J.A. Rogers*, University of Illinois at Urbana Champaign **INVITED**

Biology is curved, soft and elastic; silicon wafers are not. Semiconductor technologies that can bridge this gap in form and mechanics will create new opportunities in devices that adopt biologically inspired designs or require intimate integration with the human body. This talk describes the development of ideas for electronics that offer the performance of state-of-the-art, wafer-based systems but with the mechanical properties of a rubber band. We explain the underlying materials science and mechanics of these approaches, and illustrate their use in bio-integrated, 'tissue-like' electronics with unique capabilities for mapping cardiac electrophysiology, in both endocardial and epicardial modes, and for performing electrocorticography. Demonstrations in live animal models illustrate the functionality offered by these technologies, and suggest several clinically relevant applications.

10:40am EM+SS+AS+NS-ThM9 **Structure, Dynamics and Mechanism of a Single-Molecule Electric Motor**, *C.J. Murphy, C.H. Sykes*, Tufts University

Future nano-electronic devices, such as fluid pumps, sensors and switches, will rely on rotating molecules bound to surfaces as key components. To operate these devices, it is important to understand and direct molecular rotation at this interface. We utilized a Low Temperature Scanning Tunneling Microscope (LT-STM) to both drive and measure the rotation of a single asymmetric thioether molecule bound to a copper (111) surface. Due to the hexagonal arrangement of the underlying Cu atoms the rotor molecule has six favorable orientations, with an asymmetrical barrier to rotation around the Cu-S bond. The symmetry of this barrier is dependent on the surface bound chirality. Rotation of the molecule can be driven by either thermal or electrical means. In thermally driven systems, there is no preferred direction of rotation. In order to measure the rate of anisotropic rotation, the system is cooled to 5 K, and a tunneling current is applied to periodically excite the molecule, resulting in a flashing ratchet like mechanism of molecular rotation. The progression of molecular orientations relative to the tip can be determined by the exponential dependence of tunneling current on distance. This allows evaluation of the rate, direction and magnitude of rotation between these orientations in real time. We aim to further interrogate this novel mechanism for electrically-driven motion by quantifying the lifetime of the rotor in each stable orientation and the transitions between these states as a function of tunneling current and voltage.

11:00am EM+SS+AS+NS-ThM10 **Semiconductor Nanostructures for Efficient Thermoelectric Energy Conversion**, *Z. Aksamija*, University of Wisconsin Madison

Thermoelectric (TE) refrigeration using semiconductor-based nanostructures, such as nanowires, nanoribbons, and superlattices, is an attractive approach for targeted cooling of local hotspots inside integrated circuits due to inherently no moving parts, ease of miniaturization and on-chip integration, and the nanostructures' enhanced TE conversion efficiency. In addition, thermoelectric power generation enables the reuse of waste heat in a variety of applications, from low-power and energy-efficient designs to internal combustion engines and solar cells. Thermoelectric efficiency, measured by the figure-of-merit ZT , is dictated by the ratio of electronic power factor $S^2\sigma$ over the total thermal conductivity. Consequently, largest gains in TE conversion efficiency have come from the ability to reduce thermal conductivity. This is especially true in nanostructures, where small physical dimensions lead to reduced thermal transport due to the scattering of lattice waves, or phonons, with the boundaries of the nanostructure. The design of efficient semiconductor thermocouples requires a thorough understanding of both charge and heat

transport; therefore, thermoelectricity in semiconductor-based nanostructures requires that both electronic and thermal transport are treated on equal footing. SOI nano-membranes and membrane-based nanowires and ribbons show promise for application as efficient thermoelectrics, which requires both high electronic power factor and low thermal conductivity. I will present numerical simulation and modeling of both carrier and phonon transport in ultrathin silicon nanomembranes and gated nanoribbons. We show that the thermoelectric response of Si-membrane-based nanostructures can be improved by employing the anisotropy of the lattice thermal conductivity, revealed in ultrathin SOI nanostructures due to boundary scattering, or by using a gate to provide additional carrier confinement and enhance the thermoelectric power factor. Furthermore, we explore the consequences of nanostructuring on silicon/germanium and SiGe alloy superlattices, and show that the drastic reduction of thermal conductivity in these structures comes from the increased interaction of lattice waves with rough interfaces and boundaries. Finally we demonstrate reduced thermal conductivity in both suspended and supported graphene nanoribbons (GNRs), which exhibit strong anisotropy due to interaction of lattice waves with line edge roughness (LER) and the competition between LER and substrate scattering. The talk will conclude with an outlook for future nanostructured thermoelectric based on nanocrystalline and nanocomposite semiconductors, and nanopatterned graphene.

11:20am **EM+SS+AS+NS-ThM11 UV Ozone Irradiation Induced Defect Formation in Graphene/PZT Devices**, C.X. Zhang, D.M. Fleetwood, M.L. Alles, R.D. Schrimpf, Vanderbilt University, E.B. Song, S. Kim, K. Galatsis, K.L. Wang, University of California at Los Angeles, E.X. Zhang, Vanderbilt University

Graphene based materials are promising candidates for integration into future integrated circuit technologies. Initial studies of the effects of electron-beam and proton irradiation have been performed on graphene materials, but there remain significant questions about the nature of the conductivity and the defects that influence its material and electronic properties. We have found that low-energy x-ray irradiation can lead to significant shifts in the charge neutral point and increases in resistance of suspended graphene layers and graphene layers on SiO₂. For graphene-on-SiO₂ structures, the reaction oxygen atoms may be supplied either by ozone in the ambient air, or by the adjacent SiO₂ substrate. Similar reactions may be observed for hydrogen, for devices exposed to x-ray and/or UV ozone (UVO) irradiation. Moreover, we also have found that graphene/PZT ferroelectric field-effect transistors (FFETs) are sensitive to UVO irradiation. The conducting channel in these devices is a single graphene layer. The device functions as a nonvolatile memory with reverse hysteresis, where charge trapping and detrapping in the PZT layer leads to a large memory window that is robust to x-ray irradiation and/or memory state cycling. When these devices are exposed to UVO irradiation, the memory window of the device decreases slightly with exposure time. In addition, an increase is observed in the slope of the I-V curves, along with a small positive shift in current-voltage characteristics. These results are consistent with the formation of negatively charged surface states on the graphene layer during the UVO exposure, which are most likely associated with adsorbed oxygen. The degradation in the I-V characteristics recovers somewhat with room temperature annealing. At the AVS meeting, the detailed electrical response will be described, and a physical model will be presented for the UVO degradation and recovery mechanisms.

11:40am **EM+SS+AS+NS-ThM12 Switching Molecular Kondo Effect by Chemical Reactions**, H. Kim, ISSP, University of Tokyo, Japan, Y.H. Chang, KAIST, Korea, M.H. Chang, Korea University, Y.-H. Kim, KAIST, Korea, S.-J. Kahng, Korea University

Motivated by spintronics applications, the methods to control Kondo effect have been actively studied in magnetic adsorbates on metal surfaces using scanning tunneling microscopy, but they were limited to the processes that required external energy supply from scanning tunneling microscope tip. We report new methods to control molecular Kondo effect by using bimolecular chemical reactions. A chemical binding between diatomic molecules and Co-porphyrin was exploited to switch off, or reset the molecular Kondo effect. The Kondo effect was switched back on using scanning tunneling microscope manipulation as well as thermal desorption. These methods rely on the hybridized pairing of unpaired spins in d₂ and π^* orbitals of Co-porphyrin and diatomic molecules, respectively, as supported by our density functional theory calculation results. Our study opens up ways to control the molecular Kondo effect using an enormous variety of bimolecular chemical reactions.

12:00pm **EM+SS+AS+NS-ThM13 Quantifying the Local Seebeck Coefficient using Scanning Thermoelectric Microscopy (SThEM)**, J.C. Walrath, Y.H. Lin, K.P. Pipe, R.S. Goldman, University of Michigan

Thermoelectric (TE) devices allow reliable solid-state conversion of heat to electricity. The efficiency of a TE device is determined by the figure of

merit, ZT, which is sensitive to the Seebeck coefficient, S. Traditional S measurements are used to quantify thermally-induced electron transport on a macroscopic scale. A promising alternative method for nanoscale measurements of S is scanning thermoelectric microscopy (SThEM). In SThEM, an unheated scanning tunneling microscopy (STM) tip acts as a high-resolution voltmeter to measure the thermally-induced voltage, V, induced by a temperature gradient in a heated sample. SThEM has been utilized to measure V across a GaAs p-n junction [1], with the spatial profile of S determined through a comparison of the measured V with a simulation of a network of resistors and voltage sources, based upon a theoretical S-value [2]. Although this approach is useful for predicting the measured V, it does not provide a method for direct conversion of the measured V to a local S. We have developed a Fourier heat conduction model to calculate a temperature profile matrix, thereby enabling direct conversion between the measured V and the local S. According to our model, SThEM can be optimized by fine-tuning several parameters, including the cone angle of the STM tip and the relative thermal conductivity of the tip and sample. We applied our model to SThEM data across a GaAs p-n junction [1] and improved the agreement between the measured and theoretical S by 40%. Our progress towards SThEM measurements of CoSb₃ and InAs quantum dots will also be discussed. This material is based upon work supported by the Department of Energy under Award Number DE-PI0000012. Y.H. Lin and R.S. Goldman are supported in part by DOE under contract No. DE-FG02-06ER46339.

[1] H.K. Lyeo, A.A. Khajetoorians, L. Shi, K.P. Pipe, R.J. Ram, A. Shakouri, and C. K. Shih, *Science* **303**, 816 (2004).

[2] Z. Bian, A. Shakouri, L. Shi, H.K. Lyeo and C.K. Shih, *Appl. Phys. Lett.* **87**, 053115 (2005)

Energy Frontiers Focus Topic

Room: 15 - Session EN+NS-ThM

Batteries and Fuel Cells

Moderator: Y. Wu, Purdue University

8:00am **EN+NS-ThM1 Advanced Polymer Electrolyte Materials for Fuel Cell Applications**, A.M. Herring, Colorado School of Mines
INVITED

Proton exchange membrane (PEM) fuel cells are still the most desirable component of future zero emission, high efficiency automobiles fueled with hydrogen. However, their unit cost, ease of operation, and reliability must be reduced which includes eliminating the humidifier from the fuel cell system. Currently the commercial PEM is fabricated from a perfluorosulfonic acid (PFSA) polymer such as Nafion[®]. Unfortunately PFSA ionomers must be fully hydrated to achieve practical levels of proton conductivity which can only be achieved in vehicles operating at an inlet RH of 85% which still necessitates the use of a humidifier and undesirable complex water management and recovery. To achieve the goal of a PEM that can operate at temperatures from freezing to 120°C using dry inlet gases it will be necessary to develop new PEMs that are based on new chemistries or dramatically improved morphologies of existing chemistries. The versatility of the polymer electrolyte fuel cell could be expanded to more complex fuels with the use of an anion exchange membrane (AEM). An AEM fuel cell could potentially utilize less expensive metal catalysts and have the ability to oxidatively cleave carbon-carbo bonds.

Ionomers are generally perceived as being phase separated materials. However, the optimal morphology that an ionomer should adopt and that would be practical is still being debated. This situation is not helped by the uncertainty of the morphology adopted under operating fuel cell conditions of the incumbent material. Here I will describe a study that contrasts fully amorphous materials with materials designed to have phase separated morphologies of known symmetries and dimensions. While the designed materials allow us to probe certain concepts of ion conduction with pore shape and size, they do not necessarily out perform the amorphous materials. Curiously we show that the role of water has more to do with morphological changes in flexible materials than enhancing ion conduction in non-sulfonic acid based materials. This has implications for the fabrication of thin robust films that will be needed for an operating fuel cell. In the case of AEMs while a cation has yet to be found that is stable under hot and dry operation, water may be a necessary evil rather than an enhancer of anion conduction.

8:40am **EN+NS-ThM3 Rational Design of Competitive Electrocatalysts for Hydrogen Fuel Cells**, S. Stolbov, M. Alcántara Ortigoza, University of Central Florida

The large-scale commercial application of hydrogen fuel cells requires efficient and cost-effective electrocatalysts for the oxygen reduction reaction (ORR), which occurs on the cathode. We demonstrate that rational design can render electrocatalysts possessing both virtues. In this work, by unifying the knowledge on surface morphology, composition, electronic structure and reactivity, we find that tri-metallic sandwich-like structures are an excellent choice for optimization. Their constituting species are designed to couple synergistically rendering reaction-environment stability, cost-effectiveness and high catalytic activity. This cooperative-action concept enabled us to predict two Pt-free ORR electrocatalysts: Pd/Fe/W(110) and Au/Ru/W(110) [1]. Density functional theory calculations of the reaction free-energy diagrams indicate that these materials are more active toward ORR than the so far best Pt-based catalysts.

1. S. Stolbov and M. Alcántara Ortigoza; *J. Phys. Chem. Letts.* **3**, 463 (2012)

9:00am **EN+NS-ThM4 Nanocomposite Materials for Lithium Ion Batteries**, G. Yushin, Georgia Institute of Technology **INVITED**

High power energy storage devices, such as supercapacitors and Li-ion batteries, are critical for the development of zero-emission electrical vehicles, large scale smart grid, and energy efficient cargo ships and locomotives. The energy storage characteristics of supercapacitors and Li-ion batteries are mostly determined by the specific capacities of their electrodes, while their power characteristics are influenced by the maximum rate of the ion transport. The talk will focus on the development of nanocomposite electrodes capable to improve both the energy and power storage characteristics of the state of the art devices. Carbon-polymer and carbon-metal oxide nanocomposites have been demonstrated to greatly exceed the specific capacitance of traditional electrodes for supercapacitors. Selected materials showed the unprecedented ultra-fast charging and discharging characteristics. Intelligently designed silicon-carbon-polymer composites showed up to 8 times higher specific capacity than graphite, the conventional anode material in Li-ion batteries, and stable performance for over 1000 cycles. In order to overcome the limitations of traditional composites precise control over the materials' structure and porosity at the nanoscale was required.

9:40am **EN+NS-ThM6 Engineering Li₄Al₂Si₂O Ionic Conductive Thin Films by Atomic Layer Deposition for Lithium-ion Battery Applications**, Y.-C. Perng, J. Cho, D. Membreno, N. Cirigliano, B. Dunn, J.P. Chang, University of California, Los Angeles

Lithium (Li)-ion batteries have drawn much attention for their outstanding performance in portable electronics applications with the potentials to function as a power source for further miniaturized devices, including micro-systems through the utilization of 3-dimensional electrodes based on high aspect ratio pillars. To realize this potential, an ultra-thin and highly conformal electrolyte layer is needed to coat the 3D electrode array. The ionic conductor lithium aluminosilicate (LiAlSiO₄) synthesized by atomic layer deposition (ALD) is a promising electrolyte material for 3D battery applications not only due to its high ionic conductivity along its c-axis resulting from channels formed by the alternating tetrahedra of aluminum-oxygen (Al-O) and silicon-oxygen (Si-O), but also expected to provide similar improved cell cyclability, as reported in the preliminary studies of ultra-thin metal-oxide ALD coatings on electrodes.

The self-limiting characteristic of ALD allows for precise control of thickness and composition of complex oxides and results in a highly conformal and pinhole-free coating suitable in 3D micro-battery applications or electrolyte surface coatings. The metal precursors used in this work are tetraethyl orthosilicate (TEOS), trimethylaluminum (TMA) and lithium t-butoxide (LTB). These precursors, along with water vapor as the oxidant, were used to deposit SiO₂, Al₂O₃ and Li₂O, with the deposition rates in the range of 0.8–2Å/cycle, respectively. The deposition rate of stoichiometric LiAlSiO₄ was ~20Å/cycle at a temperature of 290°C. The concentration of each metal element in Li_xAl_ySi_zO (LASO) thin films was found to correlate closely to ALD cycles and the associated incubation times. The crystallinity of the films after post-deposition rapid thermal annealing (RTA) was a function of cation atomic percentage. Li-ionic conductivities and the activation energy of as-deposited LASO films with respect to lithium contents as well as their relation to the film thickness were studied. The LASO ALD coating on 3D features, such as NWs and nanoparticles (NPs), were confirmed to be conformal and uniform by transmission electron microscopy (TEM) imaging. The cell performance as well as cyclability enhancement from Li_xAl_ySi_zO was investigated for a silicon-nanowire 3D microbattery, where SiNW was used as an anode, to

explore the potentials of a solid-state SiNW battery with a solid-oxide electrolyte.

10:40am **EN+NS-ThM9 Titanium Oxide and Lithium Titanium Oxide Coated 3D Nanoelectrodes for Li-ion Microbatteries**, G. Pattanaik, J. Haag, M.F. Durstock, Air Force Research Laboratory

Titanium oxide based materials, including both Li-titanates and various TiO₂ polymorphs are promising alternatives to carbonaceous anode materials for Li-ion rechargeable batteries because of their higher voltage operation (enhanced safety), relatively small volume expansion upon lithiation, minimal electrode/electrolyte interface reactivity (nonexistent SEI layer), inexpensive and biocompatible non-toxic nature. Nanoscale three-dimensional (3D) architectures of current collectors for microbatteries would significantly increase the areal capacity over their planar counterparts, if the active Li-insertion electrode material could be coated conformally. The nanoscale thickness of the active electrode layer in combination with an electronically conducting 3D nanoarchitecture of the current collector should enable high areal capacity and fast charge-discharge rates.

Atomic layer deposition (ALD) is capable of growing conformal ultra thin films on complex 3D surface morphologies. We have used ALD to grow conformal layers of titanium oxide and lithium titanium oxide on various 3D nanoarchitectures including high aspect ratio nanoporous Al₂O₃ templates, template-electrodeposited 3D metal nanowire arrays and carbon nanotube buckypapers. The precursors for ALD used in this study include lithium t-butoxide, tetrakis(dimethylamido)titanium (TDMAT) and water. We have been able to grow conformal layers with controllable thickness at nanometer scale uniformly coated around the high aspect ratio features.

A significant increase in areal capacity (up to two orders of magnitude) was obtained in anatase TiO₂ coated Ni nanowire arrays over 2D thin film electrodes of a similar footprint. ALD TiO₂ coated buckypapers showed specific capacities in excess of 200 mAh/g at C/10, with 70% of the capacity retained at 5C. At 1C, 95% of the initial capacity is retained after 500 charge/discharge cycles. ALD deposition of LiOx and TiOx and subsequent thermal annealing leads to a combination of TiO₂ and spinel lithium titanium oxide (Li₄Ti₅O₁₂) phases. The presence of these phases is reflected in XRD as well as electrochemical charge-discharge curves. This presentation will discuss a systematic study of the ALD growth of 3D titanium oxide and lithium titanium oxide nanostructures and their electrochemical characterization.

11:20am **EN+NS-ThM11 The Contribution of Auger Electron Spectroscopy to a Better Understanding of the Lithiation Process Occurring in Si-based Anodes Designed for Li-ion Batteries**, E. Radvanyi, E. De Vito, W. Porcher, S. Jouanneau, CEA Grenoble, France

With a specific capacity of almost 3580 mAh.g⁻¹ at room temperature (corresponding to the Li₁₅Si₄ alloy), silicon is a promising element for designing new efficient anodes in Li-ion battery technology. However, because of huge material volumic expansion (around 300%) during the lithiation process¹, leading to a quick pulverization of the electrode², silicon has been used only as an additive to graphite in commercial cells so far³. In order to improve Si-based electrodes cyclability, a better understanding of the lithium insertion mechanisms is among the key issues⁴. The study of the lithiation process in silicon particles is particularly challenging. Indeed, a complete amorphization of the material during cycling⁴ makes difficult the use of surface characterization techniques based on beam diffraction (e.g. X-rays or electrons). In this study, we have used Auger Electron Spectroscopy (AES) to study these mechanisms. Poor attention has been focused on AES in the battery research field so far^{5,6}. In this work we emphasize its interest, notably for the study of the lithiation mechanisms in silicon particles. The first part of this work is dedicated to the study of Li-Si alloys by using AES. Several crystalline Li_xSi alloys (Li₇Si₃, Li₁₃Si₄ and Li₂₂Si₅) have been synthesized and characterized by X-Ray diffraction and AES. It appears that the atomic relative concentrations obtained by AES for the elements Li and Si are accurate with a tolerance of approximately 10%. The effect of Ar⁺ sputtering has also been investigated. After this initial work, six electrodes based on silicon particles have been analyzed by using AES for different "State Of Charge" (SOC) within the first electrochemical cycle.

For each SOC, several silicon particles have been investigated individually. Li and Si depth concentration profiles have been achieved by following Li (KLL) and Si (LVV) Auger transitions. Thanks to the good spatial resolution (17 nm at 10kV/1nA), it is possible to detect inhomogeneities of Li concentration at the particle surface. Based on the results obtained on different silicon particles at several SOC, a lithiation model is proposed and discussed.

(1) Beaulieu, L. Y.; Hatchard, T. D.; Bonakdarpour, A.; Fleischer, M. D.; Dahn, J. R. *J. Electrochem. Soc.* **2003**, *150*(11), A1457-A1464

- (2) Kasavajjula, U.; Wang, C.; Appleby, A. J. *J. Power Sources* **2007**, *163* (2), 1003-1039
- (3) www.hitachi.com
- (4) Zhang, W. J. *J. Power Sources* **2011**, *196* (1), 13-24
- (5) Morigaki, K. I.; Ohta, A. *J. Power Sources* **1998**, *76* (2), 159-166
- (6) Kim, Y. J.; Lee, H.; Sohn, H. J. *Electrochem. Comm.* **2009**, *11* (11), 2125-2128

11:40am **EN+NS-ThM12 Organic/Inorganic Composite Materials as Anodes for Lithium Ion Batteries**, *M. Thakur, R.B. Pernites*, Rice University, *M. Isaacson*, Lockheed Martin Space Systems, *M.S. Wong*, Rice University, *S.L. Sinsabaugh*, Lockheed Martin MS2, *S.L. Biswal*, Rice University

Silicon continues to draw great interest as an anode material for lithium ion batteries due to its large specific capacity for lithium. Electrochemical etching silicon is one of several anode materials of interest, but its energy density is oftentimes limited due to its attachment to an unreactive silicon substrate. Here, we present a novel "liftoff" method by which a freestanding macroporous silicon film (MPSF) is electrochemically detached from the underlying bulk silicon and combined with pyrolyzed polyacrylonitrile (PAN), a conductive polymer. We report the performance of these silicon thin films with and without pyrolyzed PAN.

Electron Transport at the Nanoscale Focus Topic Room: 16 - Session ET+NS+EM-ThM

Electron Transport at the Nanoscale: Nanowires and Junctions

Moderator: K. Clark, Oak Ridge National Laboratory, A.-P. Li, Oak Ridge National Laboratory

8:00am **ET+NS+EM-ThM1 Functional Imaging of Semiconductor Nanowires and Devices**, *L.J. Lauhon*, Northwestern University **INVITED** Microscopy has played a central role in the advancement of nanoscience and nanotechnology by enabling the direct visualization of nanoscale structure, and by extension predictive models of novel physical behaviors. Correlated imaging of nanoscale structure *and* properties is an important frontier that can provide a rational basis for engineering new materials and devices. I will describe our approach to correlated functional imaging with a focus on semiconductor nanowires. Nanocrystal growth modes such as the vapor-liquid-solid process provide the ability to tailor nanoscale structure and composition in three dimensions, creating new opportunities in a range of applications including light harvesting and solid state lighting. In this context, we have explored a number of important processing-structure-property relationships using atom probe tomography, scanning transmission electron microscopy, Raman microspectroscopy, and scanning photocurrent microscopy. From these studies, we develop a more comprehensive understanding of the influence of geometry, size, defects, dopants, and interfaces on carrier generation, recombination, and transport in nanostructured materials. This quantitative approach to characterization of model systems aims to identify applications that can derive significant benefits from the adoption of unconventional nanostructured materials.

8:40am **ET+NS+EM-ThM3 Electronic Transport and Structure Relations in Self-Assembled GdSi₂ Quantum Wires**, *S.Y. Qin, T. Kim*, Oak Ridge National Laboratory, *Y. Zhang, W. Ouyang*, University of California Irvine, *H. Weitering*, The University of Tennessee, *C. Shih*, The University of Texas at Austin, *A.P. Baddorf*, Oak Ridge National Laboratory, *R. Wu*, University of California Irvine, *A.-P. Li*, Oak Ridge National Laboratory

Quantum wires are extremely narrow one-dimensional (1D) materials where electron motion is allowed only along the wire direction, and is confined in the other two directions. Quantum wires, as a smallest electronic conductor, are expected to be a fundamental component in all quantum electronic architectures. The electronic conductance in quantum wires, however, is often dictated by structural instabilities and electron localization at the atomic scale. Adding interwire coupling can often lead to the formation of charge density waves. In both cases, the metallic state is not stable and a metal to insulator transition (MIT) occurs at low temperature. [1] Here we show that robust metallic conductance can be stabilized by interwire coupling, while the isolated single nanowires exhibit a MIT due to quantum localization.

We grow the quantum wires of GdSi₂ on Si(100) and study the evolution of electronic transport as a function of temperature and interwire coupling as the quantum wires are self-assembled *wire-by-wire*. As shown in Fig. 1,

individual nanowires have a width of 16.7 Å, a height of 4 Å, and lengths of micrometers. These nanowires can be grown either in the form of isolated nanowires or bundles with a number of constituent wires separated by an atomic interwire spacing. We perform the correlated study of electronic properties by utilizing both scanning tunneling microscopy and nanotransport measurements on the same nanowire. [2] The approach takes advantage of our developments in fabricating nanocontacts using a field-induced atom emission process to bridge the atomic wires and the mesoscopic transport electrodes. [3] A MIT is revealed in isolated nanowires, while a robust metallic state is obtained in wire bundles at low temperature. The results provide a rare glimpse of the intrinsic structure-transport relations and the influence of local environments at the atomic scale. This research was conducted at the Center for Nanophase Materials Sciences, which is sponsored at Oak Ridge National Laboratory by the Office of Basic Energy Sciences, U.S. Department of Energy.

1. Changgan Zeng, P.R.C. Kent, Tae-Hwan Kim, An-Ping Li, Hanno H. Weitering, *Nature Materials*, **7**, 539 (2008).

2. Shengyong Qin, Tae-Hwan Kim, Wenjie Ouyang, Yanning Zhang, Hanno H. Weitering, Chih-Kang Shih, Arthur P. Baddorf, Ruqian Wu, and An-Ping Li, *Nano letters*, **12** (2), 938 (2012).

3. Shengyong Qin, Sondra Hellstrom, Zhenan Bao, Boyan Boyanov, and An-Ping Li, *Appl. Phys. Lett.* **100** (11), 022211 (2012).

9:00am **ET+NS+EM-ThM4 Multi-Segment Nanowire Heterojunctions of AuGe and Ge: Fabrication and Electrical Transport**, *X.D. Li, G.W. Meng*, Chinese Academy of Sciences, China, *S.Y. Qin, A.-P. Li*, Oak Ridge National Laboratory

One-dimensional (1D) multiple segment nanostructures that contain heterojunctions between various metals and semiconductors are of great interest due to their fascinating chemistry and size-, shape-, and material-dependent properties. Here we report on the synthesis and electronic characterization of multi - segment nanowire (NW) junctions of Au1-xGex and Ge. The 1D heterostructures are grown with a low - temperature chemical vapor deposition process, assisted by electrodeposited Au NWs inside nanochannels of anodic aluminum oxide template.[1,2] The Au-catalyzed vapor-liquid-solid growth process occurs simultaneously in multiple locations along the nanochannel, which leads to multi-segment Au1-xGex/Ge heterojunctions. The structures of the as-grown hybrid NWs, analyzed by using transmission electron microscopy and energy dispersive X-ray spectroscopy elemental mapping, show clear compositional modulation with variable modulation period and controllable junction numbers. Remarkably, both GeNW and Au1-xGexNW segments are single crystalline with abrupt interfaces and good crystallographic coherences. The electronic and transport properties of individual NW junctions are measured by using a multi-probe scanning tunneling microscope (STM). The semiconducting nature of Ge segments and the metallic behavior of Au1-xGex segments are examined by scanning tunneling spectroscopy (STS). The transport current-voltage curves across the heterojunctions show a characteristic rectifying behavior, which is discussed in association with the potential barriers at the junction. The high yield of multiple segment NW junctions and the ability to control predictably the properties of a metal-semiconductor can facilitate the applications in nanoelectronics and optoelectronics that harness multiple functionalities of hetero-interfaces.

[1] Li, X. D.; Meng, G. W.; Xu, Q. L.; Kong, M. G.; Zhu, X. G.; Chu, Z. Q.; Li, A. P. Controlled Synthesis of Germanium Nanowires and Nanotubes with Variable Morphologies and Sizes. *Nano Lett.* **2011**, *11*, 1704–1709.

[2] Li, X. D.; Meng, G. W.; Qin, S. Y.; Xu, Q. L.; Chu, Z. Q.; Zhu, X. G.; Kong, M. G.; Li, A. P. Nanochannel-Directed Growth of Multi-Segment Nanowire Heterojunctions of Metallic Au1-xGex and Semiconducting Ge. *ACS Nano* **2012**, *6*, 831–836.

9:20am **ET+NS+EM-ThM5 Single Charge Nano Memory using Nano Carbon Material**, *K. Matsumoto, T. Kamimura*, Osaka University, Japan
Single charges nano memory which can shift the threshold voltage by the stored single charge and operated at room temperature was realized using the carbon nanotube as an ultra short channel of 10nm.

The double gate stack insulator layers of Al₂O₃(3nm) and SiN_x (27nm) are deposited using the atomic layer deposition to the suspended carbon nanotube with source and drain electrodes of 70nm separation. The carbon nanotube channel was then surrounded by this double gate stack insulator layers and the gap between the source drain electrodes with the insulator layers reduced down to as small as 10nm. The gate metal was then deposited through this gap to form the gate electrode of 10nm.

The dependence of the drain current on the top gate bias shows weak oscillation along the gate bias with the period of 220mV. The oscillation is attributed to the single charge injection from CNT channel to the Al₂O₃/SiN_x interface trap, which make the threshold voltage shift of 220mV. The

injection of charge is regulated by the Coulomb blockade that stops the next charge to be injected to the trap. The around trip of the gate bias produces the hysteresis. The width of the hysteresis was also regulated by the single charge injection and shows the stepwise increase.

Thus, we have succeeded in fabricating the single charge memory operated at room temperature.

9:40am ET+NS+EM-ThM6 Combining Atomic Structure, Local Band Alignment, and Electron Transport through Individual Semiconductor Nanowires using Scanning Tunneling Microscopy, R. Timm, O. Persson, M. Hjort, M.T. Borgström, L. Samuelson, A. Mikkelsen, Lund University, Sweden

III-V semiconductor nanowires offer tremendous possibilities for device application in energy and information technology [1]. Due to their unique properties and extreme surface-to-volume ratio, it is both essential and challenging to investigate their atomic structure and to combine this information with electrical measurements on individual nanowires. Recently, we have managed to clean InAs nanowires from their native oxide and obtained first atomically resolved images of their side surfaces by using scanning tunneling microscopy (STM) [2]. Here, we present a systematic STM study covering various nanowire surface structures emerging from different III-V material systems and different crystal structures. By combining STM imaging with scanning tunneling spectroscopy (STS) measurements we simultaneously study the surface structure and local electronic properties across the interfaces of nanowire heterostructures like polytypic nanowires, p - n -junctions, and material heterostructures.

In order to go further in combining local structural and electronic characterization as well as transport measurements of nanowire devices, we have developed a new method to perform STM/S on individual nanowires *in-situ* under device operation: For this, specific heterostructure nanowires, distributed on a SiO₂/Si substrate, are contacted with metal electrodes defined by electron beam lithography. Using a combined Atomic Force Microscopy (AFM) / STM setup, we can first locate an individual nanowire in AFM mode and then acquire STM images and STS spectra on the contacted nanowire. Thus, we obtain the LDOS spatially resolved along the nanowire, even while the nanowire is externally biased via the metal contacts, allowing simultaneous transport studies. We will show and discuss initial results for different heterostructure nanowire devices, demonstrating the large potential of this new method.

Finally, we can also use the STM to measure electron transport through individual upright standing nanowires still on their growth substrate: After imaging the nanowires from top by STM [3], a point contact between the STM tip and the Au particle on top of the nanowire can be established in ultrahigh vacuum, thereby overcoming the problems in contacting single nanowires known from conventional setups. A high accuracy and reproducibility of this method has been demonstrated for InP and InAs nanowires with different doping levels [4] as well as for Schottky barrier measurements on Au/GaAs nanowires.

[1] Y. Li *et al.*, *Mater. Today* **9** (10), 18 (2006).

[2] E. Hilner *et al.*, *NanoLetters* **8**, 3978 (2008).

[3] A. Fian *et al.*, *Nano Letters* **10**, 3893 (2010).

[4] R. Timm *et al.*, *submitted* (2012).

10:40am ET+NS+EM-ThM9 Point-Contact Spectroscopy Study of Topological Insulators and Superconductors, Z. Jiang, Georgia Institute of Technology

Recently, much attention has been given to an intriguing class of materials, the so-called topological insulators. This type of material exhibits a band gap in the bulk, but gapless states on the edge or surface, which are protected by topological order and cannot be analogized to previous conventional semiconductors or insulators. When topological insulators are in contact with a superconductor (e.g., Nb, a conventional s -wave superconductor), novel proximity effect occurs. Theory predicts that the proximity induced superconducting state is spinless and p -wave like, and Majorana bound states may appear at the edges. On the other hand, in a related research avenue topological superconductors are predicted to possess unconventional pairing symmetries and gapless surface Andreev bound states. Theoretically massless Majorana fermions could be realized in such materials and used as a building block for topological quantum computation.

Here we present our point-contact spectroscopy studies of topological insulators and superconductors. Specifically, we use a superconducting Nb tip to approach the surface of topological insulators and measure the interface conductance as a function of bias voltage, temperature and magnetic field. Indeed, we find that a superconducting state can be induced at the interface when the Nb tip is in good contact with the topological insulator, as evidenced by observation of a zero-bias conductance peak in

the point-contact spectra at a temperature below the superconducting transition temperature of Nb. Such an induced superconducting state is robust even in a magnetic field up to 1T. In the study of topological superconductors, we use a normal-metal Au tip to approach the surface, and a zero-bias conductance peak is also observed. Owing to accurate control of the point-contact barrier strength (tip/sample) in our experiments, the obtained spectra are free of artificial background, and therefore can be quantitatively compared with existing theories; good agreement is achieved.

11:00am ET+NS+EM-ThM10 Identifying and Measuring the State Variables in TaOx Memristors, P.R. Mickel, M. Marinella, C.D. James, Sandia National Laboratories

We present evidence of the identification and characterization of a new state variable in TaOx memristors. Thus far, the state variable controlling the resistive switching has been believed to be the oxygen concentration in the conducting Ta filament. However, using voltage pulse measurements sensitive to small changes in resistance, we show that the changing area of the conducting filament is in fact the dominant switching mechanism. The oxygen concentration in the Ta filament is shown to control the memristor resistance for low resistances, after which we observe a clear crossover to the area state variable dominated resistance range. Voltage and temperature dependence are investigated for the switching time-scales, τ_{on} , and magnitudes of filament area change, providing insight into their driving mechanisms and the resolution limits of their modulation.

11:20am ET+NS+EM-ThM11 Terahertz Spectroscopy and Carrier Dynamics of Al Doped ZnO Nanowires, S. Balci, W. Baughman, D.S. Wilbert, G. Shen, N. Dawahre, P. Kung, S.M. Kim, The University of Alabama

Terahertz time domain spectroscopy (THz-TDS) has been widely investigated for many applications in sensing and imaging technologies over the past two decades. Terahertz wave, with a frequency between 300GHz to 10THz, is especially attractive for various applications including security monitoring, biomedical imaging, high speed electronics and communications, and chemical and biological sensing. There is also an increasing interest for nondestructive testing using the THz waves because they have unique properties of propagation through certain media and cover a number of important frequencies. For such applications, THz-TDS has become a powerful tool and measurement technique that can probe carrier dynamics at high frequencies, and thus may yield a better understanding of the characteristics of high frequency optoelectronics and many other fundamental properties of materials. Using THz-TDS, one can determine the frequency dependence of basic properties of materials, including their complex dielectric constant, refractive index and electrical conductivity. Unlike conventional Fourier-Transform spectroscopy, THz-TDS is sensitive to both the amplitude and the phase of the wave, thereby allowing for a direct approach to determining complex values of material parameters with the advantage of high signal to noise ratio and coherent detection. In addition, it is possible to carry out THz-TDS experiments without any electrical contact to the sample being probed, which significantly facilitates electrical measurements on nanostructures and nanomaterials.

In this work, we investigated the physical properties of ZnO:Al nanowires (NWs) in using THz-TDS both at room temperature and elevated temperatures for the first time. ZnO NWs were grown by thermal chemical vapor deposition and in-situ doped with Al, which increased their electrical conductivity by one order of magnitude compared to undoped nanowires. THz-TDS measurements yielded the relative change in the transmitted THz electric field magnitude and phase caused by the samples being probed, which was used to extract the nanowire material refractive indices through mathematical iterative calculations. These subsequently allowed a determination of the complex conductivity, refractive index, and absorption coefficient. To obtain the carrier dynamics parameters, we showed that the Drude-Smith model had to be applied to the frequency dependent complex conductivity in order to determine the plasma frequency and relaxation time. To gain a better understanding of the dependence on doping, the measurements were performed for both undoped ZnO NWs and Al-doped ZnO NWs, as well as a function of temperature in each case.

11:40am ET+NS+EM-ThM12 Probing Surface-Independent Minority Carrier Transport in Semiconductor Nanowires using Kelvin Probe Microscopy, A. Soudi, C. Hsu, Y. Gu, Washington State University

In advancing semiconductor nanowire-based device technologies, a quantitative knowledge of carrier transport properties is required for a rational design of devices with controlled performance. The one-dimensional confinement of charge carriers and phonons can lead to novel transport properties, and thus represents an advantage of semiconductor nanowires in electronic and opto-electronic applications. However, due to the high surface-to-volume ratio, surface effects are prevalent in nanowires, and the measured carrier transport properties are usually dominated by

surface-related processes, such as carrier trapping and recombination processes facilitated by surface states. To evaluate the intrinsic transport properties, especially those related to the confinement effects, the capability to probe surface-independent carrier transport properties is desired. Here we present studies of bulk limited minority carrier transport properties in semiconductor nanowires using the scanning Kelvin probe microscopy technique. Specifically, by measuring and modeling the spatial variations of the nanowire surface potential close to a nanowire-metal Schottky junction, both under an above-bandgap illumination and in the dark, the surface-independent minority carrier diffusion length was obtained.

Graphene and Related Materials Focus Topic Room: 13 - Session GR+AS+NS+SS-ThM

Graphene Nanostructures

Moderator: A. Kis, EPFL, Switzerland

8:00am **GR+AS+NS+SS-ThM1 Atomic and Electronic Structures of Graphene Nanoribbon made by MBE on Vicinal SiC Substrate.** *F. Komori, K. Nakatsuji, T. Yoshimura*, University of Tokyo, Japan, *T. Kajiwara, K. Takagi, S. Tanaka*, Kyushu University, Japan

Electronic states of graphene nanoribbon attract much interest because its intrinsic metallic band is modified to have a gap or a one-dimensional edge state at the Dirac energy E_D . Actually, microfabricated graphene [1] showed an energy gap at E_D , and the gap size increases with decreasing the width. Fabrication of well-controlled graphene nanoribbons on macroscopic area of a semiconductor substrate is, however, still one of the challenging issues in graphene research. Here, we report characterizations of graphene nanoribbon made by carbon molecular beam epitaxy (MBE) and a hydrogen treatment on a vicinal SiC(0001) substrate. Use of MBE is essential because graphene is made over the step edges of the SiC substrate in the case of graphene formation by widely-used thermal decomposition.

In the experiment, a $6\sqrt{3} \times 6\sqrt{3}$ structure was first made by MBE on the anisotropic terrace of the Si-terminated surface of a nitrogen-doped 6H-SiC(0001) substrate vicinal to the [1-100] direction. The tilting angle of the substrate was 4 degree, and a well-ordered step-and-terrace structure was made after cleaning the substrate by annealing in hydrogen as confirmed by atomic force microscopy. We optimized the substrate temperature and the carbon deposition rate to make a homogeneous $6\sqrt{3} \times 6\sqrt{3}$ structure on the terraces without thermal decomposition of the substrate. The surface structure was *in situ* monitored by reflection high energy electron diffraction, and the width of the $6\sqrt{3} \times 6\sqrt{3}$ area on the terrace was adjusted by monitoring the $6\sqrt{3} \times 6\sqrt{3}$ spots. After stopping the growth, the sample was exposed to hydrogen molecules at 600 °C to transform the surface $6\sqrt{3} \times 6\sqrt{3}$ layer to single-layer graphene by inserting hydrogen atoms at the interface. [2]

Graphene honeycomb lattice without the $6\sqrt{3} \times 6\sqrt{3}$ structure was confirmed by low energy electron diffraction and scanning tunneling microscopy (STM). Few point defects are seen at the graphene on the terrace in the STM images of atomic resolution. The width of graphene nanoribbon on the substrate terrace is 10-15 nm, depending on the growth condition. The electronic states of the graphene nanoribbon were studied using angle-resolved photoemission spectroscopy (ARPES) at 130 K as in the previous report. [3] The top of the π band of the graphene nanoribbon was 0.05 ~ 0.25 eV below the Fermi energy. No signal from the π^* band was detected by ARPES above the top of the π band, indicating the gap formation at E_D .

References

1. M. Y. Han *et al.*, Phys. Rev. Lett. **98**, 206805 (2007).
2. C. Riedl *et al.*, Phys. Rev. Lett. **103**, 246804 (2009).
3. K. Nakatsuji *et al.*, Phys. Rev. **B82** 045428 (2010).

8:20am **GR+AS+NS+SS-ThM2 Carrier Transport Behavior of Carbon Nanotube Transistors with Single Semiconducting and Metallic Tube.** *P. Sakalas, M. Schroter*, Technische Universität Dresden, Germany

The high interest in using carbon nanotube FETs in advanced electronics is based on their unique 1D transport properties such as quasi-ballistic transport. The high carrier velocity together with the quasi 1D tube geometry yield a very low intrinsic capacitance per tube of approximately 80 aF/mm in multitube structures. Those properties makes CNTFETs very interesting for high frequency and power applications.

CNTFETs with a single semiconducting tube yield too low current (25 μ A) for useful applications and thus the transistors with thousands tubes in parallel are being fabricated [1][2]. Unfortunately, following theory 1/3rd of all tubes are metallic. Carrier scattering is better understood for metallic tubes and it is believed that for semiconducting tubes, despite more

complexity, the same scattering mechanisms are applicable: CNTs defect scattering, physical bends and phonon scattering are present. Investigation of CNTFETs with a single semiconducting (ST), single metallic (MT) and metallic+semiconducting (MST) tubes at different lattice temperature environment was never done before and enables a deeper insight of CNT transport properties to further improve the application-oriented device behavior. It was shown that multifinger CNTFETs exhibited a weak temperature dependence of IV, RF and NF indicating a very weak electron-phonon interaction and the absence of charge-carrier freeze-out known for conventional doped semiconductors [3],[4].

In this work transistors with single ST, single MT and double MST were selected. Transistors have 800 nm channel length and features n-type behavior. IV characteristics were measured on wafer for manufacturable CNTFET process selected single CNTs at different lattice temperatures. The investigated structures have a fixed gate length of 0.35 μ m and gate width of 40 μ m. The source-drain spacing (channel length) is 800 nm. A 20 nm thick HfO₂ was used for the gate oxide. The devices were fabricated with the process technology described in [1][2]. The CNTFETs were embedded in DC pads for on-wafer measurements. Transfer characteristics of ST and MT transistor structures at ambient temperature $T_0 = 300$ K, are shown in Fig.1 and Fig.2, Fig.3, Fig.4. The drain current show saturation for ST device, typical for MOSFETs. Nevertheless the carrier transport is very different. The dependence of drain current over the temperature will enable the analysis of transport behavior of single ST and MT and coupled MST. As it is seen from Fig.3 and Fig.4 the MT transistor structure behaves as nonlinear resistor.

8:40am **GR+AS+NS+SS-ThM3 Fabrication of Chemically-isolated Graphene Nanoribbons (GNRs) by Scanning Probe Nanolithography using a Heated Probe.** *W.K. Lee, J.T. Robinson, R. Stine, C.R. Tamana, D. Gunlycke*, Naval Research Laboratory, *M. Haydell, E. Cimpoiasu*, U.S. Naval Academy, *W. King*, University of Illinois at Urbana Champaign, *P.E. Sheehan*, Naval Research Laboratory

One route to realizing graphene as a material for digital-type devices is through the lithographic patterning of graphene nanoribbons (GNRs). GNRs enable band gap engineering that is dependent on nanoribbon width and edge state. We employed two complementary AFM-based lithography techniques to pattern GNRs: (1) thermal dip-pen nanolithography (tDPN)¹ and (2) thermochemical nanolithography (TCNL)². Though inverse in approach, both techniques generate GNRs into a larger sheet of insulating chemically-modified graphene. Both lithographies were performed on CVD-grown single-layered graphene (SLG) on SiO₂/Si substrates using heated AFM probes. The first approach, tDPN, used the heated probe to deposit narrow polystyrene (PS) ribbons on pristine graphene. The areas of the graphene not protected by the polymer were then fluorinated, converting them to a highly insulating state, which leaves behind a chemically isolate GNR channel. We show that the PS protected ribbon was the only conductive pathway for active device. Secondly, we use the converse approach by using the heated AFM probe to locally reduce fluorographene back to graphene, leaving behind a conductive GNR channel. Both techniques can generate a wide range of nanoribbon widths while avoiding electron beams which can damage graphene. We discuss the relative merits of each strategy, as well as their impact on electrical properties (e.g., doping).

1. WK Lee *et al.*, *Nano Letters*, **11**, 5461, 2011
2. Z Wei *et al.*, *Science*, **328**, 1371, 2010

9:20am **GR+AS+NS+SS-ThM5 Growth of a Linear Topological Defect in Graphene as a Gate-tunable Valley Valve.** *A. Zettl, J.-H. Chen, N. Alem*, Univ. of California at Berkeley, Lawrence Berkeley Lab, *G. Autes, F. Gargiulo*, Ecole Polytechnique Fédérale de Lausanne (EPFL), Switzerland, *A. Gautam, M. Linck*, Lawrence Berkeley National Lab, *C. Kisielowski*, Lawrence Livermore National Lab, *O.V. Yazyev*, Ecole Polytechnique Fédérale de Lausanne (EPFL), Switzerland, *S.G. Louie*, Univ. of California at Berkeley, Lawrence Berkeley Lab

INVITED

The valleytronics, a zero-magnetic-field equivalent of spintronics, could be realized in graphene if a simple scheme can be conceived to generate and to detect valley polarization in the material. Here we provide the first direct experimental observation of the self-sustained, atomically controlled growth of a peculiar linear defect structure in suspended graphene. The structure consists in units of octagon and pentagon pairs (termed 5-5-8 defect) and can be grown from a single pentagon seed in graphene under electrical bias. First-principle simulations show that the 5-5-8 defect can act as a gate-tunable valley valve. The result represents a critical step towards realizing valleytronics in graphene.

10:40am **GR+AS+NS+SS-ThM9 Crystalline and Electrical Properties of Vertically-Laminated Carbon Nanowalls formed by Two-Step Growth Method.** *H. Kondo, T. Kanda,* Nagoya University, Japan, *M. Hiramatsu,* Meijo University, Japan, *K. Ishikawa, M. Sekine, M. Hori,* Nagoya University, Japan

Carbon nanowall (CNW) is one of carbon nanomaterials consisting of stacked graphene sheets, which are vertically standing on the substrate. Due to the unique properties of graphene sheets, such as high carrier mobility, large current carrying capability, and so forth, it is expected that the CNW also have such the excellent electrical and physical properties. On the other hand, In the CNWs, the bending and branching graphene sheets take a maze-like form. Therefore, due to their unique morphology and properties, the CNWs are promising as channel and electrode materials in the various types of the future nanoelectrics devices. At the construction of the CNW devices, vertical lamination of different types of CNWs is one of the useful and important technique as basic elements of the devices.

In this study, we investigated sequential two-step growth of CNWs to form the vertically-laminated structures. In this experiment, two types of CNW growth processes with different conditions were sequentially performed on Si substrate by an electron beam excited plasma-enhanced chemical vapor deposition (EBEP-CVD) using CH₄/H₂ mixture gas. Firstly, the CNW was grown at 600°C and 2.67 Pa for 10 min. Then, the second-step growth process was performed at 480°C for 10 min. The CNW samples formed only by the single-step growth at 480°C or 600°C were also prepared for comparison. Morphology and crystalline structures of CNWs were analyzed by scanning electron microscopy and Raman spectroscopy.

In the case of the single-step growth, only after the growth at 600°C, about 600 nm-thick CNWs were formed, although CNWs hardly grew at 480°C. On the other hand, in the case of the step-growth, about 1200 nm-thick CNWs were formed after the second-step growth at 480°C, compared to the single-step growth at 600°C. No boundary was found between the lower and upper region. The stacks of graphene sheets formed seamless structures. According to the Raman spectra, the crystalline structures of the CNWs were hardly changed even after the first-step growth at 600°C and the second-step growth at 480°C. This result means that the nanographene can restart to grow easily and continuously at the edges of the previously-grown graphene even at 480°C without the nucleation. These results indicate the possibility to realize the vertical junction of different types of CNWs, such as a p-n junction. At the session, the interfacial structures and electrical properties of the vertically-laminated CNWs will also be discussed.

11:00am **GR+AS+NS+SS-ThM10 Surface Modification of Vertically Oriented Graphene Electrochemical Double-Layer Capacitors.** *R.A. Quinlan,* Naval Surface Warfare Center, Carderock Division, *M. Cai,* The College of William and Mary, *A.N. Mansour,* Naval Surface Warfare Center, Carderock Division, *R.A. Outlaw,* The College of William and Mary

Previously reported efforts have identified the potential of vertically oriented graphene nanosheets in electrochemical double-layer capacitors (Miller et. al, Science 2010) for efficient AC line-filtering performance. Continued investigations to improve performance suggest that the availability of a high edge and surface defect density could be the dominant mechanism. Furthermore, charge/discharge profiles over time show that performance can actually increase as the device ages. In an effort to understand these findings, X-ray photoelectron spectroscopy, Auger electron spectroscopy and near edge absorption fine structure spectroscopy have been utilized to study the interaction of the electrolytes and solvents with the graphene-based electrode materials. The EDL capacitance of graphene nanosheets has been measured before and after Ar plasma bombardment for various times and after exposure to water, isopropanol, methanol, NaOH and KOH. Graphene nanosheet electrochemical capacitors have been disassembled and analyzed following short term and long term operation.

11:20am **GR+AS+NS+SS-ThM11 Electronic Properties and Device Applications of Wafer-Scale Graphene Nanoribbons.** *D. Jena,* University of Notre Dame **INVITED**

Graphene boasts unique physical, electronic, and optical properties. For conventional electronic device applications, the zero band gap of 2-dimensional graphene is an impediment. Opening of effective band gaps can be achieved by field-effect in bilayer graphene, or by using Klein-tunneling properties of graphene p-n junctions. However, these methods appear not to effectively scale to small dimensions. Another way to open band gaps in graphene is to make graphene nano ribbons (GNRs) and use size quantization. Though many of the properties of 2D graphene are lost in the process, GNRs become similar to semiconducting carbon nanotubes, but with planar structures and compatibility with conventional lithographic processes. In this talk, I will present our group's research progress in making such wafer-scale GNR transistors. Band gaps ~0.15 eV appear in

~10 nm wide single GNRs, and band gaps are preserved in parallel arrays of GNRs. Based on these GNRs, we measure current drives as high as 10mA/micron, which far exceeds all other semiconductor materials and seems attractive for both logic and interconnect applications. The effects of edge roughness on scattering and mobility, and the progress towards making GNR-based tunneling transistors will also be presented.

Helium Ion Microscopy Focus Topic

Room: 19 - Session HI+AS+BI+NS-ThM

Imaging and Lithography with the Helium Ion Microscope

Moderator: A. Götzhäuser, University of Bielefeld, Germany, V.S. Smentkowski, General Electric Global Research Center

8:40am **HI+AS+BI+NS-ThM3 Helium Ion Microscopy of Photonic Structures in Biological Systems.** *S.A. Boden, A. Asadollahbaik, H.N. Rutt, D.M. Bagnall,* University of Southampton, UK **INVITED**

The natural world is replete with examples of biological systems that have developed complex micro- and nano-scale structures to interact with light. Such structures, which include thin film multilayers, diffraction gratings, graded index layers and 2D and 3D photonic crystals, acting alone or in combination, allow the realization of a range of optical effects that would be impossible through the use of pigmentation alone. These effects range from the vivid iridescence observed on the skin of some species of bird, through the vibrant metallic sheen of some beetle species, to the dramatic interference patterns seen on the transparent wings of some species of fly. Lepidoptera (an order of insects that includes butterflies and moths) also provides a rich seam of examples of structural color ranging from the antireflective nipple arrays found on the eyes and wings of some species of moth to the photonic crystal structures producing vivid coloration on the wings of some butterfly species.

As these optical effects are a result of the scale of these structures being at or below that of visible light wavelengths, scanning electron microscopy (SEM) is often used to explore their form and to offer insights into their function. Recently, helium ion microscopy (HIM) has emerged as a surface imaging technique, similar to SEM but with the benefits of higher resolution and a larger depth of field. Here, HIM is used to probe the structures responsible for a number of optical effects observed in Lepidoptera. Images will be presented showing the fine details of the ribs and cross-ribs found on the highly-absorbing black ground wing scales of *Papilio ulysses* (Blue Mountain Butterfly) and the complex gyroid 3D photonic crystal structure observed underneath the top lamina on vividly green wing scales from *Parides sesostris* (Emerald-patched Cattleheart). Other examples will include the antireflective close-packed nipple array on the wings of *Cephonodes hylas* (Pellicid Hawk Moth), and cross-sections of the multilayer structures that make up the various colored wing scales of *Chrysiridia rhipheus* (Madagascan Sunset Moth).

The integrated electron flood gun on the helium ion microscope is employed to neutralize charge build-up, allowing samples to be imaged without the need of a conductive coating. This ensures that the natural surface itself is imaged at high resolution and details are not obscured by coating artefacts. In addition, by taking advantage of the large depth of field available with HIM, stereo pairs are generated to extract information on the three-dimensional nature of these structures.

9:20am **HI+AS+BI+NS-ThM5 Imaging of Carbon Nanomembranes (CNM) and Graphene with Helium Ion Microscopy.** *H. Vieker, A. Beyer, A. Polina, A. Willunat, N.-E. Weber, M. Bünenfeld, A. Winter, X. Zhang, M. Ai, A. Turchanin, A. Götzhäuser,* Bielefeld University, Germany

We present a Helium Ion Microscopy (HIM) study of carbon nanomembranes (CNMs). CNMs are extremely thin (~1 nm) nanolayers consisting only of surface. They are made via cross-linking of self-assembled monolayers (SAMs) with large-area exposures of electrons, photons or helium ions and a subsequent transfer to suitable substrates. Patterned radiation exposures allow the fabrication of perforated nanomembranes, e.g., nanosieves. After annealing at temperatures above 800K, CNMs become conductive and eventually transform into graphene. HIM images of CNMs with different precursor molecules are shown, and images of graphene from SAMs are compared with the CVD grown graphene. Capabilities of the HIM imaging of freestanding CNMs and graphene will be discussed.

10:40am **HI+AS+BI+NS-ThM9 Dopant Contrast in Helium Ion Microscopy**, Y. Chen, H. Zhang, D. Fox, C.C. Faulkner, J. Wang, J. Boland, J. Donegan, Trinity College, Ireland **INVITED**

Innovation in metrology is crucial to the future of semiconductor industry, since the miniaturization of transistors demands novel characterization technologies at and beyond the nanometre scale. Recent research has demonstrated that dopant contrast in the Helium-ion Microscope (HIM) is plausible and the HIM is a competitive platform for quantitative secondary-electron (SE) dopant mapping in terms of throughput, sensitivity, and resolution. However, the contrast mechanism of SE imaging is still debatable and it hinders further development of the technique. In this research, quantitative HIM dopant contrast of gallium-doped silicon samples has been investigated and compared with the contrast observed in a scanning electron microscope (SEM). Beam-sample interaction, signal general, as well as detection configuration have been considered via using a range of detectors in the two microscopes. It has been found that the Everhart-Thornley (E-T) secondary electron detector attached to HIM provides similar contrast to the images acquired from the InLens detector attached to SEM, while contrast reversal is observed with the SEM E-T detector. The contrast reversal also depends on the Dwell time. We have confirmed that the HIM is more sensitive to type-I SEs and a capacitance model based on charging effect has been proposed to explain the contrast reversal. Our results indicate that quantitative dopant contrast in the HIM is promising, while charging effect and imaging conditions must be carefully considered.

11:20am **HI+AS+BI+NS-ThM11 High Resolution Patterning of Carbon Nanomembranes and Graphene via Extreme UV Interference Lithography: A Helium Ion Microscopy Study**, A. Winter, A. Willunat, A. Beyer, University of Bielefeld, Germany, Y. Ekinci, Paul Scherrer Institute, Switzerland, A. Götzhäuser, A. Turchanin, University of Bielefeld, Germany

Two-dimensional (2D) carbon materials like graphene, graphene oxide, carbon nanomembranes (CNMs) or ultrathin polymeric films have recently attracted enormous interest due to their potential use in electronics, chemical and biological sensors, nanofilters, hybrid materials, etc. Most of these applications require lithographic patterning of these 2D carbon materials with the nanoscale resolution. In this respect, Extreme UV Interference Lithography (EUV-IL) provides both large-scale patterning and high resolution with an ultimate limit in the sub-10 nm range. We employ EUV-IL to generate nanopatterns in ~1 nm thick CNMs and graphene. We characterize these nanopatterns with a Helium Ion Microscope (HIM). Its high surface sensitivity and lateral resolution provide excellent conditions for imaging of the topographic and chemical features in CNMs and graphene. The possibility to routinely fabricate and characterize the nanopatterns via EUV-IL and HIM on various technologically relevant insulating substrates (e.g., oxidized silicon wafers, glass, and quartz) and with the resolution below 20 nm shows high potential of both techniques for applications in carbon-based nanotechnology.

11:40am **HI+AS+BI+NS-ThM12 Application of Helium Ion Microscope on Processing and Characterization of Nano Wires**, H.X. Guo, S. Nagano, K. Onishi, D. Fujita, National Institute for Materials Science (NIMS), Japan

Scanning helium ion microscope (SHIM) is advanced in high resolution and high focal depth of secondary electron imaging and Rutherford backscattered ion imaging.[1] It also employed in the nano pattern or fabrication on surface and other various structures, such as 2D materials, graphene.[2] It is an excellent candidate for the nano processing of 1D nano structures, such as nanowires and nanotubes.

Rhenium trioxide (ReO₃) is an unusual transition metal oxide with high electrical conductivity close to that of metals. It is well investigated for the applications of photovoltaics[3], catalyst[4], and tip for scanning tunneling microscope[5]. Various ReO₃ nano structures such as nano particles[3,6], nano wires[7], and core-shell structures have been synthesized and characterized by different methods.

In this research, ReO₃ nanowires were synthesized by a physical vapor deposition method. Etched by the helium ion beam, the diameter of part of the nanowire was decreased. During this processing, the structure and transport properties of the ReO₃ nanowire were modified with a controllable method. In this presentation, we will show the structure and properties characterization of the etched nanowires by using scanning probe microscope (SPM), transmission electron microscope (TEM) and other methods. An *in-situ* transport properties measurement system with SHIM will also be introduced in the presentation.

[1] J. Morgan, J. Notte, R. Hill, and B. Ward, *Microsc. Today*, **14**, 24(2006)

[2] D. C. Bell, M. C. Lemme, L. A. Stern, J. R. Williams, and C. M. Marcus, *Nanotech.*, **20**, 455301(2009).

[3] S. V. Bhat, S. B. Krupanidhi, and C. N. R. Rao, *Appl. Phys. Express*, **3**, 115001(2010)

[4] E. Cazzanelli, M. Castrìota, S. Marino, N. Scaramuzza, J. Purans, A. Kuzmin, R. Kalendarev, G. Mariotto, and G. Das., *J. Appl. Phys.*, **105**, 114904 (2009)

[5] S. I. Ikebe, D. Shimada, T. Akahane, and N. Tsuda., *Jpn. J. Appl. Phys.*, **30**, L405(1991)

[6] K. Biswas and C. N. R. Rao, *J. Phys. Chem. B*, **110**, 842, (2006).

[7] D. Myung, Y. Lee, J. Lee, H. K. Yu, J. L. Lee, J. M. Baik, W. Kim, M. H. Kim, *phys. status solidi-R*, **4**, 365 (2010)

Nanometer-scale Science and Technology

Room: 12 - Session NS-ThM

Nanoscale Imaging and Microscopy

Moderator: N. Camillone, Brookhaven National Laboratory

8:00am **NS-ThM1 Spin Friction Observed on the Atomic Scale**, R. Wiesendanger, B. Wolter, A. Kubetzka, K. von Bergmann, Y. Yoshida, University of Hamburg, Germany, S.-W. Hla, Ohio University

With the advent of scanning probe microscopy techniques that involve a tip and a sample in relative motion in the contact or non-contact regime, the microscopic aspects of friction have become a major branch of research called nanotribology. A significant number of recent studies in this field have concentrated on the distinction between electronic and phononic contributions to friction. For the present study, we have used the combination of spin-polarized scanning tunneling microscopy [1] and single-atom manipulation in order to move individual magnetic atoms over a magnetic template [2]. By monitoring the spin-resolved manipulation traces and comparing them with results of Monte-Carlo simulations, we have been able to reveal the characteristic friction force variations resulting from the occurrence of spin friction on the atomic scale [3].

[1] R. Wiesendanger, *Rev. Mod. Phys.* **81**, 1495 (2009).

[2] D. Serrate, P. Ferriani, Y. Yoshida, S.-W. Hla, M. Menzel, K. von Bergmann, S. Heinze,

A. Kubetzka, and R. Wiesendanger, *Nature Nanotechnology* **5**, 350 (2010).

[3] B. Wolter, Y. Yoshida, A. Kubetzka, S.-W. Hla, K. von Bergmann, and R. Wiesendanger,

Phys. Rev. Lett. (2012), in press.

8:20am **NS-ThM2 Observing Mineral Reactions in Supercritical Carbon Dioxide Utilizing High Pressure Atomic Force Microscopy**, A.S. Lea, M. Xu, K.M. Rosso, Pacific Northwest National Laboratory

Geologic sequestration of CO₂ has become an emerging enterprise for reduction of greenhouse gas emissions. Because CO₂ will be injected and stored in host rock at depths >800m, lithostatic pressure will cause the CO₂ to remain in supercritical fluid state. Knowledge of mineral-fluid chemical transformation rates at geologically relevant temperatures and pressures is expected to be an important aspect of predicting reservoir stability. Many mechanisms of mineral transformation reactions where scCO₂ is the dominant phase and water availability is low have so far remained unstudied. We have developed an atomic force microscope capable of observing *in-situ* mineral transformations under supercritical conditions (i.e., >72.8 atm and >304K) in real time.

Observations of the disappearance of a 1.5nm layer on the surface calcite is evident in anhydrous scCO₂ are consistent with the dehydration of a hydrated calcium carbonate layer and is consistent with measurements from piezoelectric force microscopy. We have also followed the formation of a water film on the surface of geologically more relevant forsterite, which is deemed to be essential in the transformation of this silicate mineral into a carbonate, and have related film thickness to water content in the scCO₂.

8:40am **NS-ThM3 Resolving Amorphous Solids - The Atomic Structure of Glass**, M. Heyde, L. Lichtenstein, H.J. Freund, Fritz-Haber-Institute, Germany **INVITED**

Vitreous silica is the basis of traditional glasses. Furthermore, it is the prototype oxide network former. Hence, it has been extensively investigated by diffraction methods, like X-ray and neutron scattering. Therefore, it is a great surprise how little is known about its atomic structure. It is impossible to directly extract ring statistics or local ring environments from diffraction. Theoretical structural models have been correlated to the diffraction data

with reasonable agreement. Nevertheless, such agreement can never be unambiguously elucidate the structure of an amorphous material.

Modern imaging techniques render the investigation of two dimensional (2D) glass systems possible. Recently, we reported on the atomic structure of a thin metal-supported vitreous silica film on Ru(0001) using scanning tunneling microscopy (STM) [1]. For the first time, it was possible to verify Zachariasen's continuous random network [2] in real space. The existence of a 2D silica glass on a graphene support has been shown by scanning transmission electron microscopy [3] suggesting that further 2D glass systems may be prepared. The investigation of 2D glass models provides the unique possibility to study unexplored properties of amorphous materials.

Herein we report on the first non-contact atomic force microscopy (nc-AFM) images of a 2D silica glass grown on Ru(0001). We will present a thorough statistical analysis and a comparison to diffraction data of 3D silica glass as well as to theoretical models, hereby showing that a 2D thin film of vitreous silica can act as a model system for the amorphous 3D network.

[1] L. Lichtenstein, C. Büchner, B. Yang, S. Shaikhutdinov, M. Heyde, M. Sierka, R. Włodarczyk, J. Sauer, and H.-J. Freund, "The Atomic Structure of a Metal-Supported Vitreous Thin Silica Film", *Angew. Chem. Int. Ed.* **51**, 404 (2012).

[2] W. H. Zachariasen, "The Atomic Arrangement in Glass", *J. Am. Chem. Soc.* **54**, 3841 (1932).

[3] P. Y. Huang, S. Kurasch, A. Srivastava, V. Skakalova, J. Kotakoski, A. V. Krashennnikov, R. Hovden, Q. Mao, J. C. Meyer, J. Smet, D. A. Muller, and U. Kaiser, "Direct Imaging of a Two-Dimensional Silica Glass on Graphene", *Nano Lett.* **12**, 1081 (2012).

9:20am **NS-ThM5 Femtosecond Time-Resolved Scanning Tunneling Microscopy on Nanostructures**, **H. Shigekawa**, University of Tsukuba, Japan

With the size reduction of structures in current electronic devices, differences in the electronic properties caused, for example, by the structural nonuniformity of each element have an ever-increasing effect on macroscopic functions. The study of nonequilibrium quantum dynamics in materials with small structures is of great importance not only from the fundamental viewpoint but also as a basis for the further development of functional devices. Real-space imaging of the transient carrier transport and transitions in nanostructures is desired to obtain a deeper understanding of current semiconductor physics. Probing the effect of local electronic structures of nano-clusters on energy transfer is important for the analysis of chemical reactions in catalytic activities and also for the development of organic solar devices. To advance such studies, a method that enables the probing of local carrier dynamics with high spatial and temporal resolution is necessary.

Recently, femtosecond time-resolved scanning tunneling microscopy (STM), which enables ultrafast phenomena on a target material to be probed with the spatial resolution of STM, has been realized by the combination of STM with ultrashort-pulse laser technologies [1-4]. In time-resolved STM, the tunnel gap of STM is illuminated by a sequence of paired laser pulses, and the change in tunneling current ΔI is measured as a function of the delay time between the paired pulses (t_d). A high temporal resolution in the femtosecond range, which is limited only by the optical pulse width, is obtained simultaneously with the atomic spatial resolution of STM. This microscopy technique is applicable to systems in which the response of the tunneling current has a nonlinear dependence on the optical excitation intensity. In the case of semiconductors, for example, the magnitude of ΔI obtained for a certain delay time t_d reflects the density of photogenerated minority carriers at t_d after the first pulse excitation, and the carrier decay processes can be observed by analyzing the delay-time dependence of ΔI . Using polarized light, spin dynamics can be probed, and the detection of signals such as phonons is also possible.

In this talk, I would like to introduce this new microscopy technique with some new results.

References

[1] Y. Terada, S. Yoshida, O. Takeuchi and H. Shigekawa, *J. of Physics: Condensed Matter* **22**, 264008 (2010). [2] Y. Terada, S. Yoshida, O. Takeuchi and H. Shigekawa, *Nature Photonics*, **4**, 12, 869 (2010). [3] Y. Terada, S. Yoshida, O. Takeuchi and H. Shigekawa, *Advances in Optic.Tech.*, 2011, 510186 (2011). [4] S. Yoshida, Y. Terada, R. Oshima, O. Takeuchi and H. Shigekawa, *Nanoscale*, 2012, **4**, 757 (2012).

9:40am **NS-ThM6 Unusual Island Formations of Iridium on Ge(111) Studied by STM**, **M. van Zijl**, C. Mullet, B. Stenger, E. Huffman, D. Lovinger, W. Mann, S. Chiang, University of California, Davis

We have used scanning tunneling microscopy (STM) to characterize the growth of iridium onto Ge(111). Iridium was deposited onto the Ge(111) c(2x8) surface at different coverages less than 1ML, and the samples were annealed to temperatures between 550K and 750K. A new form of growth was observed, consisting of pathways connecting larger iridium islands. As the annealing temperature increased, the iridium growth first formed unusual shapes with finger-like protrusions. Next, these shapes broke apart into smaller islands, which ultimately formed into larger islands at higher temperatures. High resolution images have been obtained, which allow insight into the atomic arrangements. We propose a model relating the activation energy of specific binding sites to the formation of various observed structures on the surface.

Funding from NSF CHE-0719504 and NSF PHY-1004848 (REU)

10:40am **NS-ThM9 Turning STM Images Into Chemical Understanding: Atomically Flat Si(100) Reveals the Mechanism of Silicon Oxidation**, **M.A. Hines**, M.F. Faggin, K. Bao, A. Gupta, B.S. Aldinger, Cornell University

Because of its technological importance, silicon oxidation has been studied intensely for decades; however, the disordered nature of the oxide makes these reactions notoriously difficult to understand. In this work, the oxidation reaction is coupled with a subsequent etching reaction, allowing oxidation to literally write an atomic-scale record of its reactivity into the etched surface — a record that can be read with scanning tunneling microscopy (STM) and decoded into site-specific reaction rates, and thus chemical understanding, with the aid of simulations and infrared spectroscopy. This record overturns the long-standing and much-applied mechanism for the aqueous oxidation of the technologically important face of silicon, Si(100), and shows that the unusually high reactivity of a previously unrecognized surface species leads to a self-propagating etching reaction that produces near-atomically flat Si(100) in a beaker at room-temperature — a long-standing technological goal. These findings show that, contrary to expectation, the low-temperature oxidation of Si(100) is a highly site-specific reaction and suggests strategies for functionalization by low-temperature, solution-based reactions.

11:00am **NS-ThM10 Spectroscopic Imaging of Silicon-Hafnia Interfaces**, **C. Guedj**, H. Grampeix, C. Licitra, E. Martinez, CEA, LETI, MINATEC Campus, France

New behavior and phenomena can emerge at oxide interfaces, and the nanocharacterization of these properties is a real challenge for the semiconductor industry [i]. To replace the conventional SiO₂ insulator, hafnium-based oxides have been introduced [ii,iii] into advanced CMOS devices such as MOSFETs or memories [iv], but the nanometric control of their interfacial properties still remains a critical issue. For further industrial implementation of these oxides, it is necessary to obtain sufficiently high dielectric constants and bandgaps, good thermal stability on silicon, good scalability and sufficient reliability [v] at a reasonable cost. In this presentation, we have performed spectroscopic imaging of silicon-hafnia interfaces using energy filtered high-resolution transmission electron microscopy and valence electron energy loss spectroscopy (HRTEM-VEELS), coupled with X-Ray photoelectron spectroscopy (XPS), Reflection energy loss spectroscopy (REELS), UV photoelectron spectroscopy (UPS) and spectroscopic ellipsometry. Optical absorptions and bandgap profiles across the interface are obtained and novel ordering effects like axiotaxy are locally observed. An atomic-scale modelling is proposed, and the consequences in terms of device performances are detailed.

[i] <http://www.itrs.net/Links/2011ITRS/2011Chapters/2011Metrology.pdf>

[ii] R.M. Wallace and G.D. Wilk, *Crit. Rev. Solid State Mater. Sci.* **28**, 213 (2003)

[iii] M.H. Cho et al., *Appl. Phys. Lett.* **81**, 1071 (2002)

[iv] B.Govoreanu et al., *proc. IEEE IEDM*, p 729 (2011)

[v] J. Robertson, *Solid-state electron.*, Vol. 49, p 283-293 (2005)

11:20am **NS-ThM11 Atom Probe Tomography of AlInN/GaN based HEMT Structures**, **N. Dawahre**, G. Shen, P. Tolmer, S.M. Kim, P. Kung, University of Alabama, Tuscaloosa

Group III-Nitride semiconductors have been well known for their excellent optoelectronic properties associated with a wide direct bandgap, which has led to the emergence of blue and green lasers, ultraviolet-blue-green-amber and white light emitting diodes, and ultraviolet photodetectors. They are also rapidly becoming the material family of choice for next generation of

RF-microwave devices, power amplifiers and high temperature electronics, thanks to high two-dimensional electron gas charge densities and high breakdown electric fields in these materials. GaN based materials are also more radiation resistant than conventional electronic materials, which makes them well suited for space electronics. Although less thoroughly investigated until now, lattice matched AlInN/GaN systems are promising to be a viable alternative to the current state-of-the-art strained AlGaIn/GaN devices and their reliability issues.

In this work, we present the nanoscale characterization of AlInN semiconductors and AlInN/GaN high electron mobility transistor (HEMT) structures using a combination of transmission electron microscopy (TEM) and laser assisted atom probe tomography (APT), and correlate these with the structures' electronic and optical properties, as well as the effects of irradiation. APT is an emerging technique based on the field ion emission from a needle-shaped region of interest and is capable of yielding 3D chemical mapping with atomic sensitivity and sub-nanometer spatial resolution. We report here a study of the field evaporation mechanisms from wide bandgap AlInN and GaN using a visible ps laser during APT experiments and correlate them with APT experiments (e.g. laser pulse energy, ...) in order to establish approaches for reliable chemical analysis at the nanoscale of AlInN compound alloys. We proceed to investigate the fundamental material characteristics of interest that can be extracted from a combined APT and TEM analysis, including indium segregation phenomena in AlInN, interdiffusion near the AlInN/GaN channel interfaces and interface roughness, as well as the effects of irradiation on the channel properties.

11:40am **NS-ThM12 Pit Initiation at MnS Nano-Inclusions in Carbon Steel under Exposure to Sulfate-Reducing Bacterium *D. alkanexedens*.** *J.S. Hammond*, Physical Electronics, *B.H. Davis*, *Z. Suo*, Montana State University, *I. Beech*, University of Oklahoma, *D.F. Paul*, Physical Electronics, *R. Avci*, Montana State University

Cold rolled carbon steel (1018) is a commonly used structural material in various applications, including the construction of fuel storage tanks for naval ships. *Desulfoglaeba alkanexedens* (strain ALDCT) is a known fuel-degrading, anaerobic, sulfate-reducing bacterium (SRB) [1, 2] that thrives at fuel-water interfaces in marine environments and can influence the pitting corrosion of carbon steel. It has long been postulated that MnS inclusions in carbon steel can act as sites of pitting initiation [3]. The propagation of pitting corrosion is relatively well understood; however, the initiation of pits is still a subject of controversy [4, 5]. A careful study of pit initiation and propagation associated with sulfide inclusions, particularly as they relate to microbial influenced corrosion (MIC) under anaerobic conditions, has been lacking, partly because these inclusions are mostly submicron-sized and the evolution of their corrosion is difficult to monitor. The use of nanoprobe instead of microprobe is required to determine the elemental and chemical composition and to map out the elemental distributions at the submicron scale. Quantitative surface sensitive techniques such as Auger electron spectroscopy [4, 5] are essential for monitoring the nanoscale changes associated with surface-related phenomena, including MIC. This presentation will review the results of comprehensive and systematic studies of nano-inclusions on carbon steel surfaces prior to and following exposure of the steel to a solution of a mature ALDCT culture and to abiotic sulfide as a control. The nano-inclusions were carefully characterized using a field emission Auger nanoprobe with a spatial resolution of approximately 10 nm for imaging and spectroscopy and compared with results obtained using X-ray microprobes, which typically have a spatial resolution of around 1000 nm for spectroscopy and 10 nm for imaging. The study elucidates biologically driven corrosion reactions taking place in and around nano-inclusions. The impact of this fundamental analysis on the understanding of MIC phenomenon will be discussed.

References:

1. Davidova, I.A., et al., *International Journal of Systematic and Evolutionary Microbiology*, 2006. **56**: p. 2737-2742.
2. Morris, B.E.L., J.M. Sufita, and H.H. Richnow, *Geochimica Et Cosmochimica Acta*, 2009. **73**(13): p. A907-A907.
3. G. Waglen. *Corrosion Science*, 1974. **14**: p. 331-349.
4. P. Schmuki, H. Hildebrand, A. Friedrich and S. Virtanen, *Corrosion Science*, 2005. **47**: p. 1239-1250.
5. J.E. Castle and Ruoru Ke, *Corrosion Science*, 1990. **30**(4/5): p. 409-428.
6. Support of ONR/MURI Grant No N00014-10-0946 is gratefully acknowledged.

Thin Film

Room: 10 - Session TF+EM+SE+NS-ThM

Nanostructuring Thin Films

Moderator: R.C. Davis, Brigham Young University

8:00am **TF+EM+SE+NS-ThM1 Plasma Effects in Nanostructuring Thin Films.** *K. Ostrikov*, CSIRO Materials Science and Engineering, Australia **INVITED**

In this presentation, several examples of uniquely plasma-enabled nanostructuring of thin film materials for applications in energy conversion and storage, environmental monitoring, and bio-sensing. Strong emphasis is made on atom-, energy-efficiency, and environment-friendliness of plasma-based nanotechnologies.

1. Introduction: Atom- and energy-efficient nanotechnology is the ultimate Grand Challenge for basic energy sciences as has recently been road-mapped by the US Department of Energy. This ability will lead to the energy- and matter-efficient production of functional nanomaterials and devices for a vast range of applications in energy, environmental and health sectors that are critical for a sustainable future. Here we present examples related to atom- and energy-efficient nanoscale synthesis of advanced nanomaterials for energy conversion and storage, environmental sensing, and also discuss effective cancer cell treatment using low-temperature plasmas.

2. Atom- and energy-efficient nanostructure production for energy storage: Here we show an example of a recent achievement of a very low amount of energy per atom (~100 eV/atom) in the synthesis of MoO₃ nanostructures for energy storage (e.g., Li-ion battery) applications. This was achieved by using time-programmed nanosecond repetitive spark in open air between Mo electrodes. Highly-controlled dosing of Mo and O atoms was achieved through the controlled evaporation and dissociation reactions and maintaining reactive chemistry in air. These nanomaterials show excellent electrochemical and energy storage performance.

3. Environment-friendly, single-step solar cell production: Highly-efficient (conversion efficiency 11.9%, fill factor 70 %) solar cells based on the vertically-aligned single-crystalline nanostructures have been produced without any pre-fabricated p-n junctions in a very simple, single-step process of Si nanoarray formation by etching p-type Si wafers in low-temperature environment-friendly plasmas of argon and hydrogen mixtures. The details of this process and the role of the plasma are discussed.

4. Metal-nanotube/graphene environmental and bio-sensors: Plasma processing was successfully applied for the fabrication of hybrid nanomaterials based on metal-decorated carbon nanotubes and vertically aligned graphenes. The applications of these structures in environmental (gas) and bio-sensing (SERC/plasmonic) platforms are presented. The vertically-aligned graphene structures have been grown without catalyst and any external substrate heating, owing to the unique plasma properties.

8:40am **TF+EM+SE+NS-ThM3 Directed, Liquid Phase Assembly of Patterned Metallic Films by Pulsed Laser Dewetting.** *Y. Wu*, University of Tennessee, *J.D. Fowlkes*, *M. Fuentes-Cabrera*, Oak Ridge National Laboratory, *N.A. Roberts*, *P.D. Rack*, University of Tennessee

Self-assembly of materials offer the potential to synthesize complex systems by defining the *initial and bounding* conditions if the fundamental scientific principles guiding the assembly are known. Much work has been performed studying the assembly of continuous thin polymer and metal films which reveal interesting dewetting phenomenon. Less work has been devoted to the directed assembly and pattern formation of confined or patterned metallic thin films. Meanwhile, the synthesis of functional metallic nanomaterials via self-assembly has been an effective and low-cost approach to realize many critical applications of nanoscience and nanotechnology. In this study, the dewetting and nanopattern formation of nanolithographically pre-patterned thin films of various shapes via pulsed nanosecond laser melting were investigated to understand how initial boundary conditions facilitate precise assembly. Specifically we will show experimental and computational results (continuum and molecular dynamics) illustrating how so-called synthetic perturbations can vary the dispersion of the resultant nanoparticle size and shape distribution of pseudo-one-dimensional liquid metal wires. Furthermore, we will show how controlling the shape and size of bi-metallic nanostructures, the assembly of multifunctional nanoparticles can be assembled.

9:00am **TF+EM+SE+NS-ThM4 Nanosphere Lithography for Bit Patterned Media.** *A.G. Owen*, *H. Su*, *A.M. Montgomery*, *S.M. Kornegay*, *S. Gupta*, University of Alabama

Nanosphere lithography¹⁻⁴ has been used to pattern perpendicular magnetic anisotropy Co/Pd multilayers into nanopillars for the first time for bit-

patterned media applications. A multilayer stack of Pd₁₀/[Co_{0.3}Pd₁]₉/Pt₅ nm nanolayers was deposited onto a bare silicon wafer. The nanospheres were spin-coated into a uniform monolayer and then reduced in size by plasma ashing in oxygen. The Co/Pd multilayer films were subsequently ion milled into nanopillars using the reduced nanospheres as masks. We tested two ranges of nanosphere sizes, one at about 100 nm, and the other at about 1000 nm. In order to optimize the ashing of the nanospheres, response surface methodology (RSM) was performed to optimize the ashing power and time. It was seen that ashing at low powers of less than 100 W for longer times was more effective than higher powers for short times in shrinking the nanosphere masks without damage. The subsequent ion milling of the Co/Pd films was performed at a near-perpendicular angle to minimize shadowing by the nanospheres. We will discuss some of the complex shapes the nanospheres were patterned into after ashing, and how they translated into variously sized and shaped nanopillars of Co/Pd multilayers after ion milling. Magnetometry was used to characterize the films before and after patterning, showing an improvement in the coercivity and squareness of the media after patterning with nanospheres that were shrunk, but not damaged, by ashing. Micromagnetic simulations using Object Oriented Micromagnetic Framework (OOMF) have been carried out to produce a simulated hysteresis loop which is then compared with the experimental results.

Acknowledgements

The NSF ECCS 0901858 grant, entitled "GOALI: Nanopatterned graded media" is acknowledged for support. Alton Highsmith is acknowledged for support in the UA Microfabrication Facility.

References

1. Xiao Li, T. R. Tadisina, S. Gupta, J. Vac. Sci. Technol. A **27**, Jul/Aug 2009, 1062
2. Kosmas Ellinis, A. Smyrnakis, A. Malainou, A. Tserepi, E. Gogolides, Microelectronic Engineering, **88**, 2011, 2547-2551
3. C. L. Haynes, R. P. Van Duyne, J. Phys. Chem. B **105**, 5599, 2001
4. S. M. Weekes, F. Y. Ogrin, W. A. Murray, Langmuir **20**, 11208, 2004

9:20am TF+EM+SE+NS-ThM5 Effects of Nanometer Scale Periodicity on the Self-Propagating Reaction Behaviors of Sputter-Deposited Multilayers, D. Adams, R. Reeves, Sandia National Laboratories

Nanometer-scale, vapor-deposited multilayers are an ideal class of materials for systematic, detailed investigations of reactive properties. Created in a pristine vacuum environment by sputter deposition, these high-purity materials have well-defined reactant layer thicknesses between 1 and 1000 nm, minimal void density and intimate contact between layers. If designed appropriately, these energetic materials can be ignited at a single point and exhibit a subsequent, high-temperature, self-propagating formation reaction. The nanometer-scale periodicity set through design tailors the effective diffusion length of the subsequent self-propagating reaction.

With this presentation, we describe effects of the nanometer-scale, multilayer periodicity on i) the reactivity of multilayers in different surrounding gaseous environments and ii) the reaction front morphology as viewed in the plane of the multilayer. We show that nickel/titanium and titanium/boron multilayers are affected by the surrounding gaseous environment, and describe how the magnitude of average propagation speed depends on multilayer periodicity. Fine multilayer designs are characterized by fast reaction waves, and there is no difference in average propagation speed when reacted in air (atm. pressure) versus vacuum (1 mTorr). Coarse multilayer designs are generally slower and are affected by secondary oxidation reactions when conducted in air. These thick multilayer designs are affected by the pressure of the surrounding gaseous environment with enhanced propagation speeds owing to the highly exothermic reaction of Ti with O. Regarding the effects of nanometer-scale multilayer periodicity on reaction front morphology, we show that reactive multilayers often have a smooth reaction front when layer periodicity is small. However, multilayers having larger periodicity (and hence larger effective diffusion lengths) exhibit reaction front instabilities and complex reaction front morphologies.

In this talk, we also stress how the propensity to oxidize and the propensity to form reaction front instabilities (as affected through nanometer-scale design) impact final properties of the multilayers for applications such as localized joining.

Sandia is a multiprogram laboratory managed and operated by Sandia Corporation, a wholly owned subsidiary of Lockheed Martin Company, for the United States Department of Energy's National Nuclear Security Administration under Contract DE-AC04-94AL85000.

9:40am TF+EM+SE+NS-ThM6 Ag Nanoparticles Supported by (111) Facets on Biaxial CaF₂ Nanoblades, M. Auer, D. Ye, Virginia Commonwealth University

Silver nanoparticles of different diameters were grown in an effort to study methods of preferentially orienting the geometry of metal nanoparticles. Arrays of calcium fluoride nanorods were grown on silicon substrates using oblique angle deposition at 75° incident angle. A method was then developed to grow silver nanoparticles exclusively on the (111) facet of the calcium fluoride tips. Cross sectional scanning electron microscopy and transmission electron microscopy imaging was used to verify that the nanoparticles adhered exclusively to the desired facet of the tip. Using selected area diffraction and dark field in the TEM, it was shown that the nanoparticles did grow at a [111] orientation at the interface between them and the calcium fluoride rods. Different thicknesses and diameters of nanoparticles were then grown to determine what an ideal size was to achieve the most [111] orientation of the nanoparticles.

Thin Film

Room: 11 - Session TF+NS+EM-ThM

Thin Films: Growth and Characterization-II

Moderator: C. Vallee, LTM - MINATEC - CEA/LETI, France

8:00am TF+NS+EM-ThM1 Plasma-enhanced Atomic Layer Epitaxy of AlN Films on GaN, N. Nepal, J.K. Hite, N. Mahadik, M.A. Mastro, C.R. Eddy, Jr., U.S. Naval Research Laboratory

AlN and its alloys with GaN and InN are of great interest for number of applications. In a device structure that employs an ultrathin layer of these materials, thickness control at the atomic scale is essential. Atomic layer epitaxy (ALE) is one of the most promising growth methods for control of epilayer thickness at the atomic scale. There are reports on atomic layer deposition of AlN on GaN and Si substrates [1]. In those reports, the AlN layers were either amorphous or composed of nm-sized crystallites. Since ALE is a low temperature growth process, there is significantly reduced thermal energy for adatoms to bond at preferred lattice sites and promote growth of crystalline material, therefore, surface preparation plays a very important role to ensure a crystalline layer.

In this work, we present recent efforts to improve the crystalline quality of ALE AlN layers on MOCVD grown GaN/sapphire templates, including the influence of *ex situ* and *in situ* surface pretreatments to promote uniform two-dimensional (2D) nucleation of AlN layers and ALE growth of crystalline AlN films thereupon. AlN layers were grown at 500 °C by ALE simultaneously on Si(111) and GaN/sapphire templates and characterized using spectroscopic ellipsometry (SE), x-ray diffraction (XRD), and atomic force microscopy measurements. The SE measurements indicate that the AlN growth on Si(111) is self-limited for trimethylaluminum (TMA) pulse of length 0.04 to 0.06 sec. However, the AlN nucleation has a bimodal island size distribution for TMA pulses < 0.06 sec. The AlN nucleation becomes uniform and 2D for a pulse length of 0.06 sec, therefore, this pulse length was used to study the GaN surface pretreatment on the nucleation of AlN layer. GaN surfaces were pre-treated *ex situ* with HF and HCl wet chemical etches. Alternating pulses of trimethylgallium and hydrogen plasma followed by an hour of annealing at 500 °C (emulating a Ga-flash-off process) were employed *in situ* before growing an AlN layer. For 3 cycles of Ga-flash-off the AlN nucleation is uniform and replicates the GaN surface morphology on both HF and HCl pretreated GaN. XRD measurements on 36 nm thick AlN films reveal that the ALE AlN on GaN/sapphire is crystalline with only a wurtzite structure and a (0002) peak rocking curve FWHM of 630 arc-sec, which is close to the typical value for AlN grown by MBE and MOCVD [2,3]. Electrical characterization of 2D electron gas at the AlN/GaN interface will also be presented.

References:

1. M. Alevli et al., Phys. Status SolidiA **209**, 266 (2012), and references therein.
2. T. Koyama et al., Phys. Stat. Sol. (a) **203**, 1603 (2006).
3. K. Balakrishnan et al., Phys. Stat. Sol. (c) **3**, 1392 (2006).

8:20am TF+NS+EM-ThM2 *In Situ* Infrared Spectroscopy Study of Cobalt Silicide Thin Film Growth by Atomic Layer Deposition, K. Bernal Ramos, University of Texas at Dallas, M.J. Saly, SAFC Hitech, J. Kwon, University of Texas at Dallas, M.D. Halls, Materials Design Inc., R.K. Kanjolia, SAFC Hitech, Y.J. Chabal, University of Texas at Dallas
Cobalt silicide has potential applications in microelectronics. For instance, the drive to scale down integrated circuitry (IC) has led to the consideration

of cobalt silicide (CoSi₂) as an alternative contact material for titanium silicide (TiSi₂) in future self-aligned silicide technology due to its wider silicidation window and superior thermal and chemical stability. Studies of the growth mechanisms during film deposition are critical to better understand and control thin film formation.

This work focuses on the atomic layer deposition (ALD) of cobalt silicide (CoSi₂), using (tertiarybutylallyl)cobalttricarboxyl ((tBuAllyl)Co(CO)₃) and trisilane on H-terminated silicon to uncover the film growth mechanisms. The first pulse of (tBuAllyl)Co(CO)₃ reacts completely with the H-terminated Si surface forming one monolayer of metallic silicide through the reduction of the allyl ligand by transfer of the surface hydrogen and the formation of Co-Si bonds¹. In situ infrared absorption spectra show the complete loss of H-Si bonds, and the appearance of surface-bound carbonyl and CH_x ligands after the first (tBuAllyl)Co(CO)₃ pulse on H/Si(111). Further deposition of CoSi₂ is possible only after the linear carbonyl groups (initially observed, on the surface after the first (tBuAllyl)Co(CO)₃) are removed by subsequent ALD cycles. Further ALD cycles give rise to cobalt silicide growth through ligand exchange after a nucleation period of 2–4 cycles. The resultant CoSi₂ films are characterized by a low concentration of carbon impurities in the bulk according to X-ray photoemission spectroscopy (XPS).

1 Kwon et al. Chem. Mater. 2012, 24, 1025–1030

8:40am **TF+NS+EM-ThM3 Thin Film Growth: From Gas Phase to Solid Phase – Links and Control**, *P. Raynaud*, CNRS and University Paul Sabatier – Toulouse – France **INVITED**

PECVD, PVD, ALD, sputtering processes, are widely used for thin film growth. Nevertheless, the growth mechanisms need to be controlled and understood to be able to propose stable, adaptable and reproducible processes. Gas, plasma or "volume" phase is one parameter; interaction with surfaces to be treated is the second one, the last one being the final property (ies) to be reached. The Gas phase is controlled by external parameters (pressure, power, polarization, temperature, gas mixture, type of power supply in plasma processes, type of target, duty cycle,). Moreover, these external parameters are linked to internal parameters such as: density and energy of species, type of species (neutrals, ions, electrons, radicals, photons ...), temperature, bombardment energy... Thus, interaction with surfaces and growth process (growth mode, growth rate...) are obviously controlled by these internal parameters and the couple "Gas phase/surface (nature of substrate)". The purpose of this talk is to explain through examples (In situ Infrared spectroscopy of gas phase, OES, MS, Growth modes characterization by in situ ellipsometry, RBS, ARXPS...) how to characterize (in or ex situ) the gas phase et solid phase to find links between these two phases and give some explanation of the processes "from power supply to final properties of the layer".

9:20am **TF+NS+EM-ThM5 Investigation of Precursor Infiltration and ALD Growth on Polymers and Effect on Fiber Mechanical Properties**, *R.P. Padbury*, *J.S. Jur*, North Carolina State University

Atomic layer deposition (ALD) provides the opportunity to unite the properties of organic fiber forming polymers and nanoscale inorganic films creating a hybrid material interface. Prior research has shown that ALD materials nucleation on polymers varies in composition and structure based on how the precursor interacts with the polymer chemistry and the process conditions. The purpose of this work is to explore the effect of this processing on the mechanical behavior of fibrous materials. To study this in more detail, *in-situ* quartz crystal microgravimetry (QCM) is employed to understand the material growth mechanisms of ALD TiO₂, ZnO, and Al₂O₃ on poly (acrylic acid), polyamide-6, and polyethylene terephthalate. Particular emphasis is placed on controlling the ALD precursor diffusion into the sub-surface region of these polymers. *In-situ* QCM data was complemented by *ex-situ* characterization methods such as FT-IR and TEM to examine the interaction between the precursor and polymer and the compositions of the inorganic films. Finally, these results are correlated to the mechanical performance of the ALD treated fabrics. This work has important implications on sustainable textiles processes as well as the introduction of hybrid material properties to textile systems.

9:40am **TF+NS+EM-ThM6 Atomic Layer Deposition Enabled Synthesis of Nanostructured Composite BiFeO₃/CoFe₂O₄ Thin Films for Multiferroic Applications**, *C.D. Pham*, *J.P. Chang*, University of California at Los Angeles

Multiferroic materials, that can either exist as single-phase materials or multi-phase composites, exhibit two or more forms of ferroic order such as (anti)ferroelectricity, (anti)ferromagnetism, or ferroelasticity and have been proposed for use in future non-volatile memory technology. Atomic layer deposition (ALD) is proposed as a scalable approach to synthesize multiferroic thin films and to enable the synthesis of multiferroic

composites which utilize conformal deposition onto 3-D nanostructures. Challenges that must be overcome in the ALD of multiferroic materials is the amorphous nature of as-deposited films and the difficulty in attaining the desired crystallinity and structure that would enable multiferroic properties to emerge from these materials.

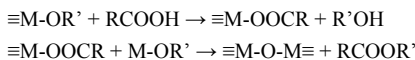
In this work, multiferroic BiFeO₃ was deposited by ALD as a single-phase multiferroic thin film as well as the ferroelectric component in a composite multiferroic using a ferrimagnetic CoFe₂O₄ mesoporous template that was synthesized using an evaporation induced di-block copolymer self-assembly technique. The ALD process used the metallorganic precursors Bi(tmhd)₃ (tmhd = 2,2,6,6-tetramethylheptane-3,5 dione) and Fe(tmhd)₃ alongside oxygen atoms produced from a coaxial waveguide microwave powered atomic beam source. A variety of ALD process conditions were studied, such as the effects of process temperature, precursor pulsing time, and precursor pulsing ratio on film composition, growth rate, and crystallization. The ALD films were able to be grown with a composition ratio Bi:Fe close to unity and with a controlled nanostructure and growth rate of ~0.7 Å/cycle. In order to achieve the desired crystalline material after rapid thermal processing, the composition and nanostructure of the as-deposited films must first be controlled via the ALD process to fit within narrow windows.

To compare the performance of the multiferroic ALD films to more well established synthesis methods, measurements of magnetic and ferro/piezoelectric properties were accomplished using SQUID magnetometry and piezoresponse force microscopy, respectively. Magnetic measurements showed that the out-of-plane remnant magnetization of a composite film at room temperature was approximately 66.4 emu/cm³ while the coercive field was approximately 1950 Oe which was comparable to epitaxial films grown by other methods such as PLD. The magnetoelectric coupling effects in the composite films were studied to assess the effectiveness of the nanostructured material approach.

10:40am **TF+NS+EM-ThM9 In Situ Infrared Spectroscopic Study of Atomic Layer Deposited TiO₂ Thin Film Formation Using Non-Aqueous Routes**, *K. Bernal Ramos*, University of Texas at Dallas, *G. Clavel*, Université Montpellier 2, France, *C. Marichy*, Universidade de Aveiro / CICECO, Portugal, *W. Cabrera*, The University of Texas at Dallas, *N. Pinna*, Universidade de Aveiro / CICECO, Portugal, *Y.J. Chabal*, University of Texas at Dallas

Atomic layer deposition (ALD) is a unique technique for the deposition of conformal and homogenous thin films, by the use of successive self-limited surface reactions. Non-aqueous sol-gel routes are elegant approaches for the synthesis of metal oxide nanomaterials.¹ High quality inorganic nanocrystals,¹ ordered hybrid materials² or ALD thin films³ can be obtained.

Our ALD approach makes use of metal alkoxides and carboxylic acids as metal and oxygen source, respectively.⁴ It is expected that the reaction of carboxylic acids with the surface alkoxide species leads to surface carboxylate species (eq. 1), in a second step an aprotic condensation reaction between surface carboxylate species and metal alkoxides leads to metal-oxide bond formation (eq. 2).



Characterization of interface properties by in situ investigation of surface reaction mechanisms during deposition of high-*k* materials provides critical information for the development of semiconductor devices, where sharp interfaces and impurity free films are sought after.

In this work, in-situ IR spectroscopy is used to investigate the mechanisms for TiO₂ growth using either acetic acid or O₃ as oxygen source and titanium isopropoxide as metal source. It is believed to avoid intermediate OH group and to lead to sharp Si-high-*k* interfaces.

The IR results of the acetic acid process show clearly a ligand exchange leading to formation of acetates at the surface (vibrational bands at 1527 and 1440 cm⁻¹) during the acetic acid pulse and then to their removal during the metal alkoxide pulse. These findings confirm the expected mechanism and demonstrate the absence of OH intermediate. However, the ligand exchange does not seem to be complete leading to accumulation of C impurities.

The in-situ study of O₃ based ALD demonstrates similarities with the above process. Indeed, formation of formate, carboxylate or carbonate species are observed function of the O₃ flow.⁵ The formation of surface carboxylic species upon reaction with O₃ leads then to similar surface states as in the case of the reaction with carboxylic acids.⁴ The mechanism of both approaches and their similarities and differences will be discussed.

1. N. Pinna and M. Niederberger, *Angew. Chem.-Int. Edit.*, 2008, **47**, 5292-5304
2. N. Pinna, *J. Mater. Chem.*, 2007, **17**, 2769-2774

3. G. Clavel, E. Rauwel, M. G. Willinger and N. Pinna, *J. Mater. Chem.*, 2009, **19**, 454-462
4. E. Rauwel, G. Clavel, M. G. Willinger, P. Rauwel and N. Pinna, *Angew. Chem.-Int. Edit.*, 2008, **47**, 3592-3595
5. J. Kwon, M. Dai, M. D. Halls, E. Langereis, Y. J. Chabal and R. G. Gordon, *J. Phys. Chem. C*, 2009, **113**, 654-660

11:00am **TF+NS+EM-ThM10 Nanomechanical Shaft-Loading Blister Testing of Thin Films**, *M. Berdova*, *A. Baby*, *J. Lyytinen*, Aalto University, Finland, *K. Grigoros*, *L. Kilpi*, *H. Ronkainen*, VTT Technical Research Center, Finland, *J. Koskinen*, *S. Franssila*, Aalto University, Finland

Atomic Layer Deposition (ALD) is important in micro- and nanoelectromechanical systems, since it provides smooth, uniform, pin-hole free, and conformal layers. In particular, ALD aluminum oxide has excellent properties such as high mechanical strength and hardness, and chemical inertness.

We propose a new technique to measure the mechanical properties of ALD thin films. In the present work, a MEMS version shaft-loading blister test used to evaluate the adhesion between ALD alumina and Cu, Cr/Cu, SiN_x, SiC_x, and Pt thin films. The test structure consists of microcylinders with diameters 1000 μm and 2000 μm, surrounded by etched annular rings making 50 μm, 100 μm and 200 μm gaps (Figure 1). The test structures are examined by applying the load along the microcylinder with a help of CSM Microindenter, inducing displacement which then causes the delamination between thin films and therefore, contributing to obtain the work of adhesion (Figure 2).

The fabrication of the test structure begins from the cleaning of double-side polished silicon wafer in hydrogen-peroxide-based (RCA) wet cleans. The following step is Atomic Layer Deposition of alumina on both sides of the wafer using trimethyl aluminium and water as precursors at 220 °C. 20 nm of Al₂O₃ is grown on one side as the etch mask, and 200 nm of Al₂O₃ is grown on another side to act both as an etch-stop mask and a testing layer. Next, the top layer is patterned to create alumina etch mask; and the rings are etched through silicon wafer by dry anisotropic Bosch process, forming this way a microcylinders supported only by 200 nm of Al₂O₃ layer. Then, thin films (300 nm thick) are deposited by sputtering, or by PECVD techniques. The silicon nitride and silicon carbide were deposited at 300 °C. Magnetron sputtering was used for deposition of Pt, Cu, and Cr/Cu thin films at room temperature. Finally, those films are released by wet etching supporting alumina layer around the microcylinder.

As a result, we have not observed the delamination for nitride and carbide films: after certain reached displacement point (7 μm for nitride, 12 μm for carbide) the films start to break. For soft films as Pt and Cu, at similar displacement values we observed the starting of delamination. Comparing copper and copper with chromium layer underneath, the delamination of the film with adhesive layer starts at higher displacement and load values, proving the adhesive action of chromium. In the case of metal films large displacement and delamination can be achieved without breaking of the film (Table 1). The proposed MEMS shaft-loading blister test might become a valuable tool for all thin film adhesion testing.

11:20am **TF+NS+EM-ThM11 Phase Formation and Thermal Stability of Arc-Evaporated ZrAlN Thin Films**, *L. Rogström*, Linköping University, Sweden, *M.P. Johansson*, SECO Tools AB, Sweden, *M. Ahlgren*, Sandvik Tooling AB, Sweden, *N. Ghafoor*, Linköping University, Sweden, *J. Almer*, Advanced Photon Source, Argonne National Lab, *L. Hultman*, *M. Odén*, Linköping University, Sweden

Transition metal nitrides are widely used as wear protective coatings due to their high hardness also at elevated temperatures. Hence, TiAlN is one of the most common materials for coating of cutting tools. Its attractive mechanical properties are connected with the phase separation of the cubic TiAlN phase when the coating is exposed to high temperatures. The related ZrAlN system is less studied while its large miscibility gap with possibility for phase separation at elevated temperatures makes this material interesting for high temperature applications. Here, we present a comprehensive study of the phase formation in arc-evaporated ZrAlN thin films and their mechanical properties and thermal stability. Zr_{1-x}Al_xN thin films with a wide range of compositions (0.12 < x < 0.73) were grown by cathodic arc-evaporation. The structure of as-deposited and annealed films was characterized by x-ray diffraction and transmission electron microscopy and the mechanical properties were determined by nanoindentation.

The structure of the as-deposited ZrAlN thin films was found to depend on the Al-content. A low Al-content (x < 0.38) results in cubic (c) structure films while for high Al-content (x > 0.70) a hexagonal (h) ZrAlN phase is obtained [1]. In the compositional range between x = 0.38 and x = 0.70, the films exhibit a nanocomposite structure with a mixture of cubic, hexagonal, and amorphous phases [1, 2]. In all films, separation of ZrN and AlN takes place during annealing. In films with a nanocomposite structure, the phase

transformation is initiated by nucleation and growth of c-ZrN in the ZrN-rich domains while the AlN-rich domains remain largely amorphous at 1100 °C [3]. Nucleation and growth of h-AlN is hindered by a high nitrogen content in the film and takes place at annealing above 1300 °C, simultaneously to loss of the excess nitrogen. The depletion of amorphous phase during annealing results in an improved hardness of the film. In the h-ZrAlN films, ZrN- and AlN-rich domains form within the hexagonal lattice during annealing above 900 °C. The formation of domains with different composition results in an increased hardness, from 24 GPa of the as-deposited film to 31 GPa of the annealed film. The c-ZrAlN phase is found to be stable to annealing temperatures of 1000 °C, while at higher temperatures, h-AlN nucleates and grows. This is different from the c-TiAlN system where spinodal decomposition occurs resulting in age hardening of the films.

- [1] L. Rogström et al., *J. Vac. Sci. Technol. A* 30 (2012) 031504.
- [2] L. Rogström et al., *Scr. Mater.* 62 (2010) 739.
- [3] L. Rogström et al., *J. Mater. Res.*, In press (2012)

11:40am **TF+NS+EM-ThM12 Ion-assisted Epitaxial Sputter-Deposition and Properties of Metastable Zr_{1-x}Al_xN(001) (0.05 x 0.25) Alloys**, *AR.B. Mei*, *B.M. Howe*, University of Illinois at Urbana Champaign, *N. Ghafoor*, *E. Broitman*, Linköping University, Sweden, *M. Sardela*, University of Illinois at Urbana Champaign, *L. Hultman*, Linköping University, Sweden, *A. Rockett*, *J.E. Greene*, *I. Petrov*, University of Illinois at Urbana Champaign, *M. Oden*, *H. Fager*, Linköping University, Sweden

Single-phase epitaxial metastable Zr_{1-x}Al_xN/MgO(001) (0.05 x 0.25) thin films were deposited by ultra-high vacuum magnetically-unbalanced reactive magnetron sputtering from a single Zr_{0.75}Al_{0.25}target at a substrate temperature of 650°C. We control the AlN content, x, in the films by varying the ion energy (5 < E_i < 55 eV) incident at the film growth surface with a constant ion to metal flux ratio of 8. The net atomic flux was decreased from 3.16 to 2.45x10¹⁵ atoms cm⁻²s⁻¹, due to efficient resputtering of deposited Al atoms (27 amu) by Ar⁺ ions (40 amu) neutralized and backscattered from heavy Zr atoms (91.2 amu). Consequentially, films varied in thickness from 400 nm to 290 nm during 20 min depositions. HfN buffer layers were deposited on the MgO(001) substrates to reduce the lattice mismatch from ~8 to ~0.5%. High resolution x-ray diffraction ω-2θ scans and reciprocal lattice mapping revealed single-phase NaCl structure with a cube-on-cube orientation relative to the substrate, (001)_{Zr1-x Alx N}|| (001)_{MgO}, and relaxed lattice parameters varying from 4.546 with x = 0.25 to 4.598 Å with x = 0.05. Film nanoindentation measurements showed that hardness decreases from 28.6 to 23.3 Gpa and Young's modulus increases from 263 Gpa to 296.8 GP as x is varied from 0.25 to 0.05. For the same range in x, electronic transport measurements established the films to have electron mobilities increasing from 2.67 to 462 cm²V⁻¹s⁻¹, resistivities decreasing from 162.4 to 25.4 μΩ-cm, and positive temperature coefficients of resistivity spanning from 0.3164 to 1.307 Ω-cm K⁻¹. Films deposited with incident ion energy above 35 eV (x < 0.08) exhibited superconductivity with T_c of 8.26 K.

Thursday Afternoon, November 1, 2012

Energy Frontiers Focus Topic
Room: 7 - Session EN+NS-ThA

Thermophotovoltaics, Thermoelectrics and Plasmonics
Moderator: R.A. Quinlan, Naval Surface Warfare Center, Cardercock Division

2:00pm **EN+NS-ThA1 Structuring of the Radiative Thermal Emission in Tungsten Inverse Opals for Thermophotovoltaic Applications, M.D. Losego**, North Carolina State University, *K.A. Arpin*, University of Illinois at Urbana Champaign, *B. Kalanyan*, North Carolina State University, *P.V. Braun*, University of Illinois at Urbana Champaign, *G.N. Parsons*, North Carolina State University

Materials with photonic bandgaps are generated by periodic mesostructuring at length-scales comparable to visible wavelengths. While photonic bandgaps are often used to control the interaction of incident light with a material (e.g. reflect incident light over a narrow bandwidth), these structures can also be used to tune the thermal emission of light. Consequently, a heated metallic photonic crystal could be used in a thermophotovoltaic (TPV) device scheme. Such a TPV would (1) absorb broadband incident solar radiation, (2) heat up, and (3) re-emits the radiation over a narrow band of energies. This narrow-band radiation could then be converted to electricity with high efficiencies using a simple single-junction solar cell. However, demonstrating narrow-band thermal emission from a multidimensional architecture remains elusive. The central challenge is finding a materials set that demonstrates the required combination of thermal stability and dielectric function in a nanostructured architecture capable of high-temperature radiant emission.

This talk will examine our development of refractory tungsten inverse-opal structures designed for thermal emission in the visible spectrum. The first generation of these structures were constructed from silica opals infiltrated with electrodeposited tungsten. While ultrathin (<20 nm) oxide ALD layers were found to improve high temperature stability (>1000°C, 12 hours) by restricting surface diffusion and limiting sintering, difficulties with massive structural cracking during the molten-salt electrodeposition process could not be overcome. Second generation devices are now being developed using a lower temperature tungsten atomic layer deposition (ALD) process. Besides the avoidance of massive structural cracking, these ALD materials appear to be denser than electrodeposited materials, further reducing the unwanted sintering effects at high temperatures. Room temperature spectra collected from these structures indicate photonic effects not seen in planar tungsten films and suggest enhanced thermal emission at visible wavelengths.

2:40pm **EN+NS-ThA3 Nanowires and Nanowire Heterostructures for Thermoelectric Energy Harvesting, Y. Wu**, Purdue University **INVITED**
Substantial efforts have been devoted to use nanostructured materials for thermoelectric energy harvesting and solid-state cooling in the past decade. However, the majority of the research is still limited in lab scale due to the incapability to mass-produce well-defined nanostructured materials with low yet industrial-compatible process. In addition, a lot of widely used thermoelectric materials contain toxic and expensive elements that prevent the large-scale deployment of the thermoelectric devices. In this presentation, we will discuss our research on the development of mass production of molecular scale nanostructures of chalcogenides and metal oxides, as well as their heterostructures, for the manufacture of thermoelectric generators operating at different temperature ranges. Particularly, we will talk about our approach to discover and investigate the non-toxic and abundant nanostructured materials to achieve an environmentally friendly process. Our preliminary research indicated that thermoelectric figure of merit (ZT) close to 2 can be achieved in the molecular scale nanowires of certain chalcogenide due to significantly enhanced power factor and reduced thermal conductivity as a result of quantum confinement.

3:40pm **EN+NS-ThA6 Plasmonic Polymer Solar Cells with Spectrally Tuned Au/SiO₂ Core/Shell Nanorods incorporated in Active Layers, V. Jankovic, J.P. Chang, UCLA**

Octadecyl tri-methoxysilane (OTMS) functionalized Au/SiO₂core/shell nanorods were incorporated into the active layers of two different polymer bulk heterojunction (BHJ) systems: a broad band gap polymer (poly(3-hexylthiophene)(P3HT):[6,6]-phenyl-C61-butyric acid methyl ester (PCB60M)) and a low band gap polymer poly{2,6-(4,8-di(5-ethylhexylthienyl)benzo[1,2-b;3,4-b']dithiophene-alt-5-dibutyltolyl-3,6-bis(5-bromothiophen-2-yl) pyrrolo[3,4-c]pyrrole-1,4-dione)} (PBDTT-

DPP):PC60BM. The extinction peaks of the Au nanorod scattering centers was tuned to match the band edge of the two polymers by controlling their aspect ratio. For the P3HT:PC60BM system with a band edge around 700 nm, the addition of the core/shell nanorods of an aspect ratio 1:2.5 (resonant frequency peak is at around $\lambda=650\text{nm}$), resulted in 8% improvement in short circuit current (J_{sc}); for the low band gap polymer system PBDTT-DPP:PC60BM with band edge around 850 nm, we tuned the resonant frequency to near-infrared region by increasing the aspect ratio to 1:4 (resonant frequency peak is at around $\lambda=800\text{nm}$), the addition of the core/shell nanorods resulted in 18% improvement in short circuit current (J_{sc}). The J_{sc} enhancement was consistent with external quantum efficiency (EQE) measurements and the EQE improvement factor matched the absorption resonance spectrum of Au/SiO₂ nanorods in both systems. This work will instruct us on how to utilize and manipulate plasmon resonance of metallic nanoparticles to improve device efficiency in different polymer solar cell systems.

4:00pm **EN+NS-ThA7 Optics and Photonics Research Priorities and Grand Challenges as Relating to Today's Energy Frontiers, E.B. Svedberg**, The National Academies

A new report from the National Research Council of the National Academies identifies research priorities and grand challenges to fill gaps in optics and photonics, a field that has the potential to advance not only the energy field but also the economy of the United States and the world, the report provides visionary directions for future technology applications, and ensure progress in energy related research. As one of its recommendations the report recommends that the federal government develop a "National Photonics Initiative" to bring together academia, industry, and government to steer federal research and development funding and activities.

Eight particular areas of technological application are discussed in separate chapters: communications, information processing, and data storage; defense and national security; energy; health and medicine; advanced manufacturing; advanced photonic measurements and applications; strategic materials for optics; and displays. Each chapter reviews updates that have occurred since the 1998 National Research Council report *Harnessing Light: Optical Science and Engineering for the 21st Century*, as well as the technological opportunities that have risen from recent advances in optical science and engineering. This presentation will focus on the energy section of the report that deals not only with energy generation but also how to reduce excessive usage of energy. The report additionally recommends actions for the development and maintenance of the photonics-driven sector of the energy industry, including both near-term and long-range goals, likely participants, and responsible agents of change.

The recommended National Photonics Initiative will help manage the breadth of rapidly expanding applications of photonics technologies, allowing both governments and industry to develop coherent strategies for technology development and deployment in the energy sector. The initiative should also spearhead a collaborative effort to improve the collection and reporting of research, development, and economic data on this sector.

Graphene and Related Materials Focus Topic
Room: 13 - Session GR+EM+NS+SS+TF-ThA

Beyond Graphene: BN and Other 2D Electronic Materials; 2D Heterostructures

Moderator: I.I. Oleynik, University of South Florida

2:00pm **GR+EM+NS+SS+TF-ThA1 X-ray Photoelectron Spectroscopy Investigation of the Valence and Conduction Band Offset at Hexagonal a-BN:H/Si Interfaces, S. King, M. French, J. Bielefeld**, Intel Corporation, *M. Jaehnig*, Intel Corporation, *M. Kuhn, B. French*, Intel Corporation

Due to a wide band gap (~ 6 eV) and close lattice matching, hexagonal boron nitride (h-BN) is of interest as a potential gate dielectric in graphene channel transistor devices. A key property for the success of h-BN as a gate dielectric in such devices is the valence and conduction band offsets at the h-BN/graphene and h-BN/gate electrode interfaces. In many graphene channel devices, amorphous or poly-Si is a desirable gate electrode material for compatibility in standard CMOS processing. In this regard, we have utilized x-ray photoelectron spectroscopy (XPS) to determine the valence band offset present at the interface between plasma enhanced chemically vapor deposited hexagonal a-BN:H and a (100) Si substrate. Combined with Reflection Electron Energy Loss Spectroscopy measurements of the a-BN:H band gap, we have also been able to determine the conduction band

offset at this interface. The combined measurements indicate a type I alignment with valence and conduction band offsets of 1.95 ± 0.1 and 2.15 ± 0.17 eV respectively.

2:20pm GR+EM+NS+SS+TF-ThA2 Monolayer Graphene-Boron Nitride 2D Heterostructures, R. Cortes, J. Lahiri, E. Sutter, P.W. Sutter, Brookhaven National Laboratory

Unusual electronic properties have been predicted for monolayer graphene-boron nitride heterostructures, but access to these properties depends on methods for controlling the formation of graphene-boron nitride interfaces [1]. Here we report on the growth and interface formation of monolayer graphene (MLG)-hexagonal boron nitride (h-BN) 2D heterostructures on Ru(0001), investigated by a combination of real-time low-energy electron microscopy (LEEM) and scanning tunneling microscopy (STM).

LEEM observations of sequential chemical vapor deposition growth show that h-BN attaches preferentially to the edges of existing MLG domains, while nucleation of h-BN on the Ru surface away from MLG is not observed at the conditions considered here. With increasing coverage, h-BN expands anisotropically and, ultimately, the substrate is covered by a continuous 2D membrane of MLG domains embedded in h-BN. The study of the 1D interface between MLG and h-BN in these membranes by STM demonstrates that, following sequential growth at high temperatures, the interface is not abrupt, but contains an intermixed zone consisting of h-BN with embedded carbon atoms. Using quantitative LEEM, we have identified processes that eliminate this intermixing and pave the way to atomically sharp graphene-boron nitride boundaries, as confirmed by STM. The application of a similar growth procedure to terminate the edges of atomically controlled graphene nanoribbons with h-BN, embedding them in a h-BN membrane, will be considered.

[1] P. Sutter, R. Cortes, J. Lahiri, and E. Sutter. *Submitted* (2012).

2:40pm GR+EM+NS+SS+TF-ThA3 Large Area Vapor Phase Growth and Characterization of MoS₂ Atomic Layers, J. Lou, S. Najmaei, Z. Liu, Y. Zhan, P. Ajayan, Rice University INVITED

Monolayer Molybdenum disulfide (MoS₂), a two-dimensional crystal with a direct bandgap, is a promising candidate for 2D nanoelectronic devices complementing graphene. Unlike conductive graphene and insulating h-BN, atomic layered MoS₂ is a semiconductor material with a direct bandgap, offering possibilities of fabricating high performance devices with low power consumption in a more straight-forward manner.

In this talk, we will discuss our recent efforts on the large area growth of MoS₂ atomic layers by a scalable chemical vapor deposition (CVD) method. The as-prepared samples can either be readily utilized for further device fabrication or be easily released from the growth substrate and transferred to arbitrary substrates. High resolution transmission electron microscopy and Raman spectroscopy on the as grown films of MoS₂ indicate that the number of layers range from single layer to a few layers. Our results on the direct growth of MoS₂ layers on dielectric leading to facile device fabrication possibilities show the expanding set of useful 2D atomic layers, on the heels of graphene, which can be controllably synthesized and manipulated for many applications.

3:40pm GR+EM+NS+SS+TF-ThA6 Formation of Silicene and 2D Si Sheets on Ag(111): Growth Mode, Structural and Electronic Properties, P. Vogt, Technical University of Berlin, Germany, T. Bruhn, A. Resta, B. Ealet, CNRS CiNaM, Marseille, France, P. De Padova, CNR-ISM, Rome, Italy, G. Le Lay, CNRS CiNaM, Marseille, France

Since the discovery of graphene enormous efforts have been invested to discover other similar 2-dimensional materials, like e.g. silicene. These 2D materials share similar structural, electronic and optical properties as graphene but are expected to differ in terms of their respective chemical reactivity and thus their applicability for electronic devices. In particular silicene could more easily be integrated into current Si-based electronics than graphene. Silicene has been predicted theoretically [1,2] but does not seem to exist in nature.

Recently, we could synthesize silicone layers grown epitaxially by depositing Si on Ag(111) surfaces. The electronic properties of these silicene layers were shown to behave as theoretically predicted [3] and the structural and electronic properties are very similar to graphene. In STM images the hexagonal 2D silicone sheet gives rise to triangular structures situated in a honeycomb arrangement with (4×4) symmetry with respect to the Ag(111) surface. A structural model derived from the STM

measurements showed a very good agreement with DFT results and exhibited a downward conical electronic dispersion resembling that of relativistic Dirac fermions at the Si K-points [3]. Depending on the growth conditions the formation of different 2D silicon arrangements can be observed: 1) Si-clusters at low deposition temperatures, 2) the formation of less ordered 2D hexagonal Si-based structures at temperatures up to 180°C, 3) the formation of the (4×4) silicene sheet around 220°C and 4) a 2D Si structure with a ($\sqrt{13} \times \sqrt{13}$)-like periodicity at higher growth temperatures exhibiting a very regular, wide range ordered Moiré-like surface pattern in STM.

Here, we will discuss the formation and epitaxial growth mode of these different 2D Si structures and the dependence on the growth parameters. We will also investigate whether these different 2D Si layers all refer to similar silicene sheets which give rise to different appearances in STM due to a varying rotation with respect to each other.

Keywords: silicene, 2D materials, graphene, Dirac fermions

References:

- [1] S. Cahangirov et al., *Phys. Rev. Lett.* **102**, 236804 (2009)
- [2] G. G. Guzman-Verri and L. C. Lew Yan Voon, *Phys. Rev. B* **76**, 75131 (2007)
- [3] P. Vogt et al., *Phys. Rev. Lett.* **108**, 155501 (2012)

4:00pm GR+EM+NS+SS+TF-ThA7 Yttria-monolayer on Pt(111) Supported Graphene: A Novel Two Dimensional Heterostructure and its Affect on Charge Doping of Graphene, R. Addou, A. Dahal, M. Batzill, University of South Florida

Yttrium oxide (Y₂O₃) is a high-k dielectric material, with promising wetting behavior of graphene [1]. In our study we grew yttria by reactive MBE on Pt(111) supported graphene to investigate the structural and electronic properties of the graphene/yttria interface. Photoemission measurements indicate that the graphene layer is covered by yttria. Scanning tunneling microscopy (STM) and low energy electron diffraction reveal that at annealing temperatures higher than 600 °C yttria forms an ordered monolayer on top of graphene. In STM, a moiré pattern is observed that is a consequence of super-positioning of a hexagonal yttria monolayer lattice with that of graphene. X-ray photoemission indicates a shift of the C1s peak by 1 eV to higher binding energy upon depositing of the yttria film. This peak shift is explained by charge doping of graphene by the underlying Pt substrate due to the change in the work function of the yttria coated graphene.

[1] Z. Wang et al. *Nano Lett.* **2010**, 10, 2024–2030; L. Ding et al. *Nano Lett.* **2009**, 9, 4209–4214.

4:20pm GR+EM+NS+SS+TF-ThA8 Probing the BCN-triangle by Computations—Outside the Carbon Corner, Jakobson, Rice University INVITED

We will discuss recent work on modeling 2D-materials “beyond graphene” [1-2]: two dimensional hexagonal h-BN, pure B polymorphs, MoS₂, etc. Lessons from graphene studies remain invaluable as they offer general approach and views on the edges [3] and interface structures and energies, and especially organization of the grain boundaries [4,5]. New dislocation cores in BN (both 5/7 and 4/8 types) lead to accordingly new physical properties of emerging polar GB [6]. Similarly, we identify the dislocation cores and the grain boundary structure for more complex polar layer-material, MoS₂ (X. Zou, unpublished). Our analysis of edge and cleavage energies helps to explain fracture patterns emerging in the course of synthesis. In principle, computations suggest possibility of metastable 2D-layers of GaN or ZnO or even their hybrids. Finally, it is important to mention clear opportunities of designing 2D-circuits by combining 2D-materials in specific functional patterns like proposed nanoroads and quantum dots [7-8] which now become a subject of experimental laboratory work.

- [1] Y. Liu et al. *Nano Lett.* **11**, 3113 (2011). [2] E. Penev, et al, *Nano Lett.* **12**, 2441 (2012). [3] Y. Liu et al. *Phys. Rev. Lett.* **105**, 235502 (2010). [4] BIY and F. Ding, *ACS Nano* **5**, 1569 (2011). [5] Ajayan and BIY, *Nature Mater.* **10**, 415 (2011). [6] Y. Liu et al. *ACS Nano* (2012). [7] A. Singh and BIY, *Nano Lett.*, **9**, 1540 (2009). [8] A. Singh, E. Penev, and BIY, *ACS Nano*, **4**, 3510 (2010).

5:00pm GR+EM+NS+SS+TF-ThA10 Single-layer MoS₂ Devices and Circuits, A. Kis, EPFL, Switzerland INVITED

Single layer MoS₂ is a recent addition to the family of 2D materials and is reminiscent of graphene except that it is an intrinsic direct band gap semiconductor with a 1.8 eV gap. We have exfoliated single layers 6.5 Angstrom thick from bulk crystals of semiconducting MoS₂, using the micromechanical cleavage technique commonly used for the production of

graphene. Our nanolayers are mechanically and chemically stable under ambient conditions. We have fabricated transistors based on single-layer MoS₂ which demonstrate that this material has several advantages over silicon for potential applications in electronics. Our transistors have room-temperature current on/off ratios higher than 10⁸, mobility higher than 780 cm²/Vs and leakage currents in the fA range. Integrated circuits based on MoS₂ have the capability to amplify signals and perform logic operations. Finally, I will show our work on suspended MoS₂ membranes that show ripples similar to those observed in graphene. MoS₂ also has superior mechanical properties: higher stiffness than steel and 30 times its breaking strength which makes it suitable for integration in flexible electronics.

References

1. B. Radisavljevic, A. Radenovic, J. Brivio, V. Giacometti, and A. Kis. Single-layer MoS₂ transistors. *Nature Nanotechnology* 6, 147, 2011. doi: 10.1038/nnano.2010.279
2. M.M. Benameur, B. Radisavljevic, J.S. Heron, S. Sahoo, H. Berger, and A. Kis. Visibility of dichalcogenide nanolayers. *Nanotechnology* 22, 125706, 2011. doi: 10.1088/0957-4484/22/12/125706
3. B. Radisavljevic, M.B. Whitwick, and A. Kis. Integrated circuits and logic operations based on single-layer MoS₂. *ACS Nano* 5, 9934, 2011. doi: 10.1021/nn203715c
4. J. Brivio, D.T.L. Alexander, and A. Kis. Ripples and Layers in Ultrathin MoS₂ Membranes. *Nano Letters* 11, 5148, 2011. doi: 10.1021/nl2022288
5. S. Bertolazzi, J. Brivio, and A. Kis. Stretching and Breaking of Ultrathin MoS₂. *ACS Nano* 5, 9703, 2011. doi: 10.1021/nn203879f

Surface Science

Room: 21 - Session SS+NS-ThA

Surface Science of Nanostructures

Moderator: J.M. Millunchick, University of Michigan

2:00pm SS+NS-ThA1 Direct Atomic Scale Imaging and Spectroscopy of III-V Semiconductor Nanowire Surfaces, A. Mikkelsen, Lund University, Sweden **INVITED**

Free-standing III-V nanowires have the potential to become central components in future electronics and photonics with applications in IT, life-science and energy[1]. The atomic scale structure and morphology of semiconductor nanowire surfaces are central in determining both growth and function of the wires. Surface diffusion and nucleation will directly influence the final appearance of the wires, and transport and optical properties of semiconductor nanowires is often governed by their surfaces.

We develop and use scanning probe and synchrotron based microscopy/spectroscopy to completely determine structure, chemistry and physical properties of III-V nanowire surfaces with extreme precision. We use our novel methods to directly image both interior and exterior surfaces of the nanowires down to the single atom level, revealing geometric structure as well as both electrical and mechanical properties[2-4]. With our rather diverse toolbox we can obtain a real understanding of the connections between nanowire structure, growth and function.

We present recent Scanning Tunneling Microscopy/spectroscopy (STM/S) results, on nanowires consisting of various III-V materials and of polytypic heterostructures with wurtzite (WZ) and zincblende (ZB) crystal segments - only possible in nanowires. We have obtained images of the atomic scale structure for all common WZ and ZB facets as well as information about the electronic structure using STS. We are now developing these methods to perform STM/S on individual nanowires under device operation. Further, we show that STM, can be used for direct top view imaging of the micrometer high free-standing nanowires. We then determine mechanical resonances up to hundreds of MHz with sub Ångström precision[4].

Finally, using synchrotron based Photo Emission / Low Energy Electron Microscopy/Spectroscopy (PEEM/LEEM/XPS) we have characterized III-V nanowire surface chemistry and electronic properties and investigated the influence of various ultra-thin dielectrics to reduce surface band-bending effects[5-8]. A complete picture of oxide thicknesses, effects on bandbending and information on axial and radial doping is obtained.

1. C.M. Lieber and Z.L. Wang, *MRS Bull.* **32**, 99 (2007), and other papers in this issue.
2. A. Mikkelsen et al, *Nature Mater.* **3**, 519 (2004) ; L. Ouattara et al, *Nano Lett.* **7**, 2859 (2007)
3. E. Hilner, et al, *Nano Lett.* **8**, 3978 (2008)
4. A. Fian, et al, *Nano Lett.* **10**, 3893 (2010)
5. R. Timm et al., *Appl. Phys. Lett.* **99**, 222907 (2011).

6. B. Mandl et al., *Nano Lett.* **10**, 4443 (2012)
7. R. Timm et al., *Microelectron. Eng.* **88**, 1091 (2011).
8. M. Hjort et al, *Appl. Phys. Lett.* **99**, 233113 (2011)

2:40pm SS+NS-ThA3 Spontaneous Assembly of Ordered Atomic Wires with a Long Interwire Distance on a Stepped Nanotemplate, B.G. Shin, M.K. Kim, D.-H. Oh, C.-Y. Park, J.R. Ahn, Sungkyunkwan University, Republic of Korea

Atomic wires do not interact directly with each other and are therefore ordered by an indirect substrate mediated interaction, whereas molecular structures can be assembled spontaneously by a direct interaction with each other. Such interwire interactions were very short and subsequently an interwire distance of ordered atomic wires were a few Å. Because of the interwire interaction, atomic wires have been described as a quasi 1D system rather than an ideal 1D system. Therefore, an atomic wire with a long interwire distance needs to study an ideal 1D system but, as mentioned before, atomic wires were not ordered with a long interwire distance. Assembly of a long interwire distance atomic wire is thus very challenging and demanded to widen experimental scope of studies on one-dimensional physics. In this study, indium atomic wires with a long interwire distance of 5.7 nm were ordered spontaneously at room temperature on a stepwise nanotemplate, a Si(557) surface. In general, interwire interactions are required to produce ordered nanowires so that other ordered atomic wires have a short interwire distance of a few Å, as described above. The long interwire distance of the ordered indium atomic wires is therefore very unique. Indium atoms were mobile at room temperature and were adsorbed on a only specific step among four steps, one (111) and three (112) steps of the reconstructed Si(557) surface, maintaining the stepwise nanotemplate structure, as observed by scanning tunneling microscopy (STM), despite the fact that the triple steps have similar local atomic structures. The energetic stability of the indium atomic wires was calculated by first-principles calculations. The reconstructed Si(557) structure model was based on the dimer-adatom-stacking fault (DAS) model and adatom-parallel dimer (AD) model of (111) and (112) facets, respectively.[1, 2] Total energy differences between indium atomic wires on the three (112) steps was very small and the most stable atomic structure was located at the second (112) step, which was consistent with STM images. STM simulations also reproduced the x2 periodicity of the In-induced atomic wires along the wire direction.

- [1] K. Takayanagi, Y. Tanishiro, M. Takahashi, and S. Takahashi, *J. Vac. Sci. Technol. A* **3**, 1502 (1985)
- [2] D. Oh, M. Kim, J. Nam, I. Song, C. Park, S. Woo, H. Hwang, C. Hwang, J. Ahn, *Phys. Rev. B*, **77**, 155430 (2008)

3:00pm SS+NS-ThA4 Influence of Surface Steps on the Initial Oxidation of TiN (100), M. Hong, S.R. Phillpot, S.B. Sinnott, University of Florida

Titanium nitride (TiN) film has extreme hardness, high chemical reactivity and high electrical conductivity and thus is widely used for wear and corrosion resistant coatings as well as diffusion barriers and gate electrodes in microelectronic devices. They are thus routinely subjected to extreme conditions such as high pressure and temperature, corrosive environments, and consequently undergo oxidation. Here, density functional theory calculations are used to determine the mechanisms associated with step-related oxidation process and the formation of TiO_x induced by both the dissociation of O₂ and Ti surface diffusion on TiN (100). Preliminary calculations reveal stable adsorption sites near surface steps for O₂ molecules and single O adatoms, both of which have adsorption energies larger than on terraces. This indicates that the dissipated energy during O₂ dissociation near the surface step is larger than that on (100) terraces so that consequent oxidation reactions can occur more easily. The calculations reveal potential O₂ dissociation paths with activation energies in the range of 1-2 eV. This work is supported by the National Science Foundation (DMR-1005779).

3:40pm SS+NS-ThA6 Growth of Ag/Ge(111) Phases Studied with LEEM and LEED, S. Chiang, C. Mullet, UC Davis

Low energy electron microscopy (LEEM) and low energy electron diffraction (LEED) were used to study the growth of structural phases of Ag deposited on Ge(111) above and below the Ag desorption temperature. Ag deposited on Ge(111) formed three main surface phases above 100°C: (4x4), (√3x√3)R30°, and (3x1). At a given coverage, (4x4) island size increased with deposition temperature and decreased with deposition rate. The (4x4) structure nucleated at steps edges and grew only at steps for samples with very high step density. While the √3 structure did not show a preference for nucleating at steps, its growth was bounded by substrate step bunches. The (3x1) was the only Ag phase on the surface for deposition at

370°C and coverage $\Theta < 0.1$ ML, forming domains large enough to be resolved in LEEM images. The (3x1) and (4x4) phases coexisted for $T < 350^\circ\text{C}$ and $0.1 < \Theta < 0.38$ ML, while the (3x1) and $\sqrt{3}$ phases coexisted for $T > 400^\circ\text{C}$ and $\Theta > 0.4$ ML. LEEM images of Ag desorption from Ge(1 1 1) at $T > 575^\circ\text{C}$ showed that Ag (4x4) and $\sqrt{3}$ phases reversibly transform to a disordered (1x1) phase, with desorption proceeding from the edges of disordered (1x1) domains and the (1x1) phase being slightly less dense than the (4x4) phase. For sufficiently high deposition rates, Ag was observed to accumulate on Ge(111) above the 575°C desorption temperature. For deposition between 580 and 640°C , a silver layer formed with a (3x1) LEED pattern; upon completion of that layer, a $\sqrt{3}$ layer formed. For deposition at 660°C , only the (3x1) layer formed. Desorption proceeded by the reverse sequence of phases.

Funded by NSF CHE-0719504 and NSF PHY-1004848

4:00pm SS+NS-ThA7 A Synchrotron XPS Study of the Radio-Frequency SF₆ Plasma Fluorination of Single-Walled Carbon Nanotubes, A.J. Barlow, NEXUS XPS Facility, Newcastle University UK, A.J. Blanch, A.D. Slattery, J.S. Quinton, Flinders University, Australia

With the ever increasing utilisation of carbon nanostructures across many fields, researchers are continuously looking for new and more efficient methods for the reliable and controllable functionalisation of these materials, in a way that is easily scalable. This is particularly true for the one dimensional carbon nanotube (CNT). While plasma science is not a new field, its application towards the covalent attachment of chemically reactive species to the sidewalls of the initially somewhat inert CNT structure has only more recently been investigated. Furthermore, in-depth studies of the plasma functionalisation of CNTs using fluorine-rich species such as sulphur hexafluoride (SF₆) are limited for a process that is capable of not only providing reactive sites for further chemical attachment but also the modification of the electronic structure of the nanotube [1, 2].

In this presentation research efforts into the fluorination of single-walled CNTs (SWCNTs) in a controlled manner using SF₆ plasma will be discussed. Control over the amount of fluorine attached to the CNT surfaces is demonstrated through variation in experimental conditions such as plasma power. Furthermore, the *type* of fluorine bonding present on the surface (covalent or semi-ionic) is shown to be controllable through the addition of oxygen containing species into the fluorination mechanism. This can be achieved through either the doping of the plasma itself with oxygen or water vapour, or by an oxidative surface pretreatment of the CNTs through wet-chemical or plasma methods. With this level of control, greatly enhanced C-F covalency can be achieved over a pure SF₆ plasma treatment alone. Results will be presented from lab-based XPS analysis of SWCNT surfaces performed at Flinders University, South Australia, as well as synchrotron-based XPS analysis performed at the Australian Synchrotron.

1. Park, K.A., Y.S. Choi, and Y.H. Lee, *Atomic and electronic structures of fluorinated single-walled carbon nanotubes*. Phys. Rev. B, 2003. **68**: p. 045429.

2. Plank, N.O.V., et al., *Electronic properties of n-type carbon nanotubes prepared by CF₄ plasma fluorination and amino functionalisation*. J. Phys. Chem. Lett. B, 2005. **109**: p. 22096-22101.

4:20pm SS+NS-ThA8 Solving the Shape of Micellar Pt Nanoparticles Supported on TiO₂(110) and γ -Al₂O₃: A STM, TEM and EXAFS Study, F. Behafarid, B. Roldan Cuenya, University of Central Florida

Nanoparticles (NPs) with well-defined sizes and shapes were synthesized via inverse micelle encapsulation methods. For 2-4 nm Pt and Au NPs supported on TiO₂(110), the shape was resolved by scanning tunneling microscopy (STM). Geometrical information on smaller Pt NPs supported on nanocrystalline γ -Al₂O₃ was extracted by a combination of transmission electron microscopy (TEM) and extended x-ray absorption fine-structure spectroscopy (EXAFS) measurements. It will be shown that the size, interparticle distance, and the geometry (2D vs 3D) of the NPs can be tuned via our micellar synthesis.

Pt NPs in the size range of 2-4 nm supported on TiO₂(110) were studied by STM after heating in UHV at high temperature ($>1000^\circ\text{C}$). This thermal treatment facilitates the melting of the NPs and the formation of NP-support epitaxial interfaces. High resolution STM images allowed us to determine the shape of the NPs as well as facet orientations. Three different shape types were observed, and each category of shapes was found to appear within a particular NP size regime. In addition, the epitaxial relationship between the NPs and the TiO₂(110) surface was investigated in order to explain the specific orientation of the NPs observed in our study. It was also found that due to interface-induced strain, the NP shapes obtained do not follow the Wulff theorem, namely $\{100\}/\{111\}$ facet area ratios deviating from the value obtained for support-free clusters.

Pt NPs in the size range of 0.8-1.5 nm supported on γ -Al₂O₃ were studied by EXAFS, and the nearest neighbor coordination numbers up to the 4th

shell were obtained following multiple scattering analysis. These coordination numbers, together with the NP diameter obtained by TEM were examined against a theoretically generated database of possible NPs shapes to determine the most representative shape of Pt NPs in each of the samples. Correlations between the reactivity and the shape of the Pt NPs were established.

4:40pm SS+NS-ThA9 Geometrical, Electronic, and Vibrational Properties of Bare and H-covered Pt_n(n=22, 33, 44, 55, and 85) Nanoparticles, G. Shaifai, S. Hong, M. Alcantara, T.S. Rahman, University of Central Florida

We have performed systematic density functional theory (DFT) calculations of the geometrical, electronic, and vibrational properties of small Pt_n nanoparticles (NPs) ($n=22, 33, 44, 55, \text{ and } 85$) and their changes with NP size and adsorbate (H₂) coverage. We find our calculated H adsorption energy to be in range of -0.42 eV and -0.62 eV, and with increasing hydrogen coverage the H adsorption energy decreases due to adsorbate-adsorbate interactions. We find increase of Pt-Pt bond length upon hydrogen adsorption and, strikingly, the red shift of the center of the *unoccupied* d-bands of the bare Pt clusters turns to a blue shift upon hydrogen adsorption in good agreement with experiment [1]. We also find that there is a net charge transfer from all Pt atoms within the NPs to all hydrogen atoms of 0.55 (Pt₂₂H₂₂) and 1.37 electrons (Pt₄₄H₄₄). Thus, the remarkable hydrogen effect on the electronic structure of Pt NPs can be attributed to charge transfer from the Pt NPs to hydrogen. Regarding the optimal H coverage on Pt NPs, our calculated free-energy phase diagram shows non-zero H coverage even at beyond 600K under ambient H₂ pressure. This work is supported in part by US-DOE under Grant No. DE-FG02-07ER46354.

[1] F. Behafarid, L.K. Ono, S. Mostafa, J. R. Croy, G. Shaifai, S. Hong, T. S. Rahman, Simon R. Bare, and B. Roldan Cuenya, submitted.

5:00pm SS+NS-ThA10 The Effect of S to Se Substitution in SAMs: Odd-Even Polymorphism of Biphenyl-Substituted Alkaneselenolate on Au(111), M. Dendzik, Jagiellonian University, Poland, A. Terfort, Goethe University, Germany, P. Cyganik, Jagiellonian University, Poland

To fabricate aromatic self-assembled monolayers (SAMs) of practical importance for molecular electronics and other applications, high level of control over the SAMs properties should be achieved. In particular, besides monitoring the electronic properties, the control of structure and stability, is an issue of equal importance. As demonstrated previously one way to improve structure and stability of these systems can be achieved by the substitution of the headgroup atom (S versus Se, which binds SAMs constituent to the substrate) [1-3]. In the present study [4], to elucidate how the S to Se substitution influences SAMs structure and stability, we investigate influence of the BPNSe/Au(111) (BPNSe, CH₃-(C₆H₄)₂-(CH₂)_n-Se-, $n=2-6$) formation temperature and compare obtained results with the corresponding data obtained for their thiol analogues i.e. for BPNs/Au(111) SAMs. Obtained STM data are discussed and analysed in view of the spectroscopic [2] and spectrometric [3] results reported by us recently for these systems, as well as compared to the previously reported STM data [1]. Observed odd-even effect in polymorphism for BPNSe/Au(111) indicates that bonding configuration at the molecule-substrate interface contributes significantly to the energetics of the SAM. We conclude that S to Se substitution increases strength of the molecule-substrate bonding at the expense of reducing strength of the Au_{surface}-Au_{bulk} and Se-C bonding.

References

- (1) P. Cyganik, K. Szelagowska-Kunstman, et al. *J. Phys. Chem. C* **2008**, *112*, 15466.
- (2) K. Szelagowska-Kunstman, P. Cyganik, et al. *Phys. Chem. Chem. Phys.* **2010**, *12*, 4400.
- (3) S. Wyczawska, P. Cyganik, A. Terfort, P. Lievens, *ChemPhysChem* **2011**, *12*, 2554.
- (4) M. Dendzik, A. Terfort, and P. Cyganik *in preparation*

5:20pm SS+NS-ThA11 Molecular Self-Assembly by Ionic Bonding in a Series of Carboxylate Species on the Cu(100) Surface, D. Skomski, S.L. Tait, Indiana University - Bloomington

To expand the catalogue of available interactions for the efficient self-assembly of highly-ordered nanoscale structures, we have investigated the formation of high-stability supramolecular networks constructed with anionic carboxylate species and sodium cations. Our experiments demonstrate that these two-component approaches can steer organic molecules towards efficient self-assembly, even with molecules that do not show a strong tendency towards long-range, two-dimensional ordering when deposited alone. Biphenyl-3,3',5,5'-tetracarboxylic acid (BTA) on Cu(100) serves as a model system to illustrate this effect. Ionic structures have been resolved with molecular and atomic resolution using scanning

tunneling microscopy (STM). Chemical shifts in the Na 1s, C 1s, and O 1s core level binding energies, measured by X-ray photoelectron spectroscopy, confirm the active chemical interactions inferred from the STM results.

Ionic self-assembly has been achieved on the Cu(100) surface with terephthalic acid, trimesic acid, as well as BTA. We have shown that the carboxylate and sodium chloride undergo a replacement reaction producing a new salt with long range periodic structure. Chemical shifts in the sodium 1s photoelectron peak have been observed upon addition of the organic species to the surface, confirming a direct interaction. Resulting extended network structures demonstrate very high stability, maintaining their supramolecular structure up to at least 165 °C. The formation of new structures illustrates the interplay between adsorbate-substrate and ionic interactions and opens new possibilities for ionic self-assemblies at surfaces with highly-ordered structure and specific chemical function.

Thursday Afternoon Poster Sessions

Nanometer-scale Science and Technology

Room: Central Hall - Session NS-ThP

Nanometer-scale Science and Technology Poster Session

NS-ThP1 Composites of Silicone Nanofilaments and TiO₂ Nanoparticles for Photocatalysis. *G.R. Meseck, R. Kontic, G.R. Patzke, S. Seeger*, University of Zurich, Switzerland

Secured access to clean water resources is a fundamental need of human society and nanoparticulate TiO₂ is amongst the most important materials for the photocatalytic degradation of organic pollutants. While TiO₂-nanoparticles (NPs) thus offer photocatalytically effective routes to wastewater treatment, separation of NPs from reaction media is difficult and catalyst recycling often impossible. Immobilization of TiO₂-NPs is therefore indispensable to facilitate handling as well as to control potential health and environmental hazards. We present silicone nanofilaments as a new flexible carrier type for TiO₂-NPs, because they can be deposited as thin carpets on a variety of substrates and their silicone nature renders them chemically and environmentally stable. We deposited TiO₂-NPs on thin carpets of silicone nanofilaments on glass slides in a convenient one-step reaction in ethanol/water mixtures from TiF₄ as precursor under mild conditions. The resulting nanocomposite material is characterized with a wide range of electron microscopy and other analytical techniques. The photocatalytic activity in the decomposition of methylene blue (MB) is proved and superior to TiO₂-NPs immobilized on bare glass supports. Furthermore, the substrates are reusable for several cycles without significant loss in activity.

NS-ThP2 Organic Vapor Adsorption on In Situ Grown Carbon Nanotube Films. *K. Bosnick, S. Ban, W.K. Hiebert, Z. Shi, C. Huang, R. Lister, M. Mleczko*, National Research Council of Canada

Organic vapor adsorption isotherms are measured on in situ grown carbon nanotube (CNT) films using piezoelectric GaPO₄ crystal microbalances as mass sensing substrates. The isotherms are Type IV and show adsorption / desorption hysteresis, consistent with a porous material. The measured porosity is 2%, a value surprisingly low given an over 90% void volume in the film estimated from density considerations. At low pressures ($p/p_0 < 0.25$) the isotherm is well fit by the Freundlich model and at intermediate pressures ($p/p_0 = 0.1-0.4$) by the Brunauer, Emmett, Teller (BET) model. Monte Carlo simulations show three consecutive adsorption processes: filling of the intratube micropores at low pressures, monolayer coverage of the CNT external surface at intermediate pressures, and capillary condensation in the intertube mesopores at high pressures. The simulation results validate the use of the BET model for surface area analysis in the experimental system. The average total accessible surface area is found to be $180 \pm 100 \text{ mm}^2$ and the specific surface area is estimated to be $45 \pm 25 \text{ m}^2/\text{g}$. Further engineering of the CNT film microstructure should lead to much higher surface areas. [Carbon 49 (2011) 3639]

NS-ThP3 Integrated Ultra-High Vacuum Tip-Enhanced Raman Spectroscopy with Molecular-Resolution Microscopy of Large Polyatomic Molecular Adsorbates on Single Crystal Surfaces. *N. Jiang, E.T. Foley, J.M. Klingsporn, M.D. Sonntag, M.C. Hersam, R.P. Van Duyne*, Northwestern University

Multiple vibrational modes have been observed for copper phthalocyanine (CuPc) adlayers on Ag(111) using ultrahigh vacuum (UHV) tip-enhanced Raman spectroscopy (TERS). Several important new experimental features are introduced in this work that significantly advance the state-of-the-art in UHV-TERS. These include (1) concurrent sub-nm molecular resolution STM imaging using Ag tips with laser illumination of the tip-sample junction, (2) laser focusing and Raman collection optics that are external to the UHV-STM that has two cryoshrouds for future low temperature experiments, and (3) all sample preparation steps are carried out in UHV to minimize contamination and maximize spatial resolution. Further, density-functional theory calculations have been carried out that allow quantitative identification of eight different vibrational modes in the TER spectra. The combination of molecular-resolution UHV-STM imaging with the detailed chemical information content of UHV-TERS allows the interactions between large polyatomic molecular adsorbates and specific binding sites on solid surfaces to be probed with unprecedented spatial and spectroscopic resolution.

NS-ThP4 An New One-step Synthesis Method for Generating Nanocarbon-supported Metal Nanoparticle. *J. Kang, L. Li, N. Zetsu, O. Takai, N. Saito*, Nagoya University, Japan

Introduction

Metal nanoparticles attract sustained attention due to their application in electrocatalysis for cell. Recently, many loading methods of nanoparticles on carbon material such as chemical reductions, electrochemical reductions, sol-gel polymerization and ultrasonic vibration have been reported for the generation of cell electrode. However, these methods generally require either reducing agent to reduce metal ions or removal of residues from the solution dispersed nanoparticles and its dispersibility and loading amount is poor. To supplement these weaknesses, in this study, the Au, Ag, Pt, Au-Pt bimetallic alloyed nanoparticles were synthesized simultaneously with carbon nanoball (Au, Ag, Pt, Au-Pt/CNB) by our progressive method, Solution Plasma Process (SPP).

Experimental Procedures

Highly porous CNBs were synthesized from 200 ml of organic. The glow discharge in solution was produced by using a bipolar pulsed power supply operated at 1.6 kV of voltage, 15 kHz of pulse frequency, 0.7ms of pulse width, and 0.3 mm electrode distance, respectively and then NPs/CNB were annealed for improvement conductivity of CNB. The nanoparticle/carbon nanoball (NPs/CNB) were characterized by X-ray diffraction (XRD), transmission electron microscopy (TEM), scanning electron microscope (SEM) Brunauer-Emmett-Teller (BET) method and cyclic voltammetry (CV)

Results and Discussion

Approximately 500mg of CNB were generated by SPP of 200ml of organic solution in 15 minute process time. As evaluated by SEM, the diameters of CNB were in a range of 20 nm to 30nm and it showed that these carbon spheres have a ball-like and chain-like morphology, accompanied with a quite uniform diameter. The Scanning Transmission Electron Microscopy (STEM) image showed that the 1~2 nm diameter of Au, Pt, Au-Pt bimetallic alloyed nanoparticles were deposited on all of CNB with high loading and dispersion. The BET surface area and the pore volume of as obtained CNB were respectively, 120~130 m²/g and 0.8~0.9 cm³/g. The average pore size could be estimated approximately as 20~25nm. Subsequent heating of the CNB at 850°C for 30 minutes under an Ar environment encouraged the increase of the BET surface area and pore volume of CNB to 250~300 m²/g and 1.1~1.3 cm³/g respectively. The average pore size was calculated around 15~16nm. These results strongly suggested that our newly developed process of NPs/CNB synthesis might be a potential method for a single-step production of nanocarbon-supported metal nanoparticle.

NS-ThP5 The Role of an Amorphous Carbon Layer on a Multi-Wall Carbon Nanotube Attached Atomic Force Microscope Tip in Making Good Electrical Contact to a Gold Electrode. *S.J. Ahn*, KRISS, Republic of Korea

Multi-wall carbon nanotube (MWNT) attached atomic force microscope (AFM) tips (MWNT tips) have good potential for use in AFM lithography. Good conducting MWNT tips are needed in such applications. However, characterizing the conductance of MWNT tips is nontrivial: making a good electrical contact between the MWNT and electrode is difficult. We observed that MWNT tips produced by hydrocarbon-deposition attachment usually do not make good electrical contacts to gold electrodes because of the thin and rough amorphous carbon layer on the MWNT that was unintentionally deposited during the attachment. We found that good contacts can be made if a more amorphous carbon layer is deposited to form a thick and smooth amorphous carbon layer on MWNTs. Good contact was made either by transformation of the amorphous carbon layer into a conducting or peel-off layer, exposing the bare MWNT surface. MWNT tips with an exposed MWNT surface showed the well-known high-current-flowing capacity and the stepped-cutting behavior of bare MWNTs. The peeling-off behavior of a thick amorphous carbon layer may be utilized in producing bare-surfaced MWNT tips that have good conductance and therefore are useful for applications.

NS-ThP6 Passivation Effects on Electrical Properties of SnO₂ Nanowires FET Treated by Nitrogen Plasma. *Y.H. Choi, P.S. Kang, J.H. Na, J.S. Kim*, Korea University, Republic of Korea, *S.-H. Choi*, Korea Institute of Science and Technology, Republic of Korea, *M.Y. You, G.T. Kim*, Korea University, Republic of Korea

SnO₂ (tin oxide) are used in various research fields such as thin film transistors (TFTs), flexible and transparent nanowire transistors, and gas sensors, because of large band gap of 3.6 eV, high electron mobility and a

high surface-to-volume ratio. However, the electrical characteristics of SnO₂ nanowires FETs are not so stable in ambient conditions due to the chemical reactions between oxygen molecules in air and oxygen vacancies in SnO₂ nanowires. To improve the device reliabilities of SnO₂ nanowires FETs, the N₂ plasma were treated. The N₂ plasma treatments on SnO₂ nanowires FETs led to the reduction of the hysteresis width in the transfer characteristics. Also the threshold voltage shifted to the positive direction. Even though the reliability of SnO₂ nanowires FETs is improved after the N₂ plasma treatment, unnecessary degradations can be induced with time in an ambient environment, requiring the passivation process. The PMMA and the carbon polymers deposited by CF₄ plasma treatments were used for the passivation of the SnO₂ nanowire FET devices. To investigate the effect of the passivation, the unpassivated and the passivated devices have been compared. The changes of the mobility and the carrier concentration were separately analyzed, indicating the different behaviors with or without the passivation.

NS-ThP7 Application of Rolling Circle Amplification and Thermal Dynamic Principle for Manipulating the Interparticle Spacing of Gold Nanoparticle Chains. *Y.P. Lu, M.Y. Lin, Y.-C. Ou*, National Applied Research Laboratories, Taiwan, Republic of China

Biomolecular nanotechnology draws a lot of attention in organizing DNA sequence, which can architecturally build up a nano-sized scaffold, because of their potential utility in nano-machines and biosensing. According to the DNA complementary base-pairing interactions and aptamer design, DNA backbone has further been used for the construction of a variety of geometric objects and anchoring sites for functionalized proteins or metals. A simple and applicable procedure to miniature nanostructures is expected to enhance the detection sensitivity of devices. It is important to construct the metallic nanoparticle chain with different interparticle spacing because the organized metallic nanoparticles self-assembled from DNA nanostructure may affect the photoelectric properties. We successfully generate well-controlled formation of long, flexible, one dimensional gold nanoparticle (AuNP) chains by employed DNA template for self-assembly AuNP based on rolling circle amplification (RCA) technique. For the purpose of controlling the interparticle spacing of AuNP, we report the construction of long chain DNA-AuNP with or without secondary structure of DNA scaffold by using of base-pairing strategy and thermal dynamic reaction. The heating process under appropriate temperature broke the intramolecular Watson-Crick interactions to form the hairpin structure. This ultimately allowed no AuNP modified primers to hybridize with the open region of single strand DNA backbone, hence increased the interparticle spacing between each AuNP. The effect of AuNP distance in optical and electronic properties can be designed by controlling the DNA sequence and thermal dynamic reaction, and thus changed the optical and electronically characters of AuNP-based nanostructures for many applications in optoelectronics and biosensing devices fabrication.

NS-ThP8 Synthesis of Gold Nanofluids for Improved Heat Transfer using Solution Plasma. *Y.K. Heo, M.A. Bratescu, N. Saito*, Nagoya University, Japan

In recent years, the development of high speed devices and their integrated circuits has facing some obstacles owing to localized heat generation in terms of safety and efficiency of devices. Nanofluids which were defined fluids containing nanometer-size particles, have been researched for their high and efficient heat transfer. It was reported that heat transfer enhancement was due to the Brownian motion of the nanoparticles contained in the fluids. Therefore, the diameter of nanoparticles in nanofluids is a key-factor in order to develop new heat transfer systems with higher energy-efficiency.

Recently our research group has developed a new synthesis method for well-defined nanoparticles in an aqueous solution, by solution plasma process (SPP). This process allows us to fabricate solutions containing high quantity of small monodispersed nanoparticles in order to obtain a heat transfer system with improved efficiency.

In this research, we aimed to reveal the heat transfer of nanofluids. The solution containing monodispersed gold nanoparticles was synthesized by SPP using a DC bipolar pulsed power supply. Gold nanofluids were synthesized with various concentrations of 0.1, 0.3, 0.6, 0.9 mM HAuCl₄ and 4 times KOH of each HAuCl₄ concentration in distilled water. The reaction time is 15 minutes. The solution plasma optical and electrical conditions were measured by OES and oscilloscope. The evaluation of the synthesized nanoparticles was performed by TEM analysis and UV vis spectroscopy. The dispersion stability was evaluated using zeta potential. In addition, KD2 pro & viscometer were used for heat transfer analysis of the synthesized nanofluids.

The decrease of the nanoparticles diameter from 13.8 ± 4.3 nm to 5.6 ± 1.4 nm was measured in dependence with the precursor concentration. The viscosity of the nanofluid increased with precursor concentration from 1.95

mPa·s to 2.05 mPa·s at 283 K (Viscosity of Di Water is 1.51 mPa·s.). A precursor concentration of 0.9 mM produced the smallest nanoparticles diameter of 5.6 ± 1.4 nm, and the highest increase of the thermal conductivity of 29.4 %.

NS-ThP9 Post Ion-Implant Growth of Epitaxial Graphene on 6H-SiC. *J. Seo, H. Shin, J.-H. Park, J.R. Ahn*, Sungkyunkwan University, Republic of Korea

Graphene, a two-dimensional sheet of sp²-bonded carbon arranged in a honeycomb lattice has attracted significant attention due to its interesting characteristics such as high carrier mobility, optical transparency, mechanical strength, and possible applications in various fields. Among the techniques developed for producing graphene, epitaxial growth on silicon carbide (SiC) is a promising method for large-scale production. Ion implantation is also a mature technology in large-scale electronic industry, which can take the epitaxial graphene into the semiconductor foundries.

Here we studied post ion-implant growth of epitaxial graphene on 6H-SiC substrates according to ion fluences, acceleration voltages, and substrate temperatures. N⁺ ions at 40-145keV were implanted with fluences of 1×10^{17} N⁺/cm² and 3×10^{17} N⁺/cm² into 6H-SiC substrates under room temperature (RT) and 650°C. The ion distributions and structural variations in the implanted samples have been studied using secondary ion mass spectrometry (SIMS) and transmission electron microscopy (TEM) both before and after the graphene growth. This study revealed that the implanted N⁺ ion distributions in 6H-SiC are robust up to ~1330°C at which the epitaxial graphene begins to grow on Si-face of 6H-SiC and the graphene is formed only when the substrates are maintained at 650°C during ion implantation. This is believed to be due to the prominent damage recovery of 6H-SiC in high temperature implantations. The high crystallinity of the epitaxial graphene grown on the damage-recovered 6H-SiC was confirmed by photoelectron spectroscopy and low-energy electron diffraction.

NS-ThP11 Preparation of Metal Nanoparticles within Mesoporous Silica via Solution Plasma Process (SPP). *W. Yaowarat, N. Saito*, Nagoya University, Japan

Recently, nanoparticles within mesoporous silica have been extensively studied due to their significant physicochemical characteristic. It is widely used in various applications such as instant microbial inhibition, sensor, catalyst, and electronic devices. As previously reported that nanoparticles within mesoporous silica could be synthesized by chemical treatment and calcination. However, high temperature and long time treatment must be required.

Solution plasma process (SPP) is a new plasma system which could be used to synthesis metal nanoparticles. SPP is superior to other conventional methods, in term of ease of handling, low temperature, and short time treatment. It is therefore of our interest to apply the solution plasma process to prepare metal nanoparticles within mesoporous silica. The voltage, frequency and pulse width of solution plasma conditions were fixed at 1.6 kV, 15 KHz, and 2 μs, respectively. 1 mM of AgNO₃ solution with 0.2 g mesoporous silica was treated with solution plasma for 15 minutes. The plasma-treated sample was filtrated prior to air dry for overnight. The dried sample was characterized by transmission electron microscopy (TEM). The TEM results showed that the silver nanoparticles could be performed during solution plasma treatment and filled within nanoscale channels of mesoporous silica matrix. This suggested that the solution plasma process could be a potential method for prepare metal nanoparticles within mesoporous silica.

NS-ThP12 The Electrical Property of the Interface Between Dielectrophoresis (DEP)-Aligned Single-Walled Carbon Nanotubes and Semiconductors. *M. Hines, Z. Xiao*, Alabama A&M University

The dielectrophoresis (DEP) method was used to align and deposit single-walled carbon nanotubes for the fabrication of high-performance single-walled carbon nanotube field-effect transistors (CNTFETs). Semiconducting materials such as silicon and germanium were used as the source/drain contact material in the fabrication of CNTFETs for improving the device electrical performance. The DEP-aligned carbon nanotubes were mesh networks interconnecting with metallic nanotubes and semiconducting nanotubes. The vacuum-based deposition such as e-beam evaporation and sputtering deposition was used to grow the silicon and germanium thin films, and clean room-based microfabrication techniques such as UV lithography was used to fabricate the CNTFETs. The electrical property of fabricated CNTFETs were measured and characterized. The semiconductors can significantly increase the ratio of the switch-on/off electrical currents in the fabricated CNTFETs. The electrical property of the interface between the single-walled carbon nanotubes and the semiconductors and the fabricated CNTFETs will be reported in the conference.

NS-ThP14 Field Emission Based Hydrogen Sensing Characteristics from Carbon Nanotubes Synthesized on Catalytical Substrates, C. Dong, Wenzhou University, Republic of China

A new hydrogen sensing concept is demonstrated based on the field emission from multi-walled carbon nanotubes. The low emission currents rise in proportional to hydrogen partial pressures above from 10^{-9} to 10^{-5} Torr. Catalytic Ni participated C-H reactions in low emission regime are considered the key factor of the sensing behavior. Simple setup, tiny structure, high sensitivity, and fast recovery make this innovative technique attractive to build miniature low cost hydrogen sensors for low pressure applications.

Friday Morning, November 2, 2012

Electronic Materials and Processing

Room: 14 - Session EM+NS-FrM

Low-Resistance Contacts to Nanoelectronics

Moderator: S. Zollner, New Mexico State University

8:20am EM+NS-FrM1 **Electrical Transport on Chemically Modified Silicon-on-Insulator Substrates**, G.P. Lopinski, National Research Council of Canada **INVITED**

Electrical transport of semiconductor surfaces and nanostructures are strongly influenced by interfacial processes. Adsorption and reaction events which result in charge re-distribution can modulate conductivity through long-range electric field effects. These effects are being exploited to tailor electronic properties of nanomaterials and devices as well as in the development of electrically-based chemical and biological sensors. Silicon-on-insulator(SOI) substrates, in which the top layer is thinner than the depletion length, are particularly well-suited for demonstrating and investigating the effects of surface processes on electrical transport. Measurements on hydrogen terminated H-SOI substrates (with both (100) and (111) orientations) have demonstrated that adsorption of certain polar molecules (water, pyridine and ammonia) results in large reversible increases in conductivity, attributed to charge transfer effects which induce accumulation of majority carriers on n-type and minority carrier channels (inversion) on p doped substrates. Adsorption of the prototypical electron acceptor tetracyanoethylene (TCNE) results in a strong decrease in conductivity on n-type substrates due to depletion of majority carriers. This effect is not fully reversible due to reactions of TCNE with the H-terminated surface. Use of SOI substrates also facilitates formation of point contact pseudo-MOSFETs, allowing transistor characteristics to be obtained without the need for device fabrication. This approach has been shown to be a simple and straightforward way to monitor the effect of adsorption and reaction events on the electronic properties of the silicon substrate. Pseudo-MOSFET measurements have been used to monitor surface reactions such as ambient oxidation of the H-terminated surface. Gas phase photochemical reaction of alkenes has been used to chemically passivate these surfaces while maintaining a low density of electrically active defects ($<1 \times 10^{11} \text{ cm}^{-2}$). These alkyl monolayer passivated SOI surfaces show a large reversible response to TCNE, suggesting they can function as good ultrathin gate dielectrics for sensing applications.

9:00am EM+NS-FrM3 **Evidence for Single Electron Tunnel Junction using Gold Nanoparticles on Oxide-Free Si(111)**, L. Caillard, O. Seitz, P. Campbell, University of Texas at Dallas, O. Pluchery, Université Pierre et Marie Curie, France, Y.J. Chabal, University of Texas at Dallas

It has been suggested that the phenomenon of Coulomb blockade could be achieved by placing a metallic nanoparticle between two tunnel junctions. While the Coulomb blockade has been well established theoretically and demonstrated on metal substrates¹, it is more challenging to observe on semiconductor surfaces due in part to the defective nature of the interfaces and to the depletion layer. We present an experimental study of two ultra small-capacitance normal tunnel junctions connected in series between the Si substrate and a STM tip. To achieve such a structure, we use an amine-terminated self-assembled monolayer (SAM) grafted on silicon (111) as the insulator layer, acting as a linker to attach gold nanoparticles on the surface. The SAM layer is grafted directly on oxide-free silicon through a Si-C bond formation using hydrosilylation reactions and is characterized by a low interface state density². Moreover, this SAM layer provides a long-term passivation (weeks) of the interface that prevents oxidation of the substrate during Au nanoparticle deposition. The SAM quality is characterized using an extensive range of techniques, including in-situ IR spectroscopy, spectroscopic ellipsometry, X-ray photoelectron spectroscopy (XPS) and Atomic force microscopy (AFM). The second capacitance is formed by the gap between the gold nanoparticle and the tip of the Scanning tunneling microscope/spectroscopy (STM/S). The current-voltage measurements have been performed in ultra high vacuum. Several parameters have been investigated: silicon doping level, sample temperature, and size of the gold nanoparticles (AuNPs), ranging from 1 to 15 nm. The junction is achieved by either grafting synthesized AuNPs or depositing evaporated gold directly on the SAM. Preliminary data confirm that coulomb staircases are observed under different conditions, mostly clearly for highly doped substrates at low temperature (10K). The steps width and height of these Coulomb staircases depend on particle size. These results are an important step toward future control for single electron transistor and flash memory applications.

[1] Zhang, H.; Yasutake, Y.; Shichibu, Y.; Teranishi, T.; Majima, Y., Tunneling resistance of double-barrier tunneling structures with an alkanethiol-protected Au nanoparticle. *Phys. Rev. B*, 72, (20) (2005)

[2] D. Aureau, Y. Varin, K. Roodenko, O. Seitz, O. Pluchery and Y. J. Chabal, Controlled Deposition of Gold Nanoparticles on Well-Defined Organic Monolayer Grafted on Silicon Surfaces. *Phys. Chem. C*, 114 (33), pp 14180–14186 (2010)

9:20am EM+NS-FrM4 **A Distribution of Variable Size Sn-islands on 0.8 nm Oxide/ Si (111): Local MOS Properties and Tunneling Studied with Synchrotron Radiation**, A. Silva, Universidade Nova de Lisboa, Portugal, K. Pedersen, Aalborg University, Denmark, Z.S. Li, Aarhus University, Denmark, P. Morgen, University of Southern Denmark

The thinnest possible uniform and stable oxide layer grown thermally on Si (111) is 0.8 nm thick. This oxide is grown at around 500°C, in a self-limiting process, which has earlier been fully characterized with surface sensitive, high-resolution core level photoemission at the ASTRID storage ring facility at Aarhus, Denmark. Such oxides are too thin for use in current generations of CMOS-devices, yet they have potential applications in devices, where controlled tunneling could be of importance, or as diffusion barriers. To study the tunneling properties of this oxide covering the Si (111) surface isolated nanometer-sized Sn islands in different diameters and concentrations were deposited at 500°C and became negatively charged, with different charges depending on their size. The deposition was done from a Knudsen source in a way programmed to produce a systematic variation of the Sn coverage across about 2 cm of the surface. This is done to allow locally resolved photoemission characterization of the system, at a resolution (with a photon beam width) of around 150 micron. The resulting shifts of Si 2p and Sn 4d core levels at, and across the surface, with varying amounts of Sn, and charge on the Sn islands, are used to determine the local changes in band bending and fields in the oxide. This method thus offers a unique possibility to evaluate MOS properties of nano-systems in-situ without direct electrical contacts.

9:40am EM+NS-FrM5 **Signatures of Interface Band Structure and Parallel Momentum Conservation of Hot Electrons across Metal-Semiconductor Schottky Diodes**, J. Garramone, Northwestern University, J. Abel, R. Balsano, University at Albany-SUNY, S. Barraza-Lopez, University of Arkansas at Fayetteville, V.P. LaBella, University at Albany-SUNY

Understanding hot electron transport and scattering through materials and interfaces is important for conventional integrated circuit technologies and futuristic applications such as hot carrier photovoltaics and hydrogen sensing. In this presentation, the hot electron attenuation length of Ag is measured utilizing ballistic electron emission microscopy (BEEM) on nanoscale Schottky diodes for Si(001) and Si(111) substrates. Marked differences in the attenuation length are observed at biases near the Schottky barrier depending upon the substrate orientation, increasing by an order of magnitude only for Si(001), while remaining unchanged for Si(111). These results provide clear evidence that the crystallographic orientation of the semiconductor substrate and parallel momentum conservation affect the hot electron transport across these interfaces. A theoretical model reproduces the effect that combines a free-electron description within the metal with an ab-initio description of the electronic structure of the semiconductor.

10:00am EM+NS-FrM6 **Metal-Fullerene Interfaces: A Dynamic System**, P. Reinke, J.B. McClimon, H. Sahalov, University of Virginia

Fullerenes and other small organic molecules are used in organic solar cells, organic LEDs and molecular electronics system, and the interface between the organic layer and the metal electrode is critical to achieve the desired functionality. The majority of studies focusses on the interaction of molecules with metal surface, and the interaction of metals with organic surfaces has garnered much less attention. However, the addition of metal to an organic layer surface has been one of the bottlenecks in the fabrication of molecular electronics devices. We therefore present here a comprehensive study of the metal interaction with fullerene surfaces. Our past research has investigated the deposition of Au and Si on fullerene surfaces, and our presentation here focuses on the interface to transition metals Vanadium and Tungsten. All of these systems show a dynamic behavior: the metal atoms are highly mobile and thus perturb the C₆₀ matrix substantially.

The fullerene and metal atoms/films are deposited by electron beam and thermal evaporation, and the interface formation is observed with STM under UHV conditions in a sequential manner. V immediately diffuses into the fullerene matrix, and surface clusters are sparse. The STM images reflect the change in the local electronic structure of the molecules through

the interaction with sub-surface V: the apparent height of molecules in contact with V is reduced, and their rotation ceases and the molecular orbitals can be identified by the characteristic C_{60} substructure within the molecule.

We suggest that the subsurface V forms complexes with C_{60} where charge donation to the fullerene cage occurs, and preferential bonding to the hexagonal face determines the molecule orientation. The increase of V concentration leads to agglomeration of V-clusters and consequently the extension of regions with a smaller apparent height in the filled state images. The charge exchange between metal clusters and fullerene matrix allows to observe the V-cluster growth within the matrix. The empty state images are essentially flat, and show small variations in topography and cracks in the fullerene layer for large V-concentrations (~0.6 to 1 ML). We will present a comprehensive model for the diffusion of V through the matrix, the complex formation and cluster growth. The behavior of W is distinguished by a larger percentage of surface clusters, and the dynamics of cluster formation within the matrix will be compared to V. However, both transition metals do not destroy the C_{60} matrix, but only react to form carbides at elevated temperatures.

10:20am **EM+NS-FrM7 Scaling Silicide Contacts in Microelectronics: At What Size will Material Characteristics affect Device Properties ?**, **C. Lavoie**, IBM T.J. Watson Research Center **INVITED**

With the continued scaling of CMOS technology, the typical contact area to the source and drain of a CMOS device can now reach below 1000 nm^2 . At these nano-dimensions, typical intrinsic contact resistivities of $1 \times 10^{-8} \Omega\text{-cm}^2$, easily lead to resistances exceeding the $K\Omega$ solely for crossing the interface silicide-silicon. Such resistances are unacceptable as they dominate the overall resistance of a device. In an attempt to mitigate this increase in interfacial resistance with contact area reduction, much research has been performed concentrating on the tailoring of material properties of both the silicide and the semiconductor substrate as well as on the optimization of contact geometries and the advanced engineering of interfaces. As the size of the contact reaches dimensions that are similar or smaller than the typical microstructure of the expected poly crystalline material, some dramatic effects are to be anticipated. First, the presence of a single grain during the silicidation eliminates the typical dominant diffusion path: grain boundaries. As a result, phase nucleation and kinetics of growth can only proceed through the silicide bulk or the available interfaces. This will likely retard formation of the desired phases in the narrowest dimensions. Another expected disadvantage of very small contacts resides in the variability of the intrinsic contact resistance discussed above. It is accepted that the Schottky barrier height of a given silicide to a silicon substrate varies with substrate orientation. As a result, variation of crystal orientation from contact to contact may lead to dramatic effects on contact resistance. This orientation variation can originate from either a variation in silicide texture from contact to contact or a variation in device geometry (i.e. silicidation on Si(100), Si(110) or Si nanowire device depending on geometry). In this presentation, we will first explain how the importance of contact resistivity has caused a shift in contact engineering from yield and defect control towards the optimization of device performance. We will then describe some of the challenges involved in building arrays of nanostructures and characterizing them.

11:00am **EM+NS-FrM9 Compositional Dependence of the Dielectric Function and Optical Conductivity of NiPt Alloy Thin Films**, **L.S. Abdallah**, **T. Tawalbeh**, **I.V. Vasiliev**, **S. Zollner**, New Mexico State University, **C. Lavoie**, IBM T.J. Watson Research Center, **A. Ozcan**, IBM Systems and Technology Group, **M. Raymond**, GLOBALFOUNDRIES

Optical properties of metals are less well known than those of insulators and semiconductors, because it is hard to achieve similar purity and crystallinity in metals. Many metals are reactive and easily form oxides, or they exhibit significant surface roughness. We report the dielectric function and optical conductivity of Ni-Pt alloys as a function of composition (10 to 25 atomic % Pt) from 0.8 to 6.5 eV. Our films are 10 nm thick and were prepared by physical vapor deposition (co-sputtering from pure Ni and Pt targets). To avoid reaction between Si and the metal alloy, films were deposited on thick thermal oxides (220 nm). Some films were annealed at 500°C for 30 s. Similar Ni-Pt alloys are used as Ohmic contacts in CMOS device processing, to achieve highly stable low-resistance contacts between copper back-end metallization and front-end silicon transistors. Our results will enable in-line process control of Ni-Pt alloy deposition using spectroscopic ellipsometry.

Since our metal thickness is below the penetration depth, the interference from the thick SiO_2 layers creates artifacts when extracting the optical conductivity. We minimize this issue by acquiring the ellipsometric angles over a broad range of incidence angles (20° to 80°), which varies the optical path length and thus shifts the interference problems to different energies. Our resulting dielectric functions are similar to those tabulated by Palik for pure Ni. The data are dominated by a Drude divergence due to free carriers

at low photon energies. We can remove this divergence by multiplying with the photon energy. We find several trends: (1) The optical conductivity of the annealed films is always greater than that of the as-deposited films, due to improvements in crystallinity and reduced grain boundary scattering after annealing. (2) All four alloys show conductivity peaks near 1.5 and 4 eV due to transitions from the d-like valence bands to the s-like conduction bands. (3) These peaks are significantly broader and weaker than those in pure Ni, but at the same energy. The broadenings increase with increasing Pt content. However, the amplitude of the 4 eV conductivity peak remains constant near $3500/\Omega\text{cm}$, independent of Pt content.

From electronic structure calculations for pure Ni and Pt and a Ni_3Pt ordered compound, we find that Ni, Pt, and Ni-Pt d-bands have similar energy, which explains why the 4 eV peak in the conductivity does not shift with Pt addition. Furthermore, the bandwidth of the Ni 3d bands is smaller than that of the Pt 5d bands, consistent with the increase in the broadening of the optical transitions.

This work was supported by NSF (DMR-11104934).

11:20am **EM+NS-FrM10 Ultra-Shallow Junction Formation for sub-22nm CMOS Technology and Characterization using High-resolution SIMS**, **M.J.P. Hopstaken**, **H. Wildman**, **D. Pfeiffer**, IBM T.J. Watson Research Center, **Z. Zhu**, **P. Ronsheim**, IBM Systems and Technology Group, **K.K. Chan**, **I. Lauer**, **J.S. Newbury**, **D.-G. Park**, IBM T.J. Watson Research Center

Secondary Ion Mass Spectrometry (SIMS) has shown great resilience over the last decades in keeping up with the aggressive downscaling of advanced CMOS technology. Major improvements contributing to the staying power of SIMS are lower primary ion beam energies to meet the ever more stringent depth resolution demands [1] and application of novel external standard-free calibration methods for quantification in the near-surface region [2]. Here we demonstrate state-of-the-art applications of SIMS to Ultra-Shallow Junction (USJ) formation and in-situ doped thin epitaxial layers.

We present As-USJ extension formation for nFET with junction depths below 120 \AA , obtained using low energy ion implantation and micro-second flash (μ -flash) annealing. SIMS depth profiling employing a 200 eV Cs^+ beam provides detailed information on diffusion and segregation of As at the sub-nm scale for different annealing conditions. Low energy implantation of P has been proposed as an alternative to As for the formation of Source/Drain (S/D) regions to reduce crystalline damage. This is crucially important for advanced CMOS technology based on Extremely Thin SOI or FinFET. Here, we present different analytical approaches to determine the most accurate quantification for shallow P concentration profiles in Si. Also, we have employed 3D atom probe tomography to independently determine in-depth [P] profiles for SIMS calibration purposes [3].

For pFET processes, nm-scale control of B-diffusion is instrumental to obtain highly activated and abrupt B-USJ. Here we present a novel doping strategy employing ultra-thin solid source Si:B diffusion sources—in combination with μ -flash annealing—to form the B-USJ extensions. Presence of high [B] and minimal diffusion length necessitates use of ultra low O_2^+ impact energy for accurate determination of junction depth and abruptness. Regarding S/D formation, In-Situ Boron Doped (ISBD) SiGe is an important technology element for pFET strain enhancement. Quantitative analysis of [B] in SiGe using reactive low energy O_2^+ ion sputtering is complicated due to large yield variations as a function of [Ge] [4]. We present a calibration protocol based on multiple B-implanted epitaxial $\text{Si}_{1-x}\text{Ge}_x$ standards on Si(100) with constant [Ge] ranging from 20 to 50 at.%. This approach allows for explicit correction of both SiGe sputter yield and B^+ and Ge^+ yield variations as function of [Ge], enabling quantitative analysis of ISBD SiGe.

[1] A. Merkulov et al., *JVST B* **28**(1) (2010) C1C48.

[2] W. Vandervorst et al., *AIP Conf. Proc.* **931**(1) (2007) 233-245.

[3] M.J.P. Hopstaken et al., *SIA*, DOI 10.1002/sia.4916 (2012).

[4] Z. Zhu et al., *SIA* **43**(1-2) (2011) 657-660.

11:40am **EM+NS-FrM11 A Deep Dive into the Liquid Fermi Sea**, **R.K. Schulze**, **J.C. Lashley**, **B. Mihaila**, **D.C. Wallace**, Los Alamos National Laboratory

We reexamine high resolution photoemission in some of the liquid metals accessible in a UHV environment. These include Ga, In, and Bi, and at a basic level, involves comparison of the DOS EDCs between the crystalline solid and liquid metal. The motivation is to gain an understanding of the fundamental differences between normal and anomalous melters. This includes a search for an understanding of the electronic contribution to the melt phase transformation. Normal melters, such as In, show a difference in liquid and crystal solid entropy at constant volume, $\Delta S^* = 0.8 \pm 0.1 k_B/\text{atom}$, and exhibit a volume expansion upon melting, while anomalous melters,

such as Ga and Bi, have $\Delta S^* \gg 0.8$ k_B/atom, and show a volume collapse upon melting. Observed changes to the electronic structure near the Fermi energy upon crossing the solid-liquid phase boundary will be discussed.

Graphene and Related Materials Focus Topic

Room: 13 - Session GR+EM+ET+MS+NS-FrM

Graphene Device Physics and Applications

Moderator: A. Turchanin, University of Bielefeld, Germany

8:20am **GR+EM+ET+MS+NS-FrM1 Heterointegration of Graphene with Nano and Molecular Scale Structures for High Performance Devices, X. Duan**, University of California, Los Angeles **INVITED**

Nanoscale integration of dissimilar materials with distinct compositions, structures and properties has the potential to create a new generation of integrated systems with unique functions and/or unprecedented performance to break the boundaries of traditional technologies. In this talk, I will focus my discussion on the heterointegration of graphene with a variety of nano and molecular scale structures of designed architectures to open up exciting opportunities for nanoscale device engineering. In particular, I will discuss our recent effort in integrating graphene with a self-aligned nanowire gate to create the highest speed graphene transistors, integrating graphene with plasmonic nanostructures to create multi-color high speed photodetectors, integrating graphene with nanoscale templates for the creation of graphene nanostructures, and integrating graphene with various π -conjugating molecular systems for band gap engineering and molecular sensing.

9:00am **GR+EM+ET+MS+NS-FrM3 Graphene RF: From Fundamentals to Opportunities, J.S. Moon, H.-C. Seo, M. Antcliffe, S. Lin, A. Schmitz, D. Le, C. McGuire, D. Zehnder**, HRL Laboratories LLC, L.O. Nyakiti, V.D. Wheeler, R.L. Myers-Ward, C.R. Eddy, Jr., D.K. Gaskill, P.M. Campbell, Naval Research Laboratory, K.-M. Lee, P. Asbeck, UC San Diego **INVITED**

Graphene is a topic of very active research from basic science to potential applications. Various RF circuit applications are under evaluation, which include low-noise amplifiers, frequency multipliers, mixers and high-speed radiometers. Potential integration of graphene on Silicon substrates with CMOS compatibility would also benefit future RF systems. The future success of the RF circuit applications depends on vertical and lateral scaling of graphene MOSFETs to minimize parasitics and improve gate modulation efficiency in the channel. In this presentation, we highlight recent progress in graphene materials and devices. For example, with hydrogen intercalation, a graphene wafer showed an electron mobility of 2500 cm²/Vs at 6.8×10^{12} cm⁻² carrier density, and sheet resistance of 230 ohm/square. The Ti-based ohmic contact resistance is below 100 ohm* μ m and hysteresis in HfO₂/Graphene MOSFET transfer curves are no longer concerns in RF applications. We will show graphene MOSFETs in mixer and detector applications with performances comparable to and better than the current state-of-the-art technologies. Also, we will present recent progress in graphene heterostructure based diodes with on/off ratio greater than 10⁶. In summary, while graphene is relatively new material, it shows a strong potential to become disruptive in RF applications.

This work was partially supported by DARPA, monitored by Dr. J. Albrecht, under SPAWAR contract number N66001-08-C-2048.

The views, opinions, and/or findings contained in this article/presentation are those of the author/presenter and should not be interpreted as representing the official views or policies, either expressed or implied, of the Defense Advanced Research Projects Agency or the Department of Defense.

[1] J. S. Moon and D. K. Gaskill, IEEE Trans. Microwave Theory and Techniques, p. 2702, 2011

9:40am **GR+EM+ET+MS+NS-FrM5 Graphene and Dielectric Integration: A Sticky Situation?, V.D. Wheeler, N.Y. Garces, L.O. Nyakiti, R.L. Myers-Ward, D.J. Meyer**, U.S. Naval Research Laboratory, A. Nath, George Mason University, C.R. Eddy, Jr., D.K. Gaskill, U.S. Naval Research Laboratory **INVITED**

Scalable high- κ dielectric integration is needed to realize graphene-based THz transistors. Yet, the inert nature of graphene inhibits direct application of high-quality uniform atomic layer deposition (ALD) dielectrics. While several methods have rendered the surface more susceptible to ALD[1], they often degrade mobility and/or shift the Dirac voltage due to charges within the gate stack. Recently, we developed a dry chemical functionalization approach using XeF₂ that results in conformal, thin high- κ ALD oxide films with a 10-25% improvement in graphene mobility[2], high

dielectric constants (HfO₂=18.5, Al₂O₃=8.9), and small Dirac voltage shifts (HfO₂=2V, Al₂O₃=0.1V), indicating the effectiveness of F functionalization. We will present in-depth details of our fluorination process, discuss its advantages and limitations with respect to other methods used to enhance ALD reactivity with graphene, and provide future directions for this field of study.

Fluorination of EG surfaces was performed in a Xactix X3 XeF₂ etcher operating in pulse mode. Results show that 15 nm pinhole-free Al₂O₃ and HfO₂ films are obtained with an optimized XeF₂ surface treatment prior to ALD consisting of six, 20s pulses (XeF₂=1 torr, N₂=35 torr). This optimal treatment resulted in ~6% fluorine surface coverage, as semi-ionic C-F bonds (Fls ~687eV) only, which provided additional ALD reaction sites needed to obtain uniform oxide films. This unique semi-ionic nature of the C-F bond allows the graphene lattice to maintain planarity and minimize degradation to transport properties.

Theoretical studies suggest that the semi-ionic nature of the C-F bond is related to the graphene electron sheet carrier density (n_e), requiring at least 10^{13} cm⁻² to form[3]. To test this, EG samples with similar thickness but varying n_e (2×10^{12} - 1.3×10^{13} cm⁻²) were fluorinated simultaneously using the optimal conditions above. Samples with $n_e > 1 \times 10^{13}$ cm⁻² had only semi-ionic C-F bonding, but those with $n_e < 1 \times 10^{13}$ cm⁻² had both covalent and semi-ionic bonding – verifying the theoretical calculations. The amount of covalent bonding increased as n_e decreased, and an increased pinhole density was seen in subsequent Al₂O₃ films. This implies that the underlying EG properties can impact the effectiveness of this fluorination method. Yet, by adjusting the pulse conditions one can tailor this method to still obtain uniform ALD oxides on low carrier density and even p-type EG. To this end, results of our XeF₂ approach on p-type H₂ intercalated EG samples will be shown.

1. Garces, et.al. *J/ST B* **30(3)** 03D104 (2012)

2. Wheeler, et.al. *Carbon* **50** 2307 (2012)

3. Sofo, et.al. *Phys Rev B* **83(8)** 081411(R) (2011)

10:20am **GR+EM+ET+MS+NS-FrM7 Achieving Scaled Dielectrics on Graphene Using Atomic Layer Deposition, S. Jandhyala, G. Mordi, R.M. Wallace, J. Kim**, University of Texas at Dallas

In order to realize high-performance graphene-based field-effect-devices, local gating of graphene channel is one of the foremost requirements [1]. Therefore, deposition of high-quality, scalable dielectrics on graphene is required. The ability to precisely control thickness and conformally deposit materials makes atomic layer deposition (ALD) an ideal technique for achieving such dielectrics [2]. However, ALD is a surface-reaction limited process [2] and graphene, being sp² bonded, has no *out-of-plane* covalent functional groups [3] and this can cause difficulties in initiating the ALD reaction [4]. In previous studies we have shown that using a reversibly physisorbed ozone (O₃) functionalization approach, we can deposit high quality ALD oxides (such as Al₂O₃) on graphene with thicknesses below 5 nm [5]. Further understanding regarding the interaction of O₃ and metal precursors with graphene is required for successfully applying the ozone process to deposit different oxides.

In this study, we will use *in-situ* electrical measurements of graphene devices inside an ALD chamber as a characterization technique in order to understand the adhesion mechanisms of oxidants (such as O₃ and H₂O) and metal precursors (such as trimethylaluminum-TMA, titanium tetrachloride-TiCl₄) on graphene surfaces. The characterization scheme used is packaged back-gated graphene-FETs which can detect the molecules adsorbed on the graphene surface. We will compare exfoliated graphene and chemical vapor deposited (CVD) graphene (which tends to have a higher number of defect sites). Using such *real-time* electrical measurements, the observed charge scattering mechanisms and the effect on mobility and doping due to the interaction of these molecules with graphene will be presented.

Acknowledgement

This work was funded through the South West Academy of Nanoelectronics (SWAN) program of NRI under SRC.

References

- [1] S. K. Banerjee, et al., Pro. of the IEEE **98** (12), pp. 2032-2046 (2010).
- [2] R. L. Puurunen, J. Appl. Phys. **97** (12), pp. 121301-121352, (2005)
- [3] A. H. Castro Neto, et al., Rev. Mod. Phys. **81** (1), pp. 109-162 (2009)
- [4] L. Liao, X. Duan, Mat. Sci. Eng. R **70** (3-6), pp. 354-370, (2010)
- [5] S. Jandhyala, et al., ACS Nano, **6** (3), pp. 2722-2730 (2012)

10:40am **GR+EM+ET+MS+NS-FrM8 Atomically-Smooth MgO Films Grown on Epitaxial Graphene by Pulsed Laser Deposition.** *S.C. Stuart, A.A. Sandin*, North Carolina State University, *O. Nayfeh, M.D. Dubey*, Army Research Laboratory, *J.E. Rowe, D.B. Dougherty*, North Carolina State University, *M.D. Ulrich*, Army Research Office

The growth of high quality insulating films on graphene is a crucial materials science task for the development of graphene-based spintronics because graphene is a potentially revolutionary material for electronic and spintronic applications. For efficient spin-injection, graphene is expected to suffer from the well known “conductivity mismatch” problem at metal-semiconductor spin electrode interfaces. The standard approach to mitigating this problem has been to grow thin, insulating tunnel barriers between the graphene and the magnetic metallic electrode to provide a spin-dependent resistance via the tunneling magnetoresistance effect. It has been demonstrated by several experiments that direct spin injection from a magnetic electrode to graphene is possible but using aluminum oxide or MgO tunnel barriers to assist injection in graphene spin-valve devices is more efficient if suitable oxide-graphene interfaces can be formed. To address this problem we have used pulsed laser deposition (PLD) to grow thin (1-1000 nm) magnesium oxide films directly on epitaxial graphene on SiC(0001). We observe very smooth film morphologies (typical rms roughness of ~0.4 nm) that are nearly independent of film thickness and conform to the substrate surface which had ~0.2 nm rms roughness. Surface roughness is less than 0.5 nm for thicknesses up to 1000 nm and is independent of deposition laser pulse energy within the range 300-700 mJ/pulse at rates of 1-50 Hz. X-ray diffraction shows predominant (111) and (100) orientations, indicating the possibility of doping the graphene by the polar (111) interface. Raman spectroscopy indicates that the graphene is not measurably damaged by magnesium oxide growth. This work shows that PLD is a good technique to produce graphene-oxide interfaces without pre-deposition of an adhesion layer. The films are free of defects or pinholes (that can be observed by atomic force microscopy) and can be grown at arbitrary thicknesses without increasing the roughness or damaging the graphene. The details and kinetics of the deposition process will be described with comparisons being made to other dielectric-on-graphene deposition approaches.

11:00am **GR+EM+ET+MS+NS-FrM9 Facile, Controllable Graphene-based P-N Junctions Using Self-Assembled Monolayers.** *J. Baltazar, H. Sojoudi, J. Kowalik, L. Tolbert, S. Graham, C.L. Henderson*, Georgia Institute of Technology

In this study we investigate the use of a self-assembled monolayer (SAM) to create a p-n junction in graphene films. Previous techniques rely on charge transfer from adsorbants or electrostatic gate/potentials. Here we demonstrate that, by successfully modifying the SiO₂ surface with an aminopropyltriethoxysilane (APTES) layer, and using intrinsically p-doped transferred CVD graphene films, a well-defined junction can be achieved. Field-effect transistors and p-n junction regions are fabricated prior to graphene film transfer, in order to preserve the pristine properties of the graphene. The I-V characteristic curve indicates the presence of two thermally-controllable neutrality points. This method allows a facile, controllable and low temperature fabrication of graphene p-n junctions.

11:20am **GR+EM+ET+MS+NS-FrM10 Impact of Cleaning Procedures on the Performance of Graphene-Based Field Effect Transistors.** *M. Lodge, M. Ishigami*, University of Central Florida

It is now widely accepted that surface contaminants have large effects on the performance of graphene-based field effect transistors. Various techniques are now available to clean processing residues from graphene, yet some of these techniques are chemically aggressive leaving concerns that they may damage graphene and affect the device performance. In addition, there are no consensus on the best method to produce the cleanest and, therefore, the best graphene devices.

Here, we have performed a study on the impact of various chemical treatments on the performance of field effect transistors fabricated from graphene grown using chemical vapor deposition. By measuring the impact of hydrogen-annealing, oxygen-annealing, and various solvent-based cleaning on 50 graphene field effect transistors, we generate a statistically-significant conclusion on the best cleaning technique for producing the highest performance. We will present our results along with our scanning tunneling microscopy images and Raman spectra to shed a light on the mechanism involved in each cleaning technique.

11:40am **GR+EM+ET+MS+NS-FrM11 High Efficiency Graphene Solar Cells by Chemical Doping.** *X. Miao, S. Tongay, M.K. Petterson, K. Berke, A.G. Rinzler, B.R. Appleton, A.F. Hebard*, University of Florida

We demonstrate single layer graphene/n-Si Schottky junction solar cells that under AM1.5 illumination exhibit a power conversion efficiency (PCE) of 8.6%. This performance, achieved by doping the graphene with

bis(trifluoromethanesulfonyl)amide, exceeds the native (undoped) device performance by a factor of 4.5 and is the **highest PCE** reported for graphene-based solar cells to date. Current-voltage, capacitance-voltage, and external quantum efficiency measurements show the enhancement to be due to the doping-induced shift in the graphene chemical potential that increases the graphene carrier density (decreasing the cell series resistance) and increases the cell's built-in potential (increasing the open circuit voltage) both of which improve the solar cell fill factor.

Authors Index

Bold page numbers indicate the presenter

— A —

Abdallah, L.S.: EM+NS-FrM9, **63**
Abe, M.: SP+AS+BI+ET+MI+NS-TuA11, 25
Abel, J.: EM+NS-FrM5, 62; GR+AS+NS+SP+SS-TuA11, 20
Abell, J.L.: TF+SE+NS-WeM12, **34**
Abrasonis, G.: SE+NS-MoM2, 7
Adams, D.: TF+EM+SE+NS-ThM5, **51**
Adamska, L.: GR+AS+EM+NS+SS-WeA2, 36
Addou, R.: GR+EM+NS+SS+TF-ThA7, **55**
Agarwal, S.: NS-MoM6, 4
Ahanotu, O.N.: NS+SP-MoA11, 14
Ahlgren, M.: TF+NS+EM-ThM11, 53
Ahn, J.R.: GR+EM+NS+PS+SS+TF-MoM11, 3; GR+EM+NS+PS+SS+TF-MoM4, 3; NS+EN-TuM1, 17; NS-ThP9, 60; SS+NS-ThA3, 56
Ahn, S.J.: NS-ThP5, **59**
Ai, M.: HI+AS+BI+NS-ThM5, 47
Ajayan, P.: GR+EM+NS+SS+TF-ThA3, 55
Aksamija, Z.: EM+SS+AS+NS-ThM10, **41**
Alaboson, J.M.P.: GR+AS+NS+SP+SS-TuA9, 20
Alcantara Ortigoza, M.: EN+NS-ThM3, 43; NS-MoM10, 5
Alcantara, M.: SS+NS-ThA9, 57
Aldinger, B.S.: NS-ThM9, 49
Alem, N.: GR+AS+NS+SS-ThM5, 46
Alexander, M.R.: BI+SS+NS-WeM12, 29
Allen, S.: SP+AS+BI+ET+MI+NS-TuA9, 24
Allen, T.: NS+AS+SS+SP-WeM2, 30
Alles, M.L.: EM+SS+AS+NS-ThM11, 42
Al-Mahboob, A.: IS+AS+BI+ET+GR+NS-TuA8, **22**
Almer, J.: TF+NS+EM-ThM11, 53
Altman, E.I.: SP+AS+BI+ET+MI+NS-TuA10, 24
Alvarez, C.: IS+AS+BI+ET+GR+NS-TuA7, 21
Andersen, J.N.: GR+AS+NS+SP+SS-TuA7, 19
Anderson, T.J.: GR+EM+ET+NS+TF-MoA1, 9
Antcliffé, M.: GR+EM+ET+MS+NS-FrM3, 64
Aouadi, S.: SE+NS-MoA1, **14**
Apkarian, V.A.: SP+AS+BI+ET+MI+NS-TuA3, 24
Appleton, B.R.: GR+EM+ET+MS+NS-FrM11, 65
Arman, M.A.: GR+AS+NS+SP+SS-TuA7, 19
Arnold, M.S.: GR+AS+EM+NS+SS-WeA9, 36
Arpin, K.A.: EN+NS-ThA1, 54
Asadollahbaik, A.: HI+AS+BI+NS-ThM3, 47
Asbeck, P.: GR+EM+ET+MS+NS-FrM3, 64
Ataç, D.: NS+SP-MoA9, 13
Auer, M.: TF+EM+SE+NS-ThM6, 51
Autes, G.: GR+AS+NS+SS-ThM5, 46
Auzély, R.: BI+SS+NS-WeM10, 29
Avci, R.: NS-ThM12, 50

— B —

Baby, A.: TF+NS+EM-ThM10, 53
Baddorf, A.P.: ET+NS+EM-ThM3, 44
Baehtz, C.: SE+NS-MoM2, 7
Baek, H.-J.: EN+NS-MoM1, 1
Bagnall, D.M.: HI+AS+BI+NS-ThM3, 47
Balci, S.: ET+NS+EM-ThM11, 45
Balog, J.: IS+AS+BI+ET+GR+NS-TuA3, 21
Balsano, R.: EM+NS-FrM5, 62
Baltazar, J.: GR+EM+ET+MS+NS-FrM9, **65**
Ban, S.: NS-ThP2, 59
Bao, K.: NS-ThM9, 49
Barlam, D.: OX+EM+MI+NS+TF-MoM11, 6
Barlow, A.J.: SS+NS-ThA7, **57**
Barraza-Lopez, S.: EM+NS-FrM5, 62
Barrett, N.: GR+AS+NS+SP+SS-TuA1, 19
Bartels, L.: SP+AS+BI+ET+MI+NM+NS+SS+TF-WeM5, 31
Batziil, M.: GR+AS+EM+NS+SS-WeA8, 36; GR+EM+NS+SS+TF-ThA7, 55
Baughman, W.: ET+NS+EM-ThM11, 45
Baykara, M.Z.: SP+AS+BI+ET+MI+NS-TuA10, 24

Beard, M.C.: EN+NS-MoM3, 1
Beaudry, A.L.: TF+SE+NS-WeM9, **33**
Bedzyk, M.J.: GR+AS+NS+SP+SS-TuA9, 20
Beech, I.: NS-ThM12, 50
Beechem, T.E.: GR+AS+NS+SP+SS-TuA8, 19
Behafarid, F.: SS+NS-ThA8, **57**
Bekman, H.H.P.Th.: HI+AS+NS-WeA9, 38
Belyansky, M.P.: NM+NS+MS+EM-MoA4, **11**
Bennetsen, D.T.: BI+SS+NS-WeM1, **28**
Ben-Yoav, H.: BI+SS+NS-WeM2, 28
Berdova, M.: TF+NS+EM-ThM10, **53**
Berke, K.: GR+EM+ET+MS+NS-FrM11, 65
Bernal Ramos, K.: TF+NS+EM-ThM2, **51**; TF+NS+EM-ThM9, 52
Beugin, V.: NM+NS+MS+EM-MoA6, 11
Beyer, A.: HI+AS+BI+NS-ThM11, 48; HI+AS+BI+NS-ThM5, 47
Bezares, F.J.: GR+EM+ET+NS+TF-MoA1, 9
Bhattacharya, A.: NS+AS+SS+SP-WeM12, 30
Bhattacharyya, D.: EM+SS+AS+NS-ThM4, **41**
Bielefeld, J.: GR+EM+NS+SS+TF-ThA1, 54
Bingham, N.: OX+EM+MI+NS+TF-MoM1, 5
Biswal, S.L.: EN+NS-ThM12, **44**
Blanch, A.J.: SS+NS-ThA7, 57
Blomfield, C.J.: AS+NS+SS+TF-WeA8, 35
Boden, S.A.: HI+AS+BI+NS-ThM3, **47**
Boland, J.: HI+AS+BI+NS-ThM9, 48
Bolotin, K.I.: GR+EM+ET+NS+TF-MoA3, 9
Bolvardi, H.: SE+NS-MoM8, 7
Bonnell, D.A.: NS-WeA1, 39
Borchers, J.: OX+EM+MI+NS+TF-MoM10, 6
Borgström, M.T.: ET+NS+EM-ThM6, 45
Bose, S.: OX+EM+MI+NS+TF-MoM10, 6
Bosnick, K.: NS-ThP2, **59**
Bostwick, A.: GR+EM+ET+NS+TF-MoA8, 10
Boturyn, D.: BI+SS+NS-WeM10, 29
Bratescu, M.A.: NS-ThP8, 60
Braun, P.V.: EN+NS-ThA1, 54; SE+NS-MoA10, **15**
Braunstein, P.: GR+EM+ET+NS+TF-MoA7, 9
Brett, M.J.: TF+SE+NS-WeM11, 34; TF+SE+NS-WeM5, 33; TF+SE+NS-WeM9, 33
Brocklesby, W.S.: SE+NS-MoA3, 14
Broitman, E.: TF+NS+EM-ThM12, 53
Brown, A.: BI+SS+NS-WeM2, 28
Bruhn, T.: GR+EM+NS+SS+TF-ThA6, 55
Büenfeld, M.: HI+AS+BI+NS-ThM5, 47
Burghaus, U.: NS+AS+SS+SP-WeM4, 30
Busse, C.: GR+AS+NS+SP+SS-TuA7, 19
Büyükköse, S.: NS+SP-MoA9, **13**

— C —

Cabrera, W.: TF+NS+EM-ThM9, 52
Cahill, D.G.: SE+NS-MoA10, 15
Cai, M.: GR+AS+NS+SS-ThM10, 47
Caillard, L.: EM+NS-FrM3, **62**
Caldwell, J.D.: GR+EM+ET+NS+TF-MoA1, 9
Camillone, N.: NS+AS+SS+SP-WeM12, **30**
Campbell, P.: EM+NS-FrM3, 62
Campbell, P.M.: GR+EM+ET+MS+NS-FrM3, 64
Casolo, S.: GR+AS+EM+NS+SS-WeA12, 37
Castner, D.G.: IS+AS+BI+ET+GR+NS-TuA1, 21
Caubet, P.: NM+NS+MS+EM-MoA6, 11
Ceccone, G.: NS+EN+GR-TuA2, 22
Chabal, Y.J.: EM+NS-FrM3, 62; GR+AS+EM+NS+SS-WeA1, 36; NS+SP-MoA7, 13; TF+NS+EM-ThM2, 51; TF+NS+EM-ThM9, 52
Chae, J.: GR+EM+ET+NS+TF-MoA10, **10**
Chagarov, E.: SP+AS+BI+ET+MI+NM+NS+SS+TF-WeM6, 31
Chakradhar, A.: NS+AS+SS+SP-WeM4, 30
Chan, K.K.: EM+NS-FrM10, 63
Chandra, S.: NS-MoM9, 5
Chang, C.S.: GR+EM+ET+NS+TF-MoA6, 9

Chang, J.P.: EN+NS-ThA6, 54; EN+NS-ThM6, 43; TF+NS+EM-ThM6, 52
Chang, M.H.: EM+SS+AS+NS-ThM12, 42
Chang, W.-T.: HI+AS+NS-WeA8, 38
Chang, Y.H.: EM+SS+AS+NS-ThM12, 42
Chen, J.: GR+AS+NS+SP+SS-TuA2, 19
Chen, J.-H.: GR+AS+NS+SS-ThM5, 46
Chen, L.: NS+SP-MoA8, 13; TF+SE+NS-WeM4, 33
Chen, S.: GR+AS+NS+SP+SS-TuA11, 20
Chen, X.: NS-WeA1, 39
Chen, Y.: HI+AS+BI+NS-ThM9, 48
Chhowalla, M.: NS+EN+GR-TuA8, **23**
Chiang, S.: NS-ThM6, 49; SS+NS-ThA6, **56**
Cho, H.K.: NS+EN+GR-TuA11, 23; OX+EM+MI+NS+TF-MoM2, 6
Cho, J.: EN+NS-ThM6, 43
Cho, K.J.: GR+AS+EM+NS+SS-WeA1, 36
Choi, J.: GR+EM+ET+NS+TF-MoA7, 9
Choi, J.W.: EN+NS-MoM5, **1**
Choi, J.Y.: GR+EM+NS+PS+SS+TF-MoM11, 3
Choi, S.-H.: NS-ThP6, 59
Choi, Y.H.: NS-ThP6, **59**
Chou, L.-W.: NS-WeA11, **40**
Chu, D.: NM+NS+MS+EM-MoA2, **10**
Chun, S.H.: OX+EM+MI+NS+TF-MoM2, 6
Ciarnelli, V.: BI+SS+NS-WeM12, **29**
Cimpoiasu, E.: GR+AS+NS+SS-ThM3, 46
Cirigliano, N.: EN+NS-ThM6, 43
Clark, K.: GR+EM+NS+PS+SS+TF-MoM2, 2
Clavel, G.: TF+NS+EM-ThM9, 52
Cleveland, E.: NS+EN-TuM2, 17
Cohen, K.D.: SP+AS+BI+ET+MI+NM+NS+SS+TF-WeM5, 31
Cohen, S.R.: OX+EM+MI+NS+TF-MoM11, **6**
Colby, R.: AS+NS+SS+TF-WeA3, 35; AS+NS+SS+TF-WeA4, 35
Colón Santana, J.: GR+EM+ET+NS+TF-MoA7, 9
Colpo, P.: NS+EN+GR-TuA2, 22
Conklin, D.: NS-WeA1, **39**
Conrad, E.: GR+AS+NS+SP+SS-TuA1, 19
Copel, M.W.: GR+EM+NS+PS+SS+TF-MoM8, 3
Coppée, S.: SE+NS-MoA4, 15
Coraux, J.: GR+AS+EM+NS+SS-WeA10, 37
Corso, M.: SP+AS+BI+ET+MI+NM+NS+SS+TF-WeM4, 31
Cortes, R.: GR+EM+NS+SS+TF-ThA2, **55**
Coults, S.J.: AS+NS+SS+TF-WeA8, 35
Cowin, J.: IS+AS+BI+ET+GR+NS-TuA12, 22
Cui, S.: GR+AS+NS+SP+SS-TuA2, 19
Culbertson, J.C.: GR+EM+NS+PS+SS+TF-MoM3, 2
Culver, J.: BI+SS+NS-WeM2, 28
Cumpson, P.J.: SP+AS+BI+ET+MI+NM+NS+SS+TF-WeM10, 32
Cunningham, G.B.: EN+NS-MoM11, 2
Cyganik, P.: SS+NS-ThA10, **57**
Czaplewski, D.A.: NS+SP-MoA10, **14**

— D —

Dahal, A.: GR+AS+EM+NS+SS-WeA8, **36**; GR+EM+NS+SS+TF-ThA7, 55
Davidson, M.R.: NS-WeA2, 39
Davies, M.C.: BI+SS+NS-WeM12, 29
Davis, B.H.: NS-ThM12, 50
Davis, K.O.: NM+NS+MS+EM-MoA9, **11**
Dawhreh, N.: ET+NS+EM-ThM11, 45; NS+EN-TuM3, 17; NS-ThM11, **49**
De Moure-Flores, F.: NS-MoM2, 4
De Padova, P.: GR+EM+NS+SS+TF-ThA6, 55
De Vito, E.: EN+NS-ThM11, **43**
Dean, C.: GR+EM+ET+NS+TF-MoA10, 10
Demberger, C.: NM+NS+MS+EM-MoA9, 11
Demko, A.: NS+AS+SS+SP-WeM2, 30

Dendzik, M.: SS+NS-ThA10, 57
 Deng, R.: TF+SE+NS-WeM6, 33
 Desai, T.V.: IS+AS+BI+ET+GR+NS-TuA2, 21
 Despont, M.: NS+SP-MoA2, 12
 Detslefs, B.: GR+AS+NS+SP+SS-TuA9, 20
 Devaraj, A.: AS+NS+SS+TF-WeA3, 35;
 AS+NS+SS+TF-WeA4, 35; NS-WeA10, 40
 Dewdney, J.: NS-MoM9, 5
 Dhayal, M.: NS-MoM11, 5
 Dhiman, R.: EM+SS+AS+NS-ThM3, 41
 Dick, D.: NS+SP-MoA7, 13
 Diebold, A.C.: GR+AS+NS+SP+SS-TuA11, 20
 DiLabio, G.:
 SP+AS+BI+ET+MI+NM+NS+SS+TF-WeM2,
 31
 Dimitrakopoulos, C.: GR+AS+NS+SP+SS-TuA11,
 20
 Divan, R.S.: NS+SP-MoA11, 14
 Donaldson, S.H.: BI+SS+NS-WeM5, 28
 Donegan, J.: HI+AS+BI+NS-ThM9, 48
 Dong, C.: NS-ThP14, 61
 Doudin, B.: GR+EM+ET+NS+TF-MoA7, 9
 Dougherty, D.B.: GR+AS+NS+SP+SS-TuA11, 20;
 GR+EM+ET+MS+NS-FrM8, 65
 Dowben, P.A.: GR+EM+ET+NS+TF-MoA7, 9
 Dowsett, D.: HI+AS+NS-WeA10, 38
 Draper, R.: NS+AS+SS+SP-WeM2, 30
 Drews, J.: EM+SS+AS+NS-ThM3, 41
 Driskell, J.D.: TF+SE+NS-WeM12, 34
 Duan, X.: GR+EM+ET+MS+NS-FrM1, 64
 Dubacheva, G.V.: BI+SS+NS-WeM10, 29
 Dubey, M.D.: GR+EM+ET+MS+NS-FrM8, 65
 Dudis, D.: SE+NS-MoA11, 16
 Duerig, U.: NS+SP-MoA2, 12
 Dunn, B.: EN+NS-ThM6, 43
 Durstock, M.F.: EN+NS-ThM9, 43
 Dussault, L.: NM+NS+MS+EM-MoA6, 11

— E —

Ealet, B.: GR+EM+NS+SS+TF-ThA6, 55
 Eastman, P.Y.: AS+NS+SS+TF-WeA9, 36
 Eddy, Jr., C.R.: GR+AS+NS+SP+SS-TuA9, 20;
 GR+EM+ET+MS+NS-FrM3, 64;
 GR+EM+ET+MS+NS-FrM5, 64;
 GR+EM+ET+NS+TF-MoA1, 9;
 GR+EM+NS+PS+SS+TF-MoM1, 2;
 GR+EM+NS+PS+SS+TF-MoM3, 2;
 TF+NS+EM-ThM1, 51
 Edlmayr, V.: SE+NS-MoM9, 8
 Edmonds, M.:
 SP+AS+BI+ET+MI+NM+NS+SS+TF-WeM6,
 31
 Ek, S.: SE+NS-MoM10, 8
 Elkinci, Y.: HI+AS+BI+NS-ThM11, 48
 El-Khatib, S.: OX+EM+MI+NS+TF-MoM10, 6
 El-Khoury, P.Z.: SP+AS+BI+ET+MI+NS-TuA3,
 24
 Emery, J.D.: GR+AS+NS+SP+SS-TuA9, 20
 Engstrom, J.R.: IS+AS+BI+ET+GR+NS-TuA2, 21
 Enta, Y.: GR+EM+NS+PS+SS+TF-MoM10, 3
 Ershov, M.V.: SE+NS-MoA7, 15

— F —

Facsko, S.: SE+NS-MoM2, 7
 Fager, H.: TF+NS+EM-ThM12, 53
 Faggini, M.F.: NS-ThM9, 49
 Fahey, A.J.: AS+NS+SS+TF-WeA7, 35
 Fan, X.: BI+SS+NS-WeM2, 28
 Faulkner, C.C.: HI+AS+BI+NS-ThM9, 48
 Feenstra, R.: GR+AS+NS+SP+SS-TuA10, 20
 Feldman, Y.: NS+AS+SS+SP-WeM4, 30
 Feliciano, D.M.: EN+NS-MoM6, 1
 Fernandez-Torre, D.: SP+AS+BI+ET+MI+NS-
 TuA11, 25
 Ferris, R.J.: BI+SS+NS-WeM9, 29
 Filippov, S.V.: SE+NS-MoA7, 15
 Filler, M.: NS+EN-TuM4, 17; NS-WeA11, 40
 First, P.N.: GR+AS+NS+SP+SS-TuA3, 19
 Fisher, E.R.: SE+NS-MoA6, 15
 Fitzmorris, B.C.: TF+SE+NS-WeM3, 32

Fleetwood, D.M.: EM+SS+AS+NS-ThM11, 42
 Fleischauer, M.D.: TF+SE+NS-WeM11, 34
 Foley, E.T.: NS-ThP3, 59
 Foss, M.: BI+SS+NS-WeM1, 28
 Fowlkes, J.D.: NS+SP-MoA4, 13;
 TF+EM+SE+NS-ThM3, 50
 Fox, D.: HI+AS+BI+NS-ThM9, 48
 Franke, K.J.:
 SP+AS+BI+ET+MI+NM+NS+SS+TF-WeM4,
 31
 Franssila, S.: TF+NS+EM-ThM10, 53
 French, B.: GR+EM+NS+SS+TF-ThA1, 54
 French, M.: GR+EM+NS+SS+TF-ThA1, 54
 Freund, H.J.: NS-ThM3, 48
 Fromm, F.: GR+EM+NS+PS+SS+TF-MoM10, 3
 Fruchart, O.: GR+AS+EM+NS+SS-WeA10, 37
 Fu, J.: NS+SP-MoA8, 13
 Fu, T.-Y.: HI+AS+NS-WeA8, 38
 Fuentes-Cabrera, M.: TF+EM+SE+NS-ThM3, 50
 Fujita, D.: HI+AS+BI+NS-ThM12, 48
 Fukidome, H.: GR+EM+NS+PS+SS+TF-MoM10,
 3

— G —

Gajdardziska-Josifovska, M.:
 GR+AS+NS+SP+SS-TuA2, 19
 Galatsis, K.: EM+SS+AS+NS-ThM11, 42
 Gall, D.: TF+SE+NS-WeM6, 33
 Gao, Y.: GR+EM+ET+NS+TF-MoA10, 10
 Garces, N.Y.: GR+EM+ET+MS+NS-FrM5, 64;
 GR+EM+NS+PS+SS+TF-MoM1, 2;
 GR+EM+NS+PS+SS+TF-MoM3, 2
 Gargiulo, F.: GR+AS+NS+SS-ThM5, 46
 Garramone, J.: EM+NS-FrM5, 62
 Garren, J.M.: TF+SE+NS-WeM12, 34
 Gaskill, D.K.: GR+AS+NS+SP+SS-TuA9, 20;
 GR+EM+ET+MS+NS-FrM3, 64;
 GR+EM+ET+MS+NS-FrM5, 64;
 GR+EM+ET+NS+TF-MoA1, 9;
 GR+EM+NS+PS+SS+TF-MoM1, 2;
 GR+EM+NS+PS+SS+TF-MoM3, 2
 Gassilloud, R.: NM+NS+MS+EM-MoA6, 11
 Gaub, H.E.:
 SP+AS+BI+ET+MI+NM+NS+SS+TF-
 WeM11, 32
 Gautam, A.: GR+AS+NS+SS-ThM5, 46
 Gazquez, J.: OX+EM+MI+NS+TF-MoM10, 6
 Gebbie, M.A.: BI+SS+NS-WeM5, 28
 Gembocki, O.J.: NS+EN-TuM2, 17
 Gemming, S.: SE+NS-MoM2, 7
 Gerber, T.: GR+AS+NS+SP+SS-TuA7, 19
 Ghafoor, N.: TF+NS+EM-ThM11, 53;
 TF+NS+EM-ThM12, 53
 Ghodssi, R.: BI+SS+NS-WeM2, 28
 Ghorai, S.: IS+AS+BI+ET+GR+NS-TuA9, 22
 Gilles, M.K.: IS+AS+BI+ET+GR+NS-TuA9, 22
 Girshevitz, O.: OX+EM+MI+NS+TF-MoM11, 6
 Gleason, K.K.: EM+SS+AS+NS-ThM4, 41
 Goldman, R.S.: EM+SS+AS+NS-ThM13, 42
 Göhlhäuser, A.: HI+AS+BI+NS-ThM11, 48;
 HI+AS+BI+NS-ThM5, 47
 Gong, C.: GR+AS+EM+NS+SS-WeA1, 36
 Gotlib-Vainshtein, K.: OX+EM+MI+NS+TF-
 MoM11, 6
 Götzén, J.: SP+AS+BI+ET+MI+NS-TuA10, 24
 Grady, M.: SE+NS-MoA10, 15
 Graham, S.: GR+EM+ET+MS+NS-FrM9, 65
 Grampeix, H.: NS-ThM10, 49
 Grånäs, E.: GR+AS+NS+SP+SS-TuA7, 19
 Grant-Jacob, J.A.: SE+NS-MoA3, 14
 Greene, J.E.: TF+NS+EM-ThM12, 53
 Gregory, C.W.: EN+NS-MoM11, 2
 Grigoras, K.: TF+NS+EM-ThM10, 53
 Grill, A.: GR+AS+NS+SP+SS-TuA11, 20
 Gross, L.: SP+AS+BI+ET+MI+NS-TuA1, 23
 Gu, Y.: ET+NS+EM-ThM12, 45
 Guallar-Hoyas, C.: IS+AS+BI+ET+GR+NS-TuA3,
 21
 Guedj, C.: NS-ThM10, 49
 Guerente, L.: BI+SS+NS-WeM10, 29

Gunlycke, D.: GR+AS+NS+SS-ThM3, 46
 Guo, H.X.: HI+AS+BI+NS-ThM12, 48
 Guo, J.H.: GR+EM+ET+NS+TF-MoA11, 10
 Guo, X.: NS+EN-TuM11, 18
 Gupta, A.: NS-ThM9, 49
 Gupta, S.: TF+EM+SE+NS-ThM4, 50;
 TF+SE+NS-WeM10, 33

— H —

Haag, J.: EN+NS-ThM9, 43
 Habenicht, B.: GR+AS+EM+NS+SS-WeA11, 37
 Habermann, D.: NM+NS+MS+EM-MoA9, 11
 Haehner, G.:
 SP+AS+BI+ET+MI+NM+NS+SS+TF-WeM9,
 31
 Hager, G.: AS+NS+SS+TF-WeA7, 35
 Hall, S.: EN+NS-MoM11, 2
 Halls, M.D.: TF+NS+EM-ThM2, 51
 Hammond, J.S.: NS-ThM12, 50
 Han, Y.: SS+NS-TuA11, 26
 Handa, H.: GR+EM+NS+SP+SS+TF-MoM10, 3
 Hannon, J.B.: GR+EM+NS+PS+SS+TF-MoM8, 3
 Hanrath, T.: EN+NS-MoM5, 1
 Hanus, J.: NS+EN+GR-TuA2, 22
 Hao, Y.: GR+AS+NS+SP+SS-TuA11, 20
 Hapala, P.: NS-MoM5, 4
 Harada, Y.: GR+AS+EM+NS+SS-WeA12, 37
 Haverkamp, H.: NM+NS+MS+EM-MoA9, 11
 Hawley, C.J.: NS+EN-TuM6, 18
 Haydell, M.: GR+AS+NS+SS-ThM3, 46
 Hayden, B.E.: SS+NS-TuA9, 26
 He, C.: OX+EM+MI+NS+TF-MoM10, 6
 He, G.: GR+AS+NS+SP+SS-TuA10, 20
 Hebard, A.F.: GR+EM+ET+MS+NS-FrM11, 65
 Hedrick, J.L.: NS+SP-MoA2, 12
 Hemminger, J.C.: SS+NS-TuA3, 25
 Henderson, C.L.: GR+EM+ET+MS+NS-FrM9, 65
 Henry, F.: SE+NS-MoA4, 15
 Heo, Y.K.: NS-ThP8, 60
 Hernández, S.C.: GR+EM+NS+PS+SS+TF-
 MoM1, 2
 Hernández-Hernández, A.: NS-MoM2, 4
 Hernández-Hernández, L.A.: NS-MoM2, 4
 Herrera, V.: BI+SS+NS-WeM6, 28
 Herring, A.M.: EN+NS-ThM1, 42
 Hersam, M.C.: GR+AS+NS+SP+SS-TuA9, 20;
 NS-ThP3, 59
 Hettiarachchi, C.: EN+NS-MoM6, 1
 Heyde, M.: NS-ThM3, 48
 Hiebert, W.K.: NS-ThP2, 59
 Hikita, Y.: OX+EM+MI+NS+TF-MoM3, 6
 Hines, M.: NS-ThP12, 60
 Hines, M.A.: NS-ThM9, 49
 Hiramatsu, M.: GR+AS+NS+SS-ThM9, 47
 Hirschmugl, C.: GR+AS+NS+SP+SS-TuA2, 19
 Hite, J.K.: TF+NS+EM-ThM1, 51
 Hjort, M.: ET+NS+EM-ThM6, 45
 Hla, S.-W.: NS-ThM1, 48
 Hobbs, J.K.: SP+AS+BI+ET+MI+NS-TuA7, 24
 Hoffman, R.S.: EN+NS-MoM5, 1
 Hollerweger, R.: SE+NS-MoM6, 7
 Holloway, P.H.: NS-WeA2, 39
 Holzke, C.: SP+AS+BI+ET+MI+NM+NS+SS+TF-
 WeM5, 31
 Holzner, F.: NS+SP-MoA2, 12
 Hone, J.C.: GR+EM+ET+NS+TF-MoA10, 10;
 NS+EN-TuM11, 18
 Hong, M.: SS+NS-ThA4, 56
 Hong, S.: SS+NS-ThA9, 57
 Hopstaken, M.J.P.: EM+NS-FrM10, 63
 Hordagoda, M.: OX+EM+MI+NS+TF-MoM1, 5
 Hori, M.: GR+AS+NS+SS-ThM9, 47
 Horn, K.: GR+EM+ET+NS+TF-MoA8, 10
 Horsfall, A.B.: GR+EM+NS+PS+SS+TF-MoM1, 2
 Hosemann, P.: SE+NS-MoM6, 7
 Hossain, M.Z.: NS+SP-MoA6, 13
 Hou, J.B.: SS+NS-TuA11, 26
 Hou, J.-L.: HI+AS+NS-WeA8, 38
 Howe, B.M.: SE+NS-MoA11, 16; TF+NS+EM-
 ThM12, 53

Howe, J.: GR+EM+NS+PS+SS+TF-MoM3, 2
Hsu, C.: ET+NS+EM-ThM12, 45
Hu, S.W.: SS+NS-TuA11, 26
Huang, C.: NS-ThP2, 59
Huang, L.W.: GR+EM+ET+NS+TF-MoA6, 9
Huffman, E.: NS-ThM6, 49
Hultman, L.: TF+NS+EM-ThM11, 53;
TF+NS+EM-ThM12, 53
Hutton, S.J.: AS+NS+SS+TF-WeA8, 35
Hwang, H.H.: EN+NS-MoM1, 1
Hwang, I.-S.: HI+AS+NS-WeA8, 38
Hyde, R.H.: OX+EM+MI+NS+TF-MoM1, 5
— I —
Ide, T.: GR+EM+NS+PS+SS+TF-MoM10, 3
Ingram, G.: TF+SE+NS-WeM5, 33
Isaacson, M.: EN+NS-ThM12, 44
Ishigami, M.: GR+EM+ET+MS+NS-FrM10, 65;
GR+EM+ET+NS+TF-MoA2, 9; NS+EN-
TuM11, 18
Ishikawa, K.: GR+AS+NS+SS-ThM9, 47
Ishikawa, T.: NS+EN-TuM5, 17
Israelachvili, J.N.: BI+SS+NS-WeM5, 28
Itagaki, N.: EN+NS-MoM2, 1
— J —
Jaehnig, M.: GR+EM+NS+SS+TF-ThA1, 54
James, C.D.: ET+NS+EM-ThM10, 45
Jandhyala, S.: GR+EM+ET+MS+NS-FrM7, 64
Jang, J.S.: EN+NS-MoM1, 1
Jankovic, V.: EN+NS-ThA6, 54
Jelinek, P.: NS-MoM5, 4;
SP+AS+BI+ET+MI+NS-TuA4, 24
Jena, D.: GR+AS+NS+SS-ThM11, 47
Jesse, S.: SP+AS+BI+ET+MI+NS-TuA12, 25
Ji, S.-H.: GR+EM+NS+PS+SS+TF-MoM8, 3
Jiang, K.: NM+NS+MS+EM-MoA9, 11
Jiang, N.: NS-ThP3, 59
Jiang, Z.: ET+NS+EM-ThM9, 45
Johansson, M.P.: TF+NS+EM-ThM11, 53
Johnson, C.E.: IS+AS+BI+ET+GR+NS-TuA7, 21
Johnson, J.A.: IS+AS+BI+ET+GR+NS-TuA7, 21
Johnson, M.: NS+AS+SS+SP-WeM2, 30
Jouanneau, S.: EN+NS-ThM11, 43
Joy, D.: HI+AS+NS-WeA1, 37
Jung, S.: GR+EM+ET+NS+TF-MoA10, 10
Jur, J.S.: TF+NS+EM-ThM5, 52
— K —
Kahng, S.-J.: EM+SS+AS+NS-ThM12, 42
Kajiwara, T.: GR+AS+NS+SS-ThM1, 46
Kalanyan, B.: EN+NS-ThA1, 54
Kalfon-Cohen, E.: OX+EM+MI+NS+TF-MoM11,
6
Kalinin, S.V.: SP+AS+BI+ET+MI+NS-TuA12, 25
Kamatani, K.: EN+NS-MoM2, 1
Kamimura, T.: ET+NS+EM-ThM5, 44
Kanda, T.: GR+AS+NS+SS-ThM9, 47
Kang, J.: NS-ThP4, 59
Kang, P.S.: NS-ThP6, 59
Kanjolia, R.K.: TF+NS+EM-ThM2, 51
Kant, C.: NS-MoM11, 5
Karmel, H.J.: GR+AS+NS+SP+SS-TuA9, 20
Kato, H.: NS+SP-MoA6, 13
Katoch, J.: GR+EM+ET+NS+TF-MoA2, 9
Kawai, M.: BI+SS+NS-WeM11, 29; NS+SP-
MoA6, 13
Kawai, Y.: GR+EM+NS+PS+SS+TF-MoM10, 3
Kayani, A.: NS-WeA10, 40
Keckes, J.: SE+NS-MoM5, 7
Kellogg, G.L.: GR+AS+NS+SP+SS-TuA8, 19
Kelly, S.T.: IS+AS+BI+ET+GR+NS-TuA9, 22
Kent, T.J.: SP+AS+BI+ET+MI+NM+NS+SS+TF-
WeM6, 31
Khurshid, H.: NS-MoM8, 4; NS-MoM9, 5
Kilpi, L.: TF+NS+EM-ThM10, 53
Kim, D.H.: NM+NS+MS+EM-MoA8, 11;
NS+EN+GR-TuA10, 23
Kim, G.T.: NS-ThP6, 59
Kim, H.: EM+SS+AS+NS-ThM12, 42
Kim, J.: GR+EM+ET+MS+NS-FrM7, 64

Kim, J.H.: NS+EN+GR-TuA11, 23
Kim, J.S.: NS-ThP6, 59
Kim, K.J.: EN+NS-MoM1, 1
Kim, M.K.: SS+NS-ThA3, 56
Kim, P.: GR+EM+ET+NS+TF-MoA10, 10
Kim, S.: EM+SS+AS+NS-ThM11, 42
Kim, S.M.: ET+NS+EM-ThM11, 45; NS+EN-
TuM3, 17; NS-ThM11, 49
Kim, T.: ET+NS+EM-ThM3, 44
Kim, Y.-H.: EM+SS+AS+NS-ThM12, 42
King, S.: GR+EM+NS+SS+TF-ThA1, 54
King, W.: GR+AS+NS+SS-ThM3, 46
Kinoshita, T.: GR+EM+NS+PS+SS+TF-MoM10,
3
Kinross, J.: IS+AS+BI+ET+GR+NS-TuA3, 21
Kirchlechner, C.: SE+NS-MoM5, 7
Kis, A.: GR+EM+NS+SS+TF-ThA10, 55
Kisielowski, C.: GR+AS+NS+SS-ThM5, 46
Klem, E.J.D.: EN+NS-MoM11, 2
Klingsporn, J.M.: NS-ThP3, 59
Knoll, A.W.: NS+SP-MoA2, 12
Knudsen, J.: GR+AS+NS+SP+SS-TuA7, 19
Kobayashi, T.: BI+SS+NS-WeM11, 29
Koga, K.: EN+NS-MoM2, 1
Kolosko, A.G.: SE+NS-MoA7, 15
Komarneni, M.: NS+AS+SS+SP-WeM4, 30
Komori, F.: GR+AS+NS+SS-ThM1, 46
Kondo, H.: GR+AS+NS+SS-ThM9, 47
Kondo, T.: GR+AS+EM+NS+SS-WeA12, 37
Kong, L.: GR+EM+ET+NS+TF-MoA7, 9
Kontic, R.: NS-ThP1, 59
Kornegay, S.M.: TF+EM+SE+NS-ThM4, 50
Korolkov, V.: SP+AS+BI+ET+MI+NS-TuA9, 24
Koshihara, S.: NS+EN-TuM5, 17
Koskinen, J.: TF+NS+EM-ThM10, 53
Koster, N.B.: HI+AS+NS-WeA9, 38
Kotsugi, M.: GR+EM+NS+PS+SS+TF-MoM10, 3
Kowalik, J.: GR+EM+ET+MS+NS-FrM9, 65
Krafcik, J.: NS+EN-TuM3, 17
Kraft, D.C.E.: BI+SS+NS-WeM1, 28
Krause, M.: SE+NS-MoM2, 7
Kroemker, B.: GR+AS+NS+SP+SS-TuA1, 19
Kubetzka, A.: NS-ThM1, 48
Kuemin, C.: NS+SP-MoA2, 12
Kuhn, M.: GR+EM+NS+SS+TF-ThA1, 54
Kummel, A.C.: BI+SS+NS-WeM6, 28;
SP+AS+BI+ET+MI+NM+NS+SS+TF-WeM6,
31
Kung, P.: ET+NS+EM-ThM11, 45; NS+EN-
TuM3, 17; NS-ThM11, 49
Kuo, H.-S.: HI+AS+NS-WeA8, 38
Kusova, K.: NS-MoM5, 4
Kwon, J.: TF+NS+EM-ThM2, 51
Kwon, Y.H.: OX+EM+MI+NS+TF-MoM2, 6
— L —
Labbé, P.: BI+SS+NS-WeM10, 29
LaBella, V.P.: EM+NS-FrM5, 62;
GR+AS+NS+SP+SS-TuA11, 20
LaForge, J.M.: TF+SE+NS-WeM5, 33;
TF+SE+NS-WeM9, 33
Lahiri, J.: GR+EM+NS+SS+TF-ThA2, 55
Lalany, A.: TF+SE+NS-WeM11, 34
Lampen, P.: NS-MoM8, 4
Larsen, G.K.: TF+SE+NS-WeM3, 32
Lashley, J.C.: EM+NS-FrM11, 63
Laskin, A.: IS+AS+BI+ET+GR+NS-TuA9, 22
Lauer, I.: EM+NS-FrM10, 63
Lauhon, L.J.: ET+NS+EM-ThM1, 44
Laver, M.: OX+EM+MI+NS+TF-MoM10, 6
Lavoie, C.: EM+NS-FrM7, 63; EM+NS-FrM9, 63
Lazzaroni, R.: SE+NS-MoA4, 15
Le Lay, G.: GR+EM+NS+SS+TF-ThA6, 55
Le, D.: GR+EM+ET+MS+NS-FrM3, 64;
GR+EM+ET+NS+TF-MoA2, 9; NS+EN+GR-
TuA7, 23
Lea, A.S.: NS-ThM2, 48
Lee, A.J.: NS+SP-MoA1, 12
Lee, C.-M.: GR+EM+ET+NS+TF-MoA7, 9
Lee, J.: SP+AS+BI+ET+MI+NS-TuA3, 24

Lee, J.H.: OX+EM+MI+NS+TF-MoM2, 6
Lee, J.Y.: OX+EM+MI+NS+TF-MoM2, 6
Lee, K.M.: NS+EN+GR-TuA10, 23
Lee, K.-M.: GR+EM+ET+MS+NS-FrM3, 64
Lee, W.K.: GR+AS+NS+SS-ThM3, 46
Legget, G.J.: NS+SP-MoA1, 12
Leighton, C.: OX+EM+MI+NS+TF-MoM10, 6
Leroux, C.: NM+NS+MS+EM-MoA6, 11
Letofsky-Papst, I.: SE+NS-MoM9, 8
Lewis, J.: EN+NS-MoM11, 2
Li, A.-P.: ET+NS+EM-ThM3, 44; ET+NS+EM-
ThM4, 44; GR+EM+NS+PS+SS+TF-MoM2, 2
Li, K.: NS+SP-MoA8, 13
Li, L.: NS-ThP4, 59
Li, Q.: SP+AS+BI+ET+MI+NS-TuA12, 25
Li, X.D.: ET+NS+EM-ThM4, 44
Li, Z.: SS+NS-TuA4, 26
Li, Z.S.: EM+NS-FrM4, 62; EM+SS+AS+NS-
ThM3, 41
Lian, T.: EN+NS-MoM8, 1
Lichtenstein, L.: NS-ThM3, 48
Licitra, C.: NS-ThM10, 49
Lin, C.-Y.: HI+AS+NS-WeA8, 38
Lin, M.Y.: NS-ThP7, 60
Lin, S.: GR+EM+ET+MS+NS-FrM3, 64
Lin, W.Z.: SP+AS+BI+ET+MI+NS-TuA12, 25
Lin, Y.H.: EM+SS+AS+NS-ThM13, 42
Linck, M.: GR+AS+NS+SS-ThM5, 46
Lister, R.: NS-ThP2, 59
Liu, Y.: SS+NS-TuA3, 25
Liu, Z.: GR+EM+NS+SS+TF-ThA3, 55
Livadaru, L.:
SP+AS+BI+ET+MI+NM+NS+SS+TF-WeM2,
31
Lo, E.: IS+AS+BI+ET+GR+NS-TuA1, 21
Lodge, M.: GR+EM+ET+MS+NS-FrM10, 65
Lofaro, J.C.: NS+AS+SS+SP-WeM12, 30
Longo, C.: TF+SE+NS-WeM3, 32
Lopinski, G.P.: EM+NS-FrM1, 62
Losego, M.D.: EN+NS-ThA1, 54; SE+NS-MoA10,
15
Lotze, C.: SP+AS+BI+ET+MI+NM+NS+SS+TF-
WeM4, 31
Lou, J.: GR+EM+NS+SS+TF-ThA3, 55
Lou, Y.: SS+NS-TuA4, 26
Louie, S.G.: GR+AS+NS+SS-ThM5, 46
Lovinger, D.: NS-ThM6, 49
Lu, G.: GR+AS+NS+SP+SS-TuA2, 19
Lu, T.-M.: TF+SE+NS-WeM4, 33
Lu, Y.-H.: HI+AS+NS-WeA8, 38
Lu, Y.P.: NS-ThP7, 60
Lui, Y.: IS+AS+BI+ET+GR+NS-TuA7, 21
Luther, J.M.: EN+NS-MoM3, 1
Lyytinen, J.: TF+NS+EM-ThM10, 53
— M —
Ma, Q.: SP+AS+BI+ET+MI+NM+NS+SS+TF-
WeM5, 31
Maas, D.J.: HI+AS+NS-WeA9, 38
Macak, E.: AS+NS+SS+TF-WeA8, 35
Macak, K.: AS+NS+SS+TF-WeA8, 35
Macco, B.: NS-MoM6, 4
Magel, G.A.: NS+SP-MoA4, 13
Magnone, K.:
SP+AS+BI+ET+MI+NM+NS+SS+TF-WeM5,
31
Magnuson, C.W.: GR+AS+NS+SP+SS-TuA11, 20
Mahadik, N.: TF+NS+EM-ThM1, 51
Majzik, Z.: SP+AS+BI+ET+MI+NS-TuA4, 24
Maksymovych, P.: NS+AS+SS+SP-WeM11, 30
Mancini, D.C.: NS+SP-MoA11, 14
Mann, W.: NS-ThM6, 49
Mansour, A.N.: GR+AS+NS+SS-ThM10, 47
Margarella, A.: SS+NS-TuA3, 25
Marichy, C.: TF+NS+EM-ThM9, 52
Marinella, M.: ET+NS+EM-ThM10, 45
Marquis, E.A.: AS+NS+SS+TF-WeA1, 35
Martinez, E.: NS-ThM10, 49
Martini, A.: SE+NS-MoA1, 14
Mastro, M.A.: TF+NS+EM-ThM1, 51

Mathieu, P.: NS+SP-MoA7, 13
Matsubayashi, A.: GR+AS+EM+NS+SS-WeA7, 36
Matsumoto, K.: ET+NS+EM-ThM5, 44
Matsunaga, S.: BI+SS+NS-WeM11, 29
Mattson, E.: GR+AS+NS+SP+SS-TuA2, 19
Mayer, B.: SE+NS-MoM5, 7
Mayrhofer, P.H.: SE+NS-MoM5, 7; SE+NS-MoM6, 7
McClimon, J.B.: EM+NS-FrM6, 62
McGuckin, T.: NS+EN-TuM6, 18
McGuire, C.: GR+EM+ET+MS+NS-FrM3, 64
McNeilan, J.D.: GR+AS+NS+SP+SS-TuA11, 20
Mei, A.R.B.: TF+NS+EM-ThM12, 53
Meléndez-Lira, M.: NS-MoM2, 4
Melvin, T.: SE+NS-MoA3, 14
Membreno, D.: EN+NS-ThM6, 43
Mendez, N.: BI+SS+NS-WeM6, 28
Meng, G.W.: ET+NS+EM-ThM4, 44
Menzel, D.: SS+NS-TuA1, 25
Meseck, G.R.: NS-ThP1, 59
Meyer, D.J.: GR+EM+ET+MS+NS-FrM5, 64
Meyer, G.: SP+AS+BI+ET+MI+NS-TuA1, 23
Miao, X.: GR+EM+ET+MS+NS-FrM11, 65
Michallon, P.: NM+NS+MS+EM-MoA6, 11
Michely, T.W.: GR+AS+NS+SP+SS-TuA7, 19; GR+EM+NS+PS+SS+TF-MoM5, 3
Mickel, P.R.: ET+NS+EM-ThM10, 45
Mihaila, B.: EM+NS-FrM11, 63
Mikkelsen, A.: ET+NS+EM-ThM6, 45; SS+NS-ThA1, 56
Mitterer, C.: SE+NS-MoM6, 7; SE+NS-MoM9, 8
Miyashita, H.: GR+EM+NS+PS+SS+TF-MoM10, 3
Mleczyko, M.: NS-ThP2, 59
Mohn, F.: SP+AS+BI+ET+MI+NS-TuA1, 23
Molkenboer, F.T.: HI+AS+NS-WeA9, 38
Moll, N.: SP+AS+BI+ET+MI+NS-TuA1, 23
Mönig, H.: SP+AS+BI+ET+MI+NS-TuA10, 24
Montgomery, A.M.: TF+EM+SE+NS-ThM4, 50
Moon, J.S.: GR+EM+ET+MS+NS-FrM3, 64; GR+EM+NS+PS+SS+TF-MoM1, 2
Moore, R.: GR+AS+NS+SP+SS-TuA11, 20
Moore, T.M.: NS+SP-MoA4, 13
Morales, C.: NS-MoM9, 5
Mordí, G.: GR+EM+ET+MS+NS-FrM7, 64
Morgen, P.: EM+NS-FrM4, 62; EM+SS+AS+NS-ThM3, 41
Morita, S.: SP+AS+BI+ET+MI+NS-TuA11, 25
Mousa, M.B.: NM+NS+MS+EM-MoA8, 11
Mowll, T.: GR+EM+NS+PS+SS+TF-MoM2, 2
Mráz, S.: SE+NS-MoM8, 7
Mücklich, A.: SE+NS-MoM2, 7
Muirhead, L.: IS+AS+BI+ET+GR+NS-TuA3, 21
Mukherjee, D.: EN+NS-MoM6, 1; OX+EM+MI+NS+TF-MoM1, 5
Mukherjee, P.: EN+NS-MoM6, 1; OX+EM+MI+NS+TF-MoM1, 5
Mullet, C.: NS-ThM6, 49; SS+NS-ThA6, 56
Munson, A.: GR+AS+NS+SP+SS-TuA11, 20
Muratore, C.: SE+NS-MoA1, 14
Murphy, C.J.: EM+SS+AS+NS-ThM9, 41
Music, D.: SE+NS-MoM8, 7
Mutombo, P.: SP+AS+BI+ET+MI+NS-TuA4, 24
Myers-Ward, R.L.: GR+AS+NS+SP+SS-TuA9, 20; GR+EM+ET+MS+NS-FrM3, 64; GR+EM+ET+MS+NS-FrM5, 64; GR+EM+ET+NS+TF-MoA1, 9; GR+EM+NS+PS+SS+TF-MoM1, 2; GR+EM+NS+PS+SS+TF-MoM3, 2

— N —
Na, J.H.: NS-ThP6, 59
Nabok, A.V.: NS+SP-MoA1, 12
Naes, B.E.: AS+NS+SS+TF-WeA7, 35
Nagano, S.: HI+AS+BI+NS-ThM12, 48
Nagareddy, V.K.: GR+EM+NS+PS+SS+TF-MoM1, 2
Nahif, F.: SE+NS-MoM8, 7
Najmaei, S.: GR+EM+NS+SS+TF-ThA3, 55

Nakamura, J.: GR+AS+EM+NS+SS-WeA12, 37
Nakatsuji, K.: GR+AS+NS+SS-ThM1, 46
Nanayakkara, S.: NS-WeA1, 39
Nasse, M.: GR+AS+NS+SP+SS-TuA2, 19
Natarajarathinam, A.: TF+SE+NS-WeM10, 33
Nath, A.: GR+EM+ET+MS+NS-FrM5, 64; GR+EM+ET+NS+TF-MoA1, 9; GR+EM+NS+PS+SS+TF-MoM1, 2; GR+EM+NS+PS+SS+TF-MoM3, 2
Nayfeh, O.: GR+EM+ET+MS+NS-FrM8, 65
Nayyar, N.: NS-WeA9, 39
N'Diaye, A.T.: GR+AS+EM+NS+SS-WeA10, 37
Nelson, F.J.: GR+AS+NS+SP+SS-TuA11, 20
Nepal, N.: GR+EM+ET+NS+TF-MoA1, 9; TF+NS+EM-ThM1, 51
Newbury, J.S.: EM+NS-FrM10, 63
Nigge, P.: IS+AS+BI+ET+GR+NS-TuA9, 22
Notte, J.: HI+AS+NS-WeA10, 38
Nozik, A.J.: EN+NS-MoM3, 1
Nyakiti, L.O.: GR+AS+NS+SP+SS-TuA9, 20; GR+EM+ET+MS+NS-FrM3, 64; GR+EM+ET+MS+NS-FrM5, 64; GR+EM+ET+NS+TF-MoA1, 9; GR+EM+NS+PS+SS+TF-MoM1, 2; GR+EM+NS+PS+SS+TF-MoM3, 2

— O —
Oates, T.W.H.: SE+NS-MoM2, 7
O'Brien, K.E.: NS-WeA2, 39
Ocola, L.E.: NS+SP-MoA10, 14
Oda, S.: NS+EN-TuM5, 17
Oden, M.: TF+NS+EM-ThM12, 53
Odén, M.: TF+NS+EM-ThM11, 53
Ogaki, R.: BI+SS+NS-WeM1, 28
Oh, D.-H.: NS+EN-TuM1, 17; SS+NS-ThA3, 56
Ohkouchi, T.: GR+EM+NS+PS+SS+TF-MoM10, 3
Ohta, T.: GR+AS+NS+SP+SS-TuA8, 19
Oldham, C.J.: NM+NS+MS+EM-MoA8, 11
Oleynik, I.I.: GR+AS+EM+NS+SS-WeA2, 36
Ondracek, M.: SP+AS+BI+ET+MI+NS-TuA4, 24
Onishi, K.: HI+AS+BI+NS-ThM12, 48
Oppen, F.V.: SP+AS+BI+ET+MI+NM+NS+SS+TF-WeM4, 31
Osgood, R.M.: SS+NS-TuA4, 26
Oshima, M.: GR+AS+EM+NS+SS-WeA12, 37
Ostrikov, K.: TF+EM+SE+NS-ThM1, 50
Ou, Y.-C.: NS-ThP7, 60
Outlaw, R.A.: GR+AS+NS+SS+ThM10, 47
Ouyang, W.: ET+NS+EM-ThM3, 44
Owen, A.G.: TF+EM+SE+NS-ThM4, 50
Ozcan, A.: EM+NS-FrM9, 63

— P —
Pacholski, M.L.: AS+NS+SS+TF-WeA9, 36
Padbury, R.P.: TF+NS+EM-ThM5, 52
Page, S.J.: AS+NS+SS+TF-WeA8, 35
Paiella, R.: EM+SS+AS+NS-ThM1, 41
Pal, S.: NS-MoM9, 5
Palomino, R.: NS+AS+SS+SP-WeM12, 30
Pan, H.B.: SS+NS-TuA11, 26
Pan, M.H.: SP+AS+BI+ET+MI+NS-TuA12, 25
Pan, Y.H.: SS+NS-TuA11, 26
Pandey, A.: NS-WeA10, 40
Pandey, R.R.: NS-MoM11, 5
Park, C.-Y.: GR+EM+NS+PS+SS+TF-MoM4, 3; NS+EN-TuM1, 17; SS+NS-ThA3, 56
Park, D.-G.: EM+NS-FrM10, 63
Park, H.: NS+AS+SS+SP-WeM12, 30
Park, J.H.: EN+NS-MoM1, 1
Park, J.-H.: GR+EM+NS+PS+SS+TF-MoM11, 3
Park, J.-H.: NS-ThP9, 60
Park, T.H.: NS-WeA1, 39
Parkin, J.D.: SP+AS+BI+ET+MI+NM+NS+SS+TF-WeM9, 31
Parracino, M.A.: NS+EN+GR-TuA2, 22

Parsons, G.N.: EN+NS-ThA1, 54; NM+NS+MS+EM-MoA8, 11; NS+EN+GR-TuA10, 23
Pascual, J.I.: SP+AS+BI+ET+MI+NM+NS+SS+TF-WeM4, 31
Pattanaik, G.: EN+NS-ThM9, 43
Patzke, G.R.: NS-ThP1, 59
Paul, D.F.: NS-ThM12, 50
Paul, P.: NS+SP-MoA2, 12
Paulitsch, J.: SE+NS-MoM5, 7
Pedersen, K.: EM+NS-FrM4, 62
Pelant, I.: NS-MoM5, 4
Pelissier, B.: NM+NS+MS+EM-MoA6, 11
Perdue, S.M.: SP+AS+BI+ET+MI+NS-TuA3, 24
Perea, D.E.: AS+NS+SS+TF-WeA3, 35; AS+NS+SS+TF-WeA4, 35; NS-WeA10, 40
Perez Medina, G.J.: GR+EM+ET+NS+TF-MoA7, 9
Perez Roldan, M.J.: NS+EN+GR-TuA2, 22
Perez, R.: SP+AS+BI+ET+MI+NS-TuA10, 24; SP+AS+BI+ET+MI+NS-TuA11, 25
Perng, Y.-C.: EN+NS-ThM6, 43
Pernites, R.B.: EN+NS-ThM12, 44
Persson, O.: ET+NS+EM-ThM6, 45
Petersen, E.: NS+AS+SS+SP-WeM2, 30
Petford-Long, A.: IS+AS+BI+ET+GR+NS-TuA7, 21
Petrov, I.: TF+NS+EM-ThM12, 53
Pettersson, M.K.: GR+EM+ET+MS+NS-FrM11, 65
Pfeiffer, D.: EM+NS-FrM10, 63
Pham, C.D.: TF+NS+EM-ThM6, 52
Phan, M.H.: NS-MoM8, 4; NS-MoM9, 5
Phillpot, S.R.: SS+NS-ThA4, 56
Piallat, F.: NM+NS+MS+EM-MoA6, 11
Pillatsch, L.: HI+AS+NS-WeA10, 38
Pinna, N.: TF+NS+EM-ThM9, 52
Pipe, K.P.: EM+SS+AS+NS-ThM13, 42
Pitters, J.: SP+AS+BI+ET+MI+NM+NS+SS+TF-WeM2, 31
Pitters, J.L.: HI+AS+NS-WeA7, 38
Piva, P.: SP+AS+BI+ET+MI+NM+NS+SS+TF-WeM2, 31
Pluchery, O.: EM+NS-FrM3, 62
Poelsema, B.: HI+AS+NS-WeA3, 37
Pohler, M.: SE+NS-MoM9, 8
Polina, A.: HI+AS+BI+NS-ThM5, 47
Popov, E.O.: SE+NS-MoA7, 15
Popovitz-Biro, R.: NS+AS+SS+SP-WeM4, 30
Porcher, W.: EN+NS-ThM11, 43
Portoles, J.F.: SP+AS+BI+ET+MI+NM+NS+SS+TF-WeM10, 32
Potapenko, D.V.: SS+NS-TuA4, 26
Pou, P.: SP+AS+BI+ET+MI+NS-TuA11, 25
Pradeep, N.: NS+SP-MoA8, 13
Prokes, S.M.: NS+EN-TuM2, 17
Pu, H.: GR+AS+NS+SP+SS-TuA2, 19
Putkonen, M.: NM+NS+MS+EM-MoA1, 10

— Q —
Qin, S.Y.: ET+NS+EM-ThM3, 44; ET+NS+EM-ThM4, 44
Quinlan, R.A.: GR+AS+NS+SS-ThM10, 47
Quiñones-Galván, J.G.: NS-MoM2, 4
Quinton, J.S.: SS+NS-ThA7, 57

— R —
Rack, P.D.: NS+SP-MoA4, 13; TF+EM+SE+NS-ThM3, 50
Radvanyi, E.: EN+NS-ThM11, 43
Rafaja, D.: SE+NS-MoM3, 7
Rafik, A.: GR+AS+EM+NS+SS-WeA8, 36
Rahman, T.S.: GR+EM+ET+NS+TF-MoA2, 9; NS+EN+GR-TuA7, 23; NS-MoM10, 5; NS-WeA9, 39; SS+NS-ThA9, 57
Randall, J.N.: NS+SP-MoA7, 13
Rao, M.V.: GR+EM+NS+PS+SS+TF-MoM1, 2
Raschke, M.B.: NS-WeA7, 39
Raso, R.: AS+NS+SS+TF-WeA8, 35

- Ratner, B.D.: IS+AS+BI+ET+GR+NS-TuA1, 21
Raymond, M.: EM+NS-FrM9, 63
Raynaud, P.: TF+NS+EM-ThM3, 52
Rebello de Figueiredo, M.: SE+NS-MoM6, 7
Reeves, R.: TF+EM+SE+NS-ThM5, 51
Reid, D.: NS+AS+SS+SP-WeM2, 30
Reinke, P.: EM+NS-FrM6, 62
Renaux, F.: SE+NS-MoA4, 15
Reniers, F.: SE+NS-MoA4, 15
Resta, A.: GR+EM+NS+SS+TF-ThA6, 55
Rhim, S.: GR+AS+NS+SP+SS-TuA2, 19
Richter, R.P.: BI+SS+NS-WeM10, 29
Rinzler, A.G.: GR+EM+ET+MS+NS-FrM11, 65
Roberts, A.J.: AS+NS+SS+TF-WeA8, 35
Roberts, C.J.: BI+SS+NS-WeM12, 29;
SP+AS+BI+ET+MI+NS-TuA9, 24
Roberts, N.A.: NS+SP-MoA4, 13;
TF+EM+SE+NS-ThM3, 50
Robinson, J.T.: GR+AS+NS+SP+SS-TuA8, 19;
GR+AS+NS+SS-ThM3, 46
Robinson, Z.R.: GR+AS+NS+SP+SS-TuA11, 20;
GR+EM+NS+PS+SS+TF-MoM2, 2
Rockett, A.: TF+NS+EM-ThM12, 53
Rodriguez Perez, A.: SP+AS+BI+ET+MI+NS-
TuA3, 24
Rogers, J.A.: EM+SS+AS+NS-ThM5, 41
Rogström, L.: TF+NS+EM-ThM11, 53
Rojas, G.: NS+AS+SS+SP-WeM11, 30
Roldan Cuenya, B.: SS+NS-ThA8, 57; SS+NS-
TuA7, 26
Ronkainen, H.: TF+NS+EM-ThM10, 53
Ronsheim, P.: EM+NS-FrM10, 63
Rosa, L.: GR+EM+ET+NS+TF-MoA7, 9
Ross, F.M.: GR+EM+NS+PS+SS+TF-MoM8, 3
Rossi, F.: NS+EN+GR-TuA2, 22
Rosso, K.M.: NS-ThM2, 48
Rotello, V.: BI+SS+NS-WeM3, 28
Rotenberg, E.: GR+EM+ET+NS+TF-MoA8, 10
Rougemmaile, N.: GR+AS+EM+NS+SS-WeA10,
37
Routaboul, L.: GR+EM+ET+NS+TF-MoA7, 9
Rowe, J.E.: GR+AS+NS+SP+SS-TuA11, 20;
GR+EM+ET+MS+NS-FrM8, 65
Ruoff, R.S.: GR+AS+NS+SP+SS-TuA11, 20;
GR+AS+NS+SP+SS-TuA2, 19
Rutt, H.N.: HI+AS+BI+NS-ThM3, 47
- S —
Sadowski, J.T.: IS+AS+BI+ET+GR+NS-TuA8, 22
Safron, N.: GR+AS+EM+NS+SS-WeA9, 36
Sahalov, H.: EM+NS-FrM6, 62
Saini, K.K.: NS-MoM11, 5
Saito, N.: NS-ThP11, 60; NS-ThP4, 59; NS-ThP8,
60
Sakalas, P.: GR+AS+NS+SS-ThM2, 46
Sakurai, M.: GR+AS+EM+NS+SS-WeA12, 37
Sales, B.C.: SP+AS+BI+ET+MI+NS-TuA12, 25
Salib, D.: SP+AS+BI+ET+MI+NM+NS+SS+TF-
WeM5, 31
Saly, M.J.: TF+NS+EM-ThM2, 51
Samuelson, L.: ET+NS+EM-ThM6, 45
Sandin, A.A.: GR+AS+NS+SP+SS-TuA11, 20;
GR+EM+ET+MS+NS-FrM8, 65
Santos, P.V.: NS+SP-MoA9, 13
Santoyo-Salazar, J.: NS-MoM2, 4
Sardela, M.: TF+NS+EM-ThM12, 53
Sasi-Zsabo, L.A.: IS+AS+BI+ET+GR+NS-TuA3,
21
Schafer, K.C.: IS+AS+BI+ET+GR+NS-TuA3, 21
Schlögl, M.: SE+NS-MoM5, 7; SE+NS-MoM6, 7
Schlueter, J.A.: NS+AS+SS+SP-WeM11, 30
Schmid, A.K.: GR+AS+EM+NS+SS-WeA10, 37
Schmitt, J.: OX+EM+MI+NS+TF-MoM10, 6
Schmitz, A.: GR+EM+ET+MS+NS-FrM3, 64
Schneider, J.M.: SE+NS-MoM8, 7
Schoenfeld, W.V.: NM+NS+MS+EM-MoA9, 11
Schofield, M.: GR+AS+NS+SP+SS-TuA2, 19
Schrimpf, R.D.: EM+SS+AS+NS-ThM11, 42
Schroder, U.: GR+AS+NS+SP+SS-TuA7, 19
Schroter, M.: GR+AS+NS+SS-ThM2, 46
- Schubert, E.F.: TF+SE+NS-WeM1, 32
Schulte, K.: GR+AS+NS+SP+SS-TuA7, 19
Schulze, R.K.: EM+NS-FrM11, 63
Schwarz, U.D.: SP+AS+BI+ET+MI+NS-TuA10,
24
Schwendemann, T.C.: SP+AS+BI+ET+MI+NS-
TuA10, 24
Seal, S.S.: NS+AS+SS+SP-WeM2, 30
Seeger, S.: NS-ThP1, 59
Sefat, A.S.: SP+AS+BI+ET+MI+NS-TuA12, 25
Seitz, O.: EM+NS-FrM3, 62
Sekine, M.: GR+AS+NS+SS-ThM9, 47
Semidey-Flecha, L.: GR+AS+EM+NS+SS-
WeA11, 37
Semonin, O.E.: EN+NS-MoM3, 1
Seo, H.: EN+NS-MoM2, 1
Seo, H.-C.: GR+EM+ET+MS+NS-FrM3, 64
Seo, J.: NS-ThP9, 60
Seo, J.-W.T.: NS+EN-TuM12, 18
Setvin, M.: SP+AS+BI+ET+MI+NS-TuA4, 24
Seyhan, A.: NS+EN-TuM5, 17
Seyller, Th.: GR+EM+ET+NS+TF-MoA8, 10;
GR+EM+NS+PS+SS+TF-MoM10, 3
Shafai, G.: NS-MoM10, 5
Shaifai, G.: SS+NS-ThA9, 57
Shakouri, A.: SE+NS-MoA8, 15
Shalimov, A.: SE+NS-MoM2, 7
Sharma, M.: OX+EM+MI+NS+TF-MoM10, 6
Shearer, J.C.: SE+NS-MoA6, 15
Sheehan, P.E.: GR+AS+NS+SS-ThM3, 46
Shen, G.: ET+NS+EM-ThM11, 45; NS+EN-
TuM3, 17; NS-ThM11, 49
Shepard, K.L.: GR+EM+ET+NS+TF-MoA10, 10
Shi, Z.: NS-ThP2, 59
Shigekawa, H.: NS-ThM5, 49
Shih, C.: ET+NS+EM-ThM3, 44
Shikano, T.: GR+AS+EM+NS+SS-WeA12, 37
Shimizu, H.: BI+SS+NS-WeM11, 29
Shin, B.G.: SS+NS-ThA3, 56
Shin, H.: GR+EM+NS+PS+SS+TF-MoM4, 3; NS-
ThP9, 60
Shin, H.-J.: GR+EM+NS+PS+SS+TF-MoM11, 3
Shin, N.: NS+EN-TuM4, 17; NS-WeA11, 40
Shirani, M.: EN+NS-MoM2, 1
Sholl, D.: GR+AS+EM+NS+SS-WeA11, 37
Shutthanandan, V.: AS+NS+SS+TF-WeA4, 35
Sijbrandij, S.: HI+AS+NS-WeA10, 38
Silva, A.: EM+NS-FrM4, 62
Silver, R.: NS+SP-MoA8, 13
Simanullang, M.: NS+EN-TuM5, 17
Simmons, M.Y.: NS-MoM3, 4
Sinnott, S.B.: SS+NS-ThA4, 56
Sinsabaugh, S.L.: EN+NS-ThM12, 44
Sivaram, S.: NS-WeA11, 40
Skomski, D.: SS+NS-ThA11, 57
Slattery, A.D.: SS+NS-ThA7, 57
Snyders, R.: SE+NS-MoA4, 15
Sojoudi, H.: GR+EM+ET+MS+NS-FrM9, 65
Song, E.B.: EM+SS+AS+NS-ThM11, 42
Song, I.: GR+EM+NS+PS+SS+TF-MoM4, 3;
NS+EN-TuM1, 17
Sonntag, M.D.: NS-ThP3, 59
Sottos, N.R.: SE+NS-MoA10, 15
Soudi, A.: ET+NS+EM-ThM12, 45
Spampinato, V.: NS+EN+GR-TuA2, 22
Spanier, J.E.: NS+EN-TuM6, 18
Spencer, N.D.: NS+SP-MoA2, 12
Srikanth, H.: NS-MoM8, 4; NS-MoM9, 5;
OX+EM+MI+NS+TF-MoM1, 5
Srivastava, N.: GR+AS+NS+SP+SS-TuA10, 20
Stein, M.J.: IS+AS+BI+ET+GR+NS-TuA1, 21
Steiner, M.B.: NS+EN-TuM9, 18
Stenger, B.: NS-ThM6, 49
Stine, R.: GR+AS+NS+SS-ThM3, 46
Stojak, K.: NS-MoM9, 5
Stolbov, S.: EN+NS-ThM3, 43
Stone, D.: SE+NS-MoA1, 14
Strocio, J.A.: GR+EM+ET+NS+TF-MoA10, 10
Stuart, S.C.: GR+EM+ET+MS+NS-FrM8, 65
- Su, H.: TF+EM+SE+NS-ThM4, 50; TF+SE+NS-
WeM10, 33
Subramanian, V.: AS+NS+SS+TF-WeA4, 35
Suemitsu, M.: GR+EM+NS+PS+SS+TF-MoM10,
3
Sugimoto, Y.: SP+AS+BI+ET+MI+NS-TuA11, 25
Sukenic, C.N.: OX+EM+MI+NS+TF-MoM11, 6
Sumpster, B.G.: NS+AS+SS+SP-WeM11, 30
Sun, D.Z.: SP+AS+BI+ET+MI+NM+NS+SS+TF-
WeM5, 31
Sung, C.Y.: GR+AS+NS+SP+SS-TuA11, 20
Suo, Z.: NS-ThM12, 50
Suthar, K.J.: NS+SP-MoA11, 14
Sutter, E.: GR+EM+NS+SS+TF-ThA2, 55
Sutter, P.W.: GR+AS+EM+NS+SS-WeA8, 36;
GR+EM+NS+SS+TF-ThA2, 55
Suzuki, T.: GR+AS+EM+NS+SS-WeA12, 37
Svedberg, E.B.: EN+NS-ThA7, 54
Sykes, C.H.: EM+SS+AS+NS-ThM9, 41
- T —
Taing, J.: SS+NS-TuA3, 25
Tait, S.L.: SS+NS-ThA11, 57
Takagi, K.: GR+AS+NS+SS-ThM1, 46
Takai, O.: NS-ThP4, 59
Takats, Z.: IS+AS+BI+ET+GR+NS-TuA3, 21
Tamanaha, C.R.: GR+AS+NS+SS-ThM3, 46
Tanaka, S.: GR+AS+NS+SS-ThM1, 46
Tantardini, G.F.: GR+AS+EM+NS+SS-WeA12,
37
Taschuk, M.T.: TF+SE+NS-WeM11, 34;
TF+SE+NS-WeM5, 33; TF+SE+NS-WeM9,
33
Taucer, M.:
SP+AS+BI+ET+MI+NM+NS+SS+TF-WeM2,
31
Tawalbeh, T.: EM+NS-FrM9, 63
Temple, D.S.: EN+NS-MoM11, 2
Tendler, S.J.B.: SP+AS+BI+ET+MI+NS-TuA9, 24
Teng, D.: GR+AS+EM+NS+SS-WeA11, 37
Tenne, R.: NS+AS+SS+SP-WeM4, 30
Terfort, A.: SS+NS-ThA10, 57
Thakur, M.: EN+NS-ThM12, 44
Therien, M.: NS-WeA1, 39
Thevuthasan, S.: AS+NS+SS+TF-WeA3, 35;
AS+NS+SS+TF-WeA4, 35;
IS+AS+BI+ET+GR+NS-TuA12, 22; NS-
WeA10, 40
Thomas, E.: SE+NS-MoA11, 16
Timm, R.: ET+NS+EM-ThM6, 45
Tivanski, A.: IS+AS+BI+ET+GR+NS-TuA9, 22
Tkadletz, M.: SE+NS-MoM6, 7
Todorovic, M.: SP+AS+BI+ET+MI+NS-TuA10,
24
Tolbert, L.: GR+EM+ET+MS+NS-FrM9, 65
Tolmer, P.: NS-ThM11, 49
Tongay, S.: GR+EM+ET+MS+NS-FrM11, 65
Torija, M.: OX+EM+MI+NS+TF-MoM10, 6
Trioni, M.I.: GR+AS+EM+NS+SS-WeA12, 37
Tripp, R.A.: TF+SE+NS-WeM12, 34
Tromp, R.M.: GR+EM+NS+PS+SS+TF-MoM8, 3
Tsargorodska, A.B.: NS+SP-MoA1, 12
Tsong, T.T.: HI+AS+NS-WeA8, 38
Tsuchikawa, R.: NS+EN-TuM11, 18
Tsverin, Y.: NS+AS+SS+SP-WeM4, 30
Tucker, R.T.: TF+SE+NS-WeM11, 34;
TF+SE+NS-WeM9, 33
Turchanin, A.: HI+AS+BI+NS-ThM11, 48;
HI+AS+BI+NS-ThM5, 47
Turkowski, V.: NS-WeA9, 39
Tyagi, P.: GR+AS+NS+SP+SS-TuA11, 20;
GR+EM+NS+PS+SS+TF-MoM2, 2
Tyliszczak, T.: IS+AS+BI+ET+GR+NS-TuA9, 22
- U —
Uchida, G.: EN+NS-MoM2, 1
Ulrich, M.D.: GR+EM+ET+MS+NS-FrM8, 65
Ünverdi, Ö.: SP+AS+BI+ET+MI+NS-TuA10, 24
Urban, R.: HI+AS+NS-WeA7, 38
Usami, K.: NS+EN-TuM5, 17

Ushigome, D.: GR+AS+EM+NS+SS-WeA12, 37
— **V** —
Vallée, C.: NM+NS+MS+EM-MoA6, 11
Valtiner, M.: BI+SS+NS-WeM5, 28
van der Veen, J.: NS+SP-MoA9, 13
van der Wiel, W.G.: NS+SP-MoA9, 13
Van Duyne, R.P.: NS-ThP3, 59; NS-WeA3, 39
Van Veldhoven, E.: HI+AS+NS-WeA9, 38
van Zijll, M.: NS-ThM6, 49
Vandencastelee, N.: SE+NS-MoA4, 15
Vanhove, N.: HI+AS+NS-WeA10, 38
Varela, M.: OX+EM+MI+NS+TF-MoM10, 6
Vasiliev, I.V.: EM+NS-FrM9, 63
Ventrice, Jr., C.A.: GR+AS+NS+SP+SS-TuA11, 20; GR+EM+NS+PS+SS+TF-MoM2, 2
Veyan, J.-F.: NS+SP-MoA7, 13
Vieker, H.: HI+AS+BI+NS-ThM5, 47
Vilayrganapathy, S.: NS-WeA10, 40
Voevodin, A.A.: SE+NS-MoA1, 14
Vogt, P.: GR+EM+NS+SS+TF-ThA6, 55
von Bergmann, K.: NS-ThM1, 48
Vo-Van, C.: GR+AS+EM+NS+SS-WeA10, 37
Vratzov, B.: NS+SP-MoA9, 13
— **W** —
Wallace, D.C.: EM+NS-FrM11, 63
Wallace, R.M.: GR+AS+EM+NS+SS-WeA1, 36; GR+EM+ET+MS+NS-FrM7, 64
Walrath, J.C.: EM+SS+AS+NS-ThM13, 42
Walter, A.: GR+EM+ET+NS+TF-MoA8, 10
Walton, S.G.: GR+EM+NS+PS+SS+TF-MoM1, 2
Wang, B.: IS+AS+BI+ET+GR+NS-TuA9, 22
Wang, G.-C.: TF+SE+NS-WeM4, 33
Wang, J.: HI+AS+BI+NS-ThM9, 48; NS-MoM9, 5
Wang, K.L.: EM+SS+AS+NS-ThM11, 42
Wang, L.: GR+EM+ET+NS+TF-MoA10, 10
Wang, P.: NS-WeA2, 39
Wang, Y.: EN+NS-MoM2, 1
Waters, J.: NS+EN-TuM3, 17
Waterton, C.: IS+AS+BI+ET+GR+NS-TuA1, 21
Watkins, J.: NM+NS+MS+EM-MoA10, 12
Weber, N.-E.: HI+AS+BI+NS-ThM5, 47
Weeks, S.L.: NS-MoM6, 4
Weinert, M.: GR+AS+NS+SP+SS-TuA2, 19

Weitering, H.: ET+NS+EM-ThM3, 44
Weller, T.: NS-MoM9, 5
Wenger, W.N.: EN+NS-MoM5, 1
Wheeler, V.D.: GR+AS+NS+SP+SS-TuA9, 20; GR+EM+ET+MS+NS-FrM3, 64; GR+EM+ET+MS+NS-FrM5, 64; GR+EM+ET+NS+TF-MoA1, 9; GR+EM+NS+PS+SS+TF-MoM1, 2; GR+EM+NS+PS+SS+TF-MoM3, 2
White, M.G.: NS+AS+SS+SP-WeM12, 30
Wiesendanger, R.: NS-ThM1, 48
Wilbert, D.S.: ET+NS+EM-ThM11, 45
Wildman, H.: EM+NS-FrM10, 63
Willunat, A.: HI+AS+BI+NS-ThM11, 48; HI+AS+BI+NS-ThM5, 47
Winkler, K.: GR+AS+NS+SP+SS-TuA1, 19
Winter, A.: HI+AS+BI+NS-ThM11, 48; HI+AS+BI+NS-ThM5, 47
Wirtz, T.: HI+AS+NS-WeA10, 38
Witanachchi, S.: EN+NS-MoM6, 1; OX+EM+MI+NS+TF-MoM1, 5
Wolf, H.: NS+SP-MoA2, 12
Wolkow, R.A.: HI+AS+NS-WeA7, 38; SP+AS+BI+ET+MI+NM+NS+SS+TF-WeM2, 31
Woll, A.R.: IS+AS+BI+ET+GR+NS-TuA2, 21
Wolter, B.: NS-ThM1, 48
Wong, M.S.: EN+NS-ThM12, 44
Wu, R.: ET+NS+EM-ThM3, 44
Wu, S.: GR+AS+NS+SP+SS-TuA12, 20
Wu, Y.: EN+NS-ThA3, 54; TF+EM+SE+NS-ThM3, 50
Wyrick, J.: SP+AS+BI+ET+MI+NM+NS+SS+TF-WeM5, 31
— **X** —
Xiao, Z.: NS-ThP12, 60
Xu, M.: NS-ThM2, 48
Xu, Y.: GR+AS+EM+NS+SS-WeA11, 37
— **Y** —
Yakobson, GR+EM+NS+SS+TF-ThA8, 55
Yamada, T.: BI+SS+NS-WeM11, 29
Yang, L.: IS+AS+BI+ET+GR+NS-TuA12, 22
Yaowarat, W.: NS-ThP11, 60

Yazawa, K.: SE+NS-MoA8, 15
Yazyev, O.V.: GR+AS+NS+SS-ThM5, 46
Ye, D.: TF+EM+SE+NS-ThM6, 51
Yellen, B.: BI+SS+NS-WeM9, 29
Yoshida, Y.: NS-ThM1, 48
Yoshimura, T.: GR+AS+NS+SS-ThM1, 46
You, M.Y.: NS-ThP6, 59
Young, A.: GR+EM+ET+NS+TF-MoA10, 10
Yu, J.: GR+AS+NS+SP+SS-TuA12, 20
Yu, X.-Y.: IS+AS+BI+ET+GR+NS-TuA12, 22
Yu, Z.: NS+AS+SS+SP-WeM4, 30
Yurtsever, A.: SP+AS+BI+ET+MI+NS-TuA11, 25
Yushin, G.: EN+NS-ThM4, 43
— **Z** —
Zang, F.: BI+SS+NS-WeM2, 28
Zauscher, S.: BI+SS+NS-WeM9, 29
Zegenhagen, J.: GR+AS+NS+SP+SS-TuA9, 20
Zehnder, D.: GR+EM+ET+MS+NS-FrM3, 64
Zettl, A.: GR+AS+NS+SS-ThM5, 46
Zettsu, N.: NS-ThP4, 59
Zhan, Y.: GR+EM+NS+SS+TF-ThA3, 55
Zhang, C.X.: EM+SS+AS+NS-ThM11, 42
Zhang, E.X.: EM+SS+AS+NS-ThM11, 42
Zhang, H.: HI+AS+BI+NS-ThM9, 48
Zhang, J.Z.: TF+SE+NS-WeM3, 32
Zhang, L.: GR+EM+ET+NS+TF-MoA11, 10
Zhang, X.: HI+AS+BI+NS-ThM5, 47
Zhang, Y.: ET+NS+EM-ThM3, 44
Zhang, Z.: NS+EN-TuM11, 18
Zhao, Y.: GR+EM+ET+NS+TF-MoA10, 10
Zhao, Y.-P.: TF+SE+NS-WeM12, 34; TF+SE+NS-WeM3, 32
Zhitenev, N.B.: GR+EM+ET+NS+TF-MoA10, 10
Zhou, J.: SS+NS-TuA12, 26
Zhou, Y.H.: SS+NS-TuA12, 26
Zhu, J.F.: GR+EM+ET+NS+TF-MoA11, 10; SS+NS-TuA11, 26
Zhu, Y.: SP+AS+BI+ET+MI+NM+NS+SS+TF-WeM5, 31
Zhu, Z.: EM+NS-FrM10, 63; IS+AS+BI+ET+GR+NS-TuA12, 22
Zollner, S.: EM+NS-FrM9, 63
Zunft, H.: NM+NS+MS+EM-MoA9, 11